TOPOLOGICAL EVOLUTION AND PROPERTIES OF SOL-GEL SILICA MONOLITHS

By

WANDER LUIZ VASCONCELOS

A DISSERTATION PRESENTED TO THE GRADUATE SCHOOL
OF THE UNIVERSITY OF FLORIDA
IN PARTIAL FULFILLMENT OF THE REQUIREMENTS
FOR THE DEGREE OF DOCTOR OF PHILOSOPHY

UNIVERSITY OF FLORIDA

1989

Dedicated to

my wife Josiane and my son Lucas

The concepts of topology, which are inherent in any sort of thinking about interacting systems, are almost totally unfamiliar to the ordinarily educated person. Though extraordinarily simple, the ideas of topology seem not to enter into the experience of any but the most specialized lives. As a consequence people tend to regard such ideas as strange and difficult. Thus, in inviting them to adopt the new viewpoint of microstructology, one is met with a double resistance, arising from a disinclination to abandon a familiar way of thinking and from difficulty in comprehending the new way. This is a particularly difficult obstacle to overcome and it is not likely to go away of its own accord. Some positive action will be required to stablish microstructology in the thinking of metallurgists.

Frederick Nims Rhines

ACKNOWLEDGMENTS

The author wishes to thank the following:

Dr. Larry L. Hench, supervisory committee chairman, for his continued advice and encouragement, and for the freedom he gave to the author during this research.

Dr. Robert T. DeHoff, supervisory committee cochairman, for the continued support and advice, and for the invaluable contributions in regard to all stages of this research.

Drs. Robert E. Reed-Hill, E. Dow Whitney, Richard L. Scheaffer, and Pejaver V. Rao, for the invaluable discussions and for serving on the supervisory committee.

Drs. Fereshteh Ebrahimi and Jon K. West, for the support and invaluable discussions.

Universidade Federal de Minas Gerais and CAPES (Brazilian Agency of Post-Graduation), for financial assistance to the author.

US-Air Force Office of Sponsored Research, for the support to this research.

TABLE OF CONTENTS

Page

ACKNOWLEDGMENTS iv
LIST OF TABLES ix
LIST OF FIGURES x
ABSTRACT xxx

CHAPTER

1 THE SOL-GEL METHOD 1

1.1 Introduction 1

1.2 Objectives 3

1.3 Sol-Gel Technology 6
1.3.1 Evolution of Sol-Gel Technology 6
1.3.2 Motivation for the Sol-Gel Method 8
1.3.3 The Sol-Gel Process 10
1.3.4 Structure of Sols 12
1.3.5 Mixing 15
1.3.6 Casting 21
1.3.7 Gelation 22
1.3.8 Aging 29
1.3.9 Drying 34

2 DENSIFICATION OF GEL-SILICA 42

2.1 The Sintering Process 42
2.1.1 Introduction 42
2.1.2 Mechanisms of Sintering 45
2.1.3 The Rhines-DeHoff Model 46
2.1.4 Frenkel's Model 48
2.1.5 Mackenzie-Shuttleworth's Model 50

2.1.6 Scherer's Model 53
2.1.7 Densification of Gel-Silica 55

2.2 Sol-Gel Processing 58
2.2.1 Chemical Processing of Pure Silica 58
2.2.2 Gelation and Aging 60
2.2.3 Drying 61

2.3 Large Pore Size Structures 64
2.3.1 HNO_3 Based Gels 64
2.3.2 HF Based Gels 64

2.4 Densification Processing 66
2.4.1 Partial Densification in Dry-Air Atmosphere 66
2.4.2 Stabilization and Densification Processing Using Chlorination 69

2.5 Gas Adsorption Analysis 69
2.5.1 BET Theory 69
2.5.2 Experimental Results 78

2.6 Evolution of Metric Properties During Sintering 89
2.6.1 Structural Density 89
2.6.2 Metric Properties 95

2.7 Humidity Effects on Densification 116

3 TOPOLOGICAL MODELING OF DENSIFICATION 122

3.1 Description of The Structure of Materials 122
3.1.1 The Metric Properties 122
3.1.2 The Topological Properties 127
3.1.3 Evaluation of Topological Properties 140

3.2 Topological Modeling 147
3.2.1 Introduction 147
3.2.2 Tetrahedral Modeling 151
3.2.3 Cylindrical Modeling 162
3.2.4 Spherical Modeling 165

3.3 Application of Topological Modeling to Gel-Silica 166
3.3.1 Small Pore Size Structures 166
3.3.2 Large Pore Size Structures 172

3.4 Topological Indexing 175
3.4.1 Relative Genus γ 175
3.4.2 Topological Index ß 178

3.5 Comparison of Models 187

3.6 Transmission Electron Microscopy Analysis 200

3.7 Sensitivity Analysis of the Pore Coordination Number .. 202

3.8 Topological Analysis of the Time and Humidity Effects 209

4 MECHANICAL ANALYSIS 213

4.1 The Strength of Brittle Materials 213

4.2 Microhardness 219

4.3 Flexural Testing 221

4.4 Uniaxial Compression Testing 226

4.5 Brazilian Testing 236

4.6 Fracture Analysis 238
4.6.1 Aspects of a Fracture Surface 238
4.6.2 Flexural Testing 245
4.6.3 Brazilian Testing 250

4.7 Dynamic Mechanical Analysis 263

5 THERMAL ANALYSIS 269

5.1 Thermal Expansion of Materials 269

5.2 Dilatometry 273
5.2.1 Dimensional Change Behavior of Silica Gel Monoliths 273
5.2.2 Large Pore Size Structures 278
5.2.3 Isothermal Experiments 282
5.2.4 Aspects of the Dimensional Change Curve 285

5.3 Thermogravimetric Analysis 288

6 STRUCTOLOGY 299

6.1 Concept of Structology 299

6.2 Structure and Mechanical Properties 300

6.3 Structure and Thermal Properties 332

6.4 Applications 352

6.5 Structological Analysis 358

7 CONCLUSIONS AND SUGGESTIONS FOR FUTURE WORK 367

APPENDIX 372

REFERENCES 376

BIOGRAPHICAL SKETCH 414

LIST OF TABLES

Table		Page
1.1	Silica-glass processes	4
1.2	Physico-chemical characteristics of different gel solutions	20
1.3	Gelation time for different catalysts	25
3.1	Features encountered in a polycrystalline material in relation to their dimensionalities	124
3.2	Euler characteristic (χ) of the surface M	131
3.3	Betti numbers of complexes with dimensionalities varying from 0 to 3	133
3.4	Independent topological parameters that can be associated to three-dimensional structures	138
3.5	Set of assumptions made to solve the equations corresponding to the tetrahedral geometric model	155
3.6	Set of assumptions made to solve the equations corresponding to the cylindrical geometric model	164
6.1	Coefficients of correlation (R^2) between physical properties and metric (V_V) and topological parameters (β and γ)	359

LIST OF FIGURES

Figure		Page
1.1	Tetrahedral coordination of SiO_2	2
1.2	Schematic of the sol-gel process	13
1.3	Schematic of a tri-functionally branched molecule	27
1.4	Schematic of the density variation with size for typical crystals and fractals	30
1.5	Plot of the rate of water loss from alumina gel versus water content of the gel	36
1.6	Time dependence of (a) temperature and weight; (b) absolute loss rate; and (c) loss rate per unit area for silica gel	38
1.7	Time dependence of (a) linear shrinkage, and (b) volumetric shrinkage of silica gel	39
1.8	Weight reduction (W/W_o) as a function of volumetric shrinkage (V/V_o) for silica gel	40
2.1	(a) Rounding and smoothing; (b) isolation of pores; and (c) segregation of pores	44
2.2	The three stages of sintering	47
2.3	Geometric model used in the Mackenzie-Shuttleworth's sintering model	51
2.4	Geometric model used in the Scherer's sintering model	54

Figure Page

2.5 Schematic of the sol-gel processing of gel-silica monoliths 59

2.6 Schematic of the aging temperature profile 62

2.7 Schematic of the drying temperature profile 63

2.8 Drying chamber 65

2.9 Schematic of the densification temperature profiles 67

2.10 Examples of pure silica gel monoliths densified in the range of 180 °C to 1000 °C in a dry-air atmosphere 68

2.11 Temperature profile for a chlorination experiment 70

2.12 Silica gel monoliths prepared in a dry-air atmosphere (500 °C to 1000 °C) and in a chlorine atmosphere (1150 °C) 71

2.13 The five types of adsorption isotherms as classified by Brunauer et al. W is the weight of gas adsorbed and P/P_o is the relative pressure 74

2.14 de Boer's five types of hysteresis loops 77

2.15 BET plot for a dried silica gel sample with 12 Å average pore radius 79

2.16 Volume of adsorbed gas versus partial pressure for a set of silica gel samples with 12 Å average pore radius densified in the range of 180 °C to 1150 °C 80

2.17 Volume of adsorbed gas versus partial pressure for dried silica gel samples with 12 Å, 32 Å and 81 Å average pore radii 82

Figure Page

2.18 Pore size distribution for dried silica gel samples with 12 Å, 32 Å and 81 Å average pore radii 83

2.19 Pore size distribution for silica gel samples with 12 Å average pore radius densified in the range of 180 °C to 1150 °C 84

2.20 Pore size distribution for silica gel samples with 32 Å average pore radius densified in the range of 180 °C to 1150 °C 85

2.21 Pore size distribution for silica gel samples with 81 Å average pore radius densified in the range of 180 °C to 1150 °C 86

2.22 Langmuir plots of dried silica gels with 12 Å, 32 Å and 81 Å average pore radii 87

2.23 Average pore radius versus densification temperature for samples type A 88

2.24 Variation of the average pore radius as a function of densification temperature for silica gel samples with 12 Å, 32 Å and 81 Å average pore radii 90

2.25 Variation of true density as a function of densification temperature for samples type A 91

2.26 Variation of true density as a function of densification temperature for samples type B 92

2.27 Variation of true density as a function of densification temperature for samples type C 93

2.28 Variation of true density (from polynomial equations) as a function of densification temperature for silica gel samples with 12 Å, 32 Å and 81 Å average pore radii 94

Figure Page

2.29 Variation of the volume fraction of pores (V_V) as a function of densification temperature for samples type A 96

2.30 Variation of the volume fraction of pores (V_V) as a function of densification temperature for silica gel samples with average pore radii of 12 Å, 32 Å and 81 Å 97

2.31 Variation of the surface area of pores per unit volume (S_V) as a function of densification temperature for samples type A 99

2.32 Variation of the surface area of pores per unit volume (S_V) as a function of densification temperature for silica gel samples of 12 Å, 32 Å and 81 Å average pore radii 100

2.33 Variation of the surface area of pores per unit volume (S_V) as a function of volume fraction of pores (V_V) for samples type A1 101

2.34 Variation of the surface area of pores per unit volume (S_V) as a function of volume fraction of pores (V_V) for samples type A2 102

2.35 Variation of the surface area of pores per unit volume (S_V) as a function of volume fraction of pores (V_V) for samples type A3 103

2.36 Variation of the surface area of pores per unit volume (S_V) as a function of volume fraction of pores (V_V) for samples type A4 104

2.37 Variation of the surface area of pores per unit volume (S_V) as a function of volume fraction of pores (V_V) for samples type B 105

2.38 Bulk density versus densification temperature for samples type A 107

Figure Page

2.39 Bulk density versus densification temperature for silica gel samples with 12 Å, 32 Å and 81 Å average pore radii 108

2.40 Variation of volume fraction of pores (V_V) as a function of bulk density for silica gel samples with 12 Å average pore radius 109

2.41 Variation of bulk density as a function of densification temperature for silica gel samples of 12 Å average pore radius, as measured by nitrogen gas adsorption (N) and mercury pycnometry (Hg) 110

2.42 Variation of bulk density as a function of densification temperature for silica gel samples of 81 Å average pore radius, as measured by nitrogen gas adsorption (N) and mercury pycnometry (Hg) 112

2.43 Variation of volume fraction of pores (V_V) as a function of densification temperature for samples type A kept at the densification temperature for 1 h and 10 h 113

2.44 Variation of the surface area of pores per unit volume (S_V) as a function of densification temperature for samples type A kept at the densification temperature for 1 h and 10 h 114

2.45 Variation of the volume fraction of pores (V_V) as a function of time for samples type A2 and A3 115

2.46 Variation of volume fraction of pores (V_V) as a function of densification temperature for samples type A densified in a dry-air (DA) and in a humid (OF) atmospheres 117

2.47 Variation of surface area of pores per unit volume (S_V) as a function of densification temperature for samples type A densified in a dry-air (DA) and in a humid (OF) atmospheres 118

Figure Page

2.48 Variation of bulk density as a function of densification temperature for samples type A2 densified in a dry-air (DA) and in a humid (OF) atmospheres 119

2.49 Variation of bulk density as a function of densification temperature for samples type A1 densified in a dry-air (DA) and in a humid (OF) atmospheres 120

3.1 Intersection conditions 129

3.2 (a) Sphere; (b) torus; (c) Klein bottle 132

3.3 Schematic of three-dimensional geometric shapes with zero connectivity (C) 135

3.4 Schematic of three-dimensional geometric shapes with connectivity (C) equal to one 136

3.5 Schematic of a structure formed by two linear features 141

3.6 Two-dimensional structure containing three holes 142

3.7 Schematic of a three-dimensional structure formed by two separate parts 144

3.8 Fundamental shapes used for geometric modeling 148

3.9 Tetrahedral geometric model assumed for topological modeling 149

3.10 Cylindrical geometric model assumed for topological modeling 150

3.11 Structural components of the tetrahedral geometric model 152

Figure Page

3.12 Variation of the number of nodes (N_V), number of branches (B_V) and genus (G_V) as a function of the pore coordination number (CN) when $P_V = 1$ 157

3.13 Schematic of the pore coordination number (CN) varying from 4 to 0 158

3.14 Variation of the number of nodes (N_V), number of branches (B_V), number of separate parts (P_V) and genus (G_V) as a function of the pore coordination number (CN) when Pv is variable 160

3.15 Variation of the number of nodes (N_V), number of branches (B_V), number of separate parts (P_V) and genus (G_V) as a function of the pore coordination number (CN) as assumed in the topological modeling. The points on the curves show where the experimental data obtained from samples type A are located (Model 12) 167

3.16 Variation of the number of nodes (N_V), number of branches (Bv), number of separate parts (P_V) and genus (G_V) as a function of densification temperature for samples type A1 (Model 12) 168

3.17 Variation of the number of nodes (N_V), number of branches (B_V), number of separate parts (P_V) and genus (G_V) as a function of densification temperature for samples type A2 (Model 12) 169

3.18 Variation of the number of nodes (N_V), number of branches (B_V), number of separate parts (P_V) and genus (G_V) as a function of densification temperature for samples type A3 (Model 12) 170

Figure Page

3.19 Variation of the number of nodes (N_V), number of branches (B_V), number of separate parts (P_V) and genus (G_V) as a function of densification temperature for samples type A4 (Model 12) 171

3.20 Variation of the number of nodes (N_V), number of branches (B_V), number of separate parts (P_V) and genus (G_V) as a function of densification temperature for samples type B (Model 12) 173

3.21 Variation of the number of nodes (N_V), number of branches (B_V), number of separate parts (P_V) and genus (G_V) as a function of densification temperature for samples type C (Model 12) 174

3.22 Variation of relative genus (γ) as a function of densification temperature for samples type A 176

3.23 Variation of relative genus (γ) as a function of densification temperature for silica gel samples with 12 Å, 32 Å and 81 Å average pore radius 177

3.24 Variation of the genus (G_V) as a function of densification temperature for silica gel samples with 12 Å, 32 Å and 81 Å average pore radii 179

3.25 Variation of relative genus (γ) as a function of volume fraction of pores (V_V) for samples type A1 180

3.26 Variation of relative genus (γ) as a function of volume fraction of pores (V_V) for samples type A2 181

3.27 Variation of relative genus (γ) as a function of volume fraction of pores (V_V) for samples type A3 182

3.28 Variation of relative genus (γ) as a function of volume fraction of pores (V_V) for samples type A4 183

Figure Page

3.29 Variation of relative genus (γ) as a function of volume fraction of pores (V_V) for samples type B 184

3.30 Variation of the topological index ß as a function of densification temperature for samples type A 186

3.31 Variation of the topological index ß as a function of densification temperature for silica gel samples with 12 Å, 32 Å and 81 Å average pore radii 188

3.32 Variation of the number of branches (B_V) as a function of densification temperature for silica gel samples with 12 Å, 32 Å and 81 Å average pore radii 189

3.33 Variation of volume fraction of pores (V_V) as a function of the topological index ß for samples type A1 (Model 12).. 190

3.34 Variation of volume fraction of pores (V_V) as a function of the topological index ß for samples type A2 (Model 12).. 191

3.35 Variation of volume fraction of pores (V_V) as a function of the topological index ß for samples type A3 (Model 12). 192

3.36 Variation of volume fraction of pores (V_V) as a function of the topological index ß for samples type A4 (Model 12).. 193

3.37 Variation of volume fraction of pores (V_V) as a function of the topological index ß for samples type A2 (Model 10) .. 194

3.38 Variation of the number of nodes (N_V), number of branches (B_V) and genus (G_V) as a function of densification temperature for samples type A2. Model 3 is a tetrahedral model and Model 6 is a cylindrical model 196

3.39 Variation of the number of nodes (N_V), number of branches (B_V) and genus (G_V) as a function of densification temperature for samples type A2. Model 3 assumes L and Model 4 assumes D 197

Figure Page

3.40 Variation of the number of nodes (N_V), number of branches (B_V) and genus (G_V) as a function of densification temperature for samples type A2. Model 6 assumes Pv = 1 and Model 12 accepts a variable P_V 198

3.41 Variation of the number of nodes (N_V) and number of branches (B_V) as a function of densification temperature for samples type A2. The numbers in the legend correspond to the model number 199

3.42 High-resolution transmission electron microscopy photo of a dried silica gel of 12 Å average pore radius 201

3.43 Variation of the pore coordination number (CN) as a function of densification temperature for initial CN's varying from 3 to 24 (Samples type A2) 203

3.44 Variation of the number of branches (B_V) as a function of densification temperature for samples type A. The numbers in the legend represent the pore coordination numbers in the beginning of densification (Samples type A2) 204

3.45 Variation of the number of branches (B_V) as a function of the volume fraction of pores (V_V) for assumed initial pore coordination numbers varying from 3 to 24 (Samples type A2) 206

3.46 Variation of the genus (G_V) as a function of densification temperature when the assumed initial pore coordination number varies from 3 to 24 (Samples type A2) 207

3.47 Variation of the genus (G_V) as a function of volume fraction of pores (V_V) when the assumed initial pore coordination number varies from 3 to 24 (Samples type A2) 208

Figure Page

3.48 Variation of the genus (G_V) as a function of densification temperature for samples type A1 kept at the densification temperature for 1 h and 10 h 210

3.49 Variation of the topological index ß as a function of the time the sample was held at 800 °C for samples type A1 and A2 211

3.50 Variation of the genus (G_V) as a function of densification temperature for samples type A1 densified in a dry-air (DA) atmosphere and in a humid (OF) atmosphere 212

4.1 Variation of the Vickers hardness number (VHN) as a function of densification temperature for silica gel samples of 12 Å, 32 Å and 81 Å average pore radii 220

4.2 Silica gel monoliths prepared for the tests indicated 223

4.3 Load (P) versus displacement for a four point bending test of a dried silica gel 224

4.4 Variation of flexural strength as a function of densification temperature for silica gel samples with 12 Å average pore radius 225

4.5 Variation of the flexural modulus as a function of densification temperature for silica gel samples of 12 Å average pore radius 227

4.6 Propagation of cracks in uniaxial compression 228

4.7 Variation of the uniaxial compression load (P) versus displacement for a dried silica gel 230

4.8 Variation of the compression strength as a function of densification temperature for samples type A1 and C 231

Figure Page

4.9 Variation of the compression modulus as a function of densification temperature for samples type A1, A3 and C. FQ represents fused quartz samples 233

4.10 Variation of compression strength as a function of densification temperature for samples type A1 densified in a dry-air (DA) atmosphere and in a humid (OF) atmosphere 234

4.11 Variation of compression modulus as a function of densification temperature for samples type A1 densified in a dry-air (DA) atmosphere and in a humid (OF) atmosphere 235

4.12 Stress distribution across a loaded diameter of a cylindrical sample in the Brazilian test 237

4.13 Load (P) versus displacement for a dried silica gel with 12 Å average pore radius in the Brazilian test 239

4.14 Variation of tensile strength (Brazilian test) as a function of densification temperature for samples type A1, A2 and C. FQ represents fused quartz samples 240

4.15 Schematic of a fracture surface showing the region of fracture origin, the fracture mirror, the mist and the hackle 242

4.16 Schematic of fracture surfaces showing (a) Wallner lines and (b) striations 243

4.17 SEM fracture surface of a dried silica gel sample with 12 Å average pore radius submitted to uniaxial compression 244

Figure Page

4.18 SEM fracture surfaces of a dried silica gel sample with 12 Å average pore radius submitted to four point bending. The photos represent the opposing sides of the fracture surface 246

4.19 SEM fracture surfaces of a silica gel sample with 12 Å average pore radius densified at 900 °C and submitted to four point bending. The photos represent the opposing sides of the fracture surface 247

4.20 Variation of the Vickers hardness number (VHN) with transverse position in a dried silica gel sample of 12 Å average pore radius. Positions 0 and 4.5 represent the external limiting surfaces of the specimen 248

4.21 Variation of the Vickers hardness number (VHN) with transverse position in a silica gel sample of 12 Å average pore radius densified at 900 °C. Positions 0 and 4.5 represent the external limiting surfaces of the specimen 249

4.22 Schematic of the fracture in four point bending. (a) Compression and tension regions. (b) Fracture surfaces. (c) Crack initiation at the middle of the surface under tension. (d) Crack initiation at one corner of the specimen 251

4.23 SEM fracture surface of a dried silica gel sample with 12 Å average pore radius submitted to Brazilian test 252

4.24 SEM fracture surface of a silica gel sample with 12 Å average pore radius densified at 600 °C and submitted to Brazilian test 253

4.25 SEM fracture surface of a silica gel sample with 12 Å average pore radius densified at 600 °C and submitted to Brazilian test 254

Figure Page

4.26 SEM fracture surface of a silica gel sample with 12 Å average pore radius densified at 700 °C and submitted to Brazilian test 255

4.27 SEM fracture surface of a silica gel sample with 12 Å average pore radius densified at 900 °C and submitted to Brazilian test 256

4.28 SEM fracture surface of a silica gel sample with 12 Å average pore radius densified at 1150 °C and submitted to Brazilian test 257

4.29 SEM fracture surface of a silica gel sample with 12 Å average pore radius densified at 1150 °C and submitted to Brazilian test 258

4.30 SEM fracture surface of a fused quartz sample submitted to Brazilian test 260

4.31 SEM fracture surface of a dried silica gel sample with 12 Å average pore radius submitted to Brazilian test. (a) General view; (b) detail of the secondary striations shown in (a) 261

4.32 Schematic of the observed fracture surfaces of silica gel samples in the Brazilian test. (a) Loading. (b) Fracture surface 262

4.33 Variation of tensile modulus (DMA) at 25 °C as a function of densification temperature for silica gel samples of 12 Å average pore radius 265

4.34 Variation of tensile modulus (DMA) as a function of densification temperature for silica gel samples of 12 Å average pore radius 267

Figure Page

4.35 Variation of shear modulus (DMA) as a function of densification temperature for silica gel samples of 12 Å average pore radius 268

5.1 Variation of the dimensional change with testing temperature for samples type A4 previously densified at 600 °C 274

5.2 Variation of the dimensional change with testing temperature for samples type A4 previously densified in the range of 180 °C to 1150 °C 276

5.3 Variation of the average coefficient of dimensional change (CDC_m) as a function of testing temperature for samples type A4 densified in the range of 180 °C to 1150 °C..... 277

5.4 Variation of the dimensional change with testing temperature for silica gel samples with 81 Å average pore radius densified in the range of 180 °C to 1150 °C 279

5.5 Variation of the dimensional change at 690 °C as a function of densification temperature for samples type A4 and C 280

5.6 Variation of the average coefficient of dimensional change (CDC_m) as a function of testing temperature for silica gel samples with 81 Å average pore radius densified in the range of 180 °C to 1150 °C 281

5.7 Variation of the dimensional change with time for samples type A4 densified at 900 °C and 1150 °C. The samples were heated to 700 °C in 228 min and cooled to room temperature after 10 h at 700 °C 283

5.8 Variation of the dimensional change with time for a sample type A4 densified at 1150 °C and a NBS silica standard. The samples were heated to 700 °C in 228 min and cooled to room temperature after 10 h at 700 °C 284

Figure Page

5.9 Variation of the dimensional change with time for dried silica gel samples types A4 and C. The samples were heated to 700 °C in 228 min and cooled to room temperature after 10 h at 700 °C 286

5.10 Variation of the temperature for zero expansion during heating (T_{zero}) and temperature for maximum expansion during heating (T_{max}) as a function of densification temperature for samples type A4 287

5.11 Variation of the TGA weight loss as a function of testing temperature for a dried silica gel sample type A4 289

5.12 Variation of the TGA weight loss measured from 25 °C and from 150 °C as a function of testing temperature for a dried silica gel sample type A4 291

5.13 Variation of the water content as a function of densification temperature for samples type A4 292

5.14 Variation of T_{max} as a function of the water content in silica gel samples type A4 294

5.15 Variation of T_{zero} as a function of the water content in silica gel samples type A4 295

5.16 Variation of the dimensional change measured at T_{max} as a function of the water content in samples type A4 296

5.17 Variation of the TGA weight loss measured from 25 °C and from 150 °C as a function of testing temperature for samples type A1 297

6.1 Variation of Vickers hardness number (VHN) as a function of volume fraction of pores (V_V) 301

6.2 Variation of Vickers hardness number (VHN) as a function of topological index ß 303

Figure Page

6.3 Variation of Vickers hardness number (VHN) as a function of relative genus (γ) 304

6.4 Variation of the Vickers hardness number (VHN) as a function of the pore coordination number (CN) 305

6.5 Variation of flexural strength as a function of volume fraction of pores (V_V) 306

6.6 Variation of the flexural strength as a function of topological index ß 307

6.7 Variation of flexural strength as a function of relative genus (γ) 308

6.8 Variation of flexural modulus as a function of volume fraction of pores (V_V) 310

6.9 Variation of flexural modulus as a function of topological index ß 311

6.10 Variation of flexural modulus as a function of relative genus (γ) 312

6.11 Variation of compression strength as a function of volume fraction of pores (V_V) (Samples type A1) 313

6.12 Variation of compression strength as a function of topological index ß (Samples type A1) 314

6.13 Variation of compression strength as a function of relative genus (γ) (Samples type A1) 315

6.14 Variation of compression modulus as a function of volume fraction of pores (V_V) (Samples type A1) 316

6.15 Variation of compression modulus as a function of topological index ß (Samples type A1) 318

Figure Page

6.16 Variation of compression modulus as a function of relative genus (γ) (Samples type A1) 319

6.17 Variation of compression modulus as a function of volume fraction of pores (Vv) (Samples type A2) 320

6.18 Variation of compression modulus as a function of topological index ß (Samples type A2) 321

6.19 Variation of compression modulus as a function of relative genus (γ) (Samples type A2) 322

6.20 Variation of tensile strength (Brazilian test) as a function of volume fraction of pores (V_V) (Samples type A1) 323

6.21 Variation of tensile strength (Brazilian test) as a function of topological index ß (Samples type A1) 324

6.22 Variation of tensile strength (Brazilian test) as a function of relative genus (γ) (Samples type A1) 326

6.23 Variation of tensile strength (Brazilian test) as a function of volume fraction of pores (V_V) (Samples type A2) 327

6.24 Variation of tensile strength (Brazilian test) as a function of topological index ß (Samples type A2) 328

6.25 Variation of tensile strength (Brazilian test) as a function of relative genus (γ) (Samples type A2) 329

6.26 Variation of tensile modulus (DMA) as a function of volume fraction of pores (V_V) 330

6.27 Variation of tensile modulus (DMA) as a function of surface area per unit volume (S_V) 331

Figure Page

6.28 Variation of tensile modulus (DMA) as a function of topological index ß 333

6.29 Variation of tensile modulus (DMA) as a function of relative genus (γ) 334

6.30 Variation of tensile modulus (DMA) as a function of volume fraction of pores (Vv) for testing temperatures varying from 25 °C to 250 °C 335

6.31 Variation of tensile modulus (DMA) as a function of topological index ß for testing temperatures varying from 25 °C to 250 °C 336

6.32 Variation of dimensional change at 690 °C as a function of volume fraction of pores (V_V) 337

6.33 Variation of dimensional change at 690 °C as a function of topological index ß 338

6.34 Variation of dimensional change at 690 °C as a function of relative genus (γ) 340

6.35 Variation of the average coefficient of dimensional change (CDC_m) as a function of densification temperature, for reference temperatures varying from 30 °C to 690 °C 341

6.36 Variation of dimensional change as a function of testing temperature for samples densified in the range of 500 °C to 1150 °C 343

6.37 Variation of dimensional change slope (DC_s) as a function of densification temperature 344

6.38 Variation of the average coefficient of dimensional change (CDC_m) as a function of testing temperature for silica gel samples densified in the range 180 °C to 1150 °C 346

Figure Page

6.39 Variation of coefficient of dimensional change slope (CDC_s) as a function of densification temperature 347

6.40 Variation of dimensional change slope (DC_s) as a function of volume fraction of pores (V_V) 349

6.41 Variation of dimensional change slope (DC_s) as a function of topological index ß 350

6.42 Variation of dimensional change slope (DC_s) as a function of relative genus (γ) 351

6.43 Variation of helium flow as a function of gas pressure for samples densified in the range 180 °C to 1100 °C 354

6.44 Variation of the slope of the curves helium flow versus pressure (Figure 6.43) as a function of densification temperature 355

6.45 Variation of the helium flow slope as a function of volume fraction of pores (V_V) 356

6.46 Variation of the helium flow slope as a function of relative genus (γ) 357

6.47 Schematic of the actual area in a specimen that resists the penetration of a hardness indenter 361

6.48 Schematic of the reduction in concentration of stresses when the pore connectivity decreases. (a) CN = 4; (b) CN = 2; (c) CN = 0 362

6.49 The schematic structure shown in (a) has a larger Vv of pores than the structure shown in (b), however both structures have a continuous matrix 364

6.50 The schematic structure shown in (a) has a larger pore connectivity than the structure shown in (b) 365

Abstract of Dissertation Presented to the Graduate School
of the University of Florida in Partial Fulfillment of the
Requirements for the Degree of Doctor of Philosophy

TOPOLOGICAL EVOLUTION AND PROPERTIES OF SOL-GEL SILICA MONOLITHS

By

Wander Luiz Vasconcelos

August 1989

Chairman: Dr. Larry L. Hench
Cochairman: Dr. Robert T. DeHoff
Major Department: Materials Science and Engineering

The purpose of this research is to obtain information on both structural and physical properties of sol-gel silica monoliths as the material goes through densification, and to seek possible correlations between the properties measured.

The structural properties are divided into two groups: the metric properties and the topological properties. The evaluation of metric properties was based mainly upon nitrogen gas adsorption experiments. In order to obtain topological properties some geometric models of the pore structure of silica gels are proposed, which are used in conjunction with the gas adsorption data. The gas adsorption results show that for three types of silica gel monoliths the average pore radii of 12 Å, 32 Å and 81 Å remain fairly constant during densification. The application of topological modeling to silica gel monoliths yields the number of

nodes (Nv), number of branches (Bv), number of separate parts (Pv) and the genus (Gv) of the pore network. As densification proceeds Nv and Bv go to zero as the material becomes fully dense. Pv is initially zero and increases as pores start closing in the last stage of densification, and the genus approaches zero. The topological models proposed yield consistent results; the scale of the structure obtained from the models is the same as is observed with high resolution transmission electron microscopy for dried silica gel monoliths.

The mechanical properties explored were the following: microhardness, flexural strength, flexural modulus, uniaxial compression strength, compression modulus, tensile strength (from Brazilian test), tensile storage modulus and shear storage modulus (from dynamic mechanical analysis). In general, the strength and modulus of the silica gel monoliths increase continuously as densification proceeds. Measurements of dimensional change show that the silica gels exhibit a higher thermal stability as densification proceeds. Silica gel monoliths with 81 Å average pore radius show greater thermal stability than silica gels with 12 Å average pore radius.

The strength of silica gel monoliths with 12 Å average pore radius increases relatively slowly when densified from 180 °C to about 800-900 °C. The increase in strength becomes more pronounced when the densification temperature is further increased, in the range of 900 °C to 1150 °C. The low temperature region (180-900 °C) is associated with a high pore connectivity, while the second region (900 °C to 1150 °C) is associated with pore closure, which causes stiffening of the structure.

CHAPTER 1
THE SOL-GEL METHOD

1.1 Introduction

Silica (SiO_2) in its various forms is the most abundant component of the crust of the earth. It is, therefore, no surprise that mankind has been using this component ever since the beginning of civilization. The first known silica based glasses are dated to be 4,000 to 5,000 years old [1,2]. Throughout history SiO_2 has found countless applications either in its crystalline or amorphous forms. SiO_2 has been widely used as a major component of most glasses, while its most common crystalline form, naturally occurring quartz, has many important applications such as in piezoelectric transducers.

In glasses SiO_2 has an important characteristic of glass forming because of the tetrahedral coordination of oxygen atoms around the silicon atom. Extensive studies have been done on the structure of SiO_2 glasses [3-23]. Figure 1.1 is a schematic of a structural segment of a pure silica glass. Silica glasses can be divided into two categories: (1) multicomponent silicate glasses, where SiO_2 is an important constituent but there are more elements present; and, (2) pure SiO_2 glasses, where SiO_2 is the only component. Applications for both types of silica glasses abound [1,2,24-28] and use of pure SiO_2 glasses has been markedly

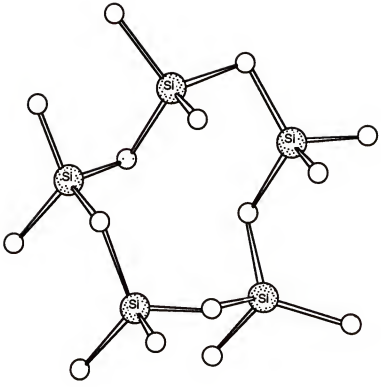

Figure 1.1 Tetrahedral coordination of SiO_2.

growing recently because of improved processing and increased ability to control the final purity of the glasses.

Traditional processing of SiO_2 glasses involve the melting of naturally occurring quartz, the silica glasses resulting from this process are called Types I and II, according to Table 1.1 [29,30]. Type I is obtained by electric melting of natural quartz crystals under vacuum, while Type II is made by flame fusion of natural quartz. Both Types I and II are usually called fused quartz. According to Hench et al. [30, p.77]

> deficiencies of fused quartz optics can include: considerable cation impurities (Type I), hydroxyl impurities (Type II), inhomogeneities, seeds, bubbles, inclusions, and microcrystallites [31]. The relative extent of these defects depends on the grade of fused quartz with a corresponding increase in cost for the better grades.

Both Types III and IV are termed synthetic fused silica. The cation impurities in Types III and IV are substantially lower than in Types I and II, because of the high purity of $SiCl_4$ used in the processing of Types III and IV [30]. However, water contents of several thousand ppm are present in Type III silica, and Cl ion in a few hundred ppm is retained as an unreacted residual in both Types III and IV silica [30].

1.2 Objectives

Sol-gel derived colloidal silica systems have been extensively studied in many different ways [28,32-34]. Alkoxide systems by other hand still lack understanding in many fundamental aspects of processing.

Table 1.1 Silica-glass processes [29,30].

Fused Quartz

Type I: Electric melting of natural quartz crystals

$$SiO_2 \text{ (quartz)} \xrightarrow[\text{vacuum}]{\text{heat}} SiO_2 \text{ (glass)}$$

Type II: Flame fusion of natural quartz crystals

$$SiO_2 \text{ (quartz)} \xrightarrow[\text{oxy-hydrogen}]{\text{heat}} SiO_2 \text{ (glass)}$$

Fused Silica

Type III: Vapor - phase hydrolysis of pure silicon tetrachloride carried out in a flame

$$SiCl_4 + O_2 + 2H_2 \longrightarrow SiO_2 \text{ (glass)} + 4HCl$$

Type IV: Oxidation of pure silicon tetrachloride which is fused electrically or by means of a plasma

$$SiCl_4 + O_2 \longrightarrow SiO_2 \text{ (glass)} + 2Cl_2$$

Gel-Silica

Type V: Gelation of alkali silicate colloidal solutions with full densification (1500 °C to 1720 °C), or
Hydrolysis and condensation of alkoxide precursor with full densification (1150 °C to 1200 °C)

$$Si(OR)_4 + 4H_2O \longrightarrow Si(OH)_2 + 4ROH$$

$$Si(OR)_4 \longrightarrow SiO_2 \text{ (dense gel-silica)} + 2H_2O$$

Type VI: Hydrolysis and condensation of alkoxide precursor with partial densification (600 °C to 950 °C)

$$Si(OR)_4 + 4H_2O \longrightarrow Si(OH)_4 + 4ROH$$

$$Si(OH)_4 \longrightarrow SiO_2 \text{ (porous gel-silica)} + 2H_2O$$

Colloidal systems generally involve larger, sub-micrometer scale structures, while alkoxide systems exhibit smaller nanometer scale structures. It is the purpose of this work to study the structural and physical evolution of nanometer scale alkoxide derived silica-gel monoliths as densification proceeds.

The purpose of this chapter is to review the sol-gel method, concerning the stages of mixing, casting, gelation, agingand drying. Chapter 2 discusses densification and is intended to describe the experimental techniques used in this study of sol-gel silica processing. Analyses of nitrogen gas adsorption and evolution of structural metric properties for gel-silicas with different pore radii are reported in Chapter 2.

Chapter 3 is concerned with the concepts of structural characterization and topological modeling of the nanometer scale structure of silica gel monoliths, and describes the topological evolution of the structure during densification. Data on the evolution of mechanical properties with densification are reported in Chapter 4. The mechanical tests under consideration involve microhardness, flexural testing, uniaxial compression testing, Brazilian testing and dynamic mechanical analysis. Chapter 5 describes experimental work on thermal properties, with emphasis on dimensional change and its correlation with the sintering process. Chapter 6 ("structology") analyses and correlates the structural data (metric and topological) with the physical properties, with the goal of obtaining additional understanding of the

the structure of sol-gel silica with densification. The conclusions of this work are presented in Chapter 7.

1.3 Sol-Gel Technology

1.3.1 Evolution of Sol-Gel Technology

Sol-gel research has grown markedly due to potentially unique applications for this new class of materials [35-43]. The beginning of interest in sol-gel derived materials dates back to mid 1800s with Ebelman [44,45] and Graham's [46] studies on silica gels. For a period from the late 1800s through the 1920s gels received special attention of chemists because of the phenomenon of Liesegang Rings [47-53]. Geffcken and Berger [54] mention sol-gel dip coatings in the literature in 1939. In the 1950s and 1960s Roy and co-workers [55-58] recognized the potential for obtaining high levels of chemical homogeneity in colloidal gels. Roy and co-workers [55-58] synthesized a large number of novel ceramic oxide compositions (involving Al, Si, Ti, Zr, etc.), that could not be made using traditional ceramic powder methods [28]. During the same period, Iler's [32] pioneering work in silica chemistry led to the commercial development of colloidal silica powders, Dupont's colloidal Ludox® spheres [28]. Stober and co-workers [59] extended Iler's findings to show that using ammonia as a catalyst for the TEOS hydrolysis reaction one could control both the morphology and the size of the powders, yielding the so called Stober

spherical silica powder [28]. The final size of the silica powder is a function of the initial concentration of water and ammonia, the type of silicon alkoxide (methyl, ethyl, butyl, pentyl esters, etc.) and alcohol (methyl, ethyl, butyl, pentyl) mixture used [28,59] and reactant temperature [60]. In the late 1960s and early 1970s the sol-gel synthesis of well defined multicomponent oxides was reported [57,61-65].

Nucleation of particles in a very short time followed by growth without supersaturation yields monodispersed colloidal oxide particles [66-68]. Using these concepts Matijevic and co-workers [69-72] have produced an enormous range of colloidal powders with controlled size and morphologies including [28] oxides (TiO_2, αFe_2O_3, Fe_3O_4, $BaTiO_3$, CeO_2); hydroxides (AlOOH, FeOOH, $Cr(OH)_3$); carbonates ($Cd(OH)CO_3$, $Ce_2O(CO_3)_2$, Ce(III)/Y HCO_3); sulfides (CdS, ZnS); metals (Fe III, Ni, Co), and various mixed phases or composites (Ni, Co, Sr ferrites), sulfides (Zn, CdS), (Pb, Cds), and coated particles (Fe_3O_4 with $Al(OH)_3$ or $Cr(OH)_3$).

The controlled hydrolysis of alkoxides has also been used to produce submicrometer TiO_2 [73], doped TiO_2 [74], ZrO_2 [75], doped ZrO_2 [75], doped SiO_2 [76], $SrTiO_3$ [77], and corderite [77] powders.

Emulsions have been employed to produce spherical powders of mixed cation oxides, such as yttrium aluminum garnets (YAG) and many other systems [28,77].

Sol-gel powder processes have been applied to fissile elements [78] where spray forms sols of UO_2, and rigid gel spheres of UO-PuO_2 are formed during passage through a column of heated liquid [28].

Both crystalline and vitreous ceramic fibers have been prepared using the sol-gel method. Compositions include TiO_2-SiO_2 and ZrO_2-SiO_2 glass fibers [79], high purity SiO_2 waveguide fibers [80-85], Al_2O_3, ZrO_2, ThO_2, MgO, TiO_2, $ZrSiO_4$, $3Al_2O_3$-$2SiO_2$ fibers [86-91]. Alumina grains sol-gel derived are important commercial products [91].

A variety of coatings and films have also been developed using sol-gel methods [28]. Of particular importance are the antireflection coatings of indium-tin-oxide (ITO), and related compositions applied to glass window panes to improve insulation characteristics [39,92,93]. Other work on sol-gel coatings is reviewed by Schroeder [94], Mackenzie [95,96] and Wenzel [97].

1.3.2 Motivation for the Sol-Gel Method

According to Hench and West [28] the motivation for sol-gel processing is primarily the potentially higher purity and homogeneity and the lower processing temperatures associated with sol-gels, compared with traditional glass melting or ceramic powder methods.

Wenzel [42] lists the following advantages of the sol-gel method:

1) High purity raw materials are available. This is specially useful in preparing fiber optic preforms with very low (ppb range) concentration of contaminants.
2) Sol-gel methods can be used to make glasses of many compositions and glasses with cations in unusual oxidation states.

Oxidation state manipulation opens the possibility of new colored glasses.

3) Highly homogeneous multi-component gels and glasses may be synthesized, or the scale of this homogeneity may be coarsened voluntarily to yield a block copolymer gel [98,99]. Homogeneity is required for the production of optical glass and fiber optic preforms. Control of structure at the molecular level will lead to glasses with unusual structures and to new glass-ceramics.
4) Dried gels can be made in a wide range of densities, surface areas and pore sizes. This may be used for catalyst design, transparent insulation, molecular sieving and in impregnation applications.
5) The sintering of sol-gel derived glasses occurs at relatively low temperatures. This opens the possibility of producing refractory glasses of high homogeneity and purity [79].
6) The rheological properties of sols allow the formation of fibers, films, and composites, by using techniques such as spinning, dip-coating, injection, impregnation, or simple mixing and casting.

Some potential applications of the sol-gel process are the following:

1) Gel-silica optics and porous gel-silica optics [29,30,100,101].
2) Catalyst supports [102-105].
3) Fiber optic waveguides [80,106].
4) Thermal insulation [107].
5) Fiber reinforced composites [108-112].
6) Optical thin films [113-116].

7) Superionic conductors [117].
8) Optical fiber coupling [118].
9) Thermal application fibers [119].
10) Structural applications [120].
11) Low thermal expansion glass [29,121].
12) Protective thin films [105,113,122,123].
13) Impregnated glasses [124-127].
14) Novel composition materials [79,128-130].
15) Coatings [113,114,131-134].

1.3.3 The Sol-Gel Process

The word "sol" describes the dispersion of colloids in liquids [96,135,136]. Colloids are described as solid particles with diameters in the range of 1 nm to 100 nm [136]. A gel is an interconnected, rigid network of sub-micrometer dimensions. The term "gel" embraces a diversity of combinations of substances which can be classified in four categories according to Flory [137]:

1) Well ordered lamellar structures.
2) Covalent polymeric network; completely disordered.
3) Polymeric networks formed through physical aggregation; predominantly disordered.
4) Particulate disordered structures.

According to Hench and West [28] three approaches are used to make sol-gel monoliths:

Method 1 - Gelation of colloidal powders.

Method 2 - Hydrolysis and polycondensation of alkoxide precursors followed by hypercritical drying of gels.

Method 3 - Hydrolysis and polycondensation of alkoxide precursors followed by drying under ambient atmosphere.

A silica gel may be formed by network growth from an array of discrete colloidal particles (Method 1), or by formation of an interconnected three-dimensional (3-D) network by the simultaneous hydrolysis and polycondensation of an organometallic precursor (Methods 2 and 3) [28]. When the pore liquid is removed as a gas phase from the interconnected network of the solid gel under hypercritical conditions (critical point of drying, Method 2), the network does not collapse and a low density material called "aerogel" is produced [28]. Aerogels can have void volumes as large as 98%, and densities as low as 0.08 g/cm^3 [28,138,139].

When the pore liquid is removed at or near ambient pressure by thermal evaporation (as used in Methods 1 and 3), the material is termed a "xerogel" [28]. If the pore liquid is primarily alcohol based, the material is called an "alcogel" [28]. The generic term "gel" is usually applied to either xerogels or alcogels, whereas aerogels are commonly designated as such [28].

Figure 1.2 shows a schematic of a typical sol-gel (xerogel or alcogel) processing sequence. As the figure shows, the processing can be divided into seven steps, as follows:

1) Mixing.
2) Casting.
3) Gelation.
4) Aging.
5) Drying.
6) Stabilization.
7) Densification.

In the next sections, steps 1 through 5 will be briefly reviewed. Steps 6 and 7 will be reviewed in Chapter 2.

1.3.4 Structure of Sols

According to Brinker and Scherer [140] the electrons surrounding a nucleus do not constitute a spatially and temporally uniform screen, but every atom is a fluctuating dipole. The effect of the dipoles is the creation of forces of attraction between atoms [140-143] which are termed van der Waals (or dispersion forces). The van der Waals forces result from three types of interaction: permanent dipole-permanent dipole (Keesom forces), permanent dipole-induced dipole (Debye forces) and transitory dipole-transitory dipole (London forces) [140].

The attractive dispersion forces are approximately additive, so that they become important for particles of colloidal dimensions, and they

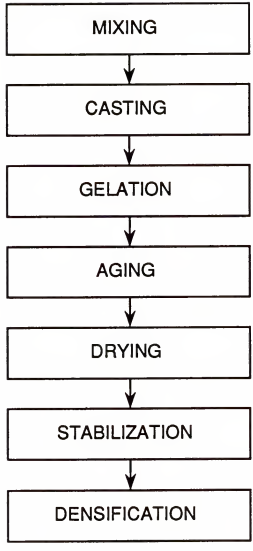

Figure 1.2 Schematic of the sol-gel process.

tend to cause flocculation of colloids [140]. For two infinite slabs separated by a distance h, the attractive potential (V_A) is given by [140]

$$V_A = \frac{-A}{12 \pi h^2}, \tag{1.1}$$

where A is the Hamaker constant.

The van der Waals forces have been investigated for silica systems [144-147], and it is possible that they play little or no role in the silica system, except possibly for colloidal particles larger than 100 nm [33].

The DLVO theory (named after Derjaguin, Landau, Verwey and Overbeek) describes the stabilization of colloids by electrostatic interactions [33,140,148]. The DLVO theory predicts that coagulation will result from reduction in the double layer repulsion, which varies depending on the pH and type and concentration of electrolytes. The effectiveness of a given electrolyte (counterions) in reducing the electrostatic repulsion depends strongly on the valence of the ion [140]. The empirical Schulze-Hardy rule [140] predicts that the concentration of electrolyte required to cause flocculation (c_f) is inversely proportional to the sixth power of the valence of the ion [140]:

$$c_f = \frac{C \varepsilon^3 (k T)^5}{A^2 e^6 z^6}, \tag{1.2}$$

where C is a constant;

ε is the dielectric constant of the solvent;

k is the Boltzmann's constant;

T is the absolute temperature;

A is Hamaker constant;

e is the electron charge;

z is the valence of the ion.

According to Brinker and Scherer [140], silica does not conform to the DLVO theory, because SiO_2 is apparently stabilized by a layer of adsorbed water that prevents coagulation.

In a sol prepared by hydrolysis of a salt, the primary particles have diameters of 3 nm to 10 nm and are nonporous [140]. However polymers that grow in alcohol-water solutions do not form dense particles, but are fractal objects [140,149-151].

1.3.5 Mixing

According to Hench and West [28] in Method 1 a suspension of colloidal powders, or sol, is formed by mechanical mixing of colloidal particles in water at a pH that prevents precipitation, as discussed by Iler [32,33]. In Methods 2 and 3 a liquid alkoxide precursor, such as $Si(OR)_4$ (where R is CH_3, C_2H_5, or C_3H_7), is hydrolyzed by mixing with water. The hydrolysis reaction of TMOS (tetramethylorthosilicate, $Si(OCH_3)$) is represented as follows:

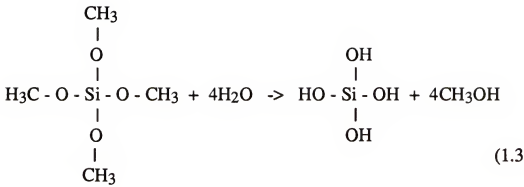

(1.3)

The hydrated silica tetrahedra interact in a condensation reaction forming -Si-O-Si- bonds, as shown in Eq.(1.4):

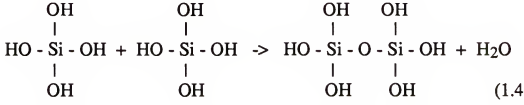

(1.4)

Additional linkage of -Si-OH tetrahedra is referred to as a polycondensation reaction, and eventually results in a SiO_2 network as shown in Eq.(1.5) [28]:

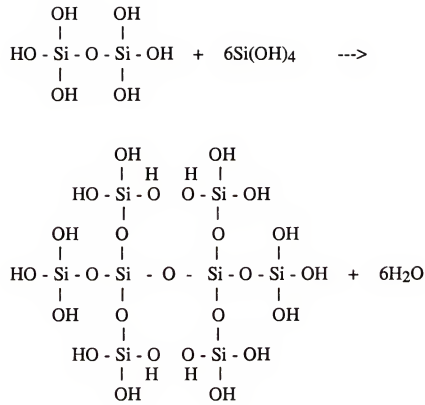

(1.5)

The -Si-O-Si- bonds are termed "siloxane" bonds, and the -Si-OH bonds are termed "silanol" bonds [140].

The hydrolysis and condensation reactions given by Eqs.(1.3) and (1.4) can be represented in a simpler way as follows:

1) Hydrolysis:

$$\text{-Si-OR} + H_2O \longrightarrow \text{-Si-OH} + \text{ROH} \qquad (1.6)$$

2) Condensation:

$$2\ \text{-Si-OH} \ \text{---}> \ \text{-Si-O-Si-} + H_2O \qquad (1.7)$$

The hydrolysis reaction rate constant is k_H, and the condensation reaction rate constant is k_C. The kinetics of hydrolysis and condensation is more complex than indicated by Eqs.(1.3) and (1.4) [28,121,140,152-168]. Many species are present in the solution, and furthermore, hydrolysis and condensation occur simultaneously [28].

The important variables that control the kinetics of hydrolysis and condensation are temperature; nature (acid or base) of electrolyte; concentration of electrolyte; nature of solvent and type of precursor [28]. Pressure also influences the gelation process [154,157,159], but it is usually not a processing variable [28].

Considering the hydrolysis of TEOS (tetraethylorthosilicate, $Si(OC_2H_5)_4$) in different solvents, Aelion et al. [152] showed that k_H increases linearly with the concentration of H^+ or H_3O^+ in acidic media and with the concentration of OH^- in basic medium.

According to Hench and West [28], the nature of the alkoxy groups on the silicon atom also influences the hydrolysis kinetic rates. In general, the longer and the bulkier the alkoxide group, the slower is the rate constant [153,158,161].

There are few data on the kinetic rates for condensation reactions [28,157,165,169,170]. Among the problems associated with the evaluation of kinetic rates one finds [28]: (1) the order of the reaction

may vary with time [163]; (2) there are several hydrolysis and condensation reactions possible, each having its own rate constant [156,170,171].

Orcel et al. [160,165,166,172,173] explored the effect of acid catalysis and formamide (a DCCA or drying control chemical additive) on the kinetics of hydrolysis and polycondensation of a TMOS silica system using ^{29}Si NMR. The data obtained [160] show that acid catalysis increases k_H by a factor of 2 and that formamide decreases k_H and slightly increases k_C.

SiO_2 particles depolymerize in an acidic medium and the resulting monosilicic acid forms a yellow complex with Mo, which can be measured optically [28]. The depolymerization rate constant (k_D) can be related to the particle diameter d, through the following empirical law [28,174]:

$$\log d = a + B \log k_D, \tag{1.8}$$

where a and b are constants.

Table 1.2 summarizes Hench and Orcel's [160] data of the effect of DCCAs and the presence of acidic conditions on the values of k_H, k_C and d of different silica-gel solutions.

Zerda and Hoang [175] determined experimentally the presence of a pentavalent transition state for the hydrolysis of $Si(OR)_4$. General expressions for the hydrolysis can be written as follows [28,175]:

Table 1.2 Physico-chemical characteristics of different gel solutions [160].

SAMPLE	SW55	SF25	SF50	SF23
$\frac{\text{vol. formamide}}{\text{vol. formamide + MeOH}}$	0	25	50	25
H_2O	DI	DI	DI	pH=3
$10^3\ k_H$ (l mol^{-1} h^{-1})	12	7	2	25
k_C (l mol^{-1} h^{-1})	29	31	0	6
d (nm)	2	2.2	2.5	-

$$OH^- + \text{-Si-}OCH_3 \longrightarrow \underset{\displaystyle OH}{\text{-Si-}OCH^-_3} \longrightarrow \text{-Si-OH} + OCH^-_3 \qquad (1.9)$$

$$H_3O^+ + \text{-Si-}OCH_3 \longrightarrow \underset{\displaystyle OH}{\overset{\displaystyle H^+}{\text{-Si-}OCH_3}} \longrightarrow$$

$$\text{-Si-OH} + CH_3OH + H^+ \qquad (1.10)$$

Quantum calculations [176-189] applied to exploration of hydrolysis reactions provide additional understanding of the process and predict the existence of the pentacoordinated silica species in the reaction path.

1.3.6 Casting

After mixing the components of the sol-gel process, a homogeneous solution is formed upon stirring. Depending on the types of reactions involved and the kinetics of hydrolysis and condensation, a specific mixing time must be selected so that the homogenization is optimum and the viscosity of the solution is appropriate for casting.

The container into which the sol is poured must have the following characteristics:

1) Appropriate shape, since the final material will keep the shape of the container.
2) Appropriate size, considering that the gel will shrink throughout the entire process and only stops shrinking when it becomes fully dense.
3) Appropriate composition, so that there will be no reactions between the sol and the internal wall of the container.
4) Appropriate surface quality, which assumes special importance in the production of optical quality materials.
5) Appropriate cleanliness, since all types of particles, dust and contaminants are undesirable in the final product and will serve as stress risers [100].
6) Appropriate thermal properties, compatible with the required processing temperatures associate with chemical reactions and possible heat treatments during the following gelation and aging steps.
7) Interfacial characteristics that prevent formation of bubbles on the gel surface which can act as stress risers during drying [100].

1.3.7 Gelation

The hydrolysis and condensation reactions that occur in the sol will eventually lead to the formation of a gel caused by clustering and linking of the particles. The three-dimensional network thus formed

will contain a continuous liquid phase permeating the space between the solid phase.

The gelation point (or gelation time, t_{gel}) is usually defined as the point at which the clustering and linking in the sol forms a three-dimensional network that can support a stress elastically [28]. The sol-to-gel transformation is not a sharp and well defined transformation, but it rather occurs continuously. Therefore, the practical determination of the gelation time is subject of many different approaches [28,33,121,140,165,190-204].

Sacks and Sheu [200] use the viscoelastic response of the gel as a function of the shear rate to determine t_{gel}. The complex shear modulus (G) at a given frequency is given by [28]

$$G = G'(\omega) + G''(\omega), \tag{1.11}$$

where G' is the shear storage modulus;

G" is the shear storage modulus loss;

ω is the frequency.

The elastic component of the sol-gel material gives rise to the storage modulus G', while the loss modulus G" comes from the viscous component [140]. The relative measure of the viscous energy losses to the energy stored in the system is defined as the loss tangent tan δ [140]:

$$\tan \delta = \frac{G''}{G'}. \tag{1.12}$$

Sacks and Sheu [200,205] pointed out that the gelation time (t_{gel}) cannot be accurately defined by a certain value of viscosity (η), since the viscosity depends on the shear rate. They suggest that t_{gel} would be best located by using the loss tangent tan δ (say, the location of the maximum or a particular value of tan δ).

The type of catalyst used in a gelation reaction can have enormous effects on the structure of the gels formed, as well as on the rapidity of the gelation process [198,206,207]. Table 1.3 [198] shows the effect of some selected catalysts on the gelation time of silica gels made from TMOS [140,208].

The temperature dependence of the gelation time can be represented by an Arrhenius type equation as follows [140]:

$$\ln (t_{gel}) = A + \frac{E}{R\,T}, \qquad (1.13)$$

where A is a constant;

E is the activation energy;

R is the gas constant.

For silica gels, E is found to be in the range of 10 to 20 kcal/mole [190,202], depending on the catalyst and alkoxy group [140].

According to Brinker and Scherer [140], it can be shown, using nuclear magnetic resonance (NMR), that the silica network is more highly cross linked when the water/alkoxide ratio is high and that the structure at the gel point (t_{gel}) is highly variable.

Table 1.3 Gelation time for different catalysts [198].

Catalyst	$\frac{\text{mole catalyst}}{\text{mole TEOS}}$	Initial pH	t_{gel} (h)
HF	0.05	1.90	12
HOAc	0.05	3.70	72
HCl	0.05	<0.05	92
HNO_3	0.05	<0.05	100
H_2SO_4	0.05	<0.05	106
NH_4OH	0.05	9.95	107
HBr	0.05	0.20	285
HI	0.05	0.30	400
No catalyst	-	5.00	1000

Different studies [151,197,207,209-213] show that acid catalyzed sols develop a linear-like structure with very little branching, whereas base catalyzed systems develop highly ramified structures.

According to Zallen [214], the Flory-Stockmayer theory (also termed classical theory, or mean field theory) is the standard theory used in physical chemistry to describe the sol-to-gel phase transition and the molecular size distributions which accompany it. The basic assumption of the Flory-Stockmayer theory [215-221] is that gelation may be modeled as a branching process. The Flory-Stockmayer theory is essentially a theory of dendritic polymerization [214]. Figure 1.3 shows a schematic of a tri-functional (z=3) branched molecule [214,215]; "z" is the functionality of the branch point (node) of the polymer.

According to Zallen [214], the Flory-Stockmayer theory is successful in predicting a sharp gel-point and the critical extent of the reaction (α_c) at which the gelation occurs, which is given by

$$\alpha_c = \frac{1}{z - 1}. \tag{1.14}$$

At a given time, the weight fraction of gel (w_g) is given by [137,140]

$$w_g = \frac{1 - (1 - p)^3}{p^3}, \tag{1.15}$$

where p is the fraction of formed bonds.

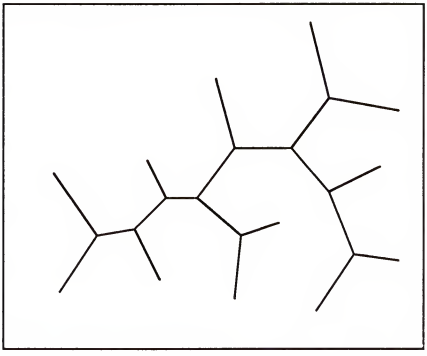

Figure 1.3 Schematic of a tri-functionally branched molecule [214,215].

Thus the Flory-Stockmayer theory can predict the distribution of molecular weights at the gel point. However, the model allows for no ring formation, leading to an increasing number of nodes as the radius of the cluster increases [28].

According to Brinker and Scherer [140], the percolation theory of gel formation does not exclude the formation of closed loops, while it has the disadvantage of not yielding analytical solutions for the percolation threshold and the size distribution of polymers. Reviews of percolation theory have been written by Stauffer et al. [222], Zallen [214] and Brinker and Scherer [140].

Using the number of bonds surrounding a site as equivalent to the functionality of the monomer, the threshold for bond percolation (p_c) can be represented by [140]

$$p_c \approx \frac{1}{(z - 1)}. \tag{1.16}$$

According to Zarzycki [223], experimental results indicate that for silica sol-gel systems p_c exists in the following range:

$$0.6 < p_c < 0.84. \tag{1.17}$$

The fractal model of structures as designated by Mandelbrot [224,225] has been applied to diffusion of particles [226-228] and sol-gel particle growth [151,223,229-231]. The nature of fractals requires that they be invariant with scale, meaning that a fractal is required to look

similar no matter what level of detail is chosen. A second requirement for fractals is that their density decreases with size, as shown in Figure 1.4 [28].

The mass of a fractal can be related to the fractal dimension (d_F) and its size (radius R) by [28]

$$M = K\ R^{d_F}, \tag{1.18}$$

where K is a constant.

1.3.8 Aging

According to Brinker and Scherer [140], the processes of change in the structure after gelation can be categorized as follows:

1) Polymerization.
2) Syneresis.
3) Coarsening.
4) Phase transformation.

Polymerization increases the connectivity of the network by means of polycondensation reactions:

$$\text{-Si-OH} + \text{HO-Si-} \longrightarrow \text{-Si-O-Si-} + H_2O \tag{1.19}$$

Zerda et al. [232], Ketls et al. [233], Smith et al. [234] and Orcel et al. [235] show that condensation reactions in silica gels continues after

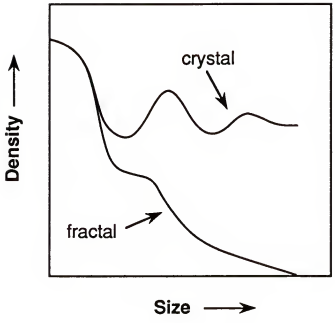

Figure 1.4 Schematic of the density variation with size for typical crystals and fractals [28].

gelation. The condensation continues to occur because of the presence of hydroxyl groups after gelation. The rate of reaction depends upon the temperature, and the concentration and the pH of the solution [140]. Because of the creation of new bridging bonds, the continued polymerization reactions strengthen and stiffen the network [140]. Aging can give rise to hydrolysis reactions [140]:

$$\text{-Si-OR} + H_2O \text{ ---> -Si-OH} + \text{ROH} \quad (1.20)$$

The reverse reaction is the re-esterification [140]:

$$\text{-Si-OH} + \text{ROH ---> -Si-OR} + H_2O \quad (1.21)$$

The re-esterification reaction can be suppressed by using an excess of water [140].

Syneresis is the shrinkage of the gel network resulting in expulsion of liquid from the pores [28,33,140,236,237]. Syneresis is generally attributed to the formation of new bonds resulting from condensation reactions or hydrogen bonding [140]. In most inorganic gel systems syneresis is an irreversible process [140].

Since in particulate gels the structure is controlled by the balance between electrostatic repulsion and attractive van der Waals forces, the extent of shrinkage is determined by the type and concentration of the electrolyte [140,238]. It should be pointed out that some particulate systems, such as alumina gels and some clays, exhibit swelling rather

than syneresis [239], because of invasion of water in the layers causing expansion [140].

Vysotskii et al. [240-242] have shown that the shrinkage rate during syneresis of silica gel has a minimum at the isoelectric point (IEP). For silica systems the IEP is at a pH of 1.7 [33,140]. Vysotskii et al. [241] and Sheinfain and Neimark [243] concluded that condensation reactions are responsible for both gelation and syneresis in silica gel systems.

Acker [244] and Jones and Fischbach [245] reported that there is a minimum solids content (4g to 5g of SiO_2 per 100 ml of sol) below which no observable shrinkage occurs.

Brinker and Scherer [140] and Scherer [237] suggested that syneresis is affected not only by condensation reactions, but also by the tendency to reduce the large solid/liquid interfacial area of the gel.

Assuming that the activation energy for formation of bonds is given by ΔE_b, then the rate of formation of bonds (dn/dt) is given by [140]

$$\frac{dn}{dt} = k' \exp\left(\frac{-\Delta E_b}{R\ T}\right), \tag{1.22}$$

where k' is a constant. Assuming that the activation energy for viscous flow is ΔE_f, then the viscosity of the solid phase is given by [140]

$$\eta = k'' \exp\left(\frac{\Delta E_f}{R\ T}\right), \tag{1.23}$$

where k" is a constant. Thus, the shrinkage rate dV/dt can be written as [140]

$$\frac{dV}{dt} = \frac{k}{\eta}\frac{dn}{dt} = k \exp\left(\frac{-(\Delta E_b + \Delta E_f)}{R\ T}\right), \qquad (1.24)$$

where k is a constant (k'k"). Equation (1.24) indicates that the activation energy for shrinkage is the sum of the activation energies for bonding and flow [140].

Brinker and Scherer [140] suggest that the shrinkage rate decreases (as the process continues) because of stiffening of the network, rather than depletion of reactive groups. The absence of syneresis in gels with very small solids contents [244,245] may indicate that the low modulus of the network is inadequate to squeeze liquid out of the pores at an appreciable rate [140].

According to Brinker and Scherer [140], coarsening (or ripening) is a process of dissolution and reprecipitation driven by differences in solubility (s) between surfaces with different radii of curvature (r). The solubility is given by [140]

$$s = s_o \exp\left(\frac{2\ \gamma_{sl}\ V_m}{R\ T\ r}\right), \qquad (1.25)$$

where s_o is the solubility of a flat plate;

γ_{sl} is the solid/liquid interfacial energy;

V_m is the molar volume of the solid.

The amount of shrinkage that occurs during drying depends on the stiffness of the network [140,246]. If the gel is aged under conditions of high solubility, the network may resist compression by capillary forces during drying [140].

Examples of phase transformations that can occur during aging include microsyneresis (in which the solid phase separates from the liquid on a local scale), and segregation of the liquid into two or more phases [140,209]. Aging may also lead to crystallization [247,248].

According to Brinker and Scherer [140], the stiffer and stronger the gel network becomes the better it can withstand the capillary pressure so aged gels shrink and crack less during drying. The structure of the gels also influences the sintering behavior, since the densification process is driven by the interfacial energy, which depends on the structure of the gel.

1.3.9 Drying

The drying behavior of porous solids have been extensively studied by Sherwood [249-251], Moore [252], Keey [253], Whitaker [254], Cooper [255], Mujumdar [256,257], Ford [258] and Scherer [259-266]. However, most of the data reported by those researchers have been on powder systems with relatively large pore sizes. The studies conducted by Kawaguchi [267] and Dwivedi, [268] have also been on large pore size gels.

Classical theory of drying divides the process into three stages [258]:

Stage 1: The constant-rate period, during which the evaporation rate is independent of the moisture content.

Stage 2: The first falling-rate period, during which the evaporation rate is usually a linear function of the moisture content [269-271].

Stage 3: The second falling-rate period, during which the evaporation rate is a non-linear function of the moisture content.

For gel systems, during the Stage 1, the evaporation of liquid is directly responsible for the decrease in volume of the gel. For large pore size systems this first stage of drying is called the constant rate period (CRP) [140], because the evaporation rate per unit area of the drying surface is independent of time [252,272]. The rate of evaporation R_E is given by [28,140,258]

$$R_E = k_E \ (p_V - p_A) , \tag{1.26}$$

where k_E is a constant;

p_V is the vapor pressure at the evaporating surface;

p_A is the ambient vapor pressure.

Dwivedi [268] shows that the rate of water loss was constant for his gels during Stage 1, as seen in Figure 1.5. Suzuki and Maeda [273] show that the evaporation rate is constant even when clay patches form on the surface of the body.

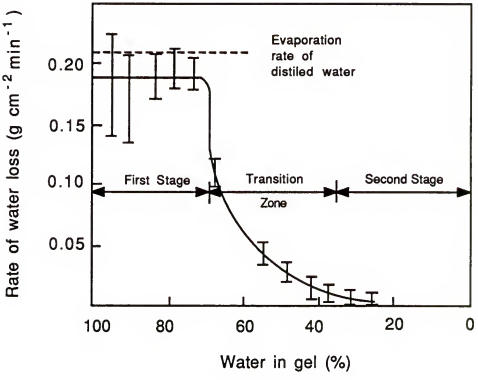

Figure 1.5 Plot of the rate of water loss from alumina gel versus water content of the gel [268].

Brinker and Scherer [140] show that a tensile stress (σ_x) is created because of a shrinkage rate difference between the inside and outside of a drying body. The tensile stress is given by [140]

$$\sigma_x \approx \frac{L\,\eta_L\,R_E}{3\,D}, \tag{1.27}$$

where L is the thickness of the drying body;

η_L is the viscosity of the liquid;

R_E is the evaporation rate;

D is the permeability of the network.

Quantitative analysis of the drying kinetics of acid catalyzed alkoxide gels by Wilson [274] and Wilson and Hench [275,276] show that for gels with average pore radius < 20 nm the rate of evaporation in Stage 1 is not constant, but decreases substantially with time as shown in Figure 1.6 [274]. As shown in Figure 1.7 by Wilson and Hench [276], there is a pronounced shrinkage of the alkoxide derived silica gel during Stage 1. During Stage 2 the dimensions of the silica gel remain practically unchanged. The relationship between relative weight (W/W_o) and relative volume (V/V_o) of the silica gel during drying is shown in Figure 1.8 [274]. According to Hench and co-workers [28,274-280] the decreasing rate of evaporation throughout Stage 1, results from the effective pore radius (the pore radius minus a layer of bond water) decreasing from 3.2 nm to 1.3 nm.

The Stage 2 of drying starts when the "critical point" is reached. During this stage shrinkage stops and the liquid flows from the pores to

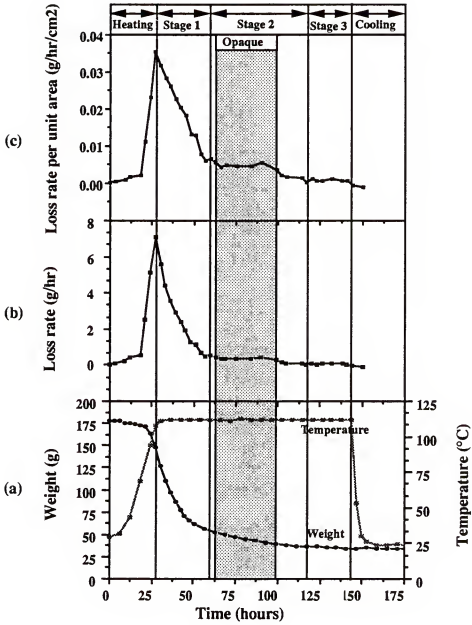

Figure 1.6 Time dependence of (a) temperature and weight; (b) absolute loss rate; and (c) loss rate per unit area for silica gel [274].

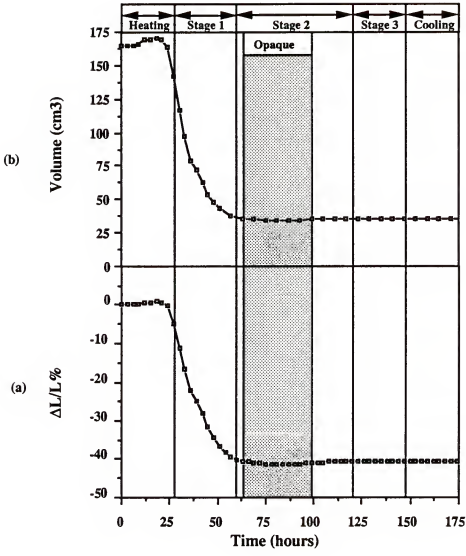

Figure 1.7 Time dependence of (a) linear shrinkage, and (b) volumetric shrinkage of silica gel [274].

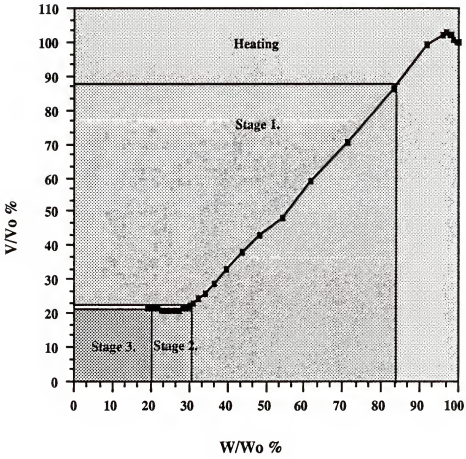

Figure 1.8 Weight reduction (W/W_o) as a function of volumetric shrinkage (V/V_o) for silica gel [274].

the surface where evaporation occurs. Whitaker [281] describes the flow of liquid as being driven by the gradient in capillary stress.

According to Wilson [274] and Wilson and Hench [275,276], shortly after entering Stage 2 the gel turns opaque, starting at the edges and progressing linearly toward the center. Possible causes of this phenomena includes phase separation of the pore liquid or exsolution of gas from the liquid. Shaw [282,283] suggests that the opaque stage is caused by light scattering from isolated pores (or groups of pores) in the emptying process.

According to Hench and West [28] the transition to Stage 3 is the hardest to identify, and its "start" is probably best defined as the "end" of the opaque stage. Wilson and Hench [276] show that Stage 3 is not affected by local changes in temperature, ambient vapor pressure, flow rate, etc.

Hench and West [28, p.75] point out that "successful drying of large gel monoliths require control of the drying rate through the opaque stage and elimination of processing defects during mixing, casting, and gelation."

CHAPTER 2
DENSIFICATION OF GEL-SILICA

2.1 The Sintering Process

2.1.1 Introduction

Based on the pioneering work of Rhines [284] densification (used as a synonym of sintering in this work) can be defined as a geometric change in which a mass of separate particles becomes a coherent body, motivated by a decrease in surface free energy. Even though this seems a simple and clear definition (and it is), Rhines [285, p.480] points out that despite of the fact that "a number of theories of sintering have been offered, no single theory accounts for the entire range of {experimental} observations." According to Johnson [286, p.137], "the lack of understanding of sintering is manifested in the diversity of opinions as to the mechanisms of the process, and the inability to predict the sintering behavior of materials." Exner and Petzow [287, p.117] go on further stating that "a general shrinkage equation presumably will never be derived due to the high complexity and the large variations of the sintering systems."

Despite the complexity of the sintering process, the driving force for the study of sintering is enormous, since most ceramic materials and a large number of metallic systems need to be sintered in some stage of their processing. The major applications of the study of sintering are

1) Better sintering products.

2) Improving sintering processing.

3) Better understanding of the process.

The driving force for densification is a decrease in surface free energy. Besides densification itself, this decrease in free energy also leads to other effects such as [284]

1) Rounding and smoothing (Figure 2.1(a)).

2) Isolation of pores (Figure 2.1(b)).

3) Segregation of pores (Figure 2.1(c)).

None of the effects above can by themselves increase the density of the material. Densification only occurs when the bulk density of the material decreases as a result of the decrease in volume fraction of pores (V_V) [288].

The pioneering attempts to quantify the geometric changes during sintering dates back to the 1920s with Tamman [289] and Hedvall and Helin's [290] works. They were followed shortly after by Balshin [291], Huttig [292-298], Frenkel [299], Pines [300], Mackenzie and Shuttleworth [301] and Kuczynski [302-304].

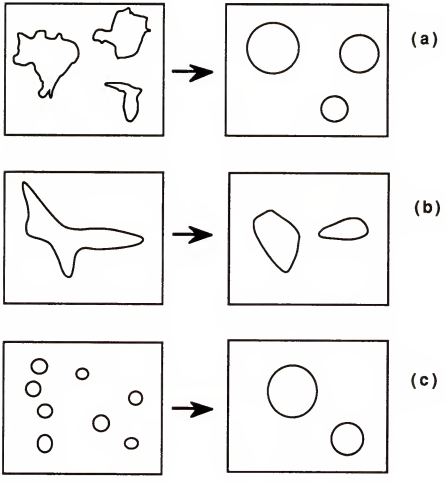

Figure 2.1 (a) Rounding and smoothing; (b) isolation of pores; and (c) segregation of pores.

2.1.2 Mechanisms of Sintering

Some of the primary proposed mechanisms of sintering are

1) Vapor transport or evaporation-condensation. The transport of mass occurs due to a gradient of pressure, which tends to decrease the total surface energy. This mechanism normally does not lead to densification, but only to local surface rounding [284].
2) Liquid transport or dissolution-precipitation. This mechanism is very similar to vapor transport and, like that, liquid transport leads only to local surface rounding.
3) Surface diffusion. Like the previous mechanism, usually this mechanism leads only to surface rounding. In this case the transport of mass is done via the motion of atoms on the surface of the material [284].
4) Volume diffusion. In this mechanism the transport of mass is done via motion of vacancies in the volume of the material. The main effect of this mechanism is some very localized change in density but it does not promote overall densification [284].
5) Bulk movement. This is the main mechanism (in fact group of mechanisms) that usually leads to the overall densification. This mechanism requires growing of the neck between particles, which is caused by a decrease in the surface free energy. Depending on the type of material, two types of bulk movement can occur:
   a) Crystalline materials: the transport of mass is done by means of atomic diffusion in the bulk.

b) Amorphous materials: the mechanism of transport of mass is by viscous flow [302].

6) Reaction sintering. It is a mechanism in which the densification occurs by means of chemical reaction.

2.1.3 The Rhines-DeHoff Model

According to Rhines [284, p.35], "despite the apparent chaos, a description of some features of the geometry of sintering is made both possible and comparatively simple by the use of the concepts of topology."

Chapter 3 presents a review on topology and its important concepts. Here it is enough to state that one of the most important concepts of topology is the genus (G), or connectivity, which can be described as [284,305]

$$G = B - N + 1, \tag{2.1}$$

where B is the number of interparticle contacts or branches;

N is the number of particles or nodes.

Based on the connectivity, the sintering process can be divided into three stages, as shown in Figure 2.2. The characteristics of the three stages of sintering are [284]

First stage: - the genus is constant at (B - N + 1);

- weld necks grow;

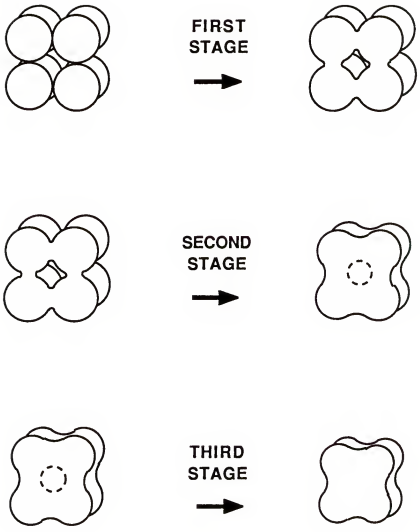

Figure 2.2 The three stages of sintering.

- the surface area is maximal.

Second stage: - the genus diminishes from (B - N + 1) towards zero;
- the pores become isolated.

Third stage: - the genus is constant at zero;
- the pores disappear.

As will be pointed out in Chapter 3, the main limitation of applying topological concepts to sintering studies is the difficulty in experimentally obtaining topological parameters. Because of this, relatively little work has been done is applying the Rhines-DeHoff model to sintering studies. The most important work in this area was carried out by the so-called "Rhines School" [306], including the work done at the University of Florida by Buteau [307], Steele [308], Aigeltinger [309] and Pinheiro [310].

2.1.4 Frenkel's Model

Frenkel [299] proposed a sintering model based on the occurrence of viscous flow. This model is based on the observation that the different mechanisms of sintering can be distinguished by the particular relationship of the radius of the neck between two particles (x) and the sintering time (t), as follows [302]:

Viscous flow $x^2 \sim t$

Vapor transport $x^3 \sim t$

Volume diffusion $x^5 \sim t$

Surface diffusion $x^7 \sim t$

The basic relationship used by Frenkel is [299]

$$\varepsilon_r = \frac{f}{\eta}, \tag{2.2}$$

where ε_r is the strain rate;

f is the acting stress (caused by surface tension);

η is the viscosity of the material.

Frenkel shows that for a viscous flow regime the following equation will be obeyed [299,302]:

$$\left(\frac{x}{a}\right)^2 = \frac{3}{2}\frac{t\gamma}{a\eta}, \tag{2.3}$$

where a is the original radius of the bonded particles;

γ is the surface energy of the material.

Kuczynski found very good agreement of this model for the sintering of spherical glass particles to glass plates [302].

The major limitations of Frenkel's model are the following assumptions of the model:

1) The radius "a" is kept constant during the entire process. This implies that Eq.(2.3) is not applicable beyond the early stages of sintering. It is usually applicable for values of linear shrinkage smaller than 10%.

2) The viscosity of the solid (η) is given by

$$\eta = \frac{k\ T}{D\ \varpi^{1/3}}\ , \tag{2.4}$$

where k is the Boltzmann constant;

T is the absolute temperature;

D is the coefficient of self-diffusion;

ϖ is the atomic volume.

Nabarro [311] showed that Frenkel's calculation of viscosity is not correct for crystalline materials.

3) The material is homogeneous and has stable values of "a" and η.

2.1.5 Mackenzie-Shuttleworth's Model

The Mackenzie-Shuttleworth's model (or simply the MS model) [301] is also a viscous flow model. It is based on a geometric model (Figure 2.3) proposed by Frohlich and Sack [312]. The basic equation assumed by the Mackenzie-Shuttleworth's model is the following [301]:

$$\rho = 1 - \left(\frac{r_1}{r_2}\right)^3\ , \tag{2.5}$$

where ρ is the density of the compact relative to the true density of the material;

r_1 and r_2 are defined in Figure 2.3.

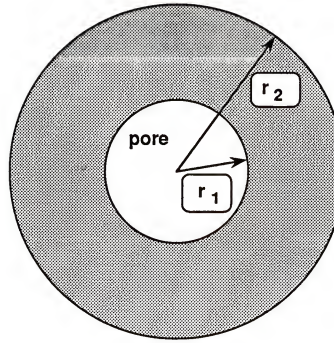

Figure 2.3 Geometric model used in the Mackenzie-Shuttleworth's sintering model [301].

Depending on the rheological behavior of the material one can obtain different equations correlating the progress of the sintering with time. Assuming for instance, that the material presents Newtonian viscosity, one obtains [301]

$$\frac{\gamma n^{1/3}}{\eta}(t - t_o) = \frac{2}{3}\left(\frac{3}{4\pi}\right)^{1/3}\left(\frac{1}{2}\ln\frac{(1+x^3)}{(1+x)^3} - \sqrt{3}\tan^{-1}\frac{2x-1}{\sqrt{3}}\right), \quad (2.6)$$

where n is the number of pores per unit volume;

x is equal to $(1 - \rho)/\rho$;

t_o is the initial time.

Assuming Bingham viscosity, the equation obtained by the MS model is [301]

$$\frac{d\rho}{dt} = \frac{3}{2}\left(\frac{4\pi}{3}\right)^{1/3}\frac{\gamma n^{1/3}}{\eta}(1-\rho)^{2/3}\rho^{1/3}\left(1 - a\left(\frac{1}{\rho} - 1\right)^{1/3}\ln\left(\frac{1}{1-\rho}\right)\right), \quad (2.7)$$

where

$$a = \sqrt{2}\left(\frac{3}{4\pi}\right)^{1/3}\frac{\tau_c}{2\gamma n^{1/3}}, \quad (2.8)$$

and τ_c is the critical shear stress for Bingham flow.

Sacks and Tseng [313] found good experimental agreement of sintering of colloidal silica glass spheres (Stober spheres) with the MS model.

Important limitations of the MS model are the following assumptions:

1) The pores are isolated. This means that this model applies better to the last stages of sintering, when the body contains only isolated closed pores.
2) The material is incompressible.
3) The material has homogeneous and stable mechanical properties.

2.1.6 Scherer's Model

Scherer's model [314-318] is also a viscous flow model. It is a geometric model which assumes a cubic array formed by intersecting cylinders to represent the structure of the solid, as shown in Figure 2.4 [318].

According to Scherer's model the rate of densification is given by [140]

$$\frac{\gamma\, n^{1/3}\, t}{\eta} = f_s(y) - f_s(y_o), \tag{2.9}$$

where

$$f_s(y) = \frac{-2}{\alpha}\left(\frac{1}{2}\ln\left(\frac{\alpha^2-\alpha y+y^2}{(\alpha+y)^2}\right) + \sqrt{3}\,\tan^{-1}\left(\frac{2y-\alpha}{\alpha\sqrt{3}}\right)\right), \tag{2.10}$$

and

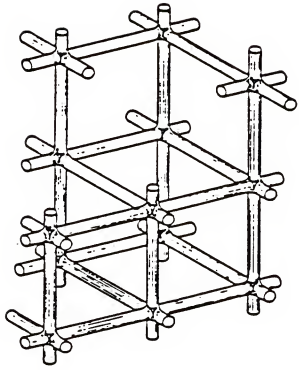

Figure 2.4 Geometric model used in the Scherer's sintering model [318].

$$y = \left(\frac{3\pi}{x} - 8\sqrt{2}\right)^{1/3}, \qquad (2.11)$$

and

$$\alpha = (8\sqrt{2})^{1/3}. \qquad (2.12)$$

Sacks and Tseng's work [313] show that the Scherer's model can be used to describe the sintering of spherical silica particles. The model has also been used to describe the sintering of a body containing two different pore sizes [318] and a distribution of pore sizes [140].

An important limitation of Scherer's model is that the model assumes a very simple geometry which cannot be applied to the later stages of densification when the cylinders start touching each other.

2.1.7 Densification of Gel-Silica

The first stages of densification of gel-silica are termed "stabilization" stages [28] which can be divided into chemical and thermal stabilization. Chemical stabilization involves removing surface silanols from the surface until a critical concentration is reached so that the surface will not rehydroxylate [28]. The thermal stabilization relates to the material being able to be used at a given temperature without reversible structural changes [28].

Many chlorine compounds can react with surface hydroxyl groups to form hydrochloric acid [319-322], which then desorbs from the gel

body at a temperature range of 400 °C (673 K) to 800 °C (1073 K) [3]. Examples of chlorine compounds that can be used for dehydroxylation of the silica gel surface include [28] $ClSi(CH_3)_3$, $Cl_2Si(CH_3)_2$, $Cl_3Si(CH_3)$, silica tetrachloride ($SiCl_4$), chlorine (Cl_2), and carbon tetrachloride (CCl_4).

Water in silica gels is present in two forms [28]: free water within the porous gel structure (i.e., physical water) and hydroxyl groups associated with the gel surface (i.e., chemical water). The work done on the hydration/dehydration characteristics of the silica gel/water system by Benesi and Jones [323], Kiselev [324], McDonald [325], Young [326], Hockey and Pethica [327], and Hair [328] can be summarized as follows:

1) Physical water can be eliminated and surface silanol (Si-O-H) groups condensed at temperatures starting at about 170°C (443 K).
2) The dehydration process is completely reversible up to about 400 °C (673 K).
3) At temperatures above 400 °C (673 K) the dehydration is irreversible as a result of shrinkage.
4) Viscous flow occurs above 850 °C (1123 K).

With a successful stabilization treatment, it is possible to manufacture monolithic dense gel-derived glasses by heating at temperatures below the melting point [30,100,107,206,329-334].

According to Hench and West [28] the amount of water in the gel has a major role in the densification behavior. The amount of water affects

the viscosity [335], which influences the sintering behavior. As shown by Nogami and Moriya [206], a gel prepared in acidic conditions has a higher surface area and water content than a gel prepared in basic conditions, and starts to densify about 200 °C sooner than the base catalyzed gel.

Young [326] found that the decrease in surface area of silica gel at high temperatures is a function of the time and temperature of the heat treatment. Many other authors [164,336-340] present a similar type of result. However, Klein et al. [331] and Brinker et al. [341] showed that certain systems display an initial increase in surface area until about 400 °C (673 K) and then the surface area decreases with further heating. The initial increase in surface area was attributed to the removal of water and organics.

According to Brinker and Scherer [342], there are at least four mechanisms that contribute for the shrinkage and densification of gels. Those four mechanisms, as described for a borosilicate-gel system, are

1) Capillary contraction, due to increase in surface energy associated with elimination of silanol (Si-OH) groups, occurs mostly at temperatures below 150 °C (423 K) and the shrinkage associated with this region is about 3% of the total shrinkage observed in the experiment.
2) Condensation-polymerization, involves formation of siloxane (Si-O-Si) groups and related loss of water and organic residues.
3) Structural relaxation, occurs via diffusive motion of atoms. This mechanism and the condensation-polymerization lead to

skeletal (structural) densification. These mechanisms occur mostly between 150 °C (423 K) and 525 °C (798 K) and the shrinkage associated with skeletal densification is about 33% of the total shrinkage.

4) Viscous sintering, associated with mass flow driven by decrease in surface energy, occurs above 525 °C (798 K) and is responsible for most of the shrinkage (about 64%).

For systems other than the borosilicate-gel studied by Brinker et al. [342], the temperatures and shrinkages described above are likely to be different.

2.2 Sol-Gel Processing

2.2.1 Chemical Processing of Pure Silica

A schematic of the sol-gel processing used in this work is shown in Figure 2.5. Based on the theory reviewed in Chapter 1, the silica-gel process can be divided into seven stages: Mixing, Casting, Gelation, Aging, Drying, Stabilization and Densification.

During mixing the chemical components are put in an intimate molecular contact and hydrolysis takes place:

$$Si(OCH_3)_4 + 4H_2O \longrightarrow Si(OH)_4 + 4CH_3OH \qquad (2.13)$$

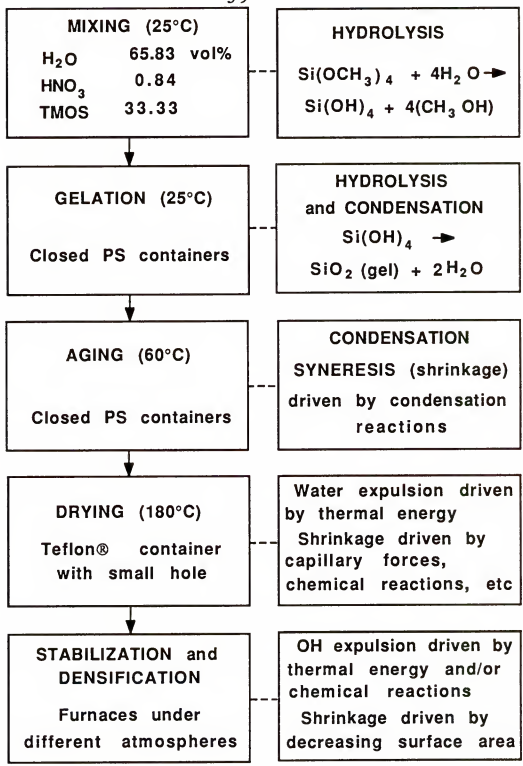

Figure 2.5 Schematic of the sol-gel processing of gel-silica monoliths.

The gelation stage is characterized by the occurrence of condensation reactions up to a point when a gel is formed. The gel formation is accompanied by a characteristic increase in viscosity. The main condensation reaction can be expressed as follows:

$$Si(OH)_4 \text{ ---> } SiO_2 \text{ (gel)} + 2H_2O \qquad (2.14)$$

Further development of condensation processes gives rise to syneresis or network shrinkage, characterizing the aging stage. During the drying stage water is eliminated from the gels driven by thermal energy and capillary forces. Shrinkage during drying is caused mainly by capillary forces but chemical reactions, osmotic forces and other factors may play a role as well [140].

During densification, OH groups are eliminated from the structure driven by increased thermal energy and by chemical reactions such as chlorination of the surface. The shrinkage and increase in density that occur during sintering are driven by the decrease in surface area of pores.

2.2.2 Gelation and Aging

The gelation of the samples prepared in this work was done by leaving the containers as cast with the solution at room temperature until the gel formation, which typically occurred in two to three days after casting.

After gelation the samples were put in an oven in the same closed polystyrene (PS) containers used for casting. One of the aging temperature profiles used is shown in Figure 2.6.

2.2.3 Drying

After aging the samples were taken out of the casting PS containers and transferred to Teflon® containers which were filled with DI (de-ionized) water. The Teflon® containers were closed and a small opening (capillary) was made in the containers.

Drying temperature profiles like the one shown in Figure 2.7 were used for drying of the samples.

Using the above procedures, four sets of cylindrical samples with different sizes were prepared. These samples are termed "samples type A", and the dimensions of the samples are

A1: diameter 12 mm; length ≈ 12 mm.
A2: diameter 5 mm; length ≈ 8 mm.
A3: diameter 8.5 mm; length ≈ 13 mm.
A4: diameter 5 mm; length ≈ 28 mm.

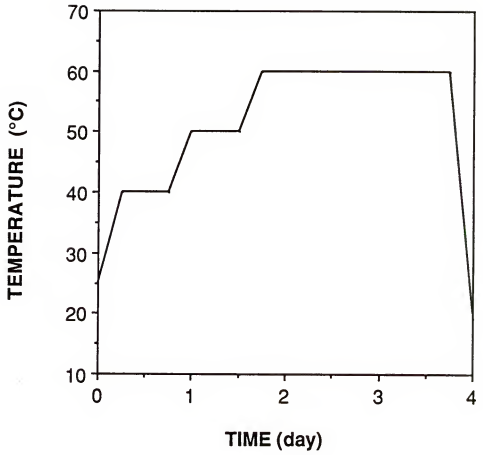

Figure 2.6 Schematic of the aging temperature profile.

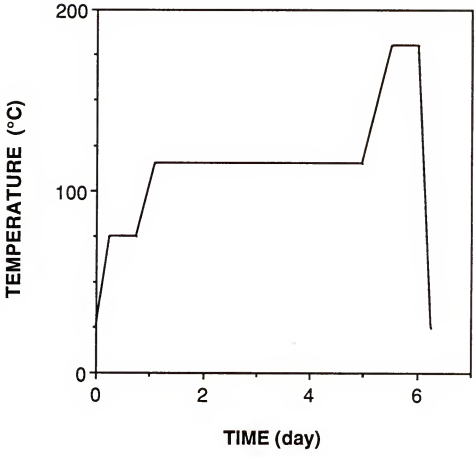

Figure 2.7 Schematic of the drying temperature profile.

2.3 Large Pore Size Structures

2.3.1 HNO_3 Based Gels

In this experiment HNO_3 was used as catalyzer, according to the process described previously (Figure 2.5). Using a special drying chamber like the one shown in Figure 2.8 [274] it is possible to obtain samples of larger pore size and larger initial (dried) volume fraction than by using the Teflon® containers. The samples obtained using the drying chamber shown in Figure 2.8 are called "samples type B". The internal volume of the drying container and the total external surface area of the gels inside the drying chamber seem to affect the drying process. It is possible that this effect is associated with changes in the equilibrium vapor pressure of the chemical components of the gel inside the drying container.

2.3.2 HF Based Gels

Replacing part of HNO_3 as catalyst for fluoride acid (HF), it is possible to change the average pore size and volume fraction of pores in the initial (dried) samples.

In the processing used in this work, 6 ml of HNO_3 was added to 485 ml of DI water. After stirring, the solution was transferred to a plastic (Teflon®) container and 20 ml of HF was added. After mixing, 250 ml

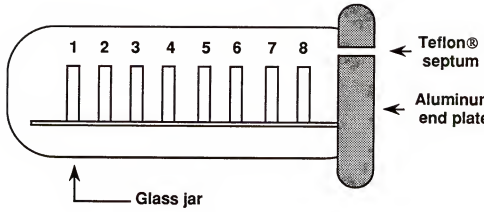

Figure 2.8 Drying chamber [274].

of TMOS was added to the solution, and after mixing for few minutes the solution was poured in polystyrene vials.

After casting the solution was left gelling for 18 hours, and the aging step was carried out in a oven at 60 °C (333 K) for two days. After aging, the samples were dried in Teflon® containers filled with DI water and containing a small capillary for vapor elimination. The drying schedule used was similar to that shown in Figure 2.7. The HF based silica gels are termed "samples type C".

2.4 Densification Processing

2.4.1 Partial Densification in Dry-Air Atmosphere

The densification experiments were carried out in tube furnaces with atmosphere control. Dried samples were put in fused quartz crucibles and introduced in the furnaces.

Samples were densified using the temperature profiles shown in Figure 2.9. During the entire process a flow of 1.0 liter/min. of dry-air (< 3 ppm of H_2O) was used. A small pressure of 12 mm of Hg inside the furnace was kept by using wash bottles filled with DI-water at the end of the furnace. Figure 2.10 shows a set of silica-gel samples densified in a dry-air atmosphere.

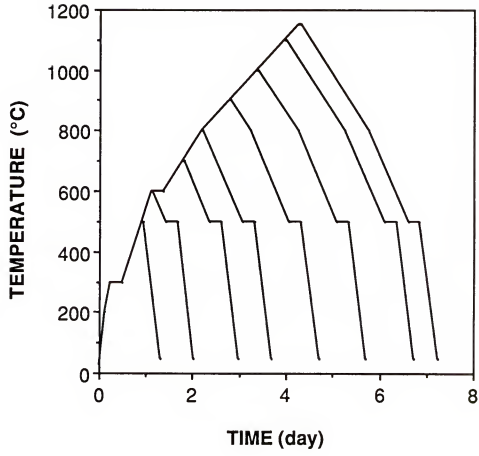

Figure 2.9 Schematic of the densification temperature profiles.

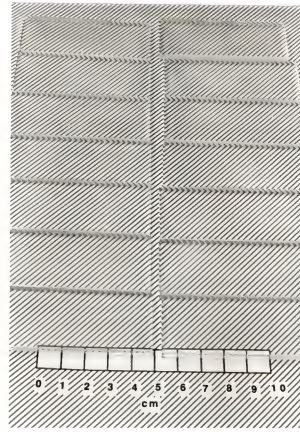

Figure 2.10 Examples of pure silica gel monoliths densified in the range of 180 °C to 1000 °C in a dry-air atmosphere.

2.4.2 Stabilization and Densification Processing Using Chlorination

Chlorine on the surface of silica-gels reacts with OH groups promoting dehydroxylation before pore closing. A typical chlorination temperature profile is shown in Figure 2.11. The step of heating to an intermediate temperature followed by a cooling to about 400 °C (673 K) is intended to promote some dehydroxylation and strength at the same time that pore closing is avoided. After the pre-stabilization in a dry-air atmosphere the samples were held in a chlorinated atmosphere for a period of 48 hours. After the chlorination treatment the silica-gels were taken to 1150 °C (1423 K) under a helium atmosphere. Figure 2.12 shows samples prepared in dry-air atmosphere (500 °C (773 K) to 1000 °C (1273 K)) and a full dense sample (1150 °C, 1423 K) prepared in a chlorine atmosphere.

2.5 Gas Adsorption Analysis

2.5.1 BET Theory

The adsorption of gases on a solid surface can be divided into two broad categories of chemical or physical adsorption, depending on the strength of the interaction between the adsorbate (gas or vapor molecule) and adsorbent (surface of the solid). The chemical adsorption (chemisorption) involves large interaction potentials associated with chemical bonding which makes the process irreversible. Physical

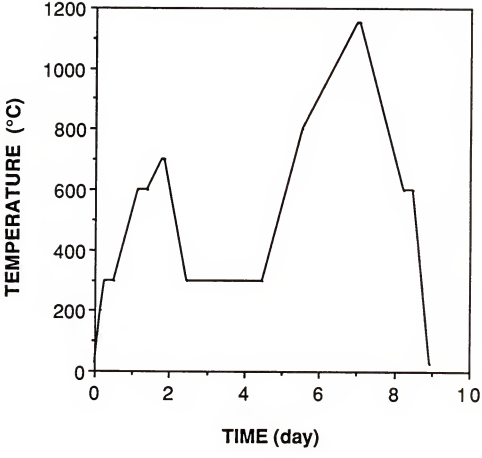

Figure 2.11 Temperature profile for a chlorination experiment.

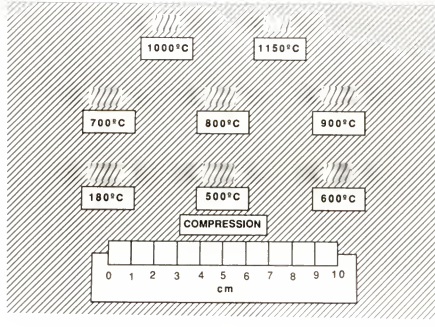

Figure 2.12 Silica gel monoliths prepared in a dry-air atmosphere (500 °C to 1000 °C) and in a chlorine atmosphere (1150 °C).

adsorption (or reversible adsorption) has the following characteristics [343]:

1) Low heats of adsorption and no disruptive structural changes on the solid surface during the adsorption process.
2) It may lead to surface coverage by more than one layer of adsorbate, enabling the measurement of pore volume.
3) Physical adsorption does not occur at elevated temperatures.
4) Since no (or extremely small) activation energy is involved the adsorption process can be achieved rapidly.
5) The adsorption process is reversible, enabling the study of the desorption process as well.
6) Physically adsorbed molecules are free to cover the entire surface and can be used to calculate surface areas (rather than number of sites).

The types of interactions that lead to physical adsorption are the following [343]:

1) Dispersion (or London [344]) forces;
2) Ion-dipole interactions;
3) Ion-induced dipole interactions;
4) Dipole-dipole interactions;
5) Quadrapole interactions.

When analyzing the pore structure through gas adsorption it is convenient to classify the pores according to their size, as in the Dubinin's classes of pores [343]:

1) Micropores, for pore radius < 15 Å;

2) Mesopores, pore radius in the range 15 Å to 500 Å;

3) Macropores, pore radius in the range 500 Å to 1000 Å;

Nitrogen gas adsorption analysis is usually not employed for structures with pore radii larger than 1000 Å (100 nm).

According to Brunauer et al. [345], the adsorption of gas on solid surfaces at a fixed temperature follows one of five possible types of "adsorption isotherms" showed in Figure 2.13. A brief description of the five types of isotherms is as follows [343]:

Type I: This type of isotherm occurs when adsorption is limited to, at most, only a few molecular layers. In the case of chemical driven adsorption (chemisorption), this type of isotherm indicates that all the surface sites are occupied for values of P/P_o tending to 1. In the case of physical adsorption, type I isotherms are encountered for micropore powder systems where the pore size does not exceed a few adsorbate molecular diameters.

Type II: This type of isotherm represents the most common type of adsorption in nonporous powders, or powders with pore diameters larger than micropores.

Type III: This type of isotherm occurs when the heat of adsorption is less than the adsorbate heat of liquefaction.

Type IV: This type of isotherm occurs on porous adsorbents possessing pore radii in the range of 15 Å to 1000 Å.

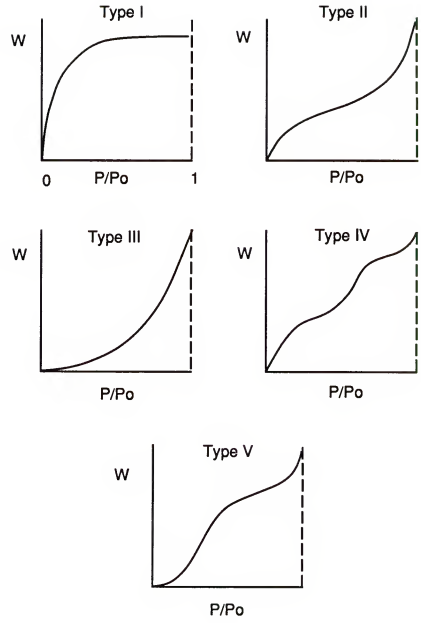

Figure 2.13 The five types of adsorption isotherms as classified by Brunauer et al. [345]. W is the weight of gas adsorbed and P/P_o is the relative pressure.

Type V: This type of isotherm occurs when the interactions between adsorbate-adsorbent are small or when the pore radii are in the range 15 Å to 1000 Å.

Langmuir [346] was able to describe the type I isotherm using a kinetic approach and the assumption that adsorption was limited to a monolayer. Brunauer, Emmett and Teller [347] developed later a more general theory (the "BET theory") that can be used to describe all the five types of isotherms. The BET theory assumes that the uppermost molecules in adsorbed stacks are in dynamic equilibrium with the gas or vapor. The BET theory assumes that the equilibrium between the vapor and the adsorbate in the first layer are described by the Langmuir theory. The final form of the BET equation is given by [343]

$$\frac{1}{W\,[(P_o/P) - 1]} = \frac{1}{W_m\,C} + \frac{C - 1}{W_m\,C}\left(\frac{P}{P_o}\right), \tag{2.15}$$

where W is the weight of vapor adsorbed;

W_m is the weight of vapor in a completed monolayer;

P is the adsorbate equilibrium pressure;

P_o is the adsorbate saturated equilibrium vapor pressure;

C is the BET constant, given by [343]

$$C = \frac{A_1\,v_1}{A_2\,v_2}\exp\left(\frac{E_1 - L}{R\,T}\right), \tag{2.16}$$

where A_1 is the condensation coefficient, or the probability of a molecule being adsorbed upon collision with the surface;

A_2 is the condensation coefficient for the second monolayer;

v_1 is the vibrational frequency of the adsorbate normal to the surface when adsorbed;

v_2 is the vibrational frequency for the second monolayer;

E_1 is the energy of adsorption;

L is the heat of liquefaction.

When the weight adsorbed (W) is plotted versus the relative pressure (P/P_o) for both adsorption and desorption processes a hysteresis loop is commonly formed. de Boer [348] has identified five types of hysteresis loops as shown in Figure 2.14. de Boer [348] correlated each type of hysteresis with pore shapes, as follows:

Type A: due principally to cylindrical pores open at both ends.

Type B: associated with slit-shaped pores or the space between parallel plates.

Type C: produced by a mixture of tapered or wedge-shaped pores with open ends.

Type D: produced by tapered or wedge-shaped pores but with narrow necks at one of both open ends.

Type E: results from McBrain's [349] "bottle neck" pores.

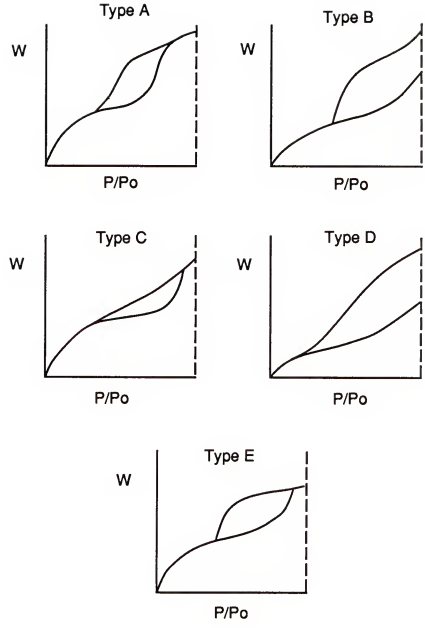

Figure 2.14 de Boer's five types of hysteresis loops [343].

Despite the qualitative correlation between type of hysteresis and shape of pores, Broekhoff and Linsen [350] point out that there is no satisfactory quantitative theory of hysteresis.

Gas (especially nitrogen) adsorption techniques and the BET theory have been extensively applied to the study of the structure of silica gels [34,351-356]. The applicability of BET theory to the study of the structure of silica-gels has been well established.

2.5.2 Experimental Results

The gas adsorption analysis was done using an automatic gas-absorption instrument, the Autosorb-6 (Quantachrome, Inc.). Based on the average pore radius of the dried silica gel monoliths obtained from the gas adsorption analysis, samples type A are also referred to as "12 Å average pore radius samples"; samples type B (dried in the large drying chamber) are also termed "32 Å average pore radius samples"; and samples type C (HF based) are also termed "81 Å average pore radius samples".

Figure 2.15 shows the BET plot for a dried gel-silica monolith sample of 12 Å average pore radius (sample type A). The data shown in Figure 2.15 is used in Eq.(2.15) in order to calculate the constant "C". Figure 2.16 represents the volumes of gas adsorbed and desorbed for samples of 12 Å average pore radius densified in the range of 180 °C (453 K) to 1150 °C (1423 K). As the densification temperature increases the volume of adsorbed gas decreases, reflecting the smaller

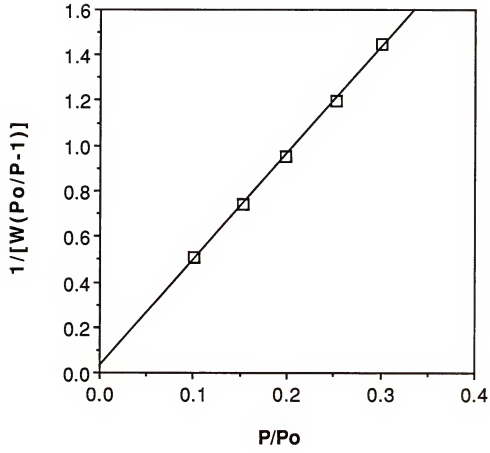

Figure 2.15 BET plot for a dried silica gel sample with 12 Å average pore radius.

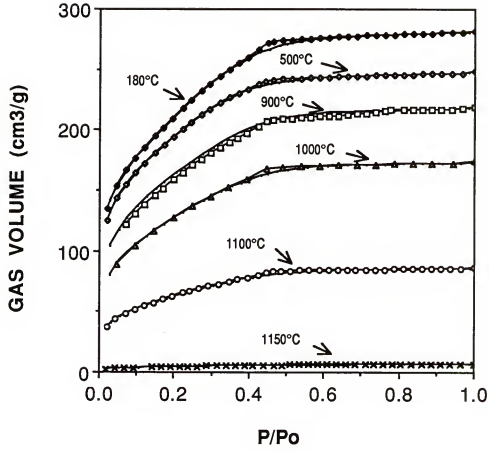

Figure 2.16 Volume of adsorbed gas versus partial pressure for a set of silica gel samples with 12 Å average pore radius densified in the range of 180 °C to 1150 °C.

porosity present as the sintering proceeds. Figure 2.17 shows the variation of adsorbed gas versus partial pressure for dried samples of 12 Å (type A), 32 Å (type B), and 81 Å (type C). The hysteresis of the adsorption-desorption curves for the 32 Å and 81 Å samples suggest that the pores in samples type B and C have ink-bottle shapes (see Figure 2.14).

Typical pore size distributions of dried samples of 12 Å, 32 Å and 81 Å average pore radii are shown in Figure 2.18. The lower limit cut-off at about 3.5 Å represents the lowest possible resolution attainable in the Nitrogen gas adsorption analysis (a Nitrogen atom cannot penetrate a pore smaller than its own size).

As the densification temperature increases the volume of pores decreases, as shown in Figure 2.19 for a set of gel-silica monoliths with 12 Å average pore radius. As the total volume of pores decreases the average pore radius remains practically unchanged. The pore size distribution curves for sets of larger average pore radius are shown in Figure 2.20 and Figure 2.21. Again, it is shown that while the total volume of pores decreases with the evolution of densification, the pore size distribution keeps about the same average pore radius.

Langmuir plots of dried samples of 12 Å, 32 Å and 81 Å average pore radii are shown in Figure 2.22.

Figure 2.23 shows the average pore radius as a function of the densification temperature for four sets of samples (A1, A2, A3 and A4) of 12 Å average pore radius. If can be seen from Figure 2.23 that the average pore radius remains fairly constant as densification proceeds, as

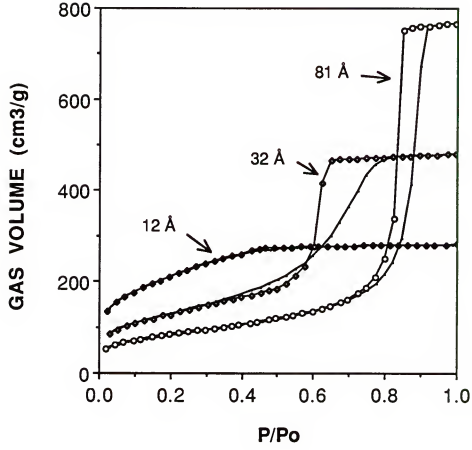

Figure 2.17 Volume of adsorbed gas versus partial pressure for dried silica gel samples with 12 Å, 32 Å and 81 Å average pore radii.

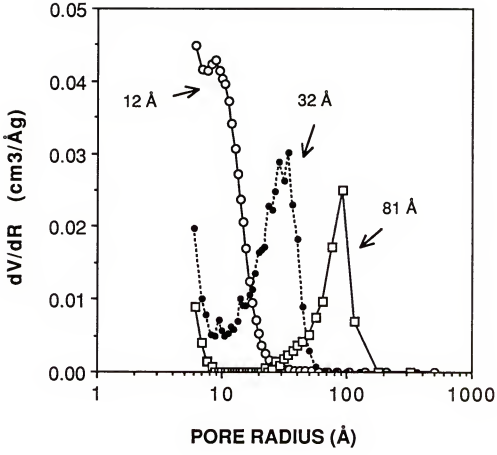

Figure 2.18 Pore size distribution for dried silica gel samples with 12 Å, 32 Å and 81 Å average pore radii.

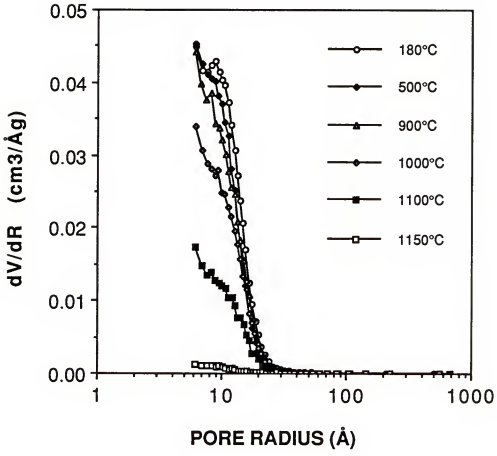

Figure 2.19 Pore size distribution for silica gel samples with 12 Å average pore radius densified in the range of 180 °C to 1150 °C.

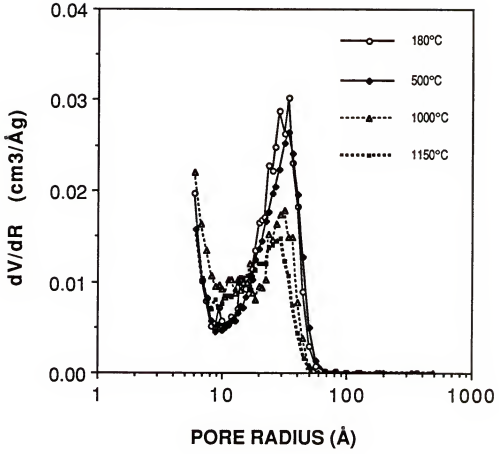

Figure 2.20 Pore size distribution for silica gel samples with 32 Å average pore radius densified in the range of 180 °C to 1150 °C.

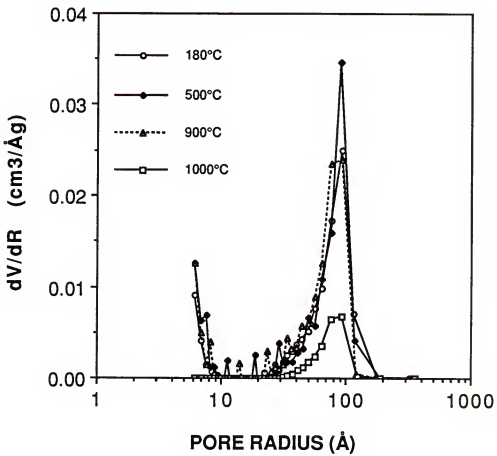

Figure 2.21 Pore size distribution for silica gel samples with 81 Å average pore radius densified in the range of 180 °C to 1150 °C.

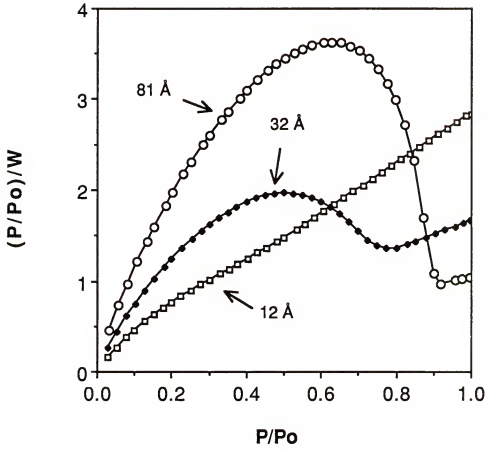

Figure 2.22 Langmuir plots of dried silica gels with 12 Å, 32 Å and 81 Å average pore radii.

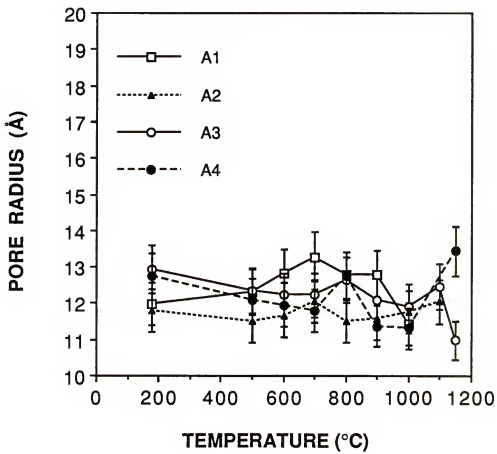

Figure 2.23 Average pore radius versus densification temperature for samples type A.

suggested by the pore size distribution curves shown in Figure 2.19. Figure 2.24 shows the variation of the average pore radius with densification temperature for samples with initial pore radii of 12 Å, 32 Å and 81 Å.

2.6 Evolution of Metric Properties During Sintering

2.6.1 Structural Density

True (or structural) density of three series of samples of 12 Å, 32 Å and 81 Å average pore radii were evaluated using a Helium micropycnometer (Quantachrome, Inc.).

The variation of true density with densification temperature for sets of 12 Å, 32 Å and 81 Å average pore radii are shown respectively in the Figures 2.25, 2.26 and 2.27. Each point in those curves represents the average of eight experimental measurements. Figure 2.28 summarizes the results shown in the previous figures. The data-points plotted in Figure 2.28 represent points on the polynomial curves obtained in Figures 2.25, 2.26 and 2.27. From those figures if can be seen that the structural density of silica-gel monoliths change as the densification proceeds. For all pore sizes tested the initial structural density of the dried samples is around 2.1 g/cm^3 to 2.15 g/cm^3. As the densification temperature increases the structural density increases to a maximum at an intermediate temperature in the range 800 °C (1073 K) to 1000 °C (1273 K). The true density decreases again when the

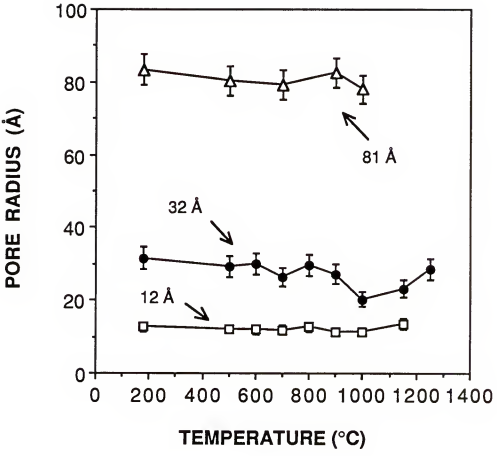

Figure 2.24 Variation of the average pore radius as a function of densification temperature for silica gel samples with 12 Å, 32 Å and 81 Å average pore radii.

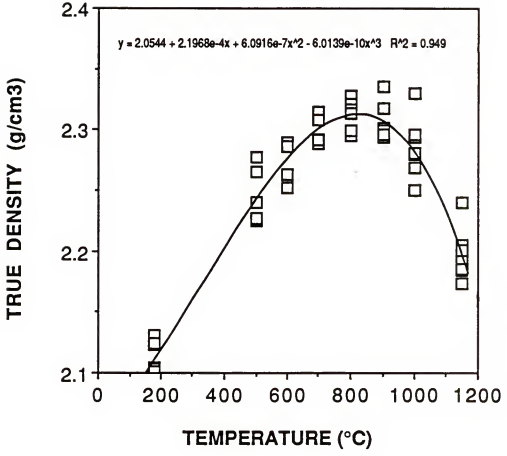

Figure 2.25 Variation of true density as a function of densification temperature for samples type A.

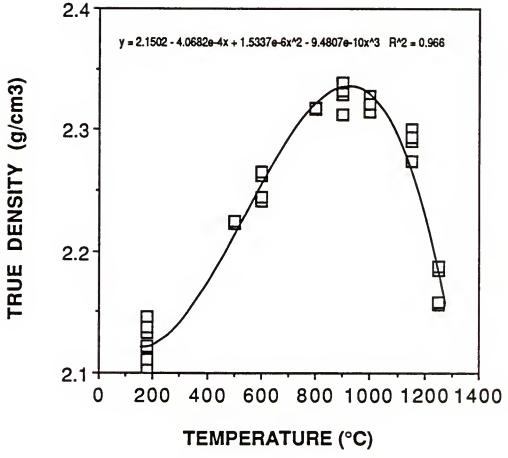

Figure 2.26 Variation of true density as a function of densification temperature for samples type B.

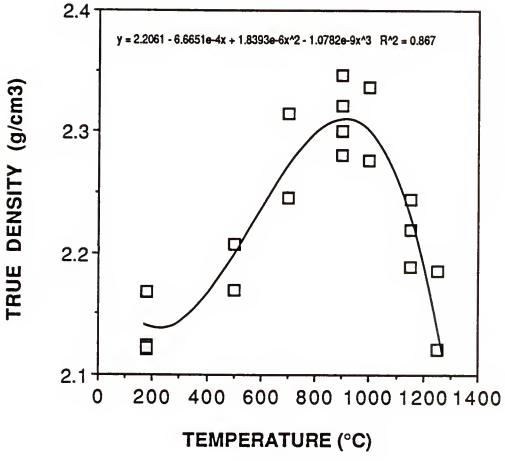

Figure 2.27 Variation of true density as a function of densification temperature for samples type C.

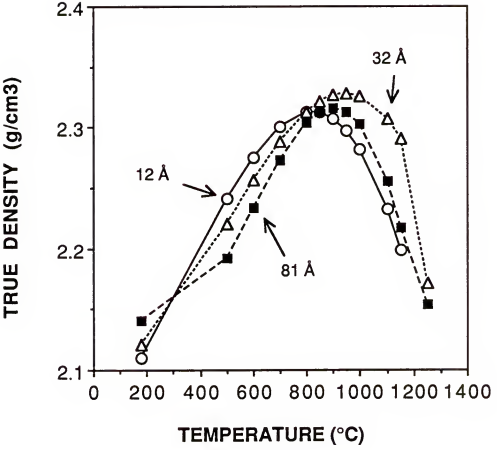

Figure 2.28 Variation of true density (from polynomial equations) as a function of densification temperature for silica gel samples with 12 Å, 32 Å and 81 Å average pore radii.

processing temperature is raised at higher values. The reasons for the structural density variations are not yet fully known but it is possible that they come from changes in the defect atomic coordination of Si in the structure.

2.6.2 Metric Properties

The variation of volume fraction of pores (V_V) with densification temperature for the four sets of samples with 12 Å average pore radius is shown in Figure 2.29. It is seen that as densification proceeds there is a continuous decrease in the volume fraction of pores. This decrease is more pronounced for temperatures just above the range 800 °C (1273 K) to 900 °C (1273 K).

Figure 2.30 shows the variation of volume fraction of pores with densification temperature for sets of samples with average pore radii of 12 Å, 32 Å and 81 Å. The samples with a larger average pore radii used in this work also present larger initial volume fraction of pores. Comparing the sets of samples with 12 Å and 32 Å pore radii, it is seen that the larger pore size samples maintain a higher volume fraction of pores during the entire process of sintering and the sharp decrease in volume fraction occurs at higher temperatures. Similar results occur for the set of samples of 81 Å pore radius except that the sharp decrease in volume fraction may be occurring at lower temperatures than for the set of samples of 32 Å pore radius.

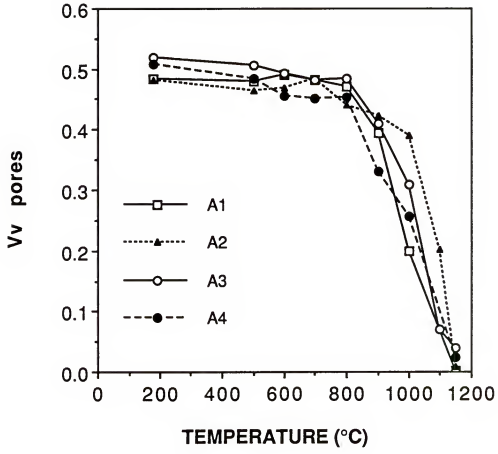

Figure 2.29 Variation of the volume fraction of pores (V_V) as a function of densification temperature for samples type A.

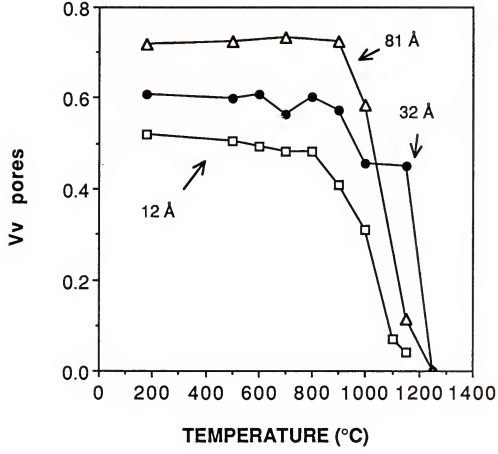

Figure 2.30 Variation of the volume fraction of pores (V_V) as a function of densification temperature for silica gel samples with average pore radii of 12 Å, 32 Å and 81 Å.

The variation of surface area of pores per unit volume with densification temperature for four sets of samples of 12 Å average pore radius is shown in Figure 2.31. Similar to the V_V evolution, it can be seen that S_V decreases with increasing processing temperature and that decrease is sharper beyond the range 800 °C (1073 K) to 900 °C (1173 K). Figure 2.32 shows the variation in S_V pores with processing temperature for samples of 12 Å, 32 Å and 81 Å average pore radii.

When surface area per unit volume (S_V) is plotted as a function of volume fraction (V_V) of pores for the samples A1, A2, A3 and A4, Figures 2.33, 2.34, 2.35 and 2.36 are obtained. Those figures show a linear relationship between S_V and V_V, representing a similar path of densification for those samples. The linearity between S_V and V_V also indicates a constant pore radius during densification, which was shown before in Figure 2.23.

Figure 2.37 shows the variation of surface area of pores per unit volume with volume fraction of pores for a set of samples of 32 Å initial average pore radius. This figure does not show the linear correspondence between S_V and V_V as seen for the 12 Å pore radius.

Using the data on pore volume per unit mass obtained from the nitrogen adsorption experiments and the data on structural density obtained from Helium pycnometry one can calculate the bulk density of the samples by using the expression:

$$\rho_b = V_p + \frac{1.0 \text{ gram}}{\rho_t}, \qquad (2.17)$$

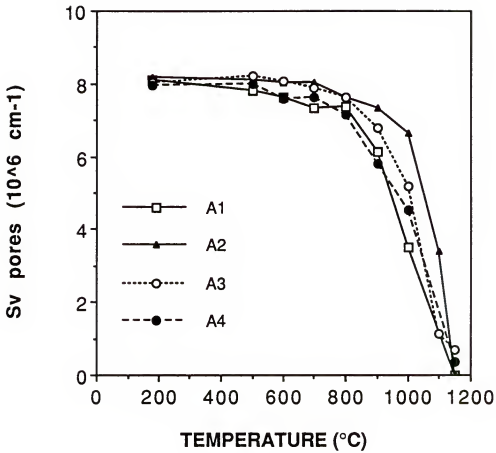

Figure 2.31 Variation of the surface area of pores per unit volume (S_V) as a function of densification temperature for samples type A.

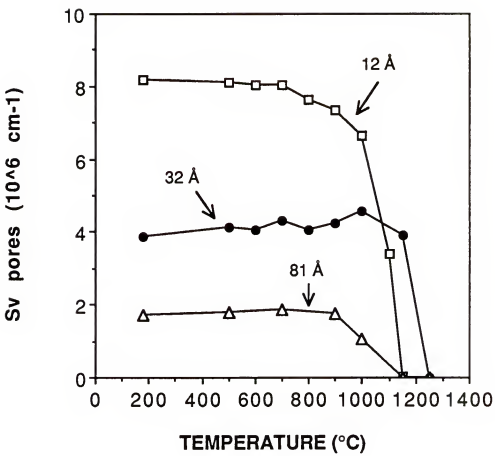

Figure 2.32 Variation of the surface area of pores per unit volume (S_V) as a function of densification temperature for silica gel samples of 12 Å, 32 Å and 81 Å average pore radii.

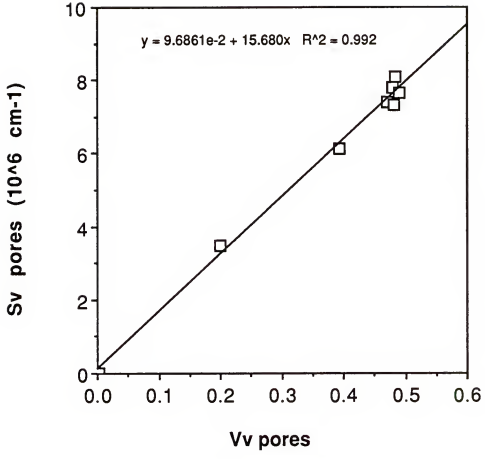

Figure 2.33 Variation of the surface area of pores per unit volume (S_V) as a function of volume fraction of pores (V_V) for samples type A1.

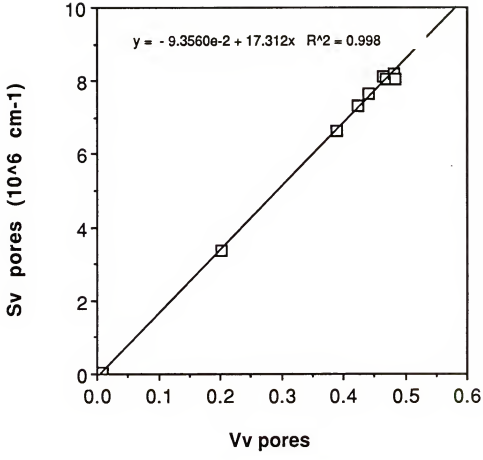

Figure 2.34 Variation of the surface area of pores per unit volume (S_V) as a function of volume fraction of pores (V_V) for samples type A2.

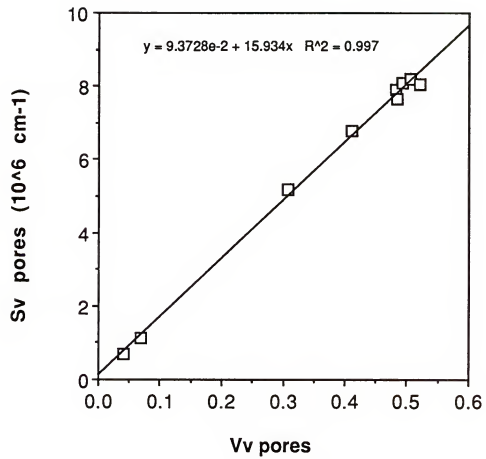

Figure 2.35 Variation of the surface area of pores per unit volume (S_V) as a function of volume fraction of pores (V_V) for samples type A3.

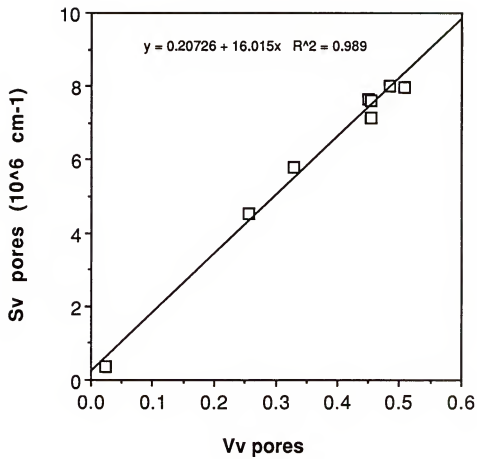

Figure 2.36 Variation of the surface area of pores per unit volume (S_V) as a function of volume fraction of pores (V_V) for samples type A4.

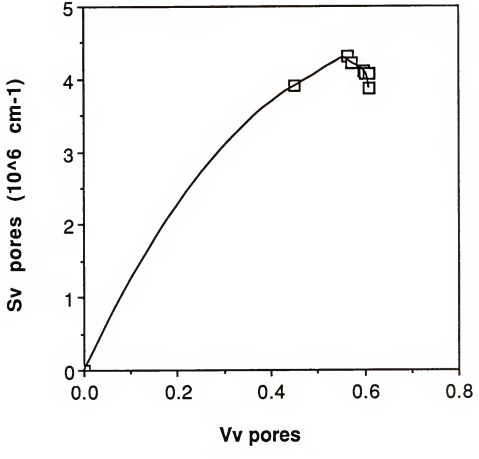

Figure 2.37 Variation of the surface area of pores per unit volume (S_V) as a function of volume fraction of pores (V_V) for samples type B.

where ρ_b is the bulk density;

V_p is the volume of pores per gram;

ρ_t is the structural (true) density.

Applying Eq.(2.17) to the data obtained for the four sets of samples of 12 Å pore radius, one obtains the variation of bulk density with densification temperature as shown in Figure 2.38. The variation of bulk density as a function of densification temperature for sets of silica gel monolithic samples with 12 Å, 32 Å and 81 Å average pore radii is shown in Figure 2.39. The variation of volume fraction of pores with bulk density for a set of 12 Å average pore radius samples is shown in Figure 2.40. There is an almost linear relationship between Vv and bulk density. The deviation from linearity is attributed to structural density variations as shown in Figure 2.25. In order to check for the appropriateness of applying Eq.(2.17) in obtaining bulk density data, a set of direct measurements of bulk density through mercury pycnometry was performed. In these experiments the bulk density is evaluated by measuring the weight of the sample and measuring the volume of the sample by weighing the volume of mercury displaced when the sample is introduced in a container filled with mercury. The results obtained are shown in Figure 2.41 for a set of 12 Å average pore radius. It can be seen that both ways of evaluating bulk density match relatively well. Since in the gas adsorption experiments the nitrogen molecules have to pass through the pores in order to probe the surface and volume of pores, that means that the pores have to be open for such a penetration of gas occur. The good agreement between the bulk

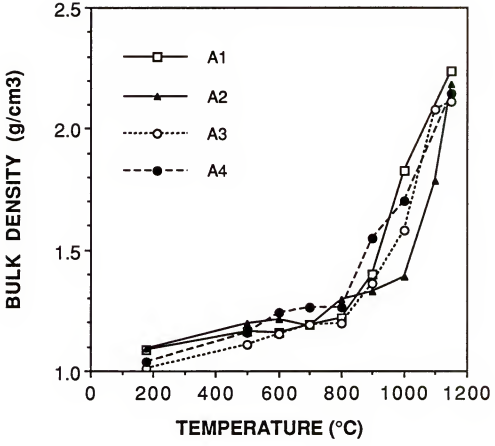

Figure 2.38 Bulk density versus densification temperature for samples type A.

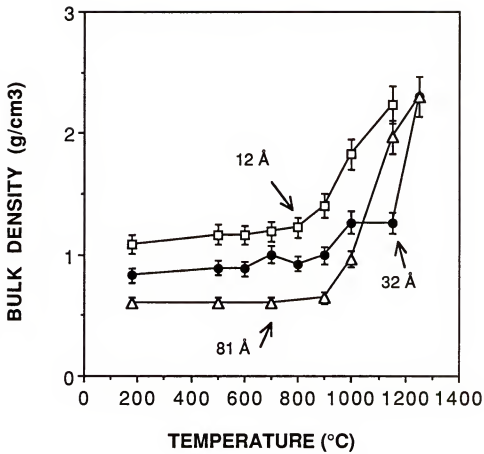

Figure 2.39 Bulk density versus densification temperature for silica gel samples with 12 Å, 32 Å and 81 Å average pore radii.

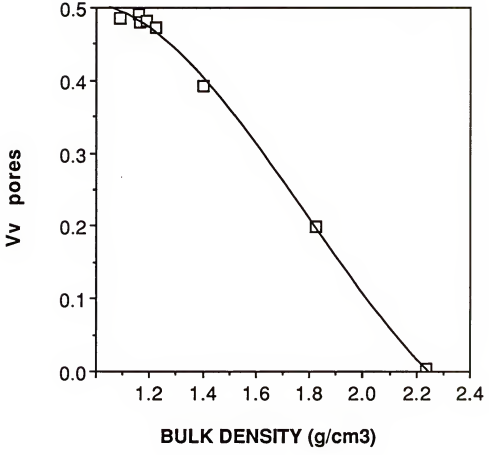

Figure 2.40 Variation of volume fraction of pores (V_V) as a function of bulk density for silica gel samples with 12 Å average pore radius.

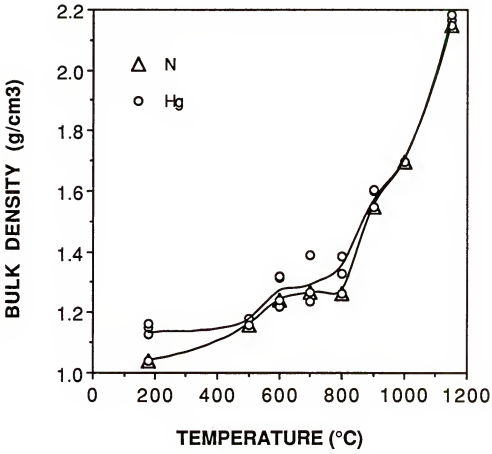

Figure 2.41 Variation of bulk density as a function of densification temperature for silica gel samples of 12 Å average pore radius, as measured by nitrogen gas adsorption (N) and mercury pycnometry (Hg).

density values obtained from gas adsorption and from the direct measurements of bulk density by mercury pycnometry, indicates that the pore network in the silica gel monoliths tested is interconnected. For a structure of a large volume fraction of closed pores (non-interconnected pores), the bulk density calculated from gas adsorption should be greater than the actual value of bulk density.

The variation of bulk density with densification temperature for 81 Å average pore radius samples, as measured by nitrogen gas adsorption and mercury pycnometry is shown in Figure 2.42. For temperatures up to 900 °C (1173 K) there is a very good correspondence between those two techniques. At higher temperatures the results obtained from the techniques differ. That difference is likely to be associated with pore closure at temperatures higher than 900 °C (1173 K) for these larger pore radius samples.

Figure 2.43 shows the variation of volume fraction of pores with densification temperature for samples kept at the densification temperature for periods of 1 h and 10 h. There seems to be only small variations in V_V between those two different processing conditions. Figure 2.44 represents the variation of surface area of pores per unit volume with densification temperature for the two different holding times of 1 h and 10 h. Figure 2.43 suggests a small decrease in S_V when the time at a given sintering temperature increases. Further information on the effect of time upon sintering can be seen in Figure 2.45. This figure shows the variation of volume fraction of pores with

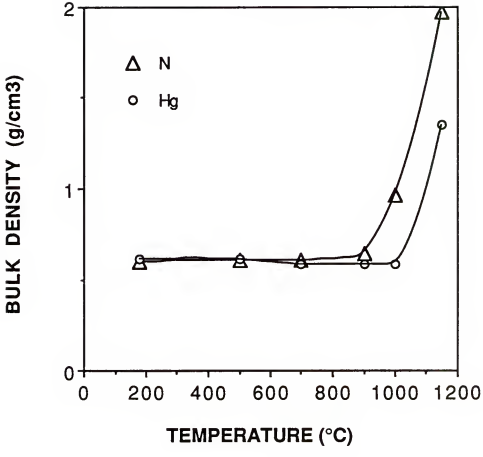

Figure 2.42 Variation of bulk density as a function of densification temperature for silica gel samples of 81 Å average pore radius, as measured by nitrogen gas adsorption (N) and mercury pycnometry (Hg).

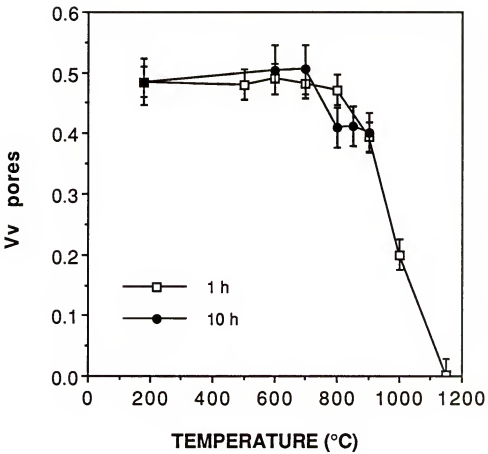

Figure 2.43 Variation of volume fraction of pores (V_V) as a function of densification temperature for samples type A kept at the densification temperature for 1 h and 10 h.

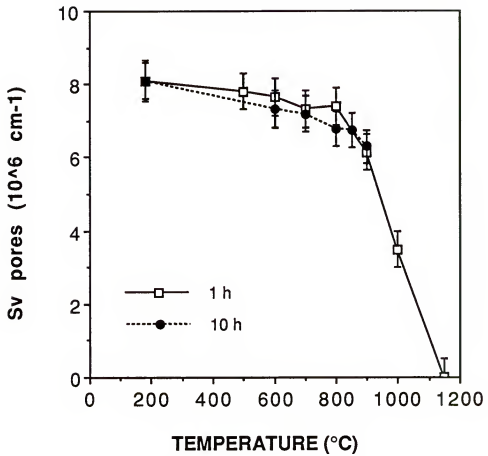

Figure 2.44 Variation of the surface area of pores per unit volume (S_V) as a function of densification temperature for samples type A kept at the densification temperature for 1 h and 10 h.

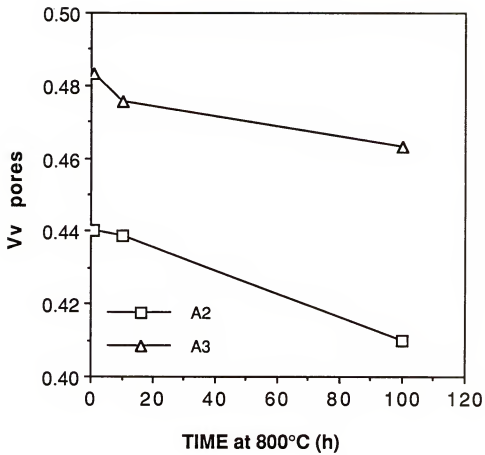

Figure 2.45 Variation of the volume fraction of pores (V_V) as a function of time for samples type A2 and A3.

holding time at 800 °C (1073 K), for two sets of 12 Å average pore radius samples.

2.7 Humidity Effects on Densification

In order to evaluate the effect of atmosphere in the sintering behavior of silica gel monoliths, samples were densified in a humid, ambient atmosphere furnaces, as opposed to using a dry-air atmosphere inside the furnace. The variation of volume fraction of pores with densification temperature for 12 Å average pore radius samples is shown in Figure 2.46 for both types of atmospheres. The figure suggests that the humid ambient causes a slightly faster decrease in V_V of pores. Similar suggestion is obtained from Figure 2.47 which shows the variation of surface area of pores per unit volume with densification temperature for both atmospheres.

The variation of bulk density with densification temperature is shown in Figure 2.48 for samples type A1 sintered in a dry-air atmosphere and in a humid atmosphere. Figure 2.49 shows similar curve for samples type A2. Both Figures 2.48 and 2.49 suggests a slightly faster increase in bulk density with temperature for samples processed in a humid atmosphere.

The relatively faster densification in a humid atmosphere can be associated with the experimentally observed fact that samples densified in humid air will bloat or foam easier (meaning at lower temperatures) than samples densified in dry-air. This fact is associated with trapping

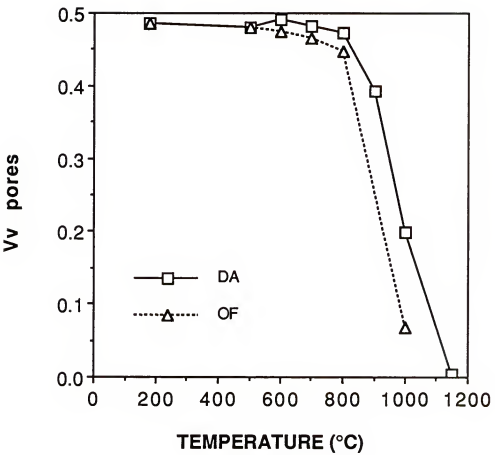

Figure 2.46 Variation of volume fraction of pores (V_V) as a function of densification temperature for samples type A densified in a dry-air (DA) and in a humid (OF) atmospheres.

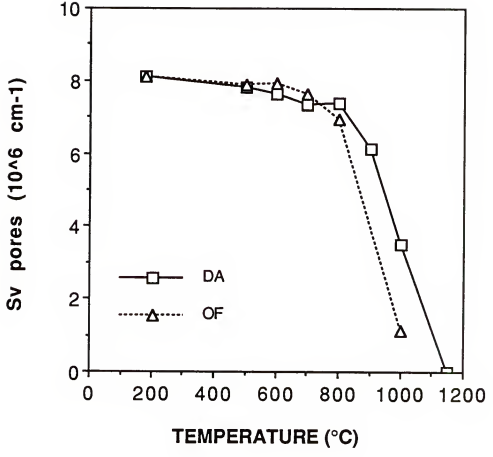

Figure 2.47 Variation of surface area of pores per unit volume (S_V) as a function of densification temperature for samples type A densified in a dry-air (DA) and in a humid (OF) atmospheres.

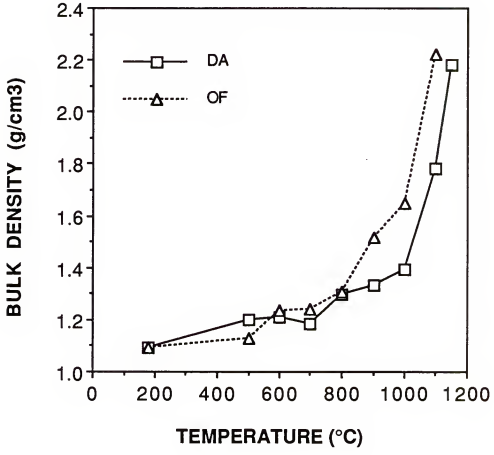

Figure 2.48 Variation of bulk density as a function of densification temperature for samples type A2 densified in a dry-air (DA) and in a humid (OF) atmospheres.

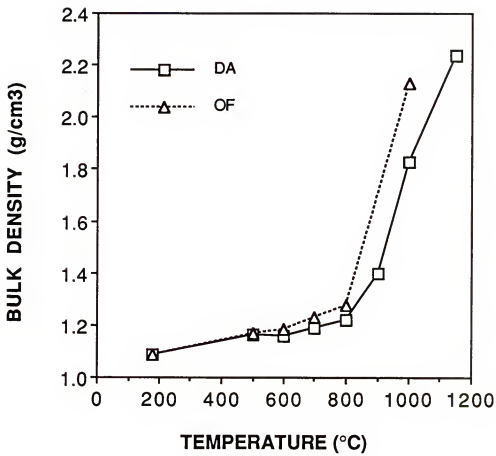

Figure 2.49 Variation of bulk density as a function of densification temperature for samples type A1 densified in a dry-air (DA) and in a humid (OF) atmospheres.

of water inside closing pores. When the temperature is raised further the increasing pressure inside the closed pores will cause the material to crack and/or foam (or bloat). For that reason, most of the samples prepared for physical testing in this work were densified in a dry-air atmosphere. This resulted in dense monolithic samples with no defects such as cracks or foaming.

CHAPTER 3
TOPOLOGICAL MODELING OF DENSIFICATION

3.1 Description of the Structure of Materials

3.1.1 The Metric Properties

According to DeHoff [357, p.4633] "in biology, function follows form; in materials science, structure determines properties." Therefore, the study of the structure of materials is the central part of materials science. In order to describe completely the structure of a material, two basic characteristics have to be defined:

1) The *constitution* of the structure, in terms of its chemical composition and components (e.g., its thermodynamic phases).
2) The *geometry* of the structure, which is described by two types of parameters: metric and topological parameters.

For the case of silica gels, for instance, the composition is pure SiO_2 (for the dense material only, because in the early stages of densification one has to take into account the presence of water, acidic solutions, organics, etc.) and it is monophasic (SiO_2 glassy phase for the fully dense gel-silica). For intermediate stages one has to recognize the presence of two phases: the SiO_2 solid network and the pores.

Since the structure of a material exists in a three-dimensional space (Euclidean space E^3), the structural parameters are usually reported per unit volume of the material. A three-dimensional structure can be decomposed into elements of dimensionalities varying from three to zero (tri-dimensional, bi-dimensional, uni-dimensional, and zero-dimensional elements).

In the case of a polycrystalline material, the presence of grain boundaries makes it straightforward to associate structural features to each dimensionality, as shown in Table 3.1 [357]. In a glassy material there will be no grains, no grain boundaries, no edges, and no corners.

According to DeHoff [357] the structural state of a material can be described by three different states:

1) The *qualitative* state, which is a list of the classes of each kind of features (cells, surfaces, lines, and points) that exist in the structure.
2) The *quantitative* state, which associates numbers and quantities to the structural features present.
3) The *topographic* state, which describes non-uniformities in the structure such as (a) gradients (variation of property with position); (b) anisotropies (variation of property with orientation), and (c) variations in spatial distributions (e.g., clustering, ordering, or associations or disassociations of one class of features with others).

Table 3.1 Features encountered in a polycrystalline material in relation to their dimensionalities [357].

Dimension	Feature
3	Cell
	Grain
2	Surface
	Boundary
1	Line
	Edge
0	Point
	Corner

Also according to DeHoff [305, p.292],

> those properties of a structure which may be classed as topological include any property which is unchanged when the structure is stretched, distorted, or twisted without limit, so long as it is neither torn nor joined to itself during the deformation. Topological properties thus have to do with the *connectivity* of a structure, and are independent of details of shape and size. It is precisely because topology abstracts geometric properties without concern about metric detail that these concepts are so valuable in characterizing complex structures.

On other hand, the metric properties of a structure change when the structure is stretched, distorted or twisted. Examples of metric properties include [305,357-365]:

1) Volume fraction (V_V), which represents the volume of a given phase or constituent divided by the total volume of the material; it can be evaluated either using stereology (via area fraction, lineal fraction or point counting) or through direct measurements of volume on the structure (e.g., using gas adsorption techniques).
2) Surface area per unit volume (S_V), which represents the surface area of a given phase or constituent divided by the total volume of the material; it can be evaluated either using stereology (via number of intercepts per unit of length or number of features per unit of length) or through direct measurements of surface on the structure (e.g., using gas adsorption techniques).
3) Total curvature of a surface per unit volume (M_V), where the total curvature is defined as the sum of the surface curvature plus the edge curvature; it can be evaluated stereologically by

counting either the number of tangents per unit area or the number of features per unit area.

4) Line length per unit volume (L_V), which can be evaluated stereologically by counting the number of quadruple points per unit area.
5) Integral curvature of a surface per unit volume (I_V), which corresponds to the net spherical image of the surface in a unit volume.
6) Integral curvature of a line per unit volume (C_V).
7) Integral torsion of a line per unit volume (F_V).

Besides those seven main metric parameters, there are average properties (or combinations of metric properties) which are very useful for certain applications. Some important average parameters are the following [357,365-370]:

1) Mean lineal intercept (λ_3), which represents the average surface-to-surface distance through a cell, and for each type of surface it is given by

$$\lambda_3 = \frac{4\,V_V}{S_V}. \tag{3.1}$$

2) Mean free lineal intercept (λ_f), which represents the average surface-to-surface distance through the other (or others) constituent, and for a given type of surface it is given by

$$\lambda_f = \frac{4(1 - Vv)}{Sv}. \tag{3.2}$$

3) Average mean curvature (H), given by

$$H = \frac{Mv}{Sv}. \tag{3.3}$$

4) DeHoff's shape parameter (D_e), defined by

$$D_e = H \lambda_3 . \tag{3.4}$$

3.1.2 The Topological Properties

According to Stillwell [371, p.2]

> topology is the branch of geometry which studies the properties of figures under arbitrary continuous transformations. Just as ordinary geometry considers two figures to be the same if each can be carried into the other by a rigid motion, topology considers two figures to be the same if each can be mapped onto the other by a one-to-one continuous function. Such figures are called topologically equivalent, or homeomorphic.

Those properties of topological spaces that are invariant under homeomorphisms are termed *topological properties* [372].

Topology is divided into two main branches [373]: (1) general topology (or point-set topology) and (2) algebraic topology (or combinatorial topology). While general topology deals with set-theoretic tools, algebraic topology uses algebra (mainly group theory).

The first known work on topology was carried out by Euler in 1752 [374]. Listing [375] seems to have been the first to use the word "topology" in 1847. Besides Listing, further pioneering work on topology was done by Cantor [376], Riemann [377] and Poincaré [378] by the end of the 19th Century, and by Riesz [379], Fréchet [380] and Moore [381] in the early 1900s. The pioneering work of introducing the topological concepts in materials science was carried out by Rhines [284] in 1958. Details on set-point topology and algebraic topology are found in an extensive list of publications [e.g., 382-390].

Algebraic topology study surfaces by "triangulating" them, that is, by dividing them up into triangular regions in such a way, that two regions which intersect do so by either contacting along a single edge or at a single corner (or vertex) of a triangle. These rectilinear triangulations are termed *simplicial complexes*. Giblin [391, p.7] points out that the advantage of reducing a surface to simplicial complexes "lies in the fact that any triangulated surface is homeomorphic to one in which the triangles are flat and the edges straight," which allows for a rigorous algebraic study of surfaces.

Each triangle has three straight edges and three vertices. The so-called *intersection conditions* that are imposed on the geometric arrangement of the triangles are [391]

Two triangles either

1) Are disjoint (Figure 3.1(a));

2) Have one vertex in common (Figure 3.1(b));

3) Have two vertices in common (Figure 3.1(c)).

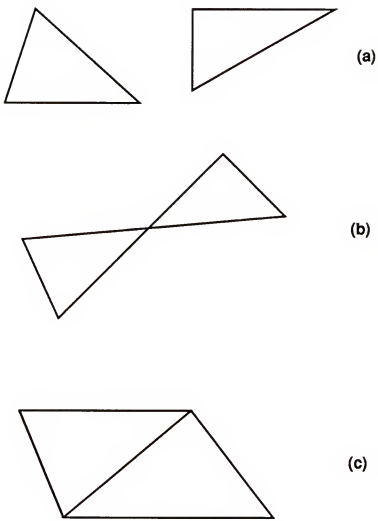

Figure 3.1 Intersection conditions.

Based on the above, a closed surface M is defined such that [391]

1) M satisfies the intersection condition;
2) M is connected;
3) For every vertex v of a triangle of M; the link of v is a simple closed polygon.

For a closed surface M, the Euler characteristic (χ) of M is defined as [389]

$$\chi(M) = V - E + T, \tag{3.5}$$

where V is the number of vertices of M;

E is the number of edges of M;

T is the number of triangles.

The Euler characteristics of various types of surface are shown in Table 3.2 [389]. Figure 3.2 [390] shows schematics of the geometric shapes mentioned in Table 3.2 (sphere, torus and Klein bottle).

Assuming W as a homology group of a finite complex associated with a topological space, a crude measure of the size of W is given by the rank (h_k) of W, or the number of elements in W. The numbers h_k are termed the *Betti numbers* of the complex. The Betti numbers are described by the symbol β_i, where i is an integer varying from 0 to n, and n is the dimensionality of the complex. Table 3.3 shows the possible Betti numbers for complexes with dimensionalities varying from 0 to 3.

Table 3.2 Euler characteristic (χ) of the surface M [389].

Surface	$\chi(M)$
Sphere	2
Connected sum of n tori	2 - 2n
Connected sum of n projective planes	2 - n
Connected sum of projective plane and n tori	1 - 2n
Connected sum of Klein bottle and n tori	- 2n

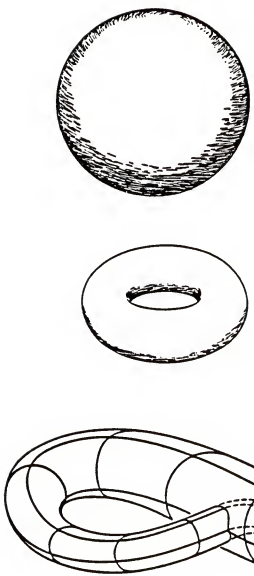

Figure 3.2 (a) Sphere; (b) torus; (c) Klein bottle [390].

Table 3.3 Betti numbers of complexes with dimensionalities varying from 0 to 3.

Dimensionality	Betti numbers
0	β_0
1	β_0, β_1
2	$\beta_0, \beta_1, \beta_2$
3	$\beta_0, \beta_1, \beta_2, \beta_3$

The zeroth Betti number (β_0) is the number of components or disjoined parts of a complex [392]. The first Betti number (β_1) is called the *connectivity number* of the surface [392]. It represents the largest number of closed curves that can be drawn on the surface of a complex without dividing the surface into two or more pieces. The second Betti number (β_2) is one for all compact, connected surfaces [392]. The third Betti number (β_3) is always zero for finite complexes imbedded in the Euclidean space E^3 [392].

According to Rhines et al. [363, p.8],

> the connectivity C of an isolated volume is defined as the number of independent closed curves that may be constructed within the volume which cannot be smoothly deformed into each other, nor shrunk to a point, without leaving the volume. Thus a sphere has a connectivity of zero since any closed curve constructed within its volume may be shrunk to a point; the sphere is a member of a class of volumes or bodies called *simply connected bodies*, all of which may be stretched or deformed into a sphere.

Figure 3.3 shows a few geometric shapes that are topologically equivalent to a sphere. A torus has a connectivity of one, since one can draw a curve (around the hole) which cannot be shrunk to a point without leaving the volume of the torus. Figure 3.4 [390] shows a few three-dimensional geometric shapes which have connectivity of one, and therefore, are topologically equivalent to a torus.

For sintered structures, the connectivity assumes very high values, specially in the initial stages of the sintering process. As the pores disappear during sintering, the connectivity decreases. Both the solid phase and the gas phase in a sintered structure have the same

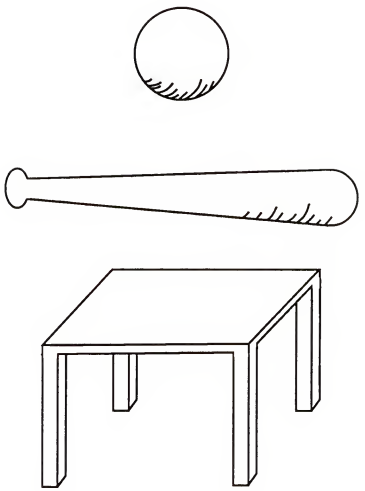

Figure 3.3 Schematic of three-dimensional geometric shapes with zero connectivity (C).

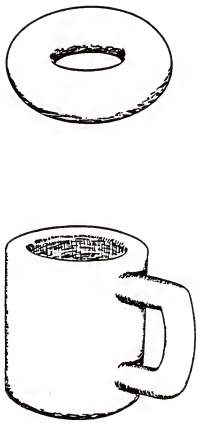

Figure 3.4 Schematic of three-dimensional geometric shapes with connectivity (C) equal to one [390].

connectivity. They are termed [363] *conjugate* to each other, because together they fill space.

While the connectivity (C) is a property of the volume, the *genus* (G) is a property of a closed surface. DeHoff [305, p.296] defines genus as "the maximum number of non-self reentrant closed curves which may be constructed on the surface without dividing it into two separate parts." Another equivalent way of defining genus is given by Massey [389]: "a surface that is the connected sum of n tori or n projective planes is said to be of genus n."

According to Rhines et al. [363, p.8],

> it can be shown that the genus of a closed surface is equal to the connectivity of either of the two volumes (solid and gas) of space which it separates. Thus, for a sintered structure, the genus of pore-solid interface, the connectivity of the pore phase, the connectivity of the solid region, . . . and the first Betti number, are all equal.

Therefore, the connectivity of the pore network in a sintered gel-silica can be expressed by either C_V^P (connectivity of the pores), C_V^S (connectivity of the solid phase), G_V (genus of the solid-pore interface) or by $ß_1$ (the first Betti number of the pore-solid interface), and all those parameters possess the same numerical value.

Since a structure is usually defined in the Euclidean space E^3 (because this is a three-dimensional world), it is useful to list the topological parameters pertaining to each dimensionality varying from zero to three as shown in Table 3.4. Zero-dimensional structures (or zero-dimensional components of a structure) can be characterized by the number of zero-dimensional entities (N^0), and there is no connectivity

Table 3.4 Independent topological parameters that can be associated to three-dimensional structures.

Dimensionality	Parameter
0	N^0
1	N^1, μ
2	N^2, G
3	N^3, C

associated with those zero-dimensional features. One-dimensional structures (or one-dimensional components of a structure) can be described by the number of one-dimensional features (N^1), and by the so-called "cyclomatic number" (μ), which is given by

$$\mu = b - n + p , \tag{3.6}$$

where b is the number of branches;
n is the number of nodes;
p is the number of components or disjoined parts of the uni-dimensional network.

Two-dimensional structures (or two-dimensional components of a structure) can be described by the number of two-dimensional features (N^2), and by the genus (G) of the two-dimensional constituents. Three-dimensional structures (or three-dimensional components of a structure) are characterized by the number of three-dimensional features (N^3), and by the connectivity (C) of the three-dimensional constituents. For all dimensionalities (0, 1, 2 and 3) of a structure, the number of features is given by the zeroth Betti number (β_o). The first Betti number (β_1) corresponds to μ (1-D), G (2-D), or C (3-D). A general expression for the first Betti number (β_1), which includes Eqs.(3.5) and (3.6) can be written as

$$\beta_1 = B - N + \beta_o , \tag{3.7}$$

where B is the number of branches;

N is the number of nodes.

3.1.3 Evaluation of Topological Properties

Figure 3.5 shows a schematic of a structure formed by an array of points (nodes) and lines (branches). For this structure one can count:

$B = 7,$

$N = 7,$

$\beta_0 = 2,$

therefore, the first Betti number (β_1) of that structure as given by Eq.(3.7) is

$$\beta_1 = \mu = 7 - 7 + 2 = 2, \tag{3.8}$$

meaning that it is possible to cut two branches of that structure without increasing the number of separate parts.

Considering the two-dimensional structure shown in Figure 3.6(a), one can count:

$B = 6,$

$N = 4,$

$\beta_0 = 1,$

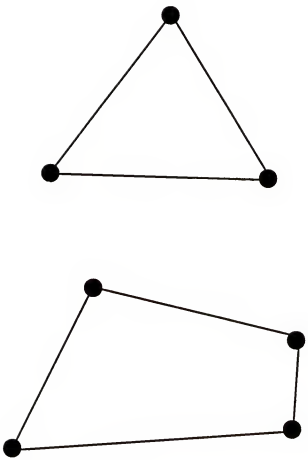

Figure 3.5 Schematic of a structure formed by two linear features.

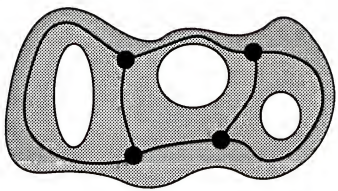

(a)

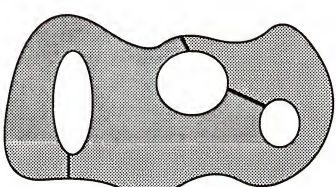

(b)

Figure 3.6 Two-dimensional structure containing three holes.

therefore, the first Betti number ($ß_1$) of that structure as given by Eq.(3.7) is

$$ß_1 = G = 6 - 4 + 1 = 3, \tag{3.9}$$

meaning that it is possible to make three cuts through the structure without dividing it into two (or more) parts. This can be directly seen by inspecting Figure 3.6(b), which shows three possible cuts in the structure without separating it. Any additional cut will divide the structure into at least two parts. Another way of obtaining the connectivity of three is by directly counting the number of holes present in the structure (3 holes).

For three-dimensional constituents of a structure, one can describe the connectivity (C) by evaluating the genus (G), because of the numerical equality between connectivity and genus. Considering Figure 3.7, one obtains

$B = 11,$

$N = 7,$

$ß_o = 2;$

therefore, Eq.(3.7) yields

$$ß_1 = G = C = 11 - 7 + 2 = 6, \tag{3.10}$$

meaning that it is possible to make six cuts in that structure without increasing the number of separate parts.

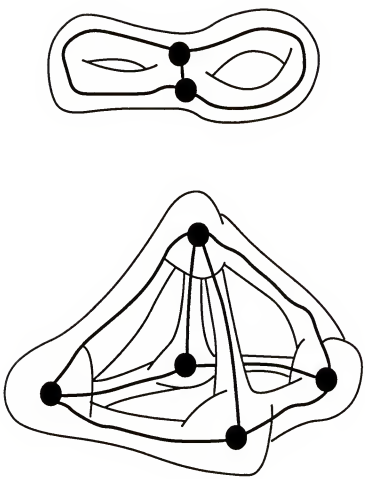

Figure 3.7 Schematic of a three-dimensional structure formed by two separate parts.

In the examples shown above it is very easy to count directly the parameters B, N and β_0. In a real structure this process is extremely difficult, because of the large numbers involved, the small scale of the structure of materials, and because of the inherent problem of identifying a branch, a node, and whether two parts of a structure are indeed separated from each other.

In materials science and biology, one needs to use the technique of serial sectioning in order to be able to directly count N, B and β_0. This technique is a series of direct observations of a polished section of a structure in such a way that after preparing, observing, and recording one section, one polishes out a small layer of the material and observe the structure just underneath the previously observed one. This process is repeated several times until it allows for a three-dimensional reconstruction of the network of branches and nodes based upon the combined analysis of the various sections. In order to calculate the topological parameters in a unit volume, accurate measurements of the thicknesses of the removed layers have to be carried out. Examples of applications of the serial sectioning technique are given by Aigeltinger [309] and DeHoff et al. [393].

The application of the technique of serial sectioning is a time-consuming and tedious process. The fundamental limitations of the technique is that one has to be able to not only see the structure, but to carefully remove a precise layer of the material and look again exactly underneath the previously observed one. As DeHoff et al. [393] and Aigeltinger [309] proved, it is feasible to carry out that task for

micrometer scale structures. However, in the case of the evaluation of topological properties of alkoxide derived silica gels such a task is not yet feasible. The difficulties in applying serial sectioning to alkoxide silica gels arise because of the small scale of the pore structures (average pore radius varying from 12 Å to 81 Å, as shown in Chapter 2). There are high-resolution transmission electron microscopes with small enough resolution to identify pores in the nanometer scale. However, as pointed out, the application of the technique requires the precise elimination of layers of well defined thicknesses (which should be of few nanometers for the case of silica gels) and the observation of the structure right underneath the previously recorded observation. All these requirements does not make it feasible to apply the serial sectioning technique to alkoxide derived silica gel monoliths.

Estimates of topological parameters can be carried out through modeling the structure and assuming fixed shapes for those structures [394-398].

In the following sections the modeling of the pore structure of silica gel monoliths will be described. The goal of such a modeling is the obtaining of topological parameters that characterize the pore structure, so that a complete description of the structure involving both types of geometric properties (metric--Chapter 2, and topological) becomes possible.

3.2 Topological Modeling

3.2.1 Introduction

When considering the possibilities of feasible shapes of pores to be used as models for evaluation of topological parameters, the limiting cases are the triangular shape and the circular shapes as seen in Figure 3.8. The triangular shape has a minimal number of sides (3) while the circular shape could represent any polygon with an infinite number of sides. Any other geometric shape has a number of sides that fall in between those two.

Assuming the triangular shape to represent the cross section of the pores of the structure, a three-dimensional view of the pore structure would look like the schematic shown in Figure 3.9, when the coordination number of pores is equal to four. Notice that the shape formed when four branches of the triangular pores meet is a tetrahedron. Therefore, this model can be referred to as tetrahedral geometric model, or triangular model.

When the circle is assumed to represent the cross section of the pores, a cylindrical model is created, as shown schematically in Figure 3.10.

In the next sections tetrahedral, cylindrical and spherical models are described. The models are numbered as follows: Model 1 assumes spherical geometry; Models 2, 3 and 4 assume $P_V = 1$ (P_V is the number of separate parts per unit volume) and the tetrahedral geometry; Models

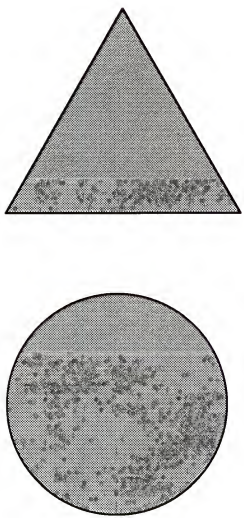

Figure 3.8 Fundamental shapes used for geometric modeling.

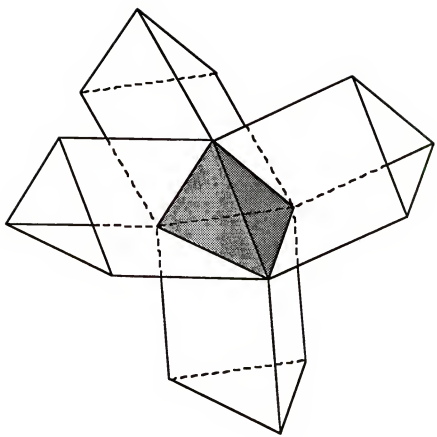

Figure 3.9 Tetrahedral geometric model assumed for topological modeling.

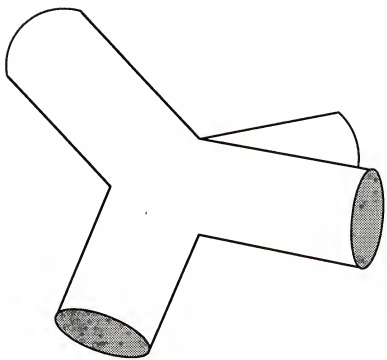

Figure 3.10 Cylindrical geometric model assumed for topological modeling.

5 and 6 assume $P_V = 1$ and cylindrical geometry; Model 7 assumes a variable P_V, a constant N_V (N_V is the number of nodes per unit volume), and cylindrical geometry; Models 8, 9 and 10 assume a variable P_V and tetrahedral geometry; and Models 11 and 12 assume a variable P_V and cylindrical geometry.

3.2.2 Tetrahedral Modeling

As shown in Figure 3.11 the tetrahedral geometric model can be decomposed into a set of branches and nodes. One can associate with each branch and each node a volume and an external surface which directly depend on the size of the branch (l) and the height of the triangle (h).

The total volume of a unit formed by one node and one branch (V_u) is given by

$$V_u = \frac{\sqrt{3}\, h^2\, (h + 6\, l)}{8}, \tag{3.11}$$

The total surface area of a unit formed by one node and one branch (S_u) is given by

$$S_u = \frac{9\, h\, l}{\sqrt{2}}. \tag{3.12}$$

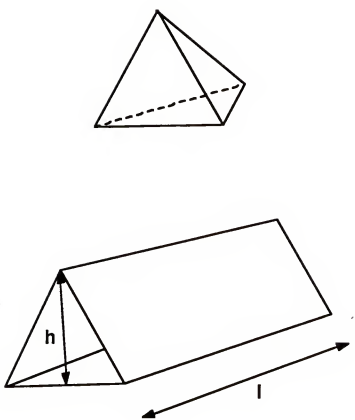

Figure 3.11 Structural components of the tetrahedral geometric model.

Assuming that one can obtain experimental evaluations of the total volume of pores and of the total surface area of pores (using BET data for instance), it is possible to associate the total volume and surface of structural units (based on the tetrahedral model) and then estimate what the total number of units (N) should be.

The ratio between the volume and the surface of a structural unit is given by

$$\frac{V_u}{S_u} = \frac{\sqrt{6}\, h^2}{72\, l} + \frac{\sqrt{6}\, h}{12}. \tag{3.13}$$

The total volume of pores (V_T) and surface area of pores (S_T) can be written as

$$V_T = N\, V_u\,, \tag{3.14}$$

and

$$S_T = N\, S_u\,. \tag{3.15}$$

Using Eq.(3.14) and Eq.(3.15), Eq.(3.13) can be rewritten as

$$\frac{V_T}{S_T} = \frac{\sqrt{6}\, h^2}{72\, l} + \frac{\sqrt{6}\, h}{12}. \tag{3.16}$$

Equation (3.16) can be expressed in terms of volume fraction of pores (V_V) and surface area of pores per unit volume (S_V). Replacing h by D (average diameter of pores) and l by L (average branch size), Eq.(3.16) can finally be written as

$$\frac{V_V}{S_V} = \frac{\sqrt{6}\, D^2}{72\, L} + \frac{\sqrt{6}\, D}{12}. \tag{3.17}$$

Using the same notation in Eq.(3.11) and Eq.(3.13), and Eq.(3.14) and Eq.(3.15) one obtains

$$V_V = \frac{\sqrt{3}}{8} N_V\, D^2\, (D + 6\, L) \tag{3.18}$$

and

$$S_V = \frac{9}{\sqrt{2}} N_V\, D\, L \tag{3.19}$$

where N_V is the number of nodes per unit volume.

Since Eqs.(3.18) and (3.19) have three unknown parameters (N_V, D and L), it is necessary to assume values for one of them (D or L) in order to solve the equations and obtain N_V.

Some possibilities for solving Eqs.(3.18) and (3.19) are shown in Table 3.5. Each type of solution gives rise to a different model, which is numbered together with the corresponding assumption. The value of N_V can, therefore, be obtained by using either Eq.(3.18) or

Table 3.5 Set of assumptions made to solve the equations corresponding to the tetrahedral geometric model.

Model 2	*Model 8*
$L = k D$	$L = k D$
$P_V = 1$	P_V = variable
Model 3	***Model 9***
$L = \frac{4 (1 - V_V)}{S_V}$	$L = \frac{4 (1 - V_V)}{S_V}$
$P_V = 1$	P_V = variable
Model 4	***Model 10***
$D = \frac{4 V_V}{S_V}$	$D = \frac{4 V_V}{S_V}$
$P_V = 1$	P_V = variable

Eq.(3.19), as follows:

$$N_V = \frac{8\ V_V}{\sqrt{3}\ D^2\ (D + 6\ L)}, \tag{3.20}$$

or

$$N_V = \frac{\sqrt{2}\ S_V}{9\ D\ L}. \tag{3.21}$$

According to Table 3.5, Models 2, 3 and 4 assume that the number of separate parts (P_V) is equal to 1 during the entire process. The main implication of this assumption is that during the last stage of densification, when the genus is equal to one, the number of nodes has to be equal to the number of branches because of the general expression

$$G_V = 1 = B_V - N_V + 1. \tag{3.22}$$

When B_V is equal to N_V the coordination number of pores (CN) is equal to two, as shown in Figure 3.12.

Figure 3.13 shows a schematic of the pore coordination number varying from 4 to 0.

As shown in Figure 3.12, Models 2, 3 and 4 assume four as the average coordination number of pores (CN) in the dried stage. That initial stage usually corresponds to a maximum number of branches, nodes and genus. As the genus decreases, during the second stage of

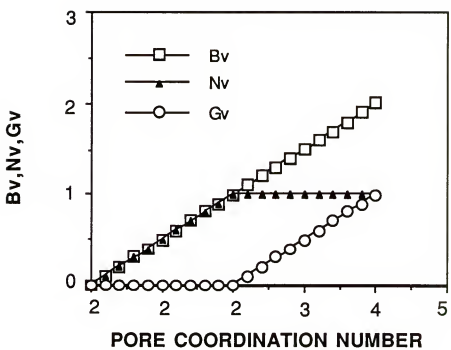

Figure 3.12 Variation of the number of nodes (N_V), number of branches (B_V) and genus (G_V) as a function of the pore coordination number (CN) when $P_V = 1$.

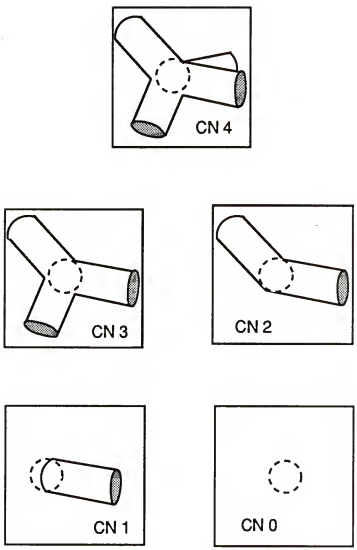

Figure 3.13 Schematic of the pore coordination number (CN) varying from 4 to 0.

densification, the number of nodes remains constant and the number of branches decreases. Models 2, 3 and 4 assume that when CN reaches 2, further elimination of branches leads to disappearance of nodes, and therefore B_V and N_V decrease, keeping CN constant at 2 during the third stage of densification. At this stage G_V is equal to 1 and is kept constant during the third stage.

Models 8, 9 and 10 have similar assumptions to Models 2, 3 and 4, except that they now consider the general expression

$$G_V = B_V - N_V + P_V , \tag{3.23}$$

and therefore P_V can assume values different from 1 in the last stage of densification. Therefore, CN goes from 4 to 0, as shown in Figure 3.14.

According to Figure 3.14, Models 8, 9 and 10 assume 4 as the average coordination number of pores (CN) in the dried stage. As the genus decreases, during the second stage of densification, the number of nodes remains constant and the number of branches decreases. The Models 8, 9 and 10 assume that when CN reaches 2, the number of separate parts (P_V) starts increasing, the number of nodes (N_V) decreases, and the number of branches (B_V) follows a different path compared to its initial trajectory.

In order to evaluate B_V, N_V, G_V and P_V experimentally during the third stage of densification, it is assumed that the number of nodes

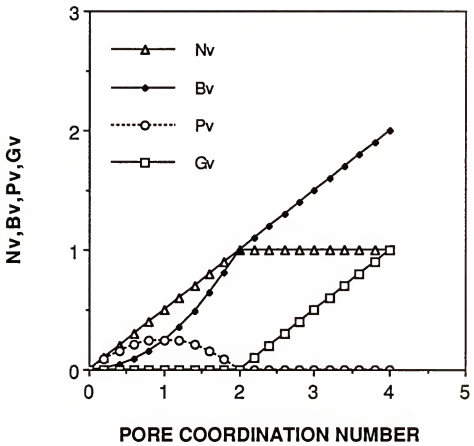

Figure 3.14 Variation of the number of nodes (N_V), number of branches (B_V), number of separate parts (P_V) and genus (G_V) as a function of the pore coordination number (CN) when P_V is variable.

follows a linear relationship with CN as shown in Figure 3.14. N_V is estimated by using the expression:

$$N_V = \frac{\sqrt{2}\, S_V}{9\, D\, L}, \tag{3.24}$$

and the coordination number is given by

$$CN = \frac{2\, N_V}{N_V{}^o}, \tag{3.25}$$

where $N_V{}^o$ is the number of nodes present in the dried stage, or the number of nodes in the plateau from CN 4 to 2.

The number of branches per unit volume (B_V) can be estimated from Eqs.(3.24) and (3.25) as follows:

$$B_V = \frac{CN\, N_V}{2}. \tag{3.26}$$

Since G_V is equal zero in the third stage of densification, P_V can be calculated as follows:

$$G_V = B_V - N_V + P_V = 0, \tag{3.27}$$

thus,

$$P_V = N_V - B_V. \tag{3.28}$$

3.2.3 Cylindrical Modeling

The cylindrical geometric model is based on the assumption that all the volume and all the surface area is associated with the cylindrical branches of the structure. In this case a node represents the point where the branches meet and it has no volume associated to it, like the node in the tetrahedral model does.

Considering D as the diameter of the cylinder and L as the average size of a cylindrical branch, the volume of a branch (or unit, V_b) is given by

$$V_b = \frac{\pi D^2 L}{4}, \tag{3.29}$$

while the surface area of a branch (S_b) is given by

$$S_b = \pi D L . \tag{3.30}$$

Replacing V_b by V_v, and S_b by S_v, and using B_v as the number of branches per unit volume, one can write Eq.(3.29) and Eq.(3.30) as

$$V_v = \frac{\pi B_v D^2 L}{4} \tag{3.31}$$

and

$$S_V = \pi B_V D L . \tag{3.32}$$

One can obtain either directly from the cylindrical shape or from Eq.(3.31) and Eq.(3.32) that the value of D is always a fixed relationship between V_V and S_V:

$$D = \frac{4 V_V}{S_V} . \tag{3.33}$$

Therefore, to obtain the value of B_V from Eq.(3.31) or Eq.(3.32) the only unknown is the parameter L. Once L is estimated the number of branches per unit volume is obtained by either Eqs.(3.31) or (3.32); i.e.,

$$B_V = \frac{4 V_V}{\pi D^2 L} , \tag{3.34}$$

or

$$B_V = \frac{4 S_V}{\pi D L} . \tag{3.35}$$

Table 3.6 shows a set of assumptions of "L" and P_V made in order to solve Eqs.(3.34) and (3.35).

Table 3.6 Set of assumptions made to solve the equations corresponding to the cylindrical geometric model.

Model 7

$$L = \frac{4\,(1 - V_V)}{S_V}$$

P_V = variable

$N_V = N_V{}^o$

Model 5

$L = k\,D$

$P_V = 1$

Model 11

$L = k\,D$

P_V = variable

Model 6

$$L = \frac{4\,(1 - V_V)}{S_V}$$

$P_V = 1$

Model 12

$$L = \frac{4\,(1 - V_V)}{S_V}$$

P_V = variable

3.2.4 Spherical Modeling

Even though a spherical model is not adequate to describe the pore structure of a silica-gel monolith, a spherical model is created in order to serve as reference or limiting case for the other models.

Assuming the spherical pores as having an average diameter D, the number of pores per unit volume (N_V) can be directly correlated with the volume fraction of pores (V_V) as follows:

$$N_V = \frac{6\,V_V}{\pi\,D^3}. \tag{3.36}$$

N_V can equally be associated with the surface area per unit volume (S_V) by the following expression:

$$N_V = \frac{S_V}{\pi\,D^2}. \tag{3.37}$$

The average diameter of a spherical pore is directly obtained from Eqs.(3.36) and (3.37):

$$D = \frac{6\,V_V}{S_V}. \tag{3.38}$$

Therefore, by experimental determination of V_V and S_V it is possible to obtain the number of "spherical pores," N_V.

3.3 Application of Topological Modeling to Gel-Silica

3.3.1 Small Pore Size Structures

The topological model as seen in Figure 3.14 is applied to samples type A (12 Å average pore radius) using the cylindrical model with a variable P_V. The result is seen in Figure 3.15, where B_V, N_V, P_V and G_V are plotted as a function of the pore coordination number (CN). When the topological parameters are plotted as a function of temperature the results are shown in Figure 3.16, for the cylindrical model with a variable P_V. Figure 3.16 thus represents the temperature dependence of the structural evolution. The initial situation in Figure 3.16 is at a temperature of 180 °C (453 K), corresponding to the dried stage. As the densification temperature increases both the number of branches (B_V) and the genus (G_V) decrease, while the number of nodes (N_V) remains constant at N_V^o (number of nodes in the dried stage), and P_V remains constant at one. The position where the pore coordination number decreases to 2 (in Figure 3.15) corresponds in Figure 3.16 to the point where B_V reaches the value of N_V^o, which occurs at a temperature just above 1000 °C (1273 K). At this point the genus goes to zero and the number of separate parts increases from one.

The application of the cylindrical model with variable P_V (Model 12) to other type A samples (12 Å average pore radius) is shown in Figures 3.17, 3.18 and 3.19. They all show a very similar type of structural evolution. The figures representing experimental data obtained in this

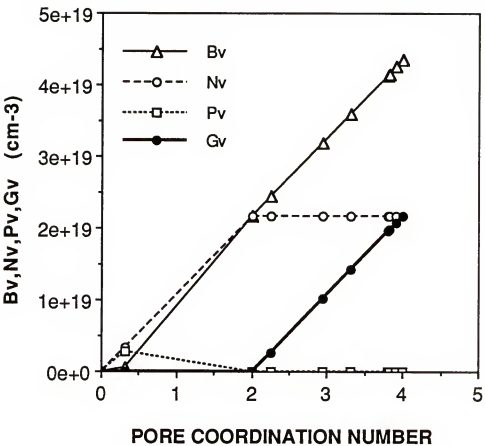

Figure 3.15 Variation of the number of nodes (N_V), number of branches (B_V), number of separate parts (P_V) and genus (G_V) as a function of the pore coordination number (CN) as assumed in the topological modeling. The points on the curves show where the experimental data obtained from samples type A are located (Model 12).

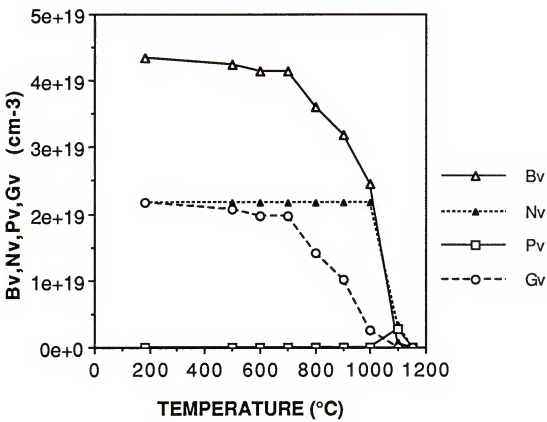

Figure 3.16 Variation of the number of nodes (N_V), number of branches (Bv), number of separate parts (P_V) and genus (G_V) as a function of densification temperature for samples type A1 (Model 12).

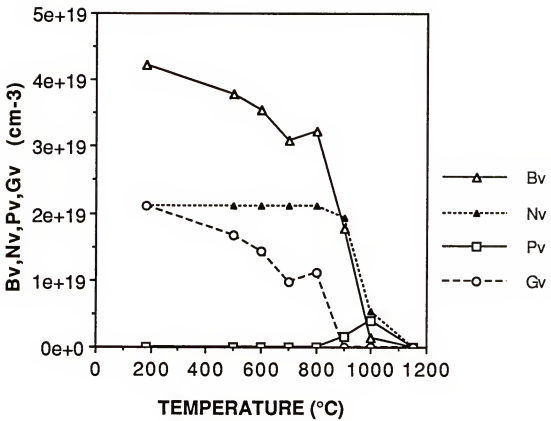

Figure 3.17 Variation of the number of nodes (N_V), number of branches (B_V), number of separate parts (P_V) and genus (G_V) as a function of densification temperature for samples type A2 (Model 12).

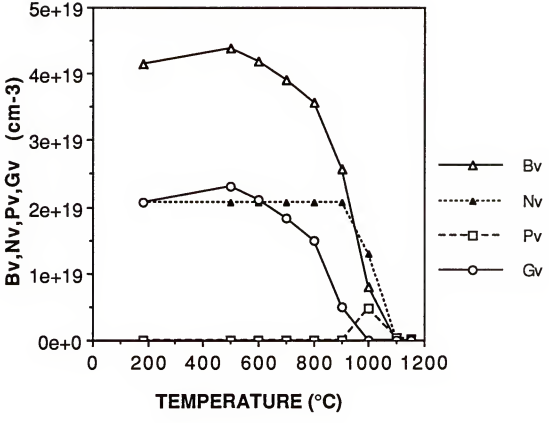

Figure 3.18 Variation of the number of nodes (N_V), number of branches (B_V), number of separate parts (P_V) and genus (G_V) as a function of densification temperature for samples type A3 (Model 12).

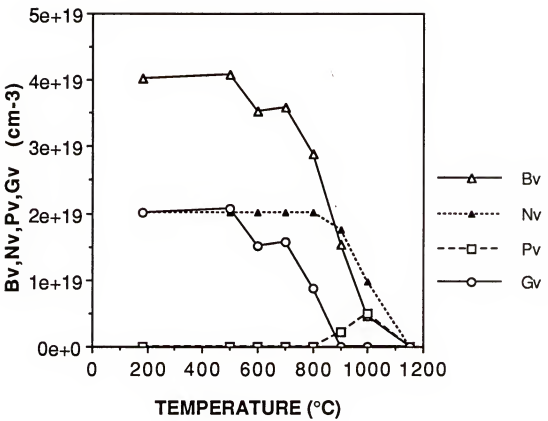

Figure 3.19 Variation of the number of nodes (N_V), number of branches (B_V), number of separate parts (P_V) and genus (G_V) as a function of densification temperature for samples type A4 (Model 12).

work are obtained either using a polynomial or simply connecting the average points, in which case local peaks or valleys in the curves do not necessarily represent an actual trend in the data. The temperature in which the genus goes to zero for all the type A samples is in the range 900 °C (1173 K) to 1100 °C (1373 K).

3.3.2 Large Pore Size Structures

Applying Model 12 (cylindrical model with variable P_V), the variation of number of separate parts (P_V) and genus (G_V) for samples type B (32 Å average pore radius) as a function of densification temperature is shown in Figure 3.20. This figure shows an increase in B_V and G_V as the densification temperature goes from 180 °C (453 K) until 900 °C (1173 K) when both B_V and G_V begin to decrease. The genus goes to zero at a temperature of 1250 °C (1523 K).

For larger pore structures (81 Å average pore radius), the variation of B_V, N_V, P_V and G_V is shown in Figure 3.21. In this case as in the previous one (32 Å pore radius), both B_V and G_V increase as the densification temperature increases from 180 °C (453 K). The genus goes to zero at a lower temperature than for the 32 Å pore radius samples.

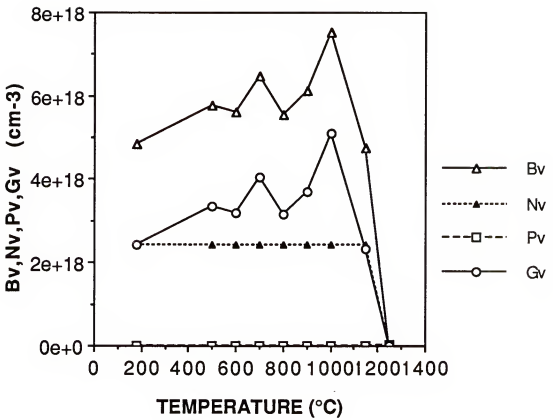

Figure 3.20 Variation of the number of nodes (N_V), number of branches (B_V), number of separate parts (P_V) and genus (G_V) as a function of densification temperature for samples type B (Model 12).

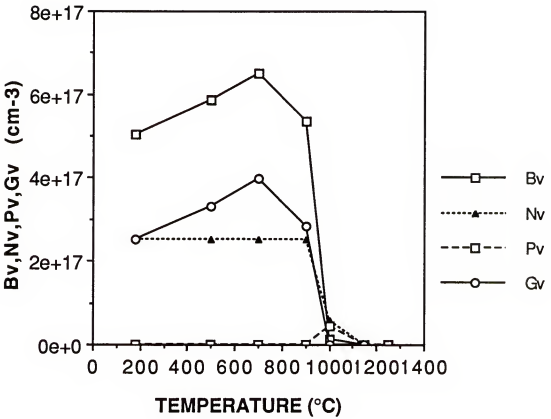

Figure 3.21 Variation of the number of nodes (N_V), number of branches (B_V), number of separate parts (P_V) and genus (G_V) as a function of densification temperature for samples type C (Model 12).

3.4 Topological Indexing

3.4.1 Relative Genus γ

In order to make it easier to compare the structural changes at different stages of densification, the concept of relative genus (γ) is introduced, being defined as follows:

$$\gamma = \frac{G_V}{G_V^o}, \tag{3.39}$$

where G_V^o is the genus of the initial as-dried state, and G_V is the genus at any given stage of densification. The usefulness of this topological index is that it permits comparison of the state of interconnection at different stages of densification, or even of different samples, without requiring the use of large numbers.

In the dried stage $G_V = G_V^o$ and $\gamma = 1$. When the genus goes to zero the relative genus $\gamma = 0$, characterizing the third stage of densification.

Figure 3.22 shows the variation of relative genus (γ) with densification temperature for four sets of samples of 12 Å average pore radius. The values of γ were obtained by applying Model 12 (cylindrical model with variable P_V). The relative genus of sets of samples of 12 Å, 32 Å and 81 Å average pore radii as a function of densification temperature is shown in Figure 3.23. The values of γ used in this figure were obtained by applying the Model 12 (cylindrical model with variable P_V). The variation of the genus of the pore

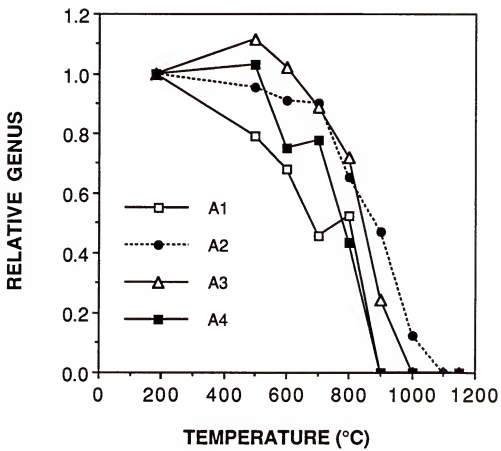

Figure 3.22 Variation of relative genus (γ) as a function of densification temperature for samples type A.

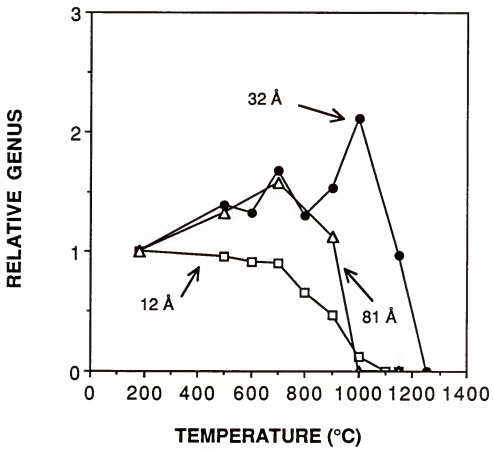

Figure 3.23 Variation of relative genus (γ) as a function of densification temperature for silica gel samples with 12 Å, 32 Å and 81 Å average pore radii.

network of silica gel monoliths as a function of densification temperature is shown in Figure 3.24.

The variation of relative genus as a function of volume fraction of pores is shown in Figures 3.25 to 3.28 for samples type A (12 Å average pore radius). Figures 3.25 to 3.28 suggest that the pore connectivity goes to zero when the volume fraction of pores is around 0.4. This is a relatively high value, suggesting that an initial pore coordination number (CN) greater than 4 would be more appropriate. This will be discussed further in section 3.7. Figure 3.29 shows the variation of relative genus as a function of volume fraction of pores for samples type B (32 Å average pore radius).

3.4.2 Topological Index ß

Because the number of nodes is constant during the second stage of densification, and the genus is constant during the third stage, the number of branches seems to be a convenient parameter to use to follow the evolution of the structure. The number of branches (B_V) varies from an initial state corresponding to the dried structure (B_V^o) until it is zero when the densification is completed. Thus, the number of nodes (N_V) does not reflect structural changes in the sample when the plateau of constant N_V is present. Also, the genus (G_V) is insensitive to structural transformations during the third stage of densification because it is zero during the third stage, when changes in B_V, N_V and P_V still occur.

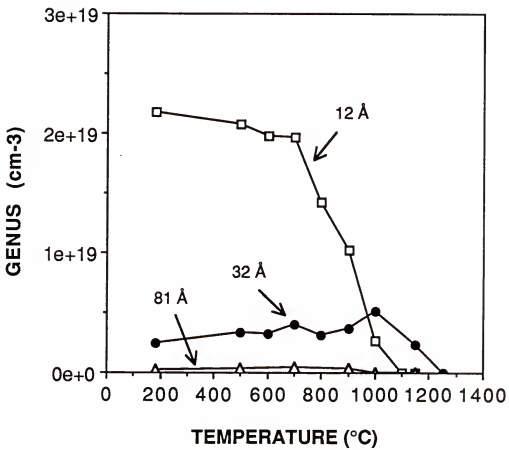

Figure 3.24 Variation of the genus (G_V) as a function of densification temperature for silica gel samples with 12 Å, 32 Å and 81 Å average pore radii.

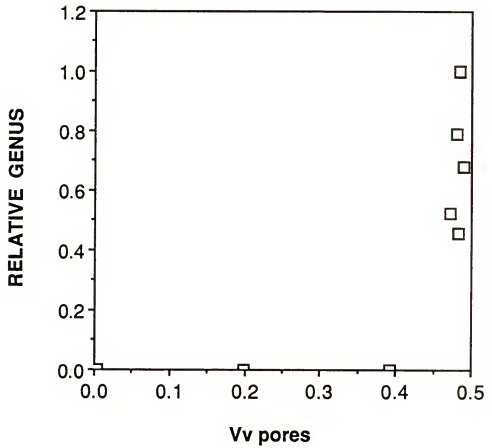

Figure 3.25 Variation of relative genus (γ) as a function of volume fraction of pores (V_V) for samples type A1.

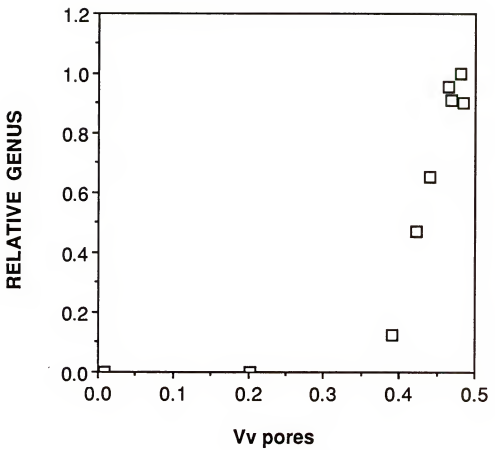

Figure 3.26 Variation of relative genus (γ) as a function of volume fraction of pores (V_V) for samples type A2.

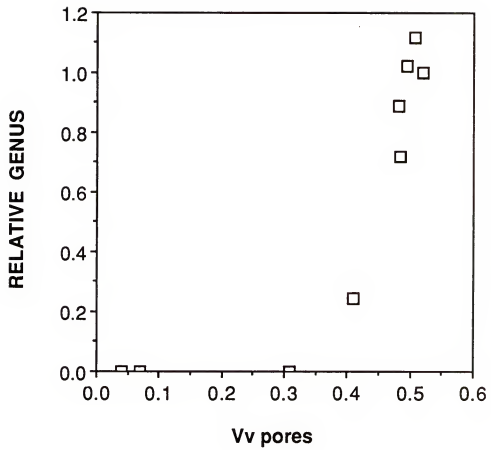

Figure 3.27 Variation of relative genus (γ) as a function of volume fraction of pores (V_V) for samples type A3.

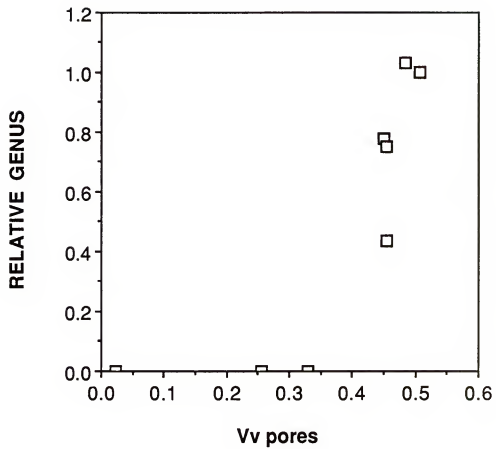

Figure 3.28 Variation of relative genus (γ) as a function of volume fraction of pores (V_V) for samples type A4.

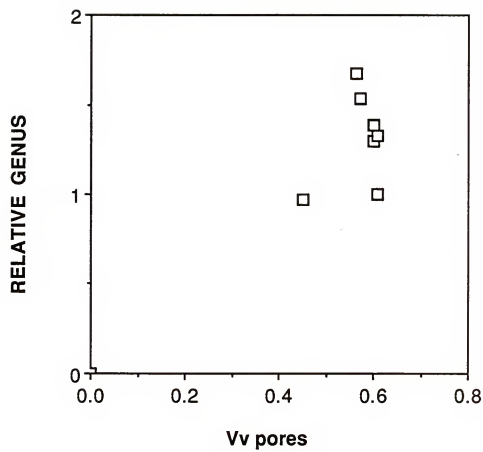

Figure 3.29 Variation of relative genus (γ) as a function of volume fraction of pores (V_V) for samples type B.

Based on the variation of the number of branches (B_V) a topological index ß (fraction of removed branches) is defined as follows:

$$ß = 1 - \frac{B_V}{B_V^o}, \tag{3.40}$$

where B_V is the number of branches at any stage of densification and B_V^o is the number of branches of the initial dried stage, which is used as reference. Therefore, in the dried stage $B_V = B_V^o$ and ß = 0, meaning the initial point of densification. When the sample becomes fully dense, the number of branches in the structure is zero and then ß = 1, characterizing a fully dense sample. Thus, if the dried stage corresponds to a maximum number of branches, the topological index ß will vary from 0 to 1 as the densification proceeds.

Again, the usefulness of such a type of topological index is that it makes it easier to compare different stages of densification for a given type of sample or between different samples by avoiding the use of large numbers. Using this index one can describe the structural evolution of a material undergoing sintering in a very simple and direct manner.

The topological index ß is shown in Figure 3.30 as a function of densification temperature for four sets of samples of 12 Å average pore radius. Model 12 was used to obtain the values of number of branches used in this section. It can be seen from Figure 3.30 that ß varies relatively slowly from 180 °C (453 K) to temperatures in the range 800 °C (1073 K) to 900 °C (1173 K) above which ß increases towards 1 very fast. The variation of topological index ß with densification

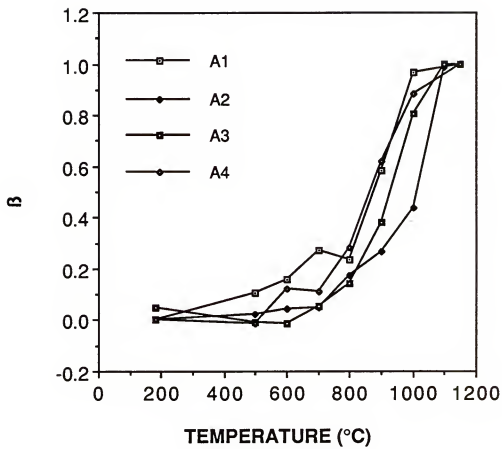

Figure 3.30 Variation of the topological index ß as a function of densification temperature for samples type A.

temperature for samples of 12 Å, 32 Å and 81 Å average pore radius is shown in Figure 3.31. If can be seen from Figure 3.19 the different behavior during densification of the gel-silicas of larger pore radius as compared to the samples of 12 Å pore radius. The variation of the number of branches (B_V) as a function of densification temperature for silica gel monoliths with 12 Å, 32 Å and 81 Å average pore radii is shown in Figure 3.32.

The variation of the topological index ß as a function of the volume fraction of pores for silica gel monoliths with 12 Å average pore radius is shown in Figures 3.33 to 3.36. In these figures Model 12 (cylindrical with variable P_V) was used. Using Model 10 (tetrahedral with variable P_V) one obtains Figure 3.37, for the variation of ß versus V_V of pores.

3.5 Comparison of Models

Depending on the shape assumed for the geometric model, it will contain a certain volume and present a certain surface area which will vary from shape to shape. Since the calculation of topological parameters depends on the volume and surface area of each geometrical unit, it is expected that different shapes will give rise to differences in the values of B_V, N_V, G_V and P_V estimated. However, any difference should be present in such a way that they do not compromise the usefulness and description of the structural evolution. Creating several different models with different assumptions covers the expected range

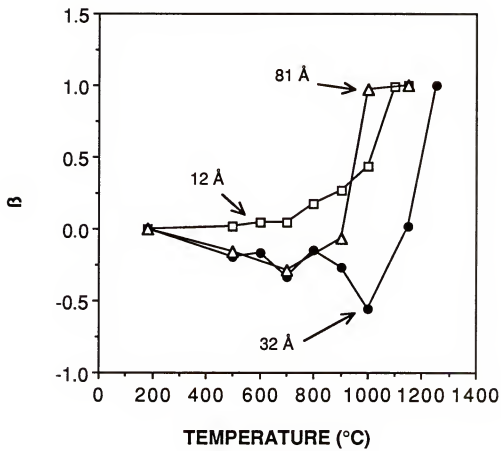

Figure 3.31 Variation of the topological index ß as a function of densification temperature for silica gel samples with 12 Å, 32 Å and 81 Å average pore radii.

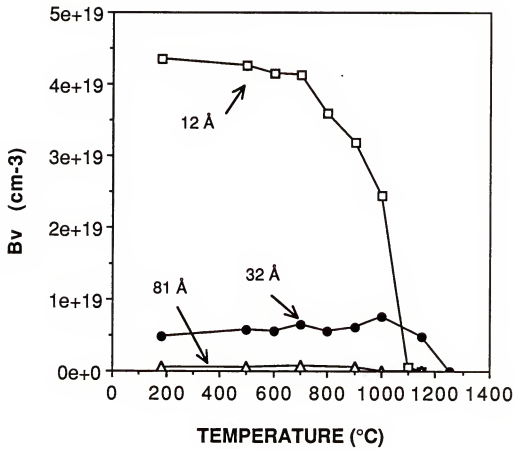

Figure 3.32 Variation of the number of branches (B_V) as a function of densification temperature for silica gel samples with 12 Å, 32 Å and 81 Å average pore radii.

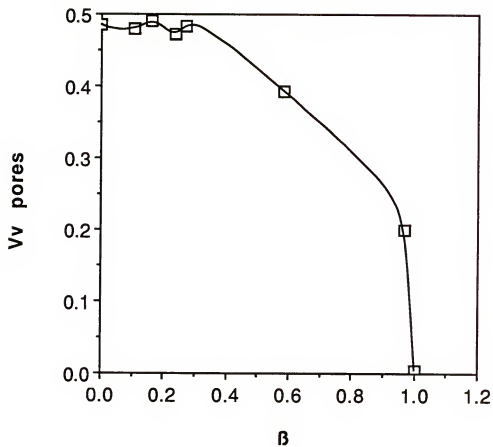

Figure 3.33 Variation of volume fraction of pores (V_V) as a function of the topological index ß for samples type A1 (Model 12).

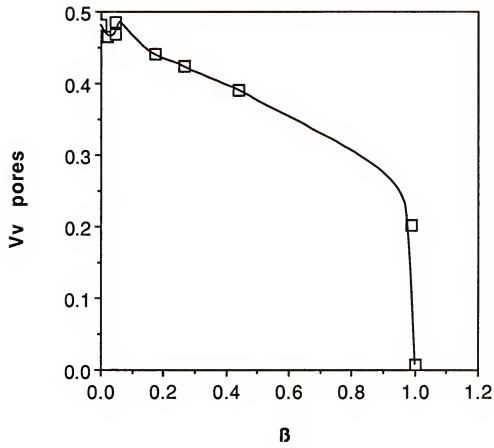

Figure 3.34 Variation of volume fraction of pores (V_V) as a function of the topological index ß for samples type A2 (Model 12).

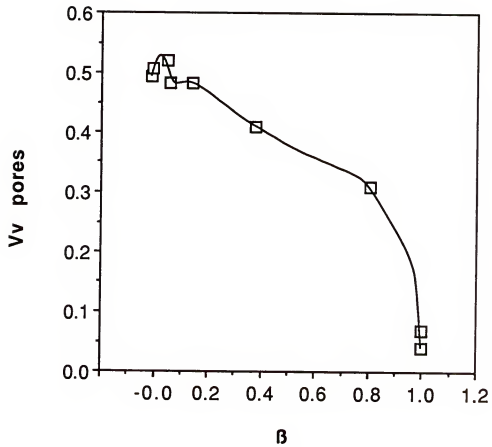

Figure 3.35 Variation of volume fraction of pores (V_V) as a function of the topological index ß for samples type A3 (Model 12).

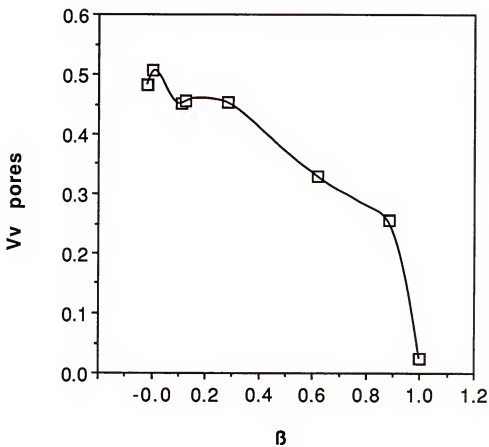

Figure 3.36 Variation of volume fraction of pores (V_V) as a function of the topological index ß for samples type A4 (Model 12).

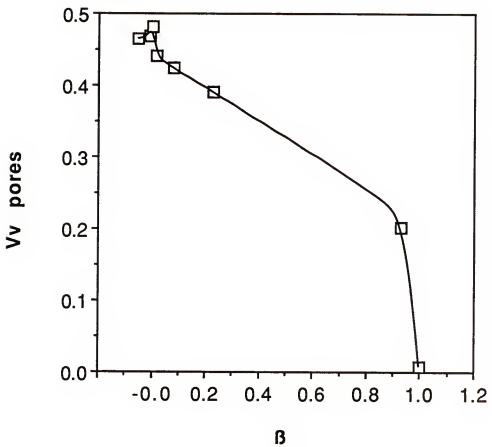

Figure 3.37 Variation of volume fraction of pores (V_V) as a function of the topological index ß for samples type A2 (Model 10).

of variations for the topological parameters during densification. When a certain path of evolution is recognized using different models and assumptions, and when the same ranges of numbers are obtained using different conditions, one can be more confident about the description of the structural transformations based on the proposed models.

The variation of number of nodes (N_V), number of branches (B_V), and genus (G_V) with densification temperature is shown in Figure 3.38, for tetrahedral (Model 3) and cylindrical (Model 6) models. The variation in the geometric shape (triangular or circular pores) seems to have a smaller effect on the values of the topological parameters than the assumption of either L (Model 3) or D (Model 4) as seen in Figure 3.39. The path of structural evolution in both cases (Figure 3.38 and Figure 3.39) is about the same, independent of the model assumed.

Figure 3.40 shows the variation of B_V, N_V, P_V and G_V for a set of 12 Å pore radius samples as a function of temperature. Model 6 shown in the figure assumes $P_V = 1$ and Model 12 accepts a variable P_V. As expected the difference between those two models (6 and 12) occurs only in the third stage of densification. That means that the very simple models can be used to describe structural changes during most of the process.

A general picture of the results obtained by various different models is shown in Figure 3.41. The number of pores (N_V) for the spherical model is shown as open circles (legend 1 N_V). The number of branches (B_V) for tetrahedral (3, 4 and 10) and cylindrical (6, 7 and 12) models

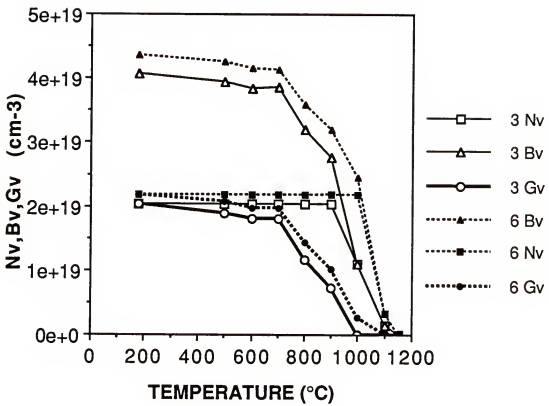

Figure 3.38 Variation of the number of nodes (N_V), number of branches (B_V) and genus (G_V) as a function of densification temperature for samples type A2. Model 3 is a tetrahedral model and Model 6 is a cylindrical model.

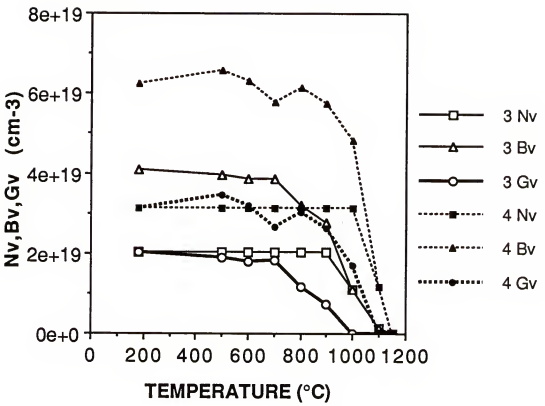

Figure 3.39 Variation of the number of nodes (N_V), number of branches (B_V) and genus (G_V) as a function of densification temperature for samples type A2. Model 3 assumes L and Model 4 assumes D.

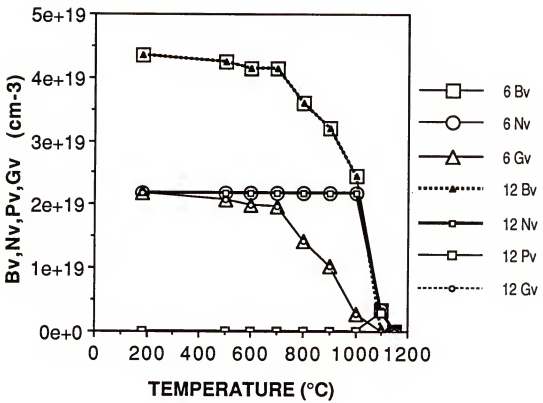

Figure 3.40 Variation of the number of nodes (N_V), number of branches (B_V) and genus (G_V) as a function of densification temperature for samples type A2. Model 6 assumes Pv = 1 and Model 12 accepts a variable P_V.

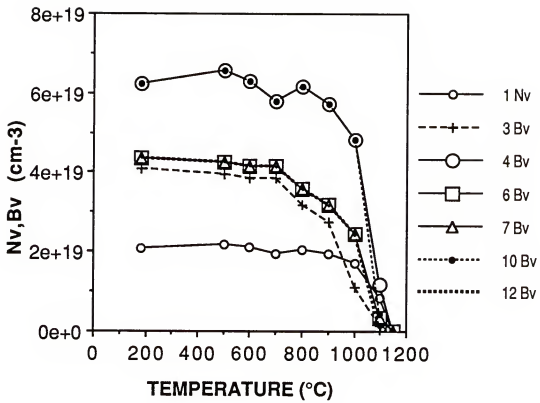

Figure 3.41 Variation of the number of nodes (N_V) and number of branches (B_V) as a function of densification temperature for samples type A2. The numbers in the legend correspond to the model number.

are also shown in Figure 3.41, with the numbers in the legend corresponding to the model number.

As pointed out before, the spherical model seems to provide a (lower), limiting case for the number of pores, even though it is not a realistic model. For a given shape, such as cylindrical, models with a variable P_V (Model 12) differ from models with $P_V = 1$ (Model 6) only during the third stage of densification. The cylindrical Model 7, which assumes a constant value for N_V during the entire process, differs from Model 12 only in the last stage of densification. For the tetrahedral model, assumptions of $D = 4V_V/S_V$, as opposed to assuming $L = 4(1 - V_V)/S_V$, lead to relatively large differences, even though the shape of the curves are very similar.

3.6 Transmission Electron Microscopy Analysis

A gel-silica sample of 12 Å average pore radius in its as dried condition was analyzed by high-resolution transmission electron microscopy (TEM) by Dr. Carrole Perry, Oxford University and Brunel Universities, London. The result is shown in Figure 3.42. The picture shows the pore structure of the dried gel-silica. As seen in the picture the scale of pore sizes is the same scale as obtained by nitrogen gas adsorption and the scale of the interpore distance is the same as the scale of interpore distance obtained from the topological models proposed. This TEM micrograph therefore gives support to the

Figure 3.42 High-resolution transmission electron microscopy photo of a dried silica gel of 12 Å average pore radius. In the photo 1 cm represents 8 nm. (Photo courtesy of Dr. Carrole Perry, Oxford and Brunel Universities, England).

proposed geometric models, by showing that the scale of the structure as obtained by using the expressions for the topological models is realistic.

3.7 Sensitivity Analysis of the Pore Coordination Number

A basic assumption of all the topological models proposed is that in its initial (dried) stage the silica gel samples present an average pore coordination number (CN) of four. The purpose of this section is to analyze the influence of CN on the determination of topological parameters, and to provide a tool so that one can change and adapt the models if an initial CN different than four is expected to yield more realistic results for any given application.

A wide range of pore coordination numbers (CN) is shown in Figure 3.43. In this figure the values of CN were calculated using the Model 12 (cylindrical, with variable P_V). Initial pore coordination numbers (CN^o) varying from 3 to 24 were chosen. Figure 3.43 shows those initial CN's at 180 °C (453 K) and as the densification temperature goes up, the values of CN decrease, until they eventually become zero.

The variation of the number of branches (B_V) with densification temperature is shown in Figure 3.44. It can be seen that the choice of the initial pore coordination number does not affect the values of B_V, except in the third stage of densification. Again, this provides one more argument for the convenience of using the number of branches (B_V) and the topological index ß to describe the evolution of the structure during densification. It should be pointed out that the curve representing the

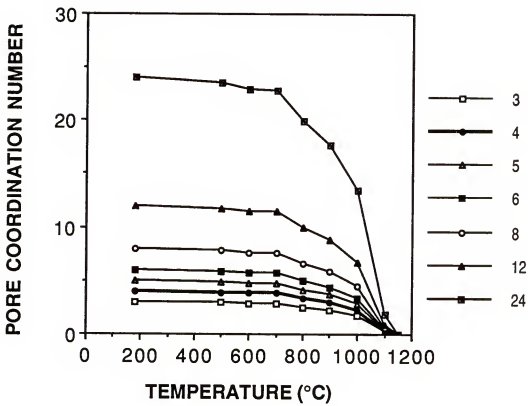

Figure 3.43 Variation of the pore coordination number (CN) as a function of densification temperature for initial CN's varying from 3 to 24 (Samples type A2).

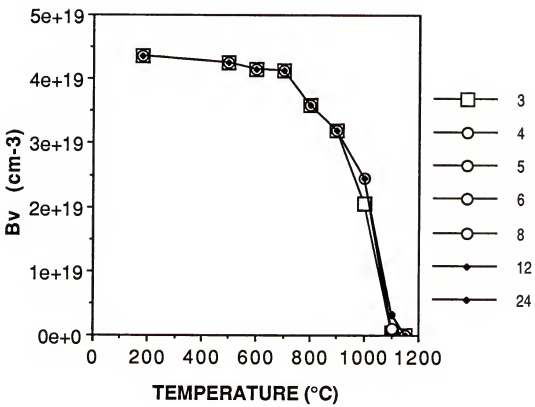

Figure 3.44 Variation of the number of branches (B_V) as a function of densification temperature for samples type A. The numbers in the legend represent the pore coordination numbers in the beginning of densification (Samples type A2).

variation of B_V with temperature is practically the same for CN's varying from 4 to 8.

The variation in the number of branches B_V as a function of the volume fraction of pores V_V is shown in Figure 3.45. Again, for CN^o's between 4 and 8 there is no variation in the path of structural change.

The variation of genus (G_V) as a function of densification temperature is shown in Figure 3.46, when CN^o varies from 3 to 24. Looking at the shape of the curves, particularly to the extrapolation of the last segment of each curve and the temperature obtained by such extrapolation it looks like CN^o's of 8 to 24 would require sharp changes in their respective curves (of variation of G_V with temperature) in order to obtain zero G_V at temperatures in the range of 1100 °C (1373 K). This suggests that CN^o's smaller than 8 would provide more realistic results when used in the models.

The variation of genus (G_V) with volume fraction of pores (V_V) is seen in Figure 3.47. In this figure, if one does not consider the last point of each curve (when V_V is minimal and G_V is equal to zero), and extrapolate each curve, the range of V_V for which $G_V = 0$ will vary approximately between $V_V = 0.3$ to $V_V = 0.4$. Thus for the wide range of initial CN^o's, pore closure should occur in that range of volume fraction of pores.

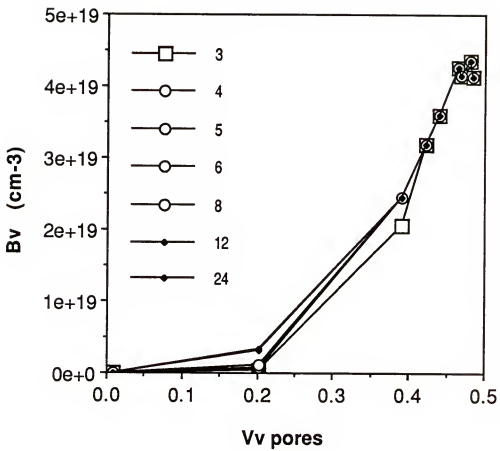

Figure 3.45 Variation of the number of branches (B_V) as a function of the volume fraction of pores (V_V) for assumed initial pore coordination numbers varying from 3 to 24 (Samples type A2).

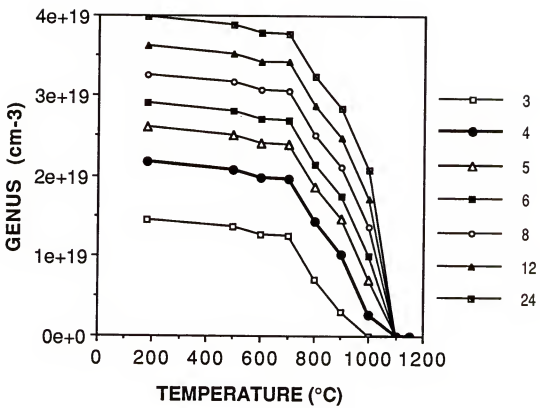

Figure 3.46 Variation of the genus (G_V) as a function of densification temperature when the assumed initial pore coordination number varies from 3 to 24 (Samples type A2).

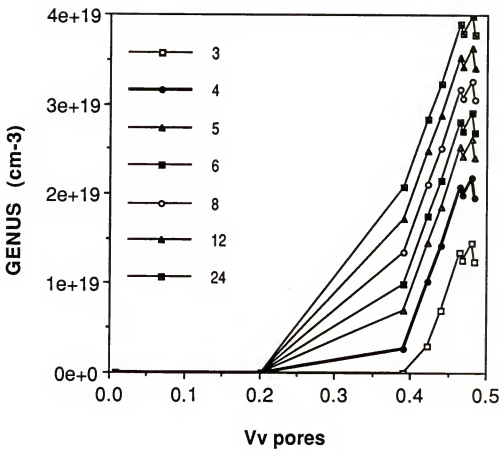

Figure 3.47 Variation of the genus (G_V) as a function of volume fraction of pores (V_V) when the assumed initial pore coordination number varies from 3 to 24 (Samples type A2).

3.8 Topological Analysis of the Time and Humidity Effects

The variation of genus (G_V) with densification temperature for 12 Å average pore radius samples is shown in Figure 3.48. A set of samples was kept at the (maximum) densification temperature for a period of 1 h (standard procedure) while a second set was kept at densification temperature for 10 h. The figure suggests that the longer the densification time the more the genus is going to decrease. A similar type of behavior can be seen in Figure 3.49 where the topological index ß is plotted as a function of the (maximum) time at the densification temperature. Figure 3.49 suggests that the longer the time used in densification at a given temperature, a larger fraction of branches will be removed from the structure.

In order to evaluate further the effect of atmosphere on the sintering behavior of gel-silica monoliths, a set of samples (A1) was densified in a dry-air (DA) atmosphere and another set in a humid (OF) atmosphere. The variation of genus with densification temperature for those samples is shown in Figure 3.50. The figure suggests that samples densified in humid atmosphere close their pores faster than samples processed in a dry-air atmosphere. This tendency could explain why samples sintered in a box-furnace (open to ambient atmosphere, with no flow of dry-air) foam or bloat much more frequently and at a lower temperature than samples densified in a closed furnace with a dry-air flow.

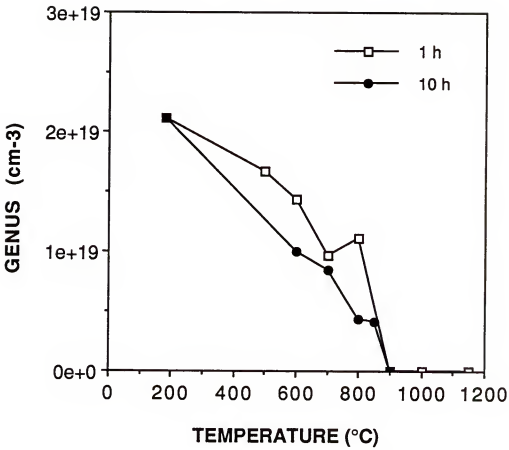

Figure 3.48 Variation of the genus (G_V) as a function of densification temperature for samples type A1 kept at the densification temperature for 1 h and 10 h.

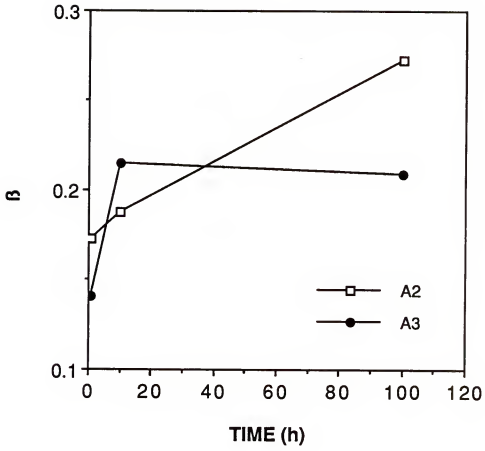

Figure 3.49 Variation of the topological index ß as a function of the time the sample was held at 800 °C for samples type A1 and A2.

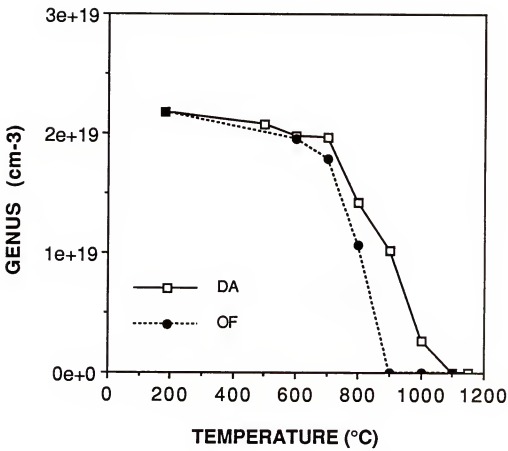

Figure 3.50 Variation of the genus (G_V) as a function of densification temperature for samples type A1 densified in a dry-air (DA) atmosphere and in a humid (OF) atmosphere.

CHAPTER 4
MECHANICAL ANALYSIS

4.1 The Strength of Brittle Materials

Strength of materials is a science that deals with the relation between external loads, internal forces, and the deformation caused by those forces [399]. In order for one to study and obtain expressions relating those loads, forces, and deformations, the following assumptions are usually made [399]:

1) The body is continuous; meaning that it contains no voids or empty spaces.
2) The body is homogeneous; meaning that it has identical properties at all points.
3) The body is isotropic; meaning that the property considered does not vary with direction or orientation.

The relationships obtained using the above assumptions form the body of the mechanics of materials, or mechanical resistance of materials.

Another approach to the problem of achieving a treatable (mathematical) aspect concerning the strength of materials is by considering that it is not a continuous body, but a discontinuous body formed by individual atoms. This is an atomistic approach, and it relates to the strength of a body as a whole to the strength of the

individual bonding between the atoms and/or molecules that compose the body. In this case it is also assumed that the body is homogeneous and isotropic, so that calculations made in the atomic scale can be extrapolated for the entire body.

Real materials have both components: the atomistic contribution and the macroscopic nature of the body. Both types of approaches can be combined in order to yield a more complete description of the mechanical state of a material. The atomistic approach provides the study of the strength of brittle materials with an upper limit for its mechanical strength. In the case of covalently bonded atoms, the force associated with atomic interactions can be represented by the Morse potential [400,401]

$$U = U_o \left(\exp(-2B\,(x-a)) - 2\,\exp(-B\,(x-a)) \right), \qquad (4.1)$$

where U is the potential energy per unit of surface area of two fracture surfaces;

U_o and B are constants;

x is the distance between the two fracture surfaces;

a is the interatomic distance of the atoms being separated.

The binding force per unit area is given by [399]

$$\frac{dU}{dx} = U_o \left(-2B \exp(-2B\,(x-a)) + 2B \exp(-B\,(x-a))\right). \qquad (4.2)$$

Assuming that Hook's law holds, and using Eq.(4.2) it can be shown that [2]

$$\sigma_T = \sqrt{\frac{E\,U_o}{8\,a}}, \tag{4.3}$$

where σ_T is the theoretical cohesive strength;

E is the Young's modulus.

Therefore, the cohesive strength of a material can be calculated by knowing the Young's modulus and U_o, which represents the binding potential at the equilibrium atomic separation (when x = a).

For a silica glass, the silicon-oxygen bond represents the strongest cohesive forces in the network; with a bond energy of 106 kcal/mole [2]. Considering a Young's modulus of 72 GPa for the silica glass, the theoretical cohesive strength is 18 GPa [2]. Hillig [402] and Proctor et al. [403] report maximum experimental values of fracture strength in the range 13-15 GPa.

Ordinary glasses usually present a much lower fracture strength (30-100 MPa) because of the presence of flaws in the surface of the glass [2]. The flaws cause concentration of stresses, causing the glass to fail at an applied load much lower than predicted theoretically.

The effect of surface flaws can be accounted for by using the Griffith equation [404,405]

$$\sigma_f = \sqrt{\frac{2\,E\,\gamma}{\pi\,c}}, \tag{4.4}$$

where σ_f is the stress required for fracture;

γ is the surface energy;

C is the flaw depth.

For an elliptical crack of length 2c in a wide plate, the maximum stress at the tip of the crack σ_{max} is given the Inglis equation [406]

$$\sigma_{max} = \sigma\left(1 + 2\sqrt{\frac{c}{\rho_t}}\right), \tag{4.5}$$

where σ is the average tensile stress;

ρ_t is the radius of curvature of the crack tip.

The rate of the crack propagation in a solid (v_c) can expressed as [407,408]

$$v_c = k\, v_l \sqrt{1 - \frac{c_o}{c}}, \tag{4.6}$$

where v_l is the longitudinal speed of sound in the solid;

c_o is half the critical length of Griffith flaw;

c is half the crack length at a given time;

k is a dimension less constant.

Equation (4.6) shows that the speed of crack propagation increases when the length of the crack increases. Reed-Hill [409] points out that this dependence of crack speed with the speed of sound occurs because the displacement of material adjacent to the crack can only occur at the speed of sound.

Experimental ways of studying the effect of cracks in the strength of brittle materials and the validity of theoretical expressions correlating the presence of flaws with strength usually involve deliberately introducing flaws in the material [407-413]. By introducing a flaw, it is possible to evaluate the effects on the strength of its size, shape, and external media [414-419]. The radial cracking that can occur around Vickers microhardness indentations seem to be particularly useful in analyzing crack growth characteristics [420-425] and toughness [426-431].

Flaws can originate from a large number of sources including processing, handling, cutting, packaging, transporting, etc., originating materials with a wide variety of flaw lengths and a corresponding wide variety of strengths [432,433].

As the size of the testing specimen increases, the chances that the sample contains a flaw also increases, meaning that larger samples are likely to have lower strength than smaller samples. Besides the effect of size, Rudnick et al. [434] points out that the fracture strength is characterized by significant scatter of data, and a stress distribution effect; e.g., strength values obtained in bending, for instance, exceed those obtained from uniform tension tests.

In a porous material (like silica gels densified at intermediate ranges of temperature) the presence of voids can influence the strength of the material. Under the application of stress the voids present in the structure can enlarge, and new voids can be formed. Together, the creation of new voids and enlargement of old ones can cause the

macroscopic effect known as *dilatancy* [435]. However, the effects of dilatancy seems to be more pronounced for relatively low volume fraction of pores (~ few percent), and also the phenomena is usually related to a non-elastic increase in volume [435].

The effect of porosity in the strength of silica-gel monoliths are likely to have at least two aspects: (1) the porosity decreases the actual cross-section of material which supports the load; and (2) pores can act as stress risers.

Because of the characteristics of brittle fracture (rapid failure and no macroscopic plastic deformation), the statistics of the data is a topic of special importance. Usually the strength data are treated as having a Gaussian (normal) distribution [399], or a Weibull distribution [399,436-441]:

$$P(x) = 1 - \exp\left(- \left(\frac{x - x_o}{\theta - x_o}\right)^m \right), \tag{4.7}$$

where $P(x)$ is the cumulative frequency distribution of random variable x;

x_o is the minimum allowable value of x;

θ is a scale parameter;

m is a shape parameter (Weibull modulus).

For design applications and for dealing with probabilities of failure the Weibull distribution is usually preferred, because it does not have the unrealistic long tails of the Gaussian distribution [399].

4.2 Microhardness

The Vickers hardness number (VHN), also called the diamond-pyramid hardness test (DPH), is defined as the load divided by the surface area of the indentation [399]. The VHN can be determined by the following equation [399]:

$$VHN = \frac{1.854\ P}{L^2}, \tag{4.8}$$

where P is the applied load (kg);

L is the average length of the diagonals of the indentation (mm).

Microhardness measurements were made using a semi-automatic LECO DM-400F Hardness Tester. A load of 0.1 kg was used for the 12 Å and 32 Å pore radius samples and 0.025 kg was used for the 81 Å pore radius samples. A loading time of 15 s was selected for all testing. The variation of Vickers hardness number (VHN) with densification temperature for sets of samples with 12 Å, 32 Å and 81 Å average pore radius is shown in Figure 4.1. It can be seen from the figure that for all sets of samples the VHN increases with increasing sintering temperatures and the rate of increase is sharper after a certain critical temperature which increases for larger pore sizes. As pointed out previously, for all the figures in this work, the error bars represent the standard error of the mean; the curve fitting is either a polynomial or just a curve that connect the average points, not implying in any trends in the data when a peak or valley occurs.

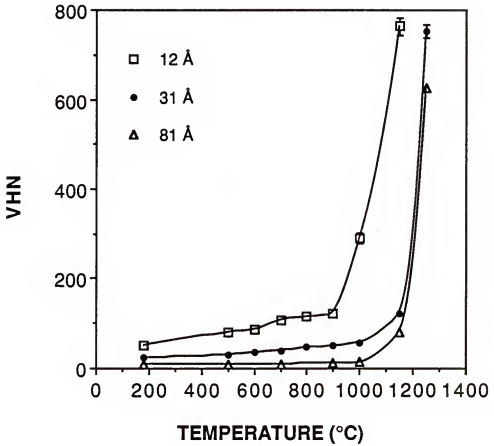

Figure 4.1 Variation of the Vickers hardness number (VHN) as a function of densification temperature for silica gel samples of 12 Å, 32 Å and 81 Å average pore radii.

The initial VHN for the dried (180 °C, 453 K) silica gel samples of 12 Å average pore radius is higher than the VHN for 32 Å average pore radius samples, which is, by its turn, higher than the VHN for 81 Å pore radius samples. Considering the VHN versus temperature curve for 12 Å pore radius samples it can be seen that there is a continuous increase in hardness as the densification temperature increase. When the sintering temperature increases above 900 °C (1173 K) the 12 Å pore radius structure shows a sharp increase in VHN. The hardness of a 12 Å pore radius sample densified at 1150 °C (1423 K) is 770 +/- 10 kg/mm^2, which is comparable to the microhardness of fused silica [442].

The variation of VHN with densification temperature for 32 Å pore radius samples (Figure 4.1) shows smaller values of hardness than for 12 Å pore radius samples sintered at same temperatures. The increase in VHN with temperature is relatively slow up to temperatures in the range of 1100 °C (1373 K) to 1150 °C (1423 K) beyond which the hardness increases sharply to a value of 750 +/- 12 kg/mm^2 at 125 °C (1523 K). Silica gels of 81 Å pore radius have a similar behavior compared to 32 Å pore radius samples and even lower values of VHN for corresponding densification temperatures. The observed hardness of a sample sintered at 1250 °C (1523 K) is 627 +/- 10 kg/mm^2.

4.3 Flexural Testing

Four points bending tests were performed in a MTS 810/442 testing machine. Example of the type of sample used in the flexural tests is

shown in Figure 4.2. All the tests were performed using a cross head speed of 0.016 mm/min in ambient air.

A typical plot of load versus displacement is shown in Figure 4.3. From the bending curves one obtains the values of the load of fracture (P) which is used in the following expression to obtain the flexural strength (σ_b) [443]

$$\sigma_b = \frac{3\ P\ (L - l)}{2\ w\ t^2}, \tag{4.9}$$

where L is the distance between the lower supporting points;

l is the distance between the upper loading points;

w is the width of the tested sample;

t is the thickness of the tested sample.

The variation of flexural strength with densification temperature is shown in Figure 4.4, for samples of 12 Å average pore radius. This figure shows a continuous increase in flexural strength as the densification temperature increases. The increase in strength is more pronounced for temperatures above 700 °C (973 K).

The flexural modulus (E_b) of the samples was calculated using the following expression (see Appendix for the derivation of this expression):

$$E_b = \frac{7\ P\ L^3}{32\ \Delta\ w\ t^3}, \tag{4.10}$$

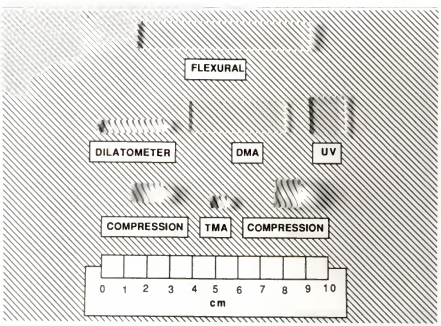

Figure 4.2 Silica gel monoliths prepared for the tests indicated.

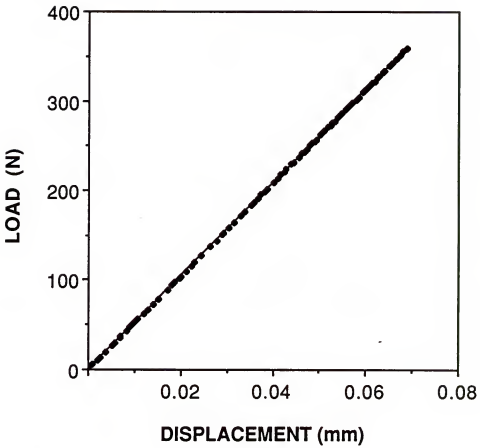

Figure 4.3 Load (P) versus displacement for a four point bending test of a dried silica gel.

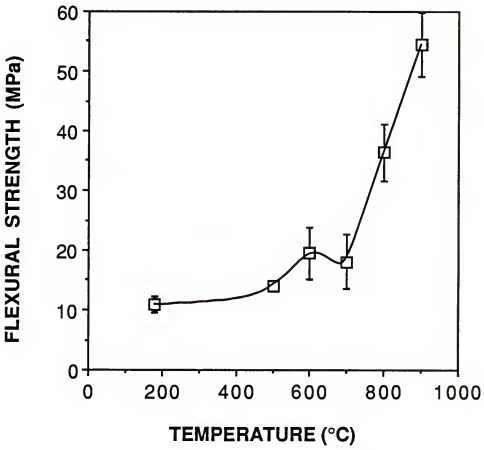

Figure 4.4 Variation of flexural strength as a function of densification temperature for silica gel samples with 12 Å average pore radius.

where Δ is the maximum displacement measured in the center of the specimen.

The variation of flexural modulus with densification temperature for 12 Å average pore radius samples is shown in Figure 4.5. The flexural modulus increases continuously with increasing sintering temperature. The increase in flexural modulus occurs more rapidly for temperatures above 900 °C (1173 K).

4.4 Uniaxial Compression Testing

For plastic solids the strength measured in uniaxial compression is the same as the strength measured in tension. In the case of brittle solids (e.g., glasses), the compressive strength is roughly 15 times larger [444]. According to Ashby and Jones [444, p.167] the reason for this is that

> cracks in uniaxial compression propagate stably (Figure 4.6) and twist out of their original orientation to propagate parallel to the compression axis. In this case, fracture is not caused by the rapid unstable propagation of one crack, but the slow extension of many cracks to form a crushed zone. It is not the size of the largest crack that counts, but that of the average size of cracks (a_{avg}).

The uniaxial compressive strength (σ_c) can be correlated to the toughness (K_{IC}) as follows [444]:

$$\sigma_c = k_u \frac{K_{IC}}{\sqrt{\pi\, a_{avg}}}, \tag{4.11}$$

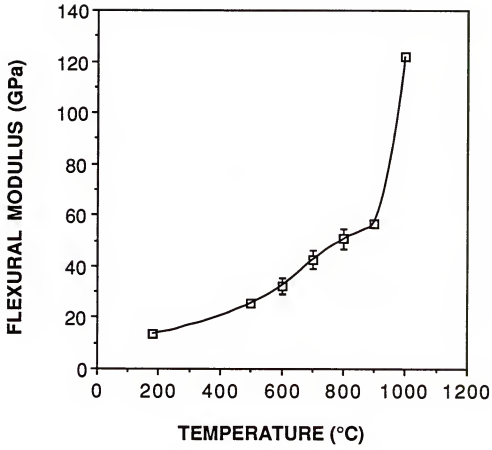

Figure 4.5 Variation of the flexural modulus as a function of densification temperature for silica gel samples of 12 Å average pore radius.

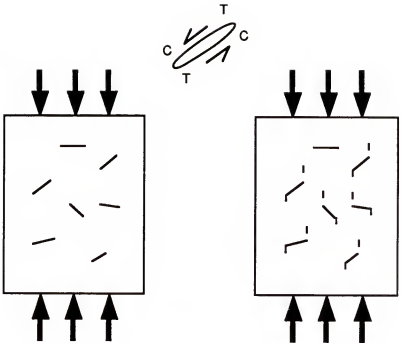

Figure 4.6 Propagation of cracks in uniaxial compression [444].

where k_u is a constant (~ 15).

A detailed analysis on the effect of pores and small cracks on the strength of brittle solids under compression is given by Ashby and Hallam [445] and Sammis and Ashby [446].

When a static uniaxial compression test is performed during a short period of time and at relatively low loading rates (e.g., 0.07 MPa/s to 0.7 MPa/s) the test is referred to as time-independent, as contrasted to time-dependent (creep) tests [447].

Two types of compression samples were prepared, as shown in Figure 4.2. Those samples were densified in the range of 180 °C (453 K) to 1000 °C (1273 K) in dry-air atmosphere, and at 1150 °C (1423 K) in a chlorine atmosphere. The specimens were tested under uniaxial compression in a MTS 810/458 at a cross head speed of 0.02 mm/min. The displacement was directly measured using a clip on gage extensometer.

A typical result of a uniaxial compression test is shown in Figure 4.7. The values of load (P) are used to obtain the compression strength (σ_c) as follows:

$$\sigma_c = \frac{P}{A}, \tag{4.12}$$

where A is the cross sectional area of the tested specimen.

The variation of compression strength with densification temperature for a set of samples of 12 Å average pore radius is shown in Figure 4.8. The figure shows an increase in compression strength as the

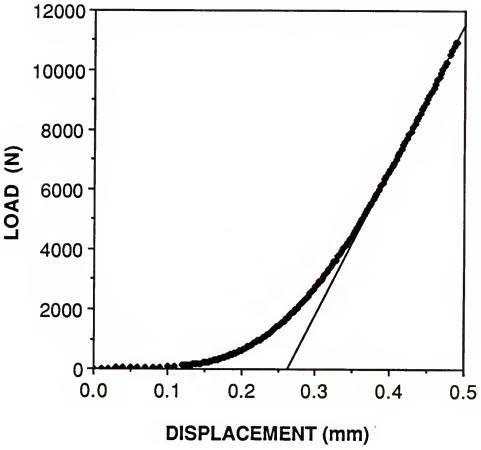

Figure 4.7 Variation of the uniaxial compression load (P) versus displacement for a dried silica gel. The straight line represents the region in the plot which was used to calculate the modulus. The initial curved region is associated with the deformation of the Teflon® lubricant.

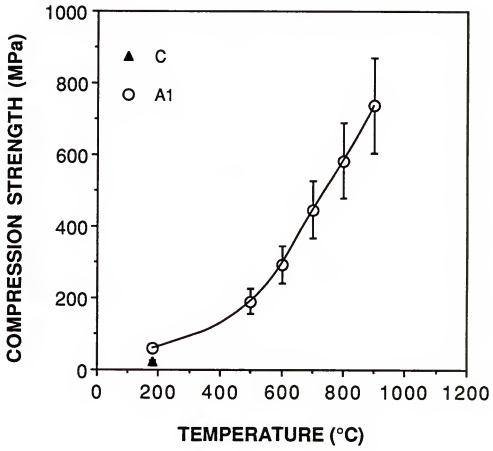

Figure 4.8 Variation of the compression strength as a function of densification temperature for samples type A1 and C.

densification temperature increases. As shown in Figure 4.8, the compression strength for a set of dried silica gels with 81 Å average pore radius (samples type C) is lower than the strength of silica gels with 12 Å average pore radius (samples type A1).

The compression modulus (E_c) was calculated using the following expression:

$$E_c = \frac{\Delta\sigma_c}{\Delta\varepsilon}, \tag{4.13}$$

where $\Delta\sigma_c$ is the variation in stress and $\Delta\varepsilon$ the variation in strain during the test, measured in the elastic region of the curve stress versus strain (not shown). Figure 4.9 shows the variation in compression modulus with densification temperature for two sets of samples of 12 Å average pore radius, as well as for a set of dried samples of 81 Å pore radius, and a set of fused quartz samples.

The effect of densification atmosphere in the compression strength is shown in Figure 4.10. Samples sintered in a dry-air (DA) atmosphere seems to have a higher compression strength than samples densified in a humid atmosphere (OF). The effect of atmosphere on the compression modulus, however, seems to be smaller, as shown in Figure 4.11. In this figure it is seen that both the compression modulus of samples processed in a dry-air and in a humid (ambient) atmosphere are very close for every tested temperature.

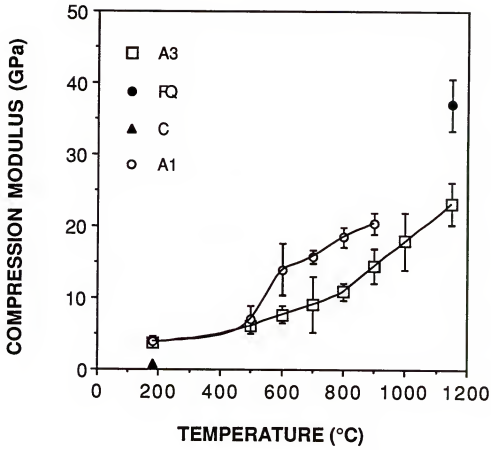

Figure 4.9 Variation of the compression modulus as a function of densification temperature for samples type A1, A3 and C. FQ represents fused quartz samples.

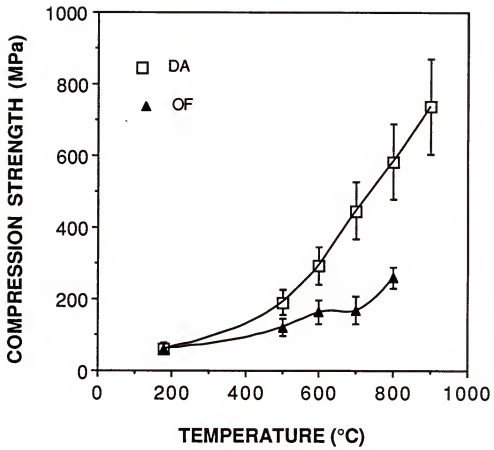

Figure 4.10 Variation of compression strength as a function of densification temperature for samples type A1 densified in a dry-air (DA) atmosphere and in a humid (OF) atmosphere.

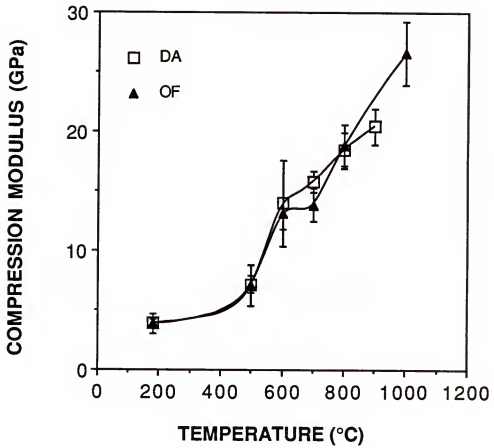

Figure 4.11 Variation of compression modulus as a function of densification temperature for samples type A1 densified in a dry-air (DA) atmosphere and in a humid (OF) atmosphere.

4.5 Brazilian Testing

The Brazilian test (also known as the diametral-compression test) was developed in the early 1950s by Carneiro and Barcellos [448] to evaluate the strength of concrete. Because of both the simplicity of the test and ease of sample preparation, and the fact that this test yields an indirect measurement of tensile strength (otherwise of difficult experimental determination for brittle materials) the Brazilian test has been used ever since for a variety of materials [449-455].

The stress distribution across a loaded diameter of a cylindrical sample is shown in Figure 4.12 [452]. The maximum tensile stress (σ_t) which acts across the diameter is given by [452]

$$\sigma_t = \frac{2\ P}{\pi\ D\ H}, \tag{4.14}$$

where P is the applied load;

D is the diameter of the specimen;

H is the length of the specimen.

Figure 4.12 shows the load being applied over a region of 1/10 of the diameter of the cylinder. If the load arc is increased to 20° the reduction in maximum tensile stress will be only 4% compared to the ideal situation when the load is applied on a line [456]. Therefore, Eq.(4.14) can be used to determine the tensile strength of cylindrical samples even in the presence of a small contact area between the sample and the loading fixtures.

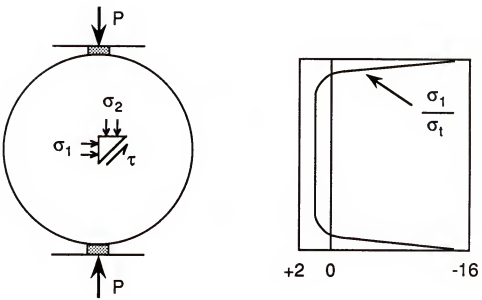

Figure 4.12 Stress distribution across a loaded diameter of a cylindrical sample in the Brazilian test [452].

Two sets of silica gel samples of 12 Å average pore radius samples were tested for the Brazilian test in a MTS 810/458 at a cross head speed of 0.02 mm/min. Teflon® tape was used as lubricant during the tests, in order to prevent failure of the samples at the contact area with the loading fixtures. A typical result obtained from the Brazilian test is shown in Figure 4.13.

The variation of tensile strength with densification temperature for gel-silica samples densified in the range of 180 °C (453 K) to 1150 °C (1423 K) is shown in Figure 4.14. There is a continuous increase in tensile strength as the sintering temperature is more pronounced for temperatures above 900 °C (1173 K). Figure 4.14 shows tensile strength values for a set of fused quartz samples, which are around the values obtained for gel-silica samples sintered at 1150 °C (1423 K). The figure also presents tensile strength values for dried samples of 81 Å average pore radius, which are lower than the corresponding values for samples of 12 Å average pore radius.

4.6 Fracture Analysis

4.6.1 Aspects of a Fracture Surface

Usually an analysis of the surface of fracture is carried out with the intention of determining the cause of the failure. This is important for aiding in materials selection, for design applications, or for improving

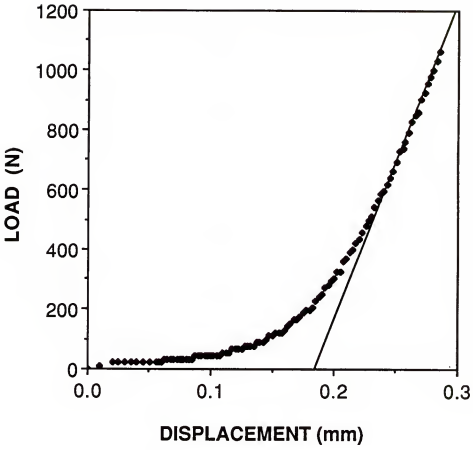

Figure 4.13 Load (P) versus displacement for a dried silica gel with 12 Å average pore radius in the Brazilian test.

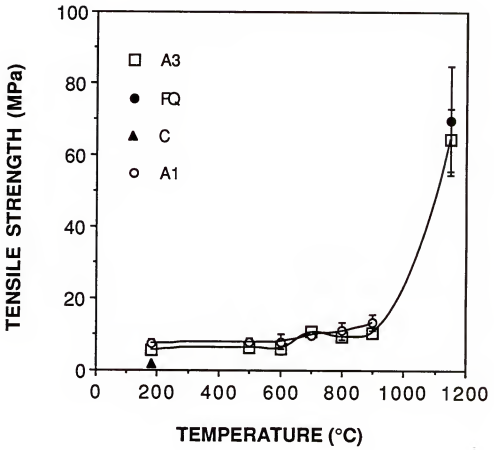

Figure 4.14 Variation of tensile strength (Brazilian test) as a function of densification temperature for samples type A1, A2 and C. FQ represents fused quartz samples.

processing or operation conditions. In the case of this research, the purposes of the fracture analysis are the following:

1) Check the validity of the tests. When the specimen breaks at contact points with the loading fixtures, for instance, the results are not considered. In most cases a visual inspection is enough for that purpose.
2) Characterize the type of surface of fracture for the silica gel samples densified in a wide range of temperatures.
3) Obtain indications on where the cracks initiate and how they propagate during the loading.

Some features commonly observed in the fracture surface of glasses are shown schematically in Figures 4.15 and 4.16 [442,457]. These figures show schematically the presence in the fracture surface of the fracture mirror, mist and hackle (Figure 4.15), and Wallner lines and striations (Figure 4.16).

In the following sections fracture surfaces of samples tested in flexural test and Brazilian test will be shown. A comprehensive analysis of fracture surfaces for the uniaxial compression test will not be carried out because for most samples a general crushing of the specimens occurred during the test, leaving no convenient fracture surface to be analyzed. Figure 4.17 shows the fracture surface of a dried silica gel sample tested under uniaxial compression. In this case, the crushing of the sample was not complete so that a piece of the ruptured sample could be analyzed. Figure 4.17 is oriented in such a way that the border shown is perpendicular to the loading fixtures. The figure suggests a

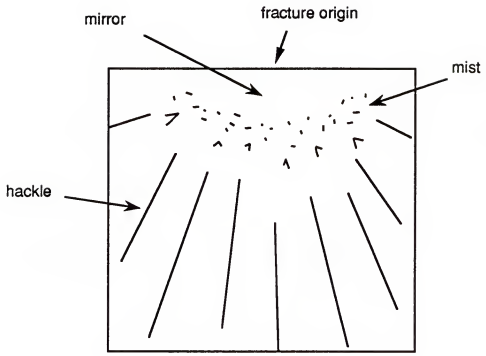

Figure 4.15 Schematic of a fracture surface showing the region of fracture origin, the fracture mirror, the mist and the hackle (Based on [442] and [457]).

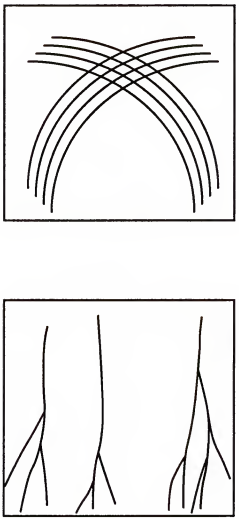

Figure 4.16 Schematic of fracture surfaces showing (a) Wallner lines and (b) striations (Based on [442] and [457]).

Figure 4.17 SEM fracture surface of a dried silica gel sample with 12 Å average pore radius submitted to uniaxial compression.

figure suggests a possible region of crack initiation, situated at the upper right part of the photomicrograph. The results observed for the uniaxial compression tests, in terms of mechanics of fracture and fracture propagation can be well represented by Figure 4.6.

4.6.2 Flexural Testing

Analysis of fractured surfaces of mechanically tested (flexural and compression) samples was carried out in a scanning electron microscope (SEM) JEOL-JSM-35CF. All samples were coated with a Au-Pd layer. A typical fracture surface of a dried gel-silica sample tested in four points bending is shown Figure 4.18. The figure shows the presence of a sharp edge formed during the fracture process, suggesting delamination of the sample caused by the bending test, besides a possible effect of the state of stress during the test. The same type of effect is present for every temperature tested, as exemplified by Figure 4.19 (sample sintered at 900 °C, 1173 K).

The delamination phenomena suggests a structural gradient inside the sample. Indeed, microhardness measurements along the transverse direction in the sample show a profile in which the hardness is higher in the center when compared to the hardness of the external surface of the sample. The variation of VHN with the transverse position in a dried sample is shown in Figure 4.20. At higher temperature of sintering the hardness gradient increases, as seen in Figure 4.21 for a sample densified at 900 °C (1173 K).

Figure 4.18 SEM fracture surfaces of a dried silica gel sample with 12 Å average pore radius submitted to four point bending. The photos represent the opposing sides of the fracture surface.

Figure 4.19 SEM fracture surfaces of a silica gel sample with 12 Å average pore radius densified at 900 °C and submitted to four point bending. The photos represent the opposing sides of the fracture surface.

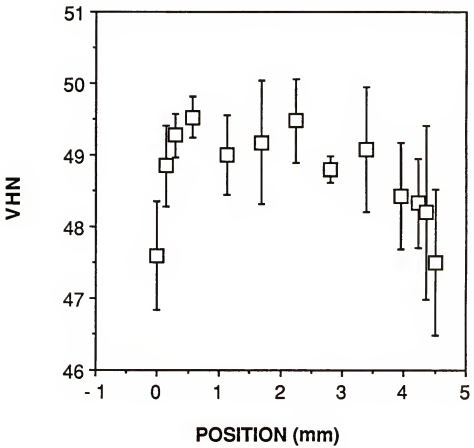

Figure 4.20 Variation of the Vickers hardness number (VHN) with transverse position in a dried silica gel sample of 12 Å average pore radius. Positions 0 and 4.5 represent the external limiting surfaces of the specimen.

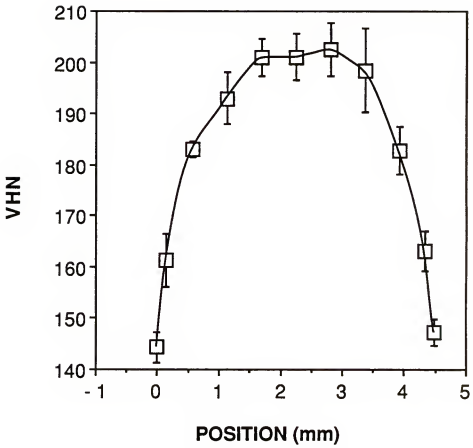

Figure 4.21 Variation of the Vickers hardness number (VHN) with transverse position in a silica gel sample of 12 Å average pore radius densified at 900 °C. Positions 0 and 4.5 represent the external limiting surfaces of the specimen.

A possible cause for the gradient in hardness is associated with the propagation of a diffusion front formed by the gas-liquid interface during the drying of the sample. As the drying front propagates, from the external surface towards the center of the sample, it creates a structural gradient which is amplified during the densification process.

The fracture behavior of silica gel monolith samples tested in four point bending, as observed in these experiments, can be summarized by Figure 4.22. Figure 4.22(a) represents the regions under compression and tension during the application of load. The crack initiates at the tensile region. Figure 4.22(b) represents a typical shape of the fracture surface observed. This shape is probably influenced by a structural gradient inside the sample. Figures 4.22(c) and 4.22(d) represent the regions where cracks were observed to initiate.

4.6.3 Brazilian Testing

Scanning electron microscopy analysis of the fracture surface of gel-silica samples densified in the range of 180 °C (453 K) to 1150 °C (1423 K) tested in the Brazilian test show characteristics of brittle fracture, i.e, the presence of no macroscopic deformation. All tested samples show characteristic striations (or river patterns), as shown in Figures 4.23 to 4.29.

Fracture surface of dried gel-silica sample is shown in Figure 4.23. Figure 4.23 was taken in one of the borders of the sample. It indicates the presence of river patterns in a direction perpendicular to the loading

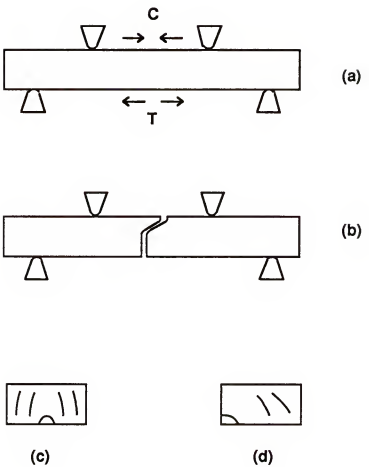

Figure 4.22 Schematic of the fracture in four point bending. (a) Compression and tension regions. (b) Fracture surfaces. (c) Crack initiation at the middle of the surface under tension. (d) Crack initiation at one corner of the specimen.

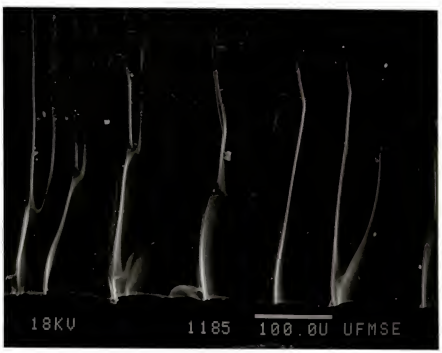

Figure 4.23 SEM fracture surface of a dried silica gel sample with 12 Å average pore radius submitted to Brazilian test.

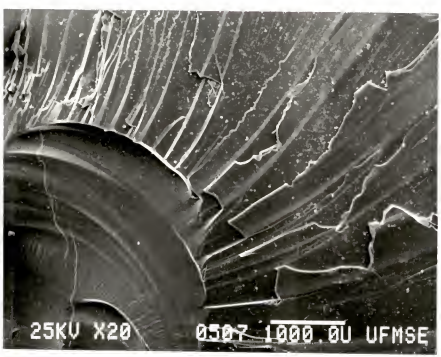

Figure 4.24 SEM fracture surface of a silica gel sample with 12 Å average pore radius densified at 600 °C and submitted to Brazilian test.

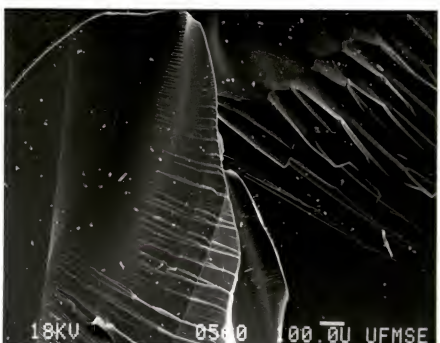

Figure 4.25 SEM fracture surface of a silica gel sample with 12 Å average pore radius densified at 600 °C and submitted to Brazilian test.

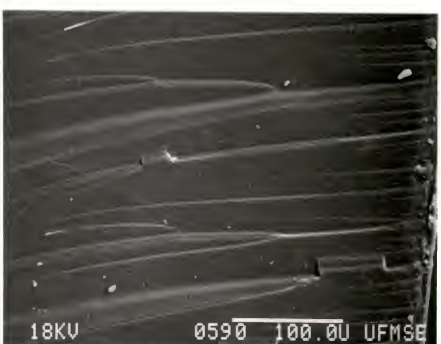

Figure 4.26 SEM fracture surface of a silica gel sample with 12 Å average pore radius densified at 700 °C and submitted to Brazilian test.

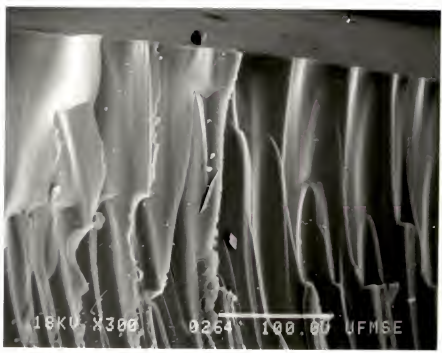

Figure 4.27 SEM fracture surface of a silica gel sample with 12 Å average pore radius densified at 900 °C and submitted to Brazilian test.

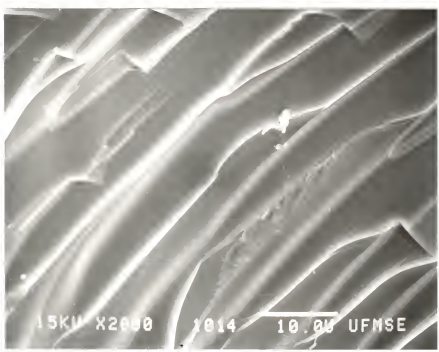

Figure 4.28 SEM fracture surface of a silica gel sample with 12 Å average pore radius densified at 1150 °C and submitted to Brazilian test.

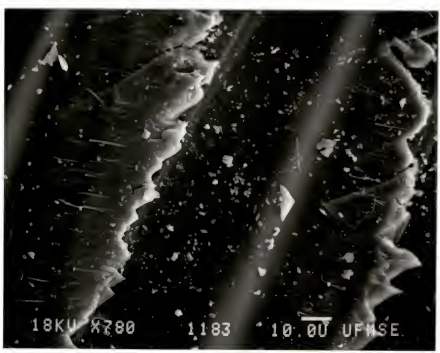

Figure 4.29 SEM fracture surface of a silica gel sample with 12 Å average pore radius densified at 1150 °C and submitted to Brazilian test.

fixtures. Figure 4.24 shows the radial propagation of river patterns out of a circular type of mirror present in the fracture surface of a silica gel sample densified at 600 °C (873 K). Figure 4.25 shows an aspect of the striations present in the fracture surface of a silica gel sample densified at 600 °C (873 K).

The fracture surface of a silica gel sample densified at 700 °C (973 K) is shown in Figure 4.26. This figure shows the striations originating in the center (region under tension) of the specimen, and propagating towards the border, where the sample touches the loading fixture. The fracture surface of a silica gel sample densified at 900 °C (1173 K) is shown in Figure 4.27. As in Figures 4.23 and 4.26, Figure 4.27 indicates that the fracture in the samples tested in the Brazilian test originates in the center of the sample, where the tension stress is maximum. Figure 4.28 shows the fracture surface of a sample densified at 1150 °C (1423 K), with the presence of striations. Figure 4.29 shows an aspect of the fracture surface of a silica gel sample densified at 1150 °C (1423 K), with the presence of "smooth" and "sharp edge" striations. Figure 4.30 shows the fracture surface of a fused quartz sample which also shows river patterns.

The striations are present in the fracture surfaces under different aspects. Figure 4.31(a) shows a river pattern present in the fracture surface of a dried silica gel. Figure 4.31(b) shows a magnified detail of Figure 4.31(a).

A schematic of the observed fracture surfaces of the silica gel samples tested in the Brazilian test is shown in Figure 4.32.

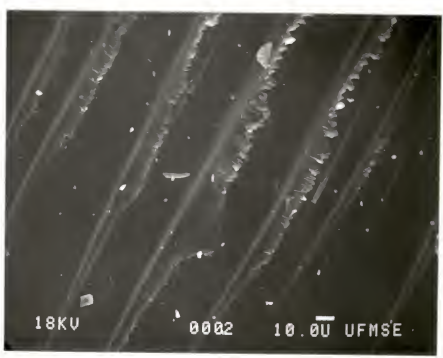

Figure 4.30 SEM fracture surface of a fused quartz sample submitted to Brazilian test.

Figure 4.31 SEM fracture surface of a dried silica gel sample with 12 Å average pore radius submitted to Brazilian test. (a) General view; (b) detail of the secondary striations shown in (a).

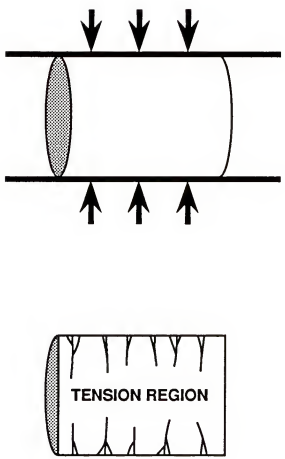

Figure 4.32 Schematic of the observed fracture surfaces of silica gel samples in the Brazilian test. (a) Loading. (b) Fracture surface (the size of the striations is shown exaggerated for clarity).

In general, it can be seen that from the dried stage (180 °C, 453 K) throughout densification, all samples exhibit brittle fracture characteristics, namely the absence of macroscopic deformation and the presence of river patterns in cleavage-like (glasses do not have actual cleavage planes) surfaces of fracture. Even though the densification process increases the strength of silica-gel monoliths, it apparently does not change the mechanics of fracture of the material, at least to a extent in which such a change could be directly observed on the fracture surface.

4.7 Dynamic Mechanical Analysis

Dynamic mechanical analysis (DMA) is a technique of mechanical spectroscopy. It measures the energy stored and dissipated during deformation.

A damped oscillation in the material will be created when it is deformed and then released of the load. The energy stored during deformation will be released in such a way that is a characteristic of each material. The frequency of the damped oscillation is a function of the elastic modulus of the material [458].

In an ideal elastic material all the energy stored is elastic. In a real material, a viscoelastic behavior is observed in which part of the stored energy will be dissipated in other forms, such as heat [458]. The greater the tendency for energy dissipation, the larger the damping of the induced oscillation.

The resonant frequency (f_o) of the mechanical system formed by the DMA and the sample is related to the Young's modulus (E) of the sample as follows [458]:

$$E = \frac{(4\ \pi^2\ f_o^2\ J_o - k)}{2\ H \left(\frac{D}{2} + L_v\right)} \left(\frac{D}{B}\right)^3, \qquad (4.15)$$

where J_o is the moment of inertia of the arm that clamps the sample;

k is the spring constant of the flexure pivots of the clamp arms;

L_v is the clamping distance;

H is the sample width;

D is the sample length;

B is the sample thickness.

More details on the DMA and on the equations used in dynamic mechanical analysis are found in references 458 to 463.

Gel-silica samples with densification temperatures varying from 180 °C (453 K) to 1000 °C (1273 K) were tested in a dynamic mechanical analyzer machine, type DMA-982 (Dupont Instruments). The tests were performed at temperature varying from 25 °C (298 K) to 400 °C (673 K).

Figure 4.33 shows the variation of tensile modulus at room temperature for a set of gel-silica samples with 12 Å average pore radius as a function of densification temperature. The tensile modulus increases continuously as the densification temperature increases, and

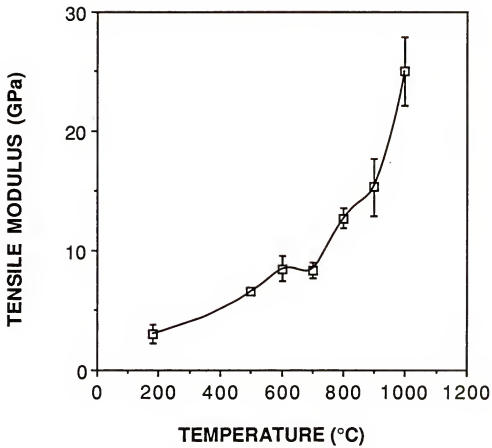

Figure 4.33 Variation of tensile modulus (DMA) at 25 °C as a function of densification temperature for silica gel samples of 12 Å average pore radius.

the increase is more pronounced for sintering temperatures above 800 °C (1073 K).

The variation of tensile modulus measured in the range of 25 °C (298 K) to 400 °C (673 K) for samples with 12 Å average pore radius samples densified in the range 180 °C (453 K) to 1000 °C (1273 K) is shown in Figure 4.34. As the testing temperature increases the tensile modulus decreases for all samples. Figure 4.35 presents similar results for the shear modulus.

It is worthwhile to note that the values of tensile modulus obtained from the DMA tests (Figure 4.33) are very close to the compression modulii obtained with the uniaxial compression tests (Figures 4.9 and 4.11). The values of tensile modulus obtained from the Brazilian tests were very similar to the results obtained from the DMA and uniaxial compression tests.

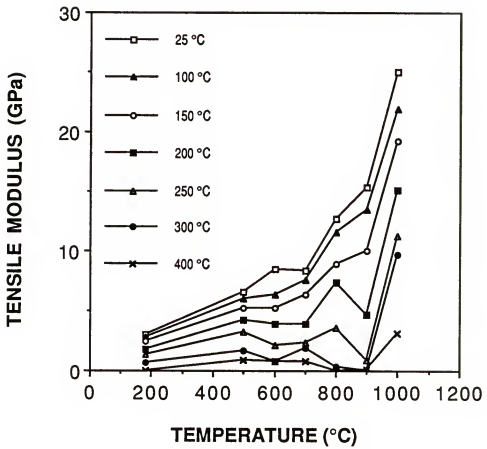

Figure 4.34 Variation of tensile modulus (DMA) as a function of densification temperature for silica gel samples of 12 Å average pore radius. The temperatures in the legend indicate the test temperature.

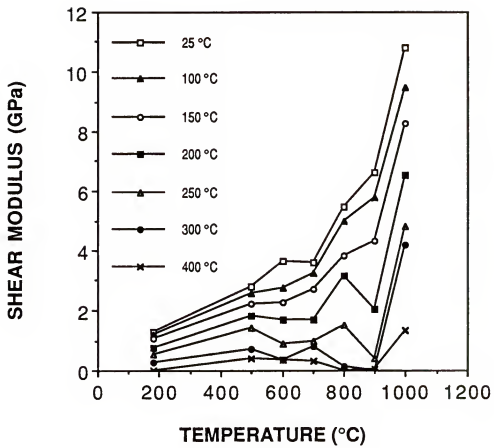

Figure 4.35 Variation of shear modulus (DMA) as a function of densification temperature for silica gel samples of 12 Å average pore radius. The temperatures in the legend indicate the test temperature.

CHAPTER 5
THERMAL ANALYSIS

5.1 Thermal Expansion of Materials

There are several variables that can influence the thermal expansion behavior of a material. The level of such a influence varies from material to material. Among those variables, the following usually have some effect on the thermal expansion:

1) State of the phases (crystalline or amorphous) [464-467].
2) Residual stress [468-470].
3) Chemistry of the surface [471-473].
4) Fictive temperature of glassy phase [474-477].
5) Occurrence of cracks [478].
6) Density [476,479].

In some cases the level of porosity does not seem to affect significantly the thermal expansion [480-482].

The coefficient of volumetric thermal expansion (α_v) is defined as [483]

$$\alpha_v = \frac{1}{V}\left(\frac{\delta V}{\delta T}\right)_p , \tag{5.1}$$

where V is the volume;

T is the absolute temperature;

P is the (constant) pressure.

Replacing in Eq.(5.1) the volume (V) by the linear dimension (L) the coefficient of linear thermal expansion (α_L) can be written as follows:

$$\alpha_L = \frac{1}{L}\left(\frac{\delta L}{\delta T}\right)_P , \qquad (5.2)$$

For isotropic materials (like glasses, for instance) $\alpha_v = 3\alpha_L$.

The coefficient of linear thermal expansion (α_v) is referred to simply as coefficient of thermal expansion, or CTE, in most of this work. The average coefficient of thermal expansion is called CTE_m in this work. The domain of averaging for CTE_m is from 30 °C (303 K) to the specified testing temperature.

Usually material expands when the temperature is increased. This is a direct consequence of the asymmetry of the potential energy curve for two adjacent atoms [484]. When the temperature increases, the amplitude of the vibrating atoms also increase. Since the amplitude of the vibrating atom is symmetric about a median position, and at the same time the potential energy curve is asymmetric, the vibrating atom moves further apart from its neighbor, causing the thermal expansion.

There are many different methods available to measure the thermal expansion of solids, as follows:

1) Push-rod methods [485-487].

2) Optical methods [488-496].

3) Interferometer methods [497-503].

4) X-ray methods [504-506].

5) Parallel plate capacitor methods [507-511].

The coefficient of thermal expansion (CTE) of materials usually varies depending on the temperature of the measurement. Hummel [512] reports an average CTE for fused silica of 0.5×10^{-6} K^{-1} (in the range 20-1000 °C, 293-1273 K); Zwikker [513] reports a CTE of 0.3×10^{-6} K^{-1} (at 0 °C, 273 K). Many investigators [514-519] use a value around 0.4×10^{-6} K^{-1} for the CTE of fused silica at 25 °C (298 K). These values are very low when compared to other glasses (e.g., for borosilicate glass the CTE at 0 °C (273 K) is 3×10^{-6} K^{-1} [513]).

According to Biscoe et al. [520],

> the small coefficient of thermal expansion of vitreous silica is due to the fact that in the continuous random network a change in volume can come only from a change in the silicon-oxygen distance. The silicon-oxygen bond is such a strong one that any such change will be small.

Small differences in the CTE of vitreous silica occur depending on the commercial grade of the glass [521]. Different commercial grades will present different levels of impurities, bubbles, and hydroxyl groups, all of which affect the thermal expansion of the glass [521].

The CTE of fully dense silica gel is reported to be smaller than the CTE for fused silica glass [29]. A possible reason for that apparent behavior was assumed to be a lower concentration of cation impurities and a larger intermolecular space between the structural units in the fully dense silica gel [29].

According to Hench and West [28] the average bond length between neighboring silicon atoms increases when water is absorbed in the structure. Because of this, the dimensional change of a silica gel can be divided into two components: (a) an intrinsic thermal expansion, due to the thermal behavior of the structural network of the silica gel; and (b) an extrinsic component, due to the effects of the adsorbed water [28].

Since factors other than the intrinsic thermal expansion can influence the behavior of a material when it is heated, the more general designation "dimensional change" (DC) will be used in this work instead of thermal expansion. The expression "coefficient of dimensional change" (CDC) will be used in this work, meaning the instantaneous slope of the curve dimensional change versus testing temperature. In a similar manner, the expression "average coefficient of dimensional change" (CDC_m) will represent the slope of the curve dimensional change versus temperature when averaged in the range of 30 °C (303 K) to the specified testing temperature. While CDC is a more general expression for CTE, CDC_m is a more general expression for CTE_m.

The purpose of the dimensional change analysis carried out in this research is to

1) Characterize the dimensional change behavior of silica gel samples densified in a wide range of temperatures (180-1150 °C, 453-1423 K).
2) Use the dimensional change behavior as an indicator of the degree of densification.

3) Obtain indirect information on the structural transformations during sintering of silica gel monoliths.

5.2 Dilatometry

5.2.1 Dimensional Change Behavior of Silica Gel Monoliths

The dimensional change experiments reported in this work were carried out using an automatic recording differential push-rod dilatometer Dilatronic II-R from Theta Industries.

A typical curve of dimensional change as a function of testing temperature for a gel-silica sample densified at 600 °C (873 K) is shown in Figure 5.1. The (linear) dimensional changes involved in most of the experiments reported in this research superimpose the effects of shrinkage (due to densification) and intrinsic thermal expansion. As seen in Figure 5.1, the initial condition is at room temperature, in which the sample is at zero dimensional change. When the sample is heated at a rate of 3 °C/min, it begin to expand up to a maximum expansion which occurs at a certain temperature, T_{max}. Beyond T_{max} the gel-silica monolith start shrinking and the expansion crosses the line of zero expansion at a certain temperature, T_{zero}. As the testing temperature increases to 700 °C (973 K), the sample continues to shrink. When the temperature reaches 700 °C (973 K) the furnace (and the sample) begin the cooling step, at a cooling rate of 3 °C/min. At high temperatures,

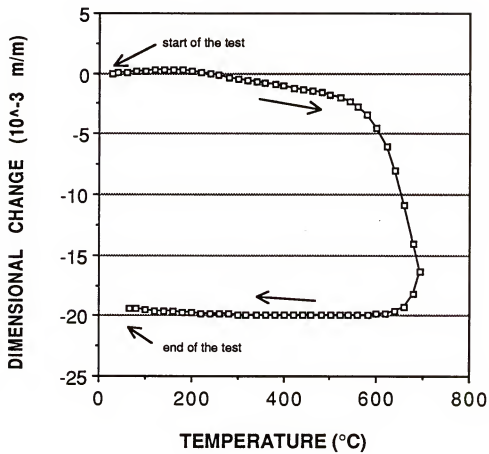

Figure 5.1 Variation of the dimensional change with testing temperature for samples type A4 previously densified at 600 °C.

the sample still shrinks significantly during cooling, but below a certain temperature the size of the sample remains fairly unchanged upon cooling. When the cooling temperature reaches about 150 °C (423 K), a small expansion occurs, because of water adsorption.

The variation of dimensional change with testing temperature for 12 Å average pore radius samples densified in the range 180 °C (453 K) to 1150 °C (1423 K) is shown in Figure 5.2. It is seen in this figure that the dried sample shrinks the most upon heating and the amount of shrinkage decreases as the sintering temperature increases. The area between the curves for heating and cooling (area of the thermal hysteresis loop) can be used to compare thermal stability among sets of samples. Another way comparing thermal stability is describing the dimensional change at a given test temperature, e.g. at 690 °C (963 K).

Similarly, the coefficient of dimensional change (CDC) is useful not only to characterize the dimensional change behavior of a material but as a tool to compare the evolution of thermal properties as the sintering proceeds. The variation of the average coefficient of dimensional change (CDC_m) with testing temperature for 12 Å average pore radius samples previously densified in the range of 180 °C (453 K) to 1150 °C (1423 K) is shown in Figure 5.3. The coefficient of dimensional change is continuously less negative as the densification temperature increases.

Analyzing the curve for the dried sample, one sees that at the beginning of the heating program, the coefficient of dimensional change is positive, corresponding in the Figure 5.2 to the initial stage where there is a positive dimensional change in the sample. The coefficient of

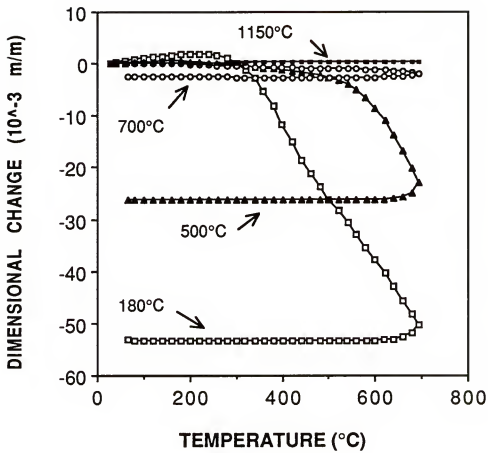

Figure 5.2 Variation of the dimensional change with testing temperature for samples type A4 previously densified in the range of 180 °C to 1150 °C.

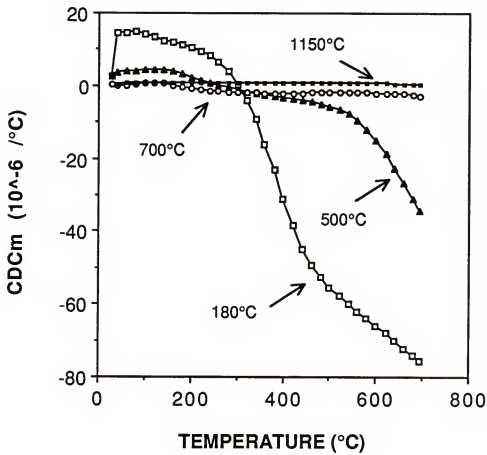

Figure 5.3 Variation of the average coefficient of dimensional change (CDC_m) as a function of testing temperature for samples type A4 previously densified in the range of 180 °C to 1150 °C.

dimensional change decreases continuously, and after a certain temperature it becomes negative, indicating shrinkage of the sample in reference to its initial size before the test begin. As the temperature of the test goes up, the coefficient of dimensional change becomes increasingly negative, indicating increasing shrinkage of the sample.

5.2.2 Large Pore Size Structures

Similarly to the small radius samples, the 81 Å pore radius samples present greater thermal stability as the densification temperature increases (Figure 5.4). Using the dimensional change at 690 °C (963 K) as an indication of the thermal stability of the samples, the 81 Å pore radius gel-silicas are thermally more stable than the 12 Å pore radius samples, as shown in Figure 5.5.

Figure 5.6 shows the variation of the average coefficient of dimensional change (CDC_m) with testing temperature for 81 Å pore radius samples densified in the range 180 °C (453 K) to 1150 °C (1423 K). Considering the curve of variation of CDC_m with temperature for the dried sample (180 °C), one sees that at low temperatures the CDC_m is positive, indicating that the specimen is expanded compared to its initial length. As the testing temperature increases, the coefficient of dimensional change becomes increasingly negative, indicating shrinkage.

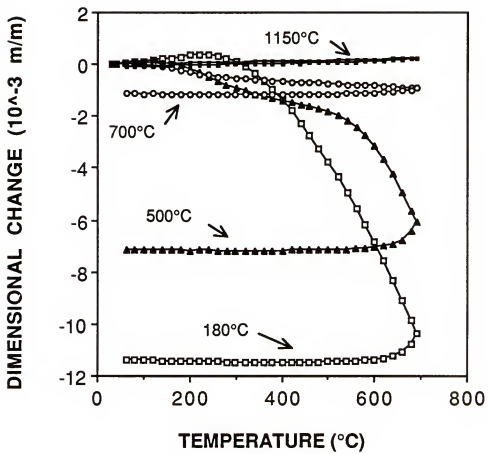

Figure 5.4 Variation of the dimensional change with testing temperature for silica gel samples with 81 Å average pore radius previously densified in the range of 180 °C to 1150 °C.

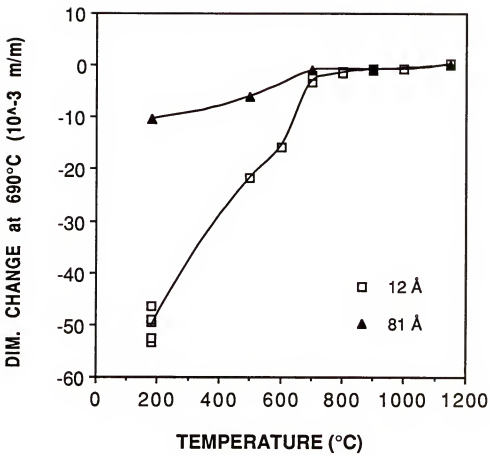

Figure 5.5 Variation of the dimensional change at 690 °C as a function of densification temperature for samples type A4 and C.

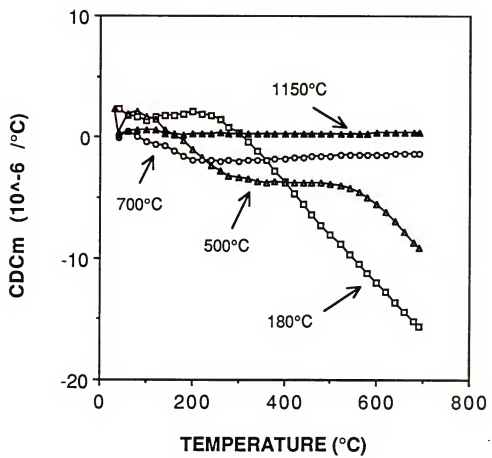

Figure 5.6 Variation of the average coefficient of dimensional change (CDC_m) as a function of testing temperature for silica gel samples with 81 Å average pore radius densified in the range of 180 °C to 1150 °C.

5.2.3 Isothermal Experiments

In order to evaluate the influence of time on the sintering behavior of gel-silica monoliths, samples were held in the dilatometer at 700 °C (973 K) for 10 hours. The heating rate (3 °C/min) was the same as the previous experiments.

The variation of dimensional change with time at 700 °C (973 K) for 12 Å pore radius samples densified at 900 °C (1173 K) and 1150 °C (1423 K) is shown in Figure 5.7. For the sample densified at 1150 °C (1423 K) as the testing temperature increases (time 0 to 228 min) there is a positive dimensional change. After the temperature reaches 700 °C (973 K) the sample stops expanding and its dimensions remain approximately unchanged with time. After 10 hours at 700 °C (973 K) (at the time 828 min), the cooling step begins and the sample shrinks back to its original dimensions. Considering now the sample densified at 900 °C (1173 K), it can be seen from Figure 5.7 that it shrinks upon heating from room temperature to 700 °C (973 K), corresponding to a variation of time from zero to 228 min. When the heating temperature reaches 700 °C (973 K) and is held at that level, the rate of shrinkage changes dramatically. From time 228 min to the end of the isothermal treatment at time 828 min, the sample densified at 900 °C (1173 K) shrinks slowly. The silica gel sample does expand slightly upon cooling from 700 °C (973 K) to room temperature due to water adsorption.

Figure 5.8 shows the variation of dimensional change with time, at a temperature of 700 °C (973 K), for a sample densified at 1150 °C

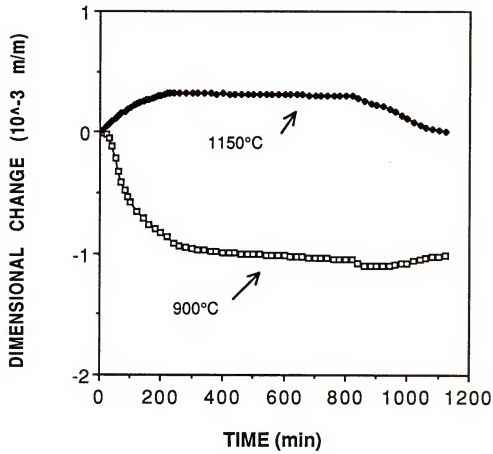

Figure 5.7 Variation of the dimensional change with time for samples type A4 densified at 900 °C and 1150 °C. The samples were heated to 700 °C in 228 min and cooled to room temperature after 10 h at 700 °C.

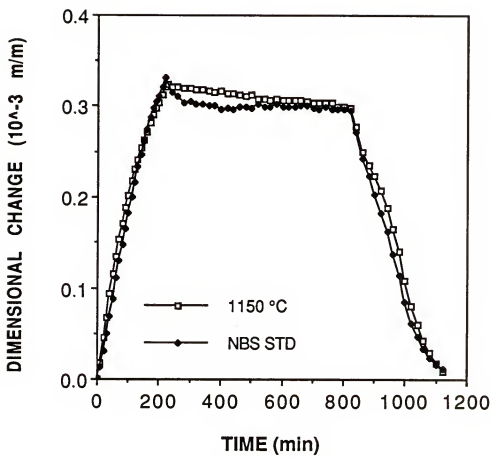

Figure 5.8 Variation of the dimensional change with time for a sample type A4 densified at 1150 °C and a NBS silica standard. The samples were heated to 700 °C in 228 min and cooled to room temperature after 10 h at 700 °C.

(1423 K) compared with a NBS silica standard. In the case of these samples, the dimensional change corresponds to intrinsic thermal expansion. Those samples present very similar behavior during the isothermal treatment and the total expansion of both samples are very close. Again, the expansion between time zero and 228 min is due to the heating step from room temperature to 700 °C (973 K). The shrinkage after time 828 min is due to the cooling step.

As shown previously in Figure 5.5, the gel-silica samples of 81 Å pore radius are thermally more stable than the 12 Å pore radius samples. That same observation can be drawn by using isothermal experiments. As seen in Figure 5.9, the 12 Å pore radius dried sample shrinks much more than the 81 Å pore radius dried sample under the same temperature profile. Again the influence of time on the shrinkage of gel-silica can be seen in Figure 5.9. As the time at 700 °C (973 K) increases (from time 228 min to 828 min) both (81 Å and 12 Å) samples shrink but at a much lower rate than during the heating period.

5.2.4 Aspects of the Dimensional Change Curve

As described before (section 5.2.1) for the dried gel-silica, as the testing temperature increases, the specimen first expands and after a certain temperature (T_{max}) it begins to shrink. The sample reaches its original length at a temperature T_{zero}, and upon further heating the sample continues to shrink until the maximum test temperature of 700 °C (973 K). Figure 5.10 shows the variation of the temperature for

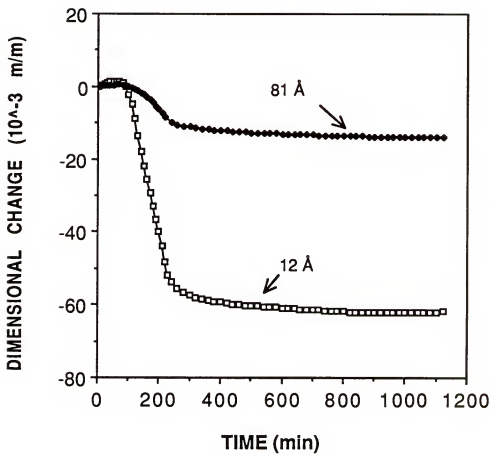

Figure 5.9 Variation of the dimensional change with time for dried silica gel samples types A4 and C. The samples were heated to 700 °C in 228 min and cooled to room temperature after 10 h at 700 °C.

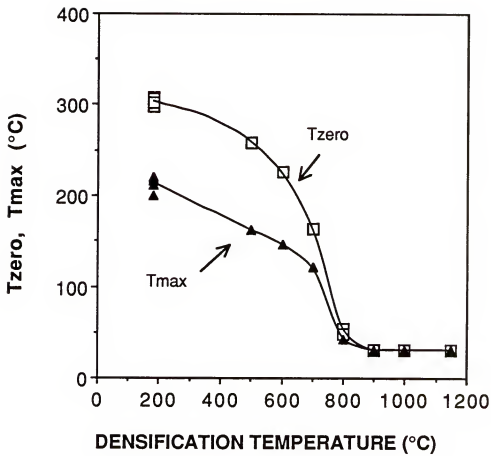

Figure 5.10 Variation of the temperature for zero expansion during heating (T_{zero}) and temperature for maximum expansion during heating (T_{max}) as a function of densification temperature for samples type A4.

maximum expansion (T_{max}) and the temperature for zero expansion (T_{zero}) as a function of densification temperature for 12 Å average pore radius samples. It can be seen from Figure 5.10 that T_{max} and T_{zero} decreases as the densification temperature increases. For samples densified at temperatures of 900 °C (1173 K) and 1000 °C (1273 K) the initial expansion cannot be seen using the initial testing temperature of 25 °C (298 K). The sample densified at 1150 °C (1423 K) does not present T_{max} and T_{zero} because it expands continuously from room temperature until 700 °C (973 K).

5.3 Thermogravimetric Analysis

Thermogravimetric analysis (TGA) was performed in a Thermogravimetric Analyzer Model 951 (Dupont Instruments). Silica gel monolithic samples densified in the range of 180 °C (453 K) to 1150 °C (1423 K) were crushed to fine powders and submitted to a TGA analysis in the testing temperature range of 25 °C (298 K) to 1150 °C (1423 K).

Before testing the samples, the powders were put in an oven at 140 °C for a period of one day, in order to obtain a homogeneous set of samples.

A typical TGA plot for a dried gel-silica is shown in Figure 5.11. That figure shows the increasing weight loss that occurs when the dried gel-silica is heated. There is a sharp decrease in the weight of the sample when it is heated from room temperature to about 150 °C

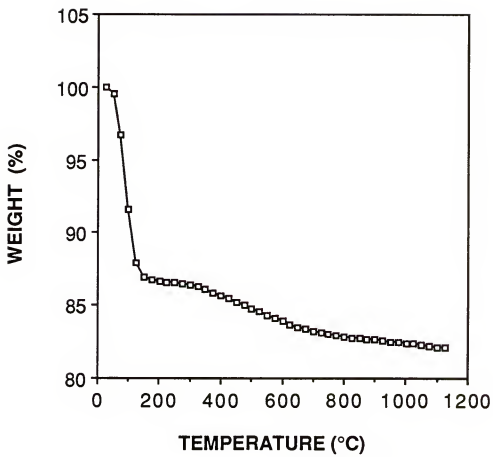

Figure 5.11 Variation of the TGA weight loss as a function of testing temperature for a dried silica gel sample type A4.

(423 K). Beyond 150 °C, the weight continues to decrease, but at a much slower rate.

The pronounced weight loss that occurs before 150 °C (423 K) is associated with elimination of water from the sample. The weight loss that occurs beyond 150 °C (423 K) is usually associated with loss of water and other volatile materials in the sample, such as organic residues.

The variation of TGA weight loss as a function of densification temperature for a set of silica gel samples of 12 Å pore radius (A2) is shown in Figure 5.12. The figure shows both the weight loss that occurs from room temperature to 1100 °C (1373 K), and the weight loss from 150 °C (423 K) to 1100 °C (1373 K). For simplification, the difference between the two types of weight loss shown in Figure 5.12 is called in this work the "water content" of the silica gels. The expression "water content" is used here in regard to the large contribution in the weight loss due to the physical water content when the silica gels are heated from room temperature to about 150 °C (423 K). When the silica gels are heated above 150 °C (423 K), water still contributes to the weight loss, but mainly in the form of elimination of OH groups. Figure 5.13 shows that as the densification temperature increases the water content in the silica gels decreases. This fact can be directly associated with the dimensional change behavior shown in Figure 5.10. The results shown in Figures 5.10 and 5.13 suggest that the initial expansion of the samples densified at lower temperatures is associated with the presence of water in the samples. As the temperature of the

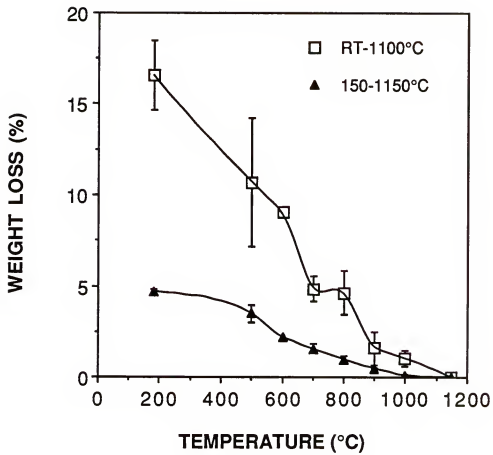

Figure 5.12 Variation of the TGA weight loss measured from 25 °C and from 150 °C as a function of testing temperature for a dried silica gel sample type A4.

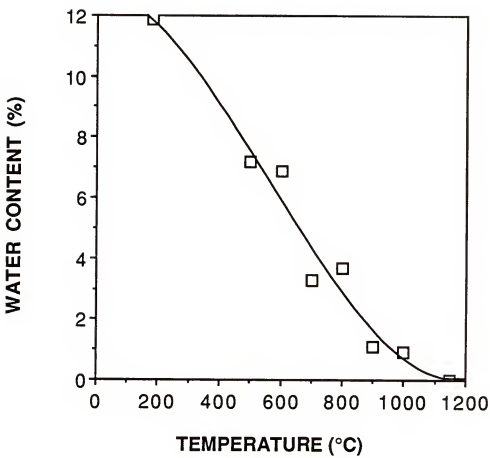

Figure 5.13 Variation of the water content as a function of densification temperature for samples type A4.

specimen increases the water present in the sample expands, contributing to the observed expansion. Figure 5.14 shows the variation of the temperature of maximum expansion (T_{max}) as a function of the water content in silica gel monoliths of 12 Å average pore radius. Figure 5.15 shows the variation of the temperature of zero expansion (T_{zero}) as a function of the water content for the same samples referred to in Figure 5.14. The variation of the dimensional change measured at T_{max} as a function of the water content in silica gel monoliths with 12 Å average pore radius is shown in Figure 5.16.

Figure 5.17 shows the variation of TGA weight loss as a function of densification temperature for a different set (A1) of 12 Å pore radius samples. The same tendency of decreasing weight loss as the densification temperature increases is observed for that set of samples.

According to the results obtained in this chapter, the dimensional changes that occur during the heating of partially dense silica gel monoliths have at least four components:

1) Intrinsic thermal expansion.
2) Effects of the presence of water.
3) Shrinkage due to densification.
4) Effect of structural defects (bubbles, cracks, etc.).

In a fully dense sample, with no adsorbed water and free of defects, the dimensional changes that occur during heating coincide with the intrinsic thermal expansion effects. This is shown by Figure 5.8, assuming that the NBS standard is defect free and has no adsorbed water.

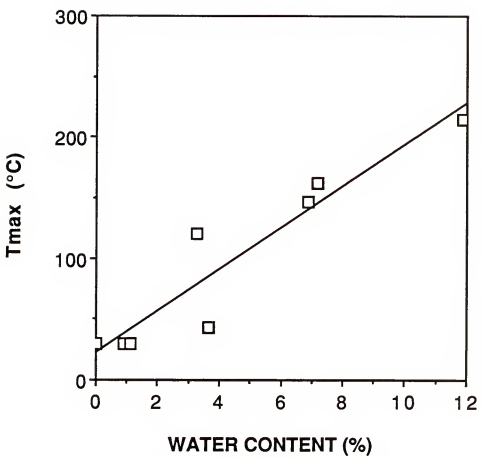

Figure 5.14 Variation of T_{max} as a function of the water content in silica gel samples type A4.

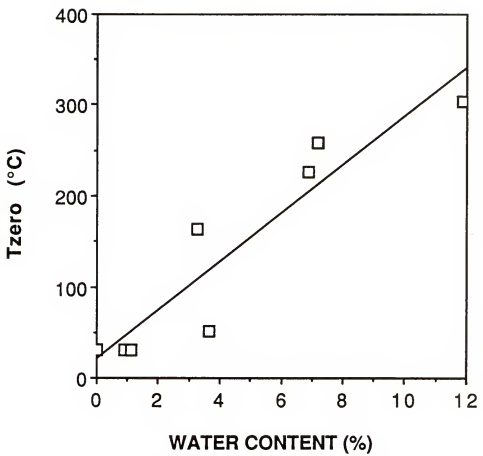

Figure 5.15 Variation of T_{zero} as a function of the water content in silica gel samples type A4.

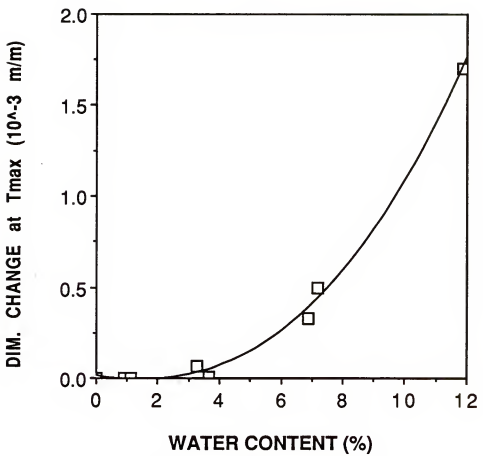

Figure 5.16 Variation of the dimensional change measured at T_{max} as a function of the water content in samples type A4.

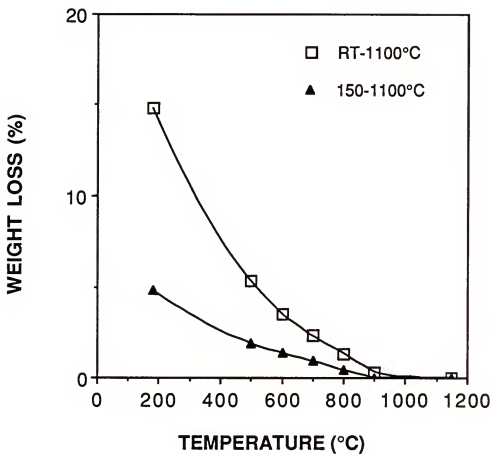

Figure 5.17 Variation of the TGA weight loss measured from 25 °C and from 150 °C as a function of testing temperature for samples type A1.

For a fully dense silica gel the values of coefficient of dimensional change (CDC) coincide with the values of coefficient of thermal expansion (CTE). In order to calculate CTE's for partially densified silica gel samples, the effects of the presence of water, shrinkage and structural defects have to be taken into account. Therefore, the observed variation in length (Δl) in silica gel monoliths can be expressed as follows:

$$\Delta l = \Delta l_t + \Delta l_s + \Delta l_w + \Delta l_d, \qquad (5.3)$$

where Δl_t is the thermal expansion component;

Δl_s is the shrinkage component;

Δl_w is the component due to the presence of water;

Δl_d is the component due to the presence of defects.

CHAPTER 6
STRUCTOLOGY

6.1 Concept of Structology

In order for a structure to be completely described, both metric and topological properties have to be taken into account. The science of correlating structural parameters with the physical properties and, ultimately, with the behavior of materials was named by Rhines [365] as "microstructology." However, because of the many different scales in which structures exist (e.g., molecules, angstrom-structures; silica gels, nanometer-structures; polycrystalline ceramics and metals, micrometer-structures; galaxies, megaparsec-structures [522]), the designation "structology" seems to be more appropriate. In this sense structure means the set of topological and metric properties necessary to characterize the geometry of a given n-dimensional manifold.

Structology deals with the definition and experimental determination of mathematical relationships between the structural parameters and the physical properties of a material, as well as the description of variations of structural properties as a function of other structural properties (the "path" of a structural transformation), and variations of structural properties with time (the "kinetics" of a structural transformation).

Many examples of application of the concepts of structology are given by Rhines [365]. The following are some few examples of phenomena that can be associated with structural properties:

1) Grain growth [523].
2) Precipitation of a second phase [524].
3) Sintering [525,526].
4) High temperature oxidation [527,528].
5) Grain boundary hardening [529-531].
6) Tensile strength [532].

The application of structology involves the following steps:

Step 1 - Measurement of structural properties.

Step 2 - Measurement of physical properties.

Step 3 - Description of relationships between the structural and physical properties, with the purpose of discovering regularities of behavior.

Step 4 - Explanation of the mechanism (or mechanisms) that lead to the structure-property relationships observed.

The objective of this research is to accomplish Steps 1, 2 and 3. However, possible explanations for the observed structure-property relationships will be given whenever possible.

6.2 Structure and Mechanical Properties

The variation of Vickers hardness number (VHN) as a function of volume fraction of pores is shown in Figure 6.1, for a set of silica gel

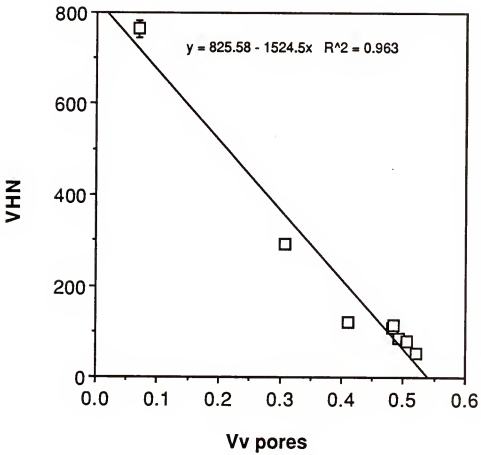

Figure 6.1 Variation of Vickers hardness number (VHN) as a function of volume fraction of pores (V_v).

samples of 12 Å average pore size. The figure suggests that smaller a V_V of pores are associated with increasing hardness of the gel-silica samples. Figure 6.2 shows the variation of VHN as a function of the topological index ß. It can be noted that the relationship between VHN and ß is not as linear as the relationship between VHN and V_V of pores. That fact suggests that the hardness of the gel-silica samples depends more on the level of porosity of the specimen than on the number of pores.

The connectivity of the pores influences the hardness in the manner shown in Figure 6.3. The hardness is nearly independent of pore connectivity up to a value of relative genus of 0.2. When the relative genus (γ) becomes smaller than 0.2 the microhardness increases considerably. During the third stage of densification, the relative genus is constant at zero and the hardness continues to increase from 300 to 770 VHN. This can be seen more clearly in Figure 6.4, which shows the variation of VHN as a function of the pore coordination number (CN). The figure shows that during the second stage of densification (CN varying from 4 to 2) VHN does not change as dramatically as when it does during the third stage (CN varying from 2 to 0). This observation suggests that pore closing promotes stiffening of the gel-silica structure to a very large degree.

The variation of flexural strength of silica gel monoliths as a function of volume fraction of pores is shown in Figure 6.5. This figure suggests a fairly good correlation between flexural strength and V_V. However, Figures 6.6 and 6.7 suggest slightly better correlations

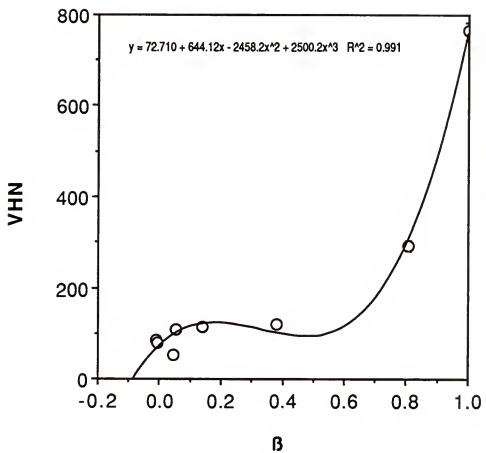

Figure 6.2 Variation of Vickers hardness number (VHN) as a function of topological index ß.

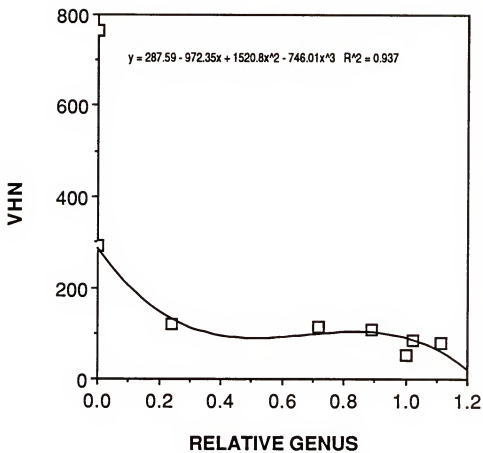

Figure 6.3 Variation of Vickers hardness number (VHN) as a function of relative genus (γ).

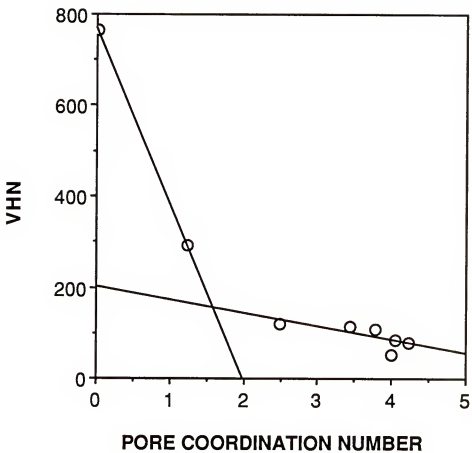

Figure 6.4 Variation of the Vickers hardness number (VHN) as a function of the pore coordination number (CN).

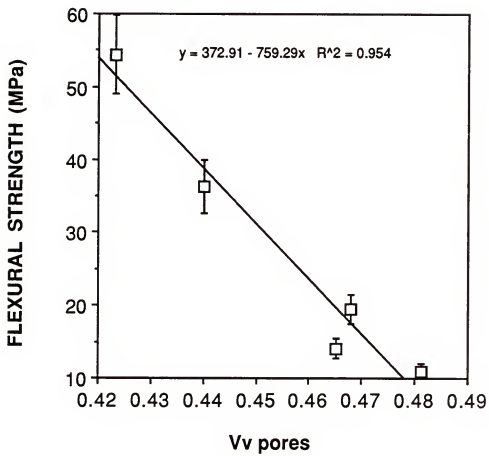

Figure 6.5 Variation of flexural strength as a function of volume fraction of pores (V_V).

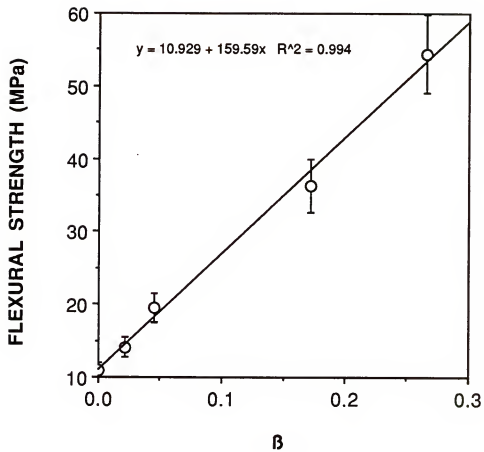

Figure 6.6 Variation of the flexural strength as a function of topological index ß.

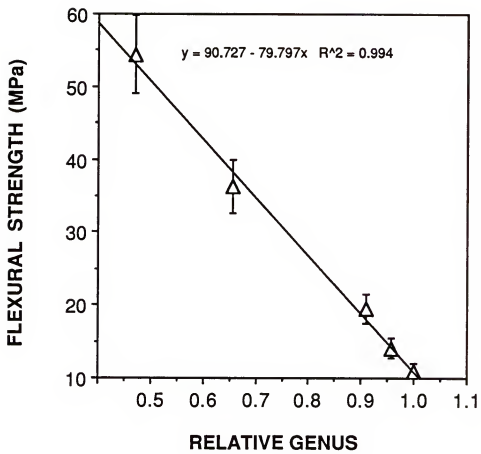

Figure 6.7 Variation of flexural strength as a function of relative genus (γ).

of flexural strength with the topological parameters (topological index ß and relative genus γ). Although it is not conclusive that ß and γ influences flexural strength more than the porosity, Figures 6.5, 6.6 and 6.7 show that the topological parameters derived are suitable for use in the study of structure-properties relationships.

The flexural modulus varies with volume fraction of pores as shown in Figure 6.8. Again the topological parameters ß and γ seem to yield better relationships with flexural modulus, as shown in Figures 6.9 (ß) and 6.10 (γ).

Figure 6.11 shows the variation of compression strength of the silica gel-monoliths (for samples type A1) as a function of volume fraction of pores. As shown in the figure, a linear relationship between V_V and compression strength does not exist in the experimental range studied, and also V_V varies within a very small range. A linear expression is derived just as a way to permit comparison between the applicability of V_V, ß and γ. Figure 6.12 shows the variation of compression strength as a function of topological index ß. This figure suggests that the compression strength correlates significantly better with variations in topological index ß than with variations in V_V. The correlation of compression strength with the pore connectivity seems to be the best for the experimental range studied, as shown by the variation of compression strength with relative genus in Figure 6.13.

The variation of compression modulus (for samples type A1) with volume fraction of pores is shown in Figure 6.14.

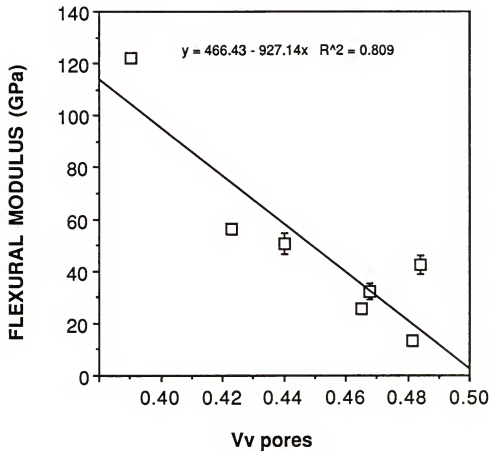

Figure 6.8 Variation of flexural modulus as a function of volume fraction of pores (V_V).

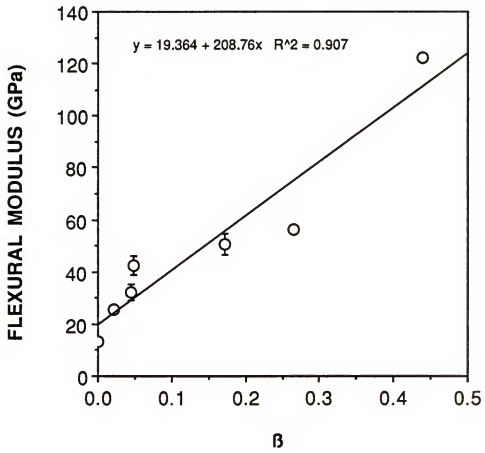

Figure 6.9 Variation of flexural modulus as a function of topological index ß.

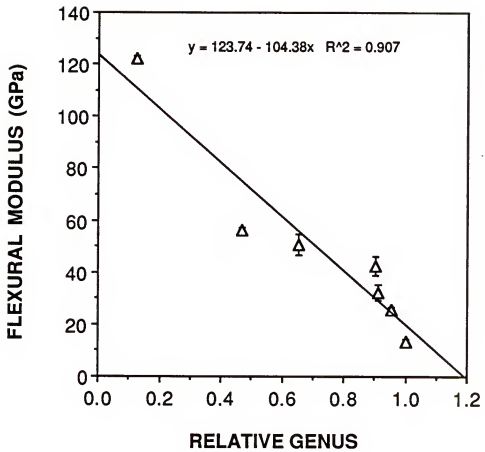

Figure 6.10 Variation of flexural modulus as a function of relative genus (γ).

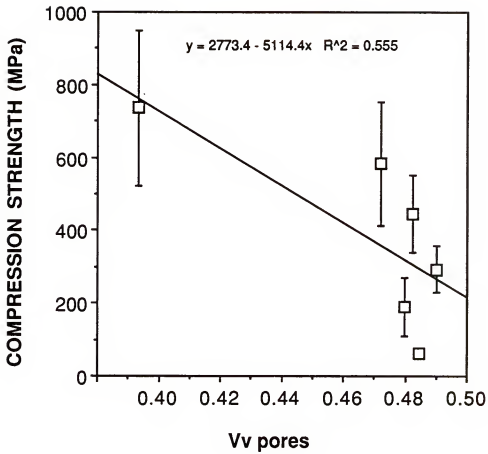

Figure 6.11 Variation of compression strength as a function of volume fraction of pores (V_V) (Samples type A1).

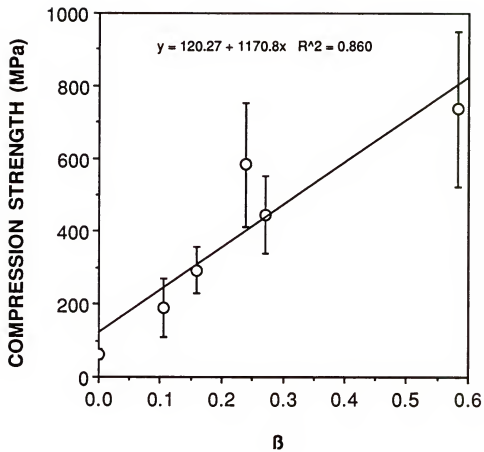

Figure 6.12 Variation of compression strength as a function of topological index ß (Samples type A1).

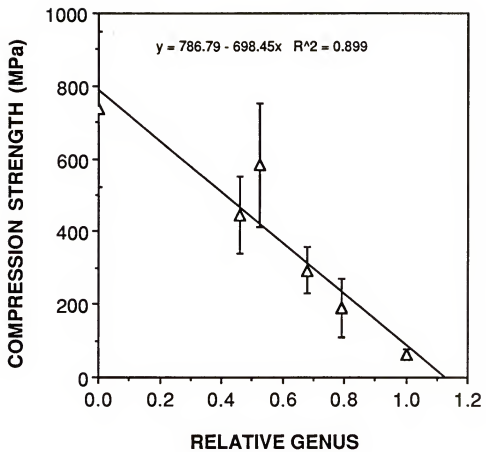

Figure 6.13 Variation of compression strength as a function of relative genus (γ) (Samples type A1).

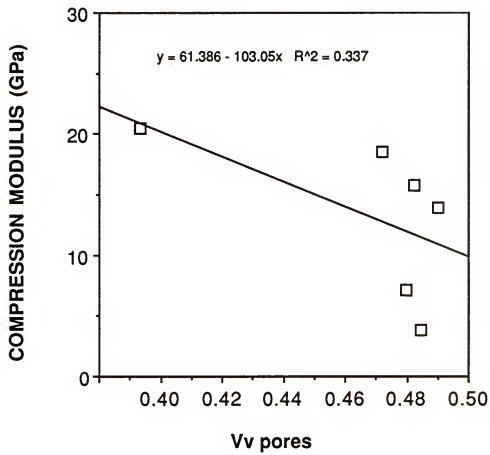

Figure 6.14 Variation of compression modulus as a function of volume fraction of pores (V_V) (Samples type A1).

As the densification takes place, V_V changes and the compression modulus changes relatively fast. Figure 6.14 suggests that for the later stages of densification (smaller values of V_V), variations in V_V produces decreasing effects in the compression modulus. The variation of compression modulus with topological index ß is shown in Figure 6.15. This figure suggests a better correlation between compression modulus and ß when compared to the relationship between compression modulus and V_V. The correlation between relative genus and compression modulus seems to be the best for the experimental range studied, as seen in Figure 6.16.

The variation of compression modulus for a second set of samples (A2) as a function of V_V, ß and γ is shown in Figures 6.17, 6.18 and 6.19 respectively. For this set of experiments again the topological parameters seem to describe better than V_V the physical evolution of the gel-silica samples. However, for this case the topological index ß, rather than the relative genus, yields a better relationship.

Figure 6.20 shows the variation of tensile strength (as obtained with the Brazilian test, for samples type A1) as a function of volume fraction of pores. The linear correspondence between tensile strength and V_V is poor, as shown by the low coefficient of correlation ($R^2 = 0.749$) and the presence of a relatively isolated data point (at V_V of around 0.40) which influences dramatically the construction of the least squares straight line. In this case the whole range of variation of V_V is very small. The variation of tensile strength with topological index ß is shown in Figure 6.21. The structure-property relationship correlates

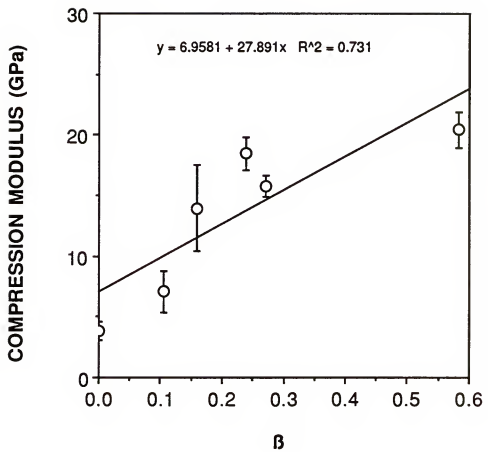

Figure 6.15 Variation of compression modulus as a function of topological index ß (Samples type A1).

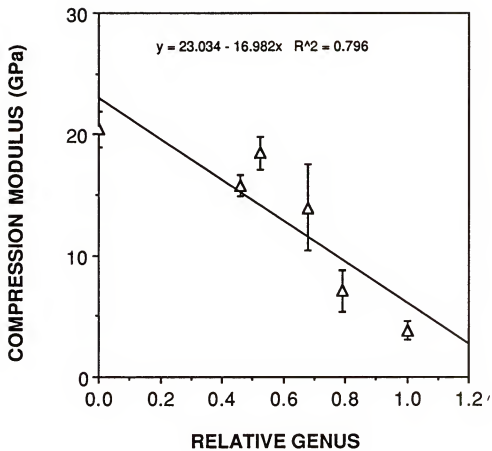

Figure 6.16 Variation of compression modulus as a function of relative genus (γ) (Samples type A1).

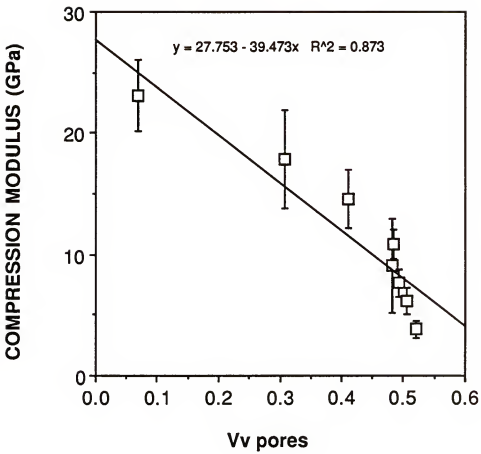

Figure 6.17 Variation of compression modulus as a function of volume fraction of pores (Vv) (Samples type A2).

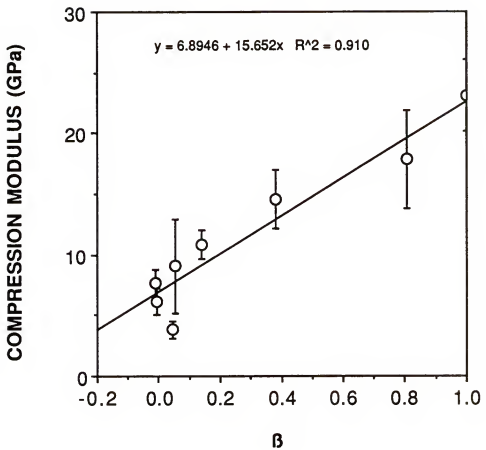

Figure 6.18 Variation of compression modulus as a function of topological index ß (Samples type A2).

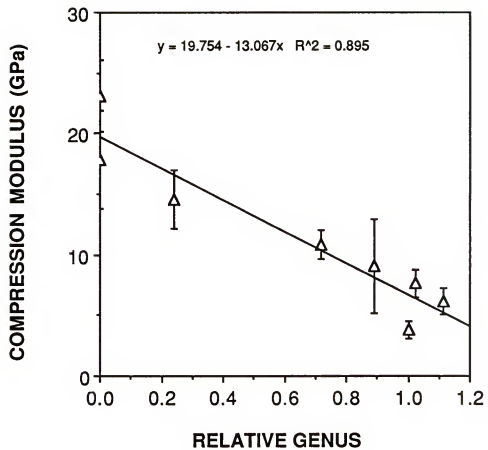

Figure 6.19 Variation of compression modulus as a function of relative genus (γ) (Samples type A2).

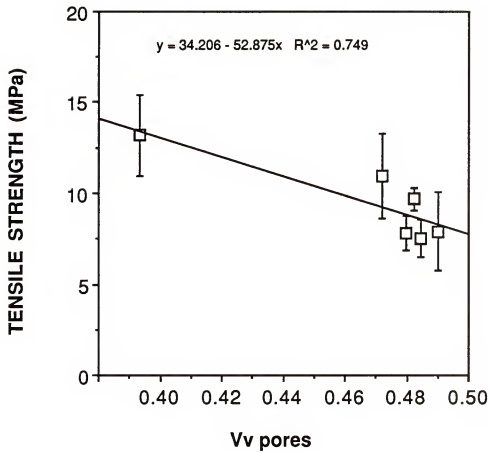

Figure 6.20 Variation of tensile strength (Brazilian test) as a function of volume fraction of pores (V_V) (Samples type A1).

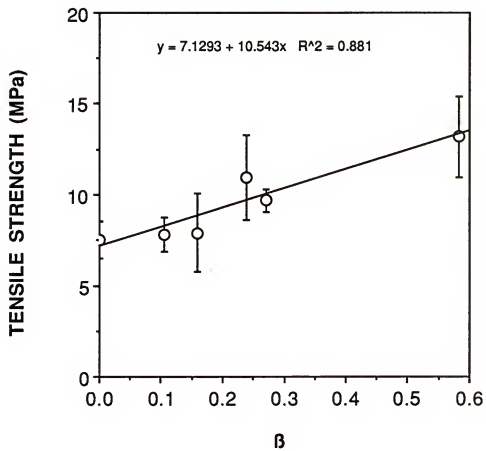

Figure 6.21 Variation of tensile strength (Brazilian test) as a function of topological index ß (Samples type A1).

better with ß than V_V. The relationship between tensile strength and relative genus (γ) is shown in Figure 6.22. For this set of samples (A1) both ß and γ yield better relationships with tensile strength than V_V does.

The relationships between tensile strength with V_V, ß and γ for a second set of samples (A2) are shown in Figures 6.23, 6.24 and 6.25 respectively. In the case of this set of samples, the tensile strength has a better linear correspondence with Vv than with the topological parameters ß and γ. It should be the noted however, that the linear equation representing the variation of tensile strength with Vv is markedly influenced by the presence of an isolated data point (at 65 MPa, as shown in Figure 6.23). The variation of tensile strength with relative genus shown in Figure 6.25 suggests again a sensitive effect of pore closing on the physical strength of gel-silica monoliths. The effect of pore closing on tensile strength is similar to the effect of pore closing on the microhardness, as seen earlier (Figure 6.3). In the case of Figures 6.23, 6.24 and 6.25 a third order polynomial was chosen to provide a better fit for the experimental points.

The variation of tensile modulus (DMA) as a function of volume fraction of pores is shown in Figure 6.26. The figure suggests a fairly good correlation between tensile modulus and V_V. The variation of tensile modulus with surface area of pores per unit volume (S_V) is shown in Figure 6.27. The relationship of tensile modulus with S_V seems to be better than with V_V, as indicated by the linear coefficient of

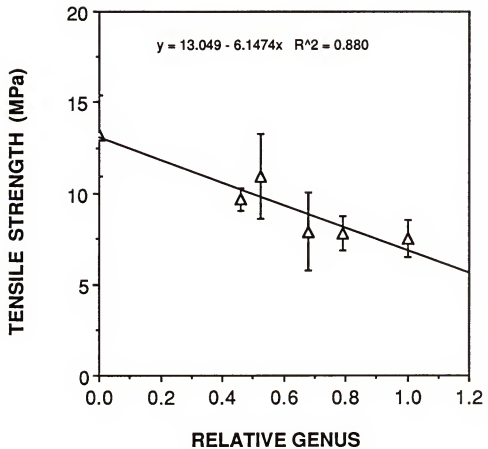

Figure 6.22 Variation of tensile strength (Brazilian test) as a function of relative genus (γ) (Samples type A1).

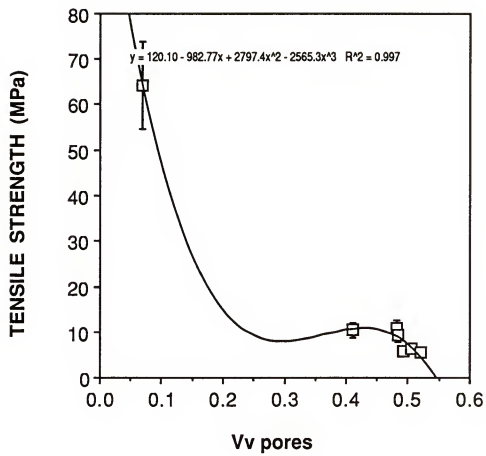

Figure 6.23 Variation of tensile strength (Brazilian test) as a function of volume fraction of pores (V_V) (Samples type A2).

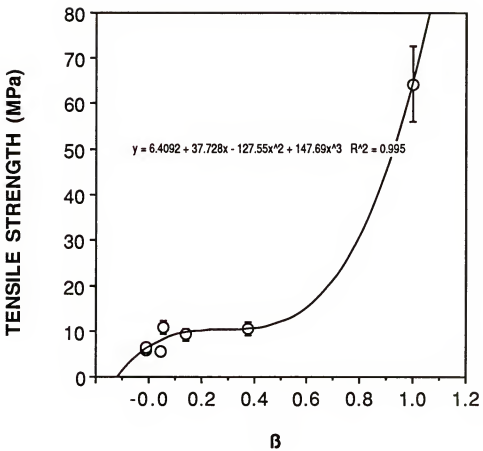

Figure 6.24 Variation of tensile strength (Brazilian test) as a function of topological index ß (Samples type A2).

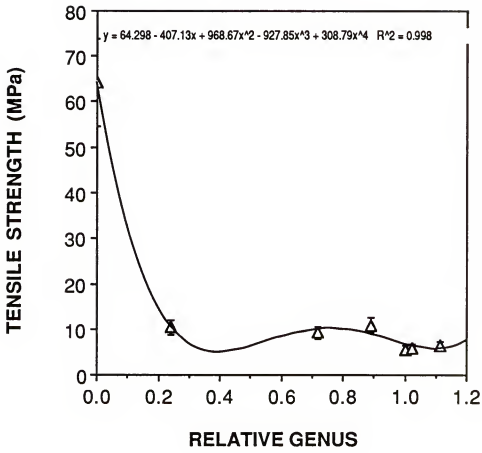

Figure 6.25 Variation of tensile strength (Brazilian test) as a function of relative genus (γ) (Samples type A2).

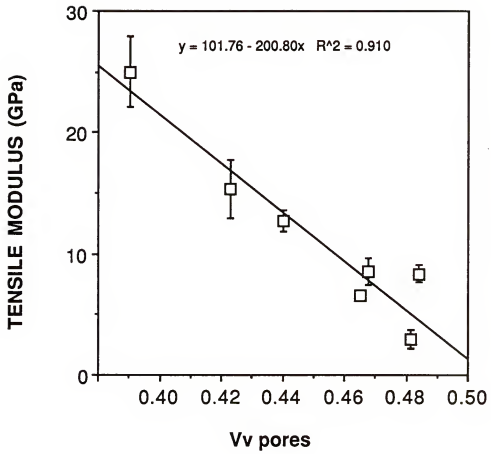

Figure 6.26 Variation of tensile modulus (DMA) as a function of volume fraction of pores (V_v).

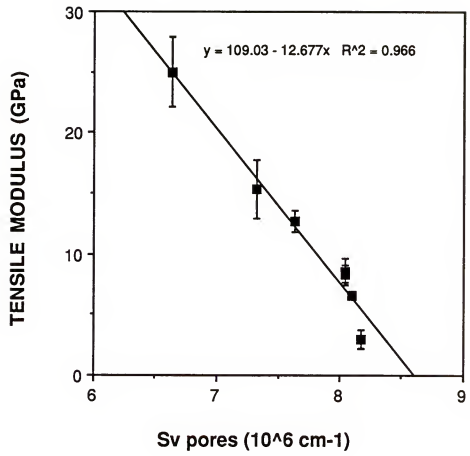

Figure 6.27 Variation of tensile modulus (DMA) as a function of surface area per unit volume (S_V).

correlation (R^2). The variation of tensile modulus with the topological parameters ß and g are shown in Figures 6.28 and 6.29 respectively. Again, the topological parameters seem to correlate better to the physical property than does the volume fraction of pores (V_v).

Figures 6.30 and 6.31 present the variation of tensile modulus (DMA) measured in the range of 25 °C (298 K) to 250 °C (523 K) as a function of V_v and ß respectively. The linear relationship between tensile modulus and the structural parameters is very poor for higher testing temperatures. However, the decrease in the gel-silica tensile modulus as the testing temperature increases can be clearly seen in both Figures 6.30 and 6.31.

6.3 Structure and Thermal Properties

The variation of dimensional change at 690 °C (963 K) as a function of volume fraction of pores is shown in Figure 6.32. At high volume fraction of pores small variations in V_v lead to large variations in the dimensional change of gel-silica. For smaller values of V_v the gel-silica specimens are more thermally stable, as shown in Figure 6.32 by the relatively small variations in dimensional change. Thus, dimensional change at 690 °C (963 K) dependence on V_v is best represented as the intersection of two straight lines.

The variation of dimensional change at 690 °C (963 K) with topological index ß is similar to that presented by V_v, i.e., an intersection of two linear relations (Figure 6.33). For the beginning of

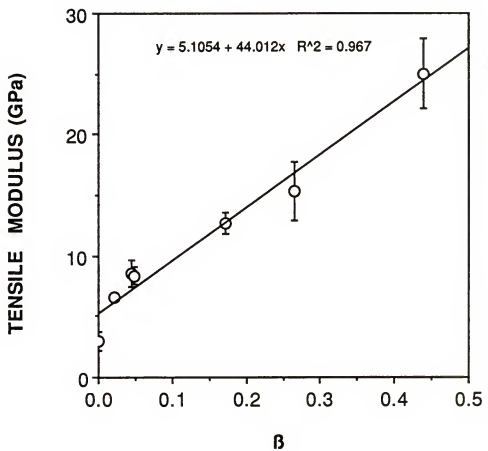

Figure 6.28 Variation of tensile modulus (DMA) as a function of topological index ß.

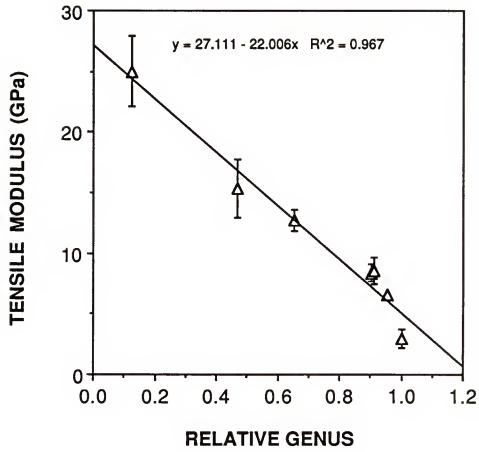

Figure 6.29 Variation of tensile modulus (DMA) as a function of relative genus (γ).

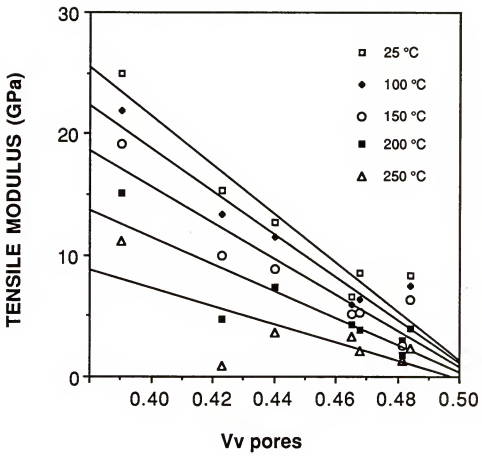

Figure 6.30 Variation of tensile modulus (DMA) as a function of volume fraction of pores (Vv) for testing temperatures varying from 25 °C to 250 °C.

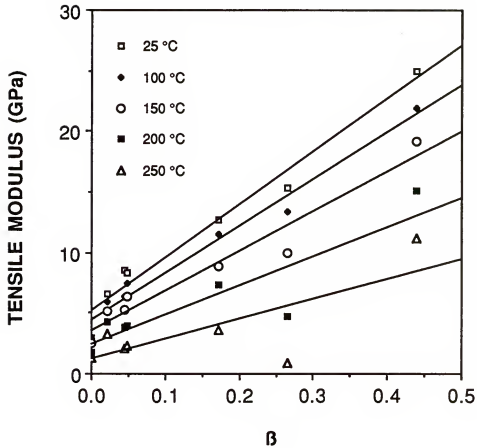

Figure 6.31 Variation of tensile modulus (DMA) as a function of topological index ß for testing temperatures varying from 25 °C to 250 °C.

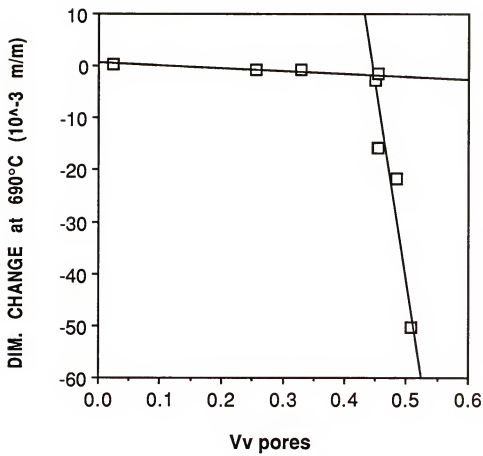

Figure 6.32 Variation of dimensional change at 690 °C as a function of volume fraction of pores (V_V).

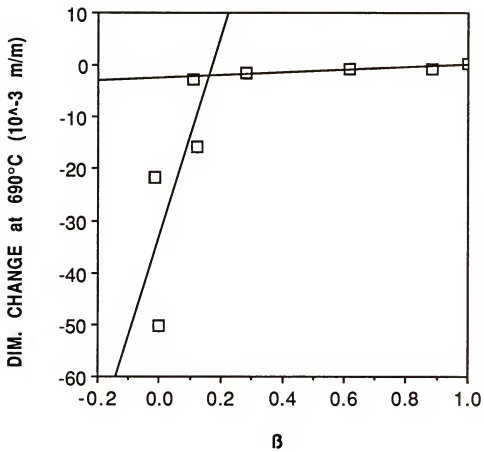

Figure 6.33 Variation of dimensional change at 690 °C as a function of topological index ß.

densification (ß varying from 0 to 0.2) the silica gel dimension changes significantly. As ß increases from 0 to 0.2, the dimensional change at 690 °C decreases from -60×10^{-3} cm/cm to less than -1×10^{-3} cm/cm. That change illustrates that a sample with higher ß will shrink less upon heating than a sample with a lower ß. For values of ß between 0.2 and 1.0 the dimensional change variations are relatively small as compared to samples in earlier stages of densification.

A similar effect is observed when one examines the dependence of dimensional change at 690 °C (963 K) on the degree of connectivity of the gel-silica structure. Figure 6.34 shows the variation of dimensional change at 690 °C (963 K) as a function of relative genus. For the dried sample (relative genus of 1) there is a large shrinkage when the specimen is heated to 690 °C (963 K). As the gel-silica densifies (relative genus going from 1 to 0) the sample becomes increasingly more thermally stable.

The observation that the silica gel monoliths increase in thermal stability as the densification takes place is valid, but also is arbitrary because the dimensional change at an arbitrary temperature (690 °C, 963 K) was chosen as reference. As shown in Figure 6.35, the average coefficient of dimensional change (CDC_m) assumes different values for different reference temperatures. The variation of CDC_m as a function of densification temperature, assuming reference temperatures in the range 30 °C (303 K) to 690 °C (963 K), is plotted in Figure 6.35. As shown by Figure 6.35, the curve of variation of CDC_m with

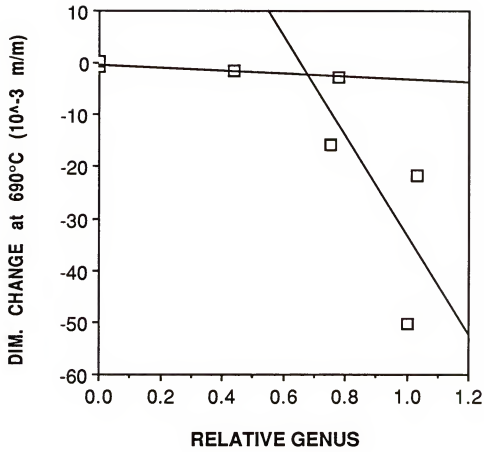

Figure 6.34 Variation of dimensional change at 690 °C as a function of relative genus (γ).

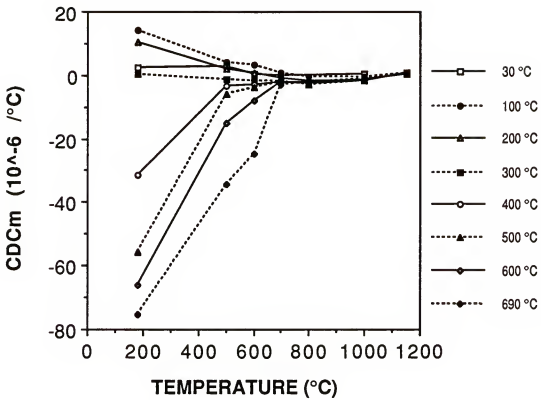

Figure 6.35 Variation of the average coefficient of dimensional change (CDC_m) as a function of densification temperature, for reference temperatures varying from 30 °C to 690 °C.

densification temperature depends on the assumed reference temperature.

Figure 6.36 shows the variation of dimensional change as a function of testing temperature, for samples densified in the range of 500 °C (773 K) to 1150 °C (1423 K). The range of testing temperature indicated in the figure is from 200 °C (473 K) to 460 °C (733 K). The lower limit of 200 °C (473 K) comes from the choosing of a temperature higher than T_{zero} (for the sample densified at 500 °C, 773 K). The upper limit of 460 °C was chosen to be smaller than the temperature of the sample densified at the lower temperature (again 500 °C, 773 K). Therefore, for the set of samples densified in the range 500 °C (773 K) to 1150 °C (1423 K) the testing temperature range of 200 °C (473 K) to 460 °C 733 K) should provide an unbiased region of dimensional change for comparisons between the thermal behavior of that set of samples. As seen in Figure 6.36, the curves of variation of dimensional change with testing temperature for all silica gel samples present good linearity, as shown by the linear coefficients of correlation.

Plotting the slopes of the dimensional change versus temperature curves (shown in Figure 6.36), as a function of densification temperature results in Figure 6.37. According to Figure 6.37 there seems to be a good linearity between the dimensional change slope (or slope between the dimensional change and testing temperature curve measured between 200 °C (473 K) and 460 °C (733 K)) and the densification temperature. The dimensional change slope (DC_s) can

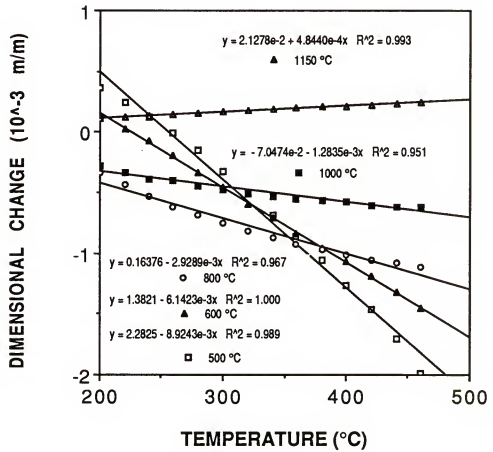

Figure 6.36 Variation of dimensional change as a function of testing temperature for samples densified in the range of 500 °C to 1150 °C.

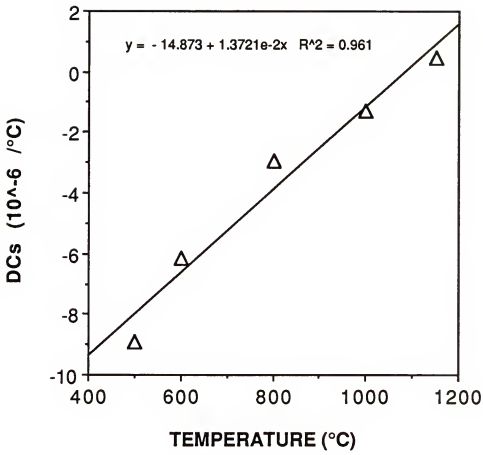

Figure 6.37 Variation of dimensional change slope (DC_S) as a function of densification temperature.

thus be used to characterize the dimensional change properties of gel-silica samples densified in the range of 500 °C (773 K) to 1150 °C (1423 K). It is important to point out that the notation "dimensional change slope" was used instead of the coefficient of dimensional change designation. The reason for that is because the dimensional change slope (DC_s), as defined and used in this work, differs from both the average coefficient of dimensional change (which uses the original length of the sample as reference) and the instantaneous coefficient of dimensional change (evaluated as a limit for each point of the curve of dimensional change versus temperature). It should be noted however that since all curves shown in Figure 6.36 are quite linear, the instantaneous coefficient of dimensional change measured at a convenient temperature inside the range 200 °C (473 K) to 460 °C (733 K) (say 300 °C, 573 K) should provide a good approximation to the "dimensional change slope" used in this work.

The variation in the average coefficient of dimensional change (CDC_m) as a function of temperature is shown in Figure 6.38. The range of testing temperature (between 340 °C (613 K) and 460 °C (733 K)) was chosen so that linear variations of the coefficient of dimensional change with temperature would occur inside the limiting temperatures. In the case of Figure 6.38 it was introduced data for dried gel-silica. From the curves of CDC_m versus temperature (Figure 6.38) the slopes were calculated, as shown in Figure 6.38. The variation of the coefficient of dimensional change slope (CDC_s) as a function of densification temperature is plotted in Figure 6.39. This figure shows

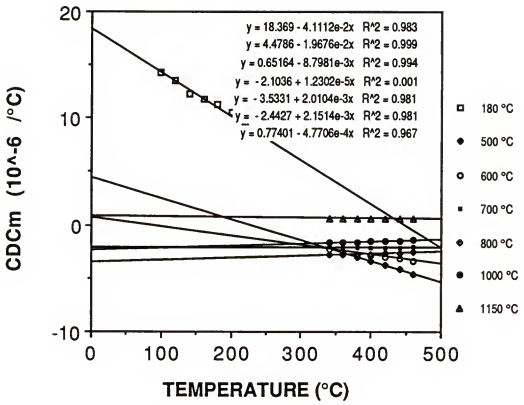

Figure 6.38 Variation of the average coefficient of dimensional change (CDC_m) as a function of testing temperature for silica gel samples densified in the range 180 °C to 1150 °C.

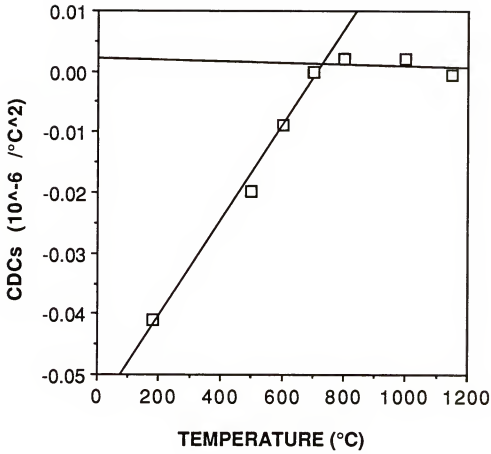

Figure 6.39 Variation of coefficient of dimensional change slope (CDC_S) as a function of densification temperature.

that larger variations in the coefficient of dimensional change with densification temperature are present for samples densified at lower temperatures. Densification at 650 °C (923 K) and above yields a stable CDC behavior, within the range of 200-460 °C (473-733 K).

The variation of the dimensional change slope (DC_s) as a function of volume fraction of pores is shown in Figure 6.40. It is seem from this figure that in the beginning of densification small variations in V_V cause relatively large dimensional variations in silica gel monoliths. For a large variation in V_V (from 0.4 to 0.0) there are relatively small variations in dimensional change. Therefore, the dimensional change behavior of gel-silica does not have a direct relationship with V_V, but appears to be the sum of two relationships. The variation of dimensional change slope (DC_s) with ß is shown in Figure 6.41. In this case, ß provides a better linear correlation (not shown in Figure 6.41) with dimensional change slope than Vv does. However the relationship between pore connectivity (as measured by γ) and dimensional change slope is the best, as seen in Figure 6.42. As densification proceeds (from γ=1 to γ=0) there is a direct correspondence between decrease in pore connectivity and dimensional change. For the third stage of densification (when γ is constant at zero) the variation in the number of pores present in the structure (as expressed by ß) can be associated with variations in the dimensional change behavior of gel-silica.

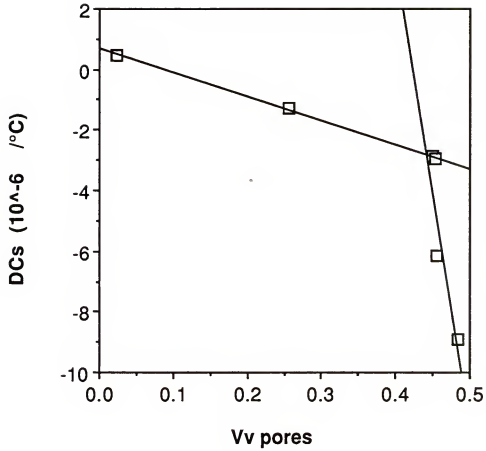

Figure 6.40 Variation of dimensional change slope (DC_s) as a function of volume fraction of pores (V_v).

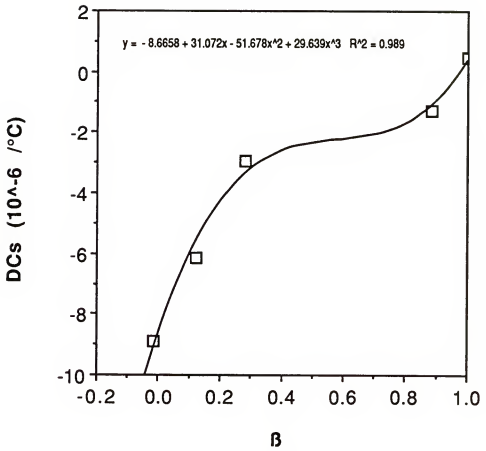

Figure 6.41 Variation of dimensional change slope (DC_S) as a function of topological index ß.

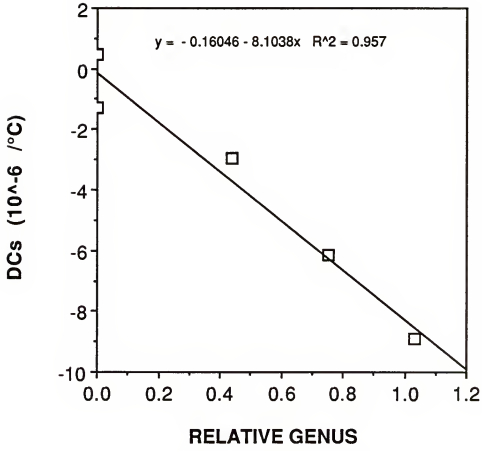

Figure 6.42 Variation of dimensional change slope (DC_S) as a function of relative genus (γ).

6.4 Applications

As showed previously both metric and topological parameters can be used to describe the evolution of the gel-silica structure during sintering. The relationships between structural parameters and physical properties obtained suggest that it may be possible to predict physical properties based on knowledge of the structural state for sets of samples processed under similar conditions.

The applicability of either metric or topological parameters is function of specific conditions of the problem. Physical properties can be correlated with both metric and topological parameters. The amount of void spaces in a structure relates with mechanical strength since pores decrease the actual cross sectional area that supports the physical force and pores also act as stress raisers. The connectivity on the other hand can be used to differentiate mechanical states associated with pore closing.

For catalytic applications of gel-silica, knowledge of the surface area of pores per unit volume is of paramount importance. However, large surface areas in a structure of closed pores would not result in large catalytic activity. The connectivity in this case is associated with the number of paths the substances can take in order for the catalytic reactions occur.

In doping and impregnation applications of porous gel-silica the volume fraction of pores is a structural parameter of obvious importance. However, in a closed pore structure no doping or

impregnation can be taken place (except through slower solid diffusion processes). Therefore, the connectivity of the structure should be known as requisite for doping and impregnation applications. Figure 6.43 shows the variation of helium flow as a function of gas pressure for samples densified in the range of 180 °C (453 K) to 1100 °C (1373 K). This experiment was carried out using samples of 1.9 mm thick attached to a sample holder directly connected to a helium gas cylinder. The gas pressure was measured directly by a regulator attached to the gas cylinder. The gas leaving the gas cylinder (at room temperature) is forced (by its own pressure) through the sample. The gas flow is measured by a bubble flowmeter connected to the sample holder. The experiment for each sample begins with a low pressure and for each pressure the gas flow through the sample is measured. Figure 6.43 indicates a larger flow of helium through samples densified at lower temperatures. For the sample densified at 1100 °C no gas flow was observed. A sample densified at 1150 °C (1423 K) also presented no gas flow in the experiment. The slope of the curves in Figure 6.43 are plotted as a function of densification temperature in Figure 6.44. The variation of the slope of helium flow rate as a function of volume fraction of pores is presented in Figure 6.45. The variation of the slope of helium flow rate with relative genus is shown in Figure 6.46. Comparing Figures 6.45 and 6.46 and the shape of Figure 6.44 with Figures 2.27 (V_V versus temperature) and 3.21 (relative genus versus temperature) it can be seen that the gas flow through gel-silica

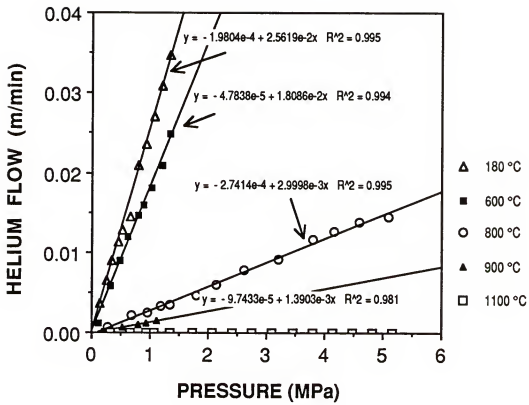

Figure 6.43 Variation of helium flow as a function of gas pressure for samples densified in the range 180 °C to 1100 °C.

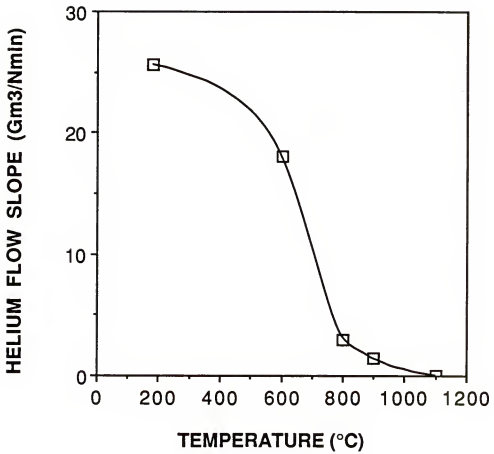

Figure 6.44 Variation of the slope of the curves helium flow versus pressure (Figure 6.43) as a function of densification temperature.

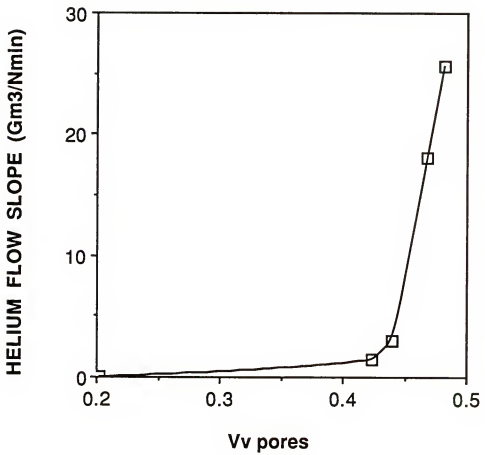

Figure 6.45 Variation of the helium flow slope as a function of volume fraction of pores (V_v).

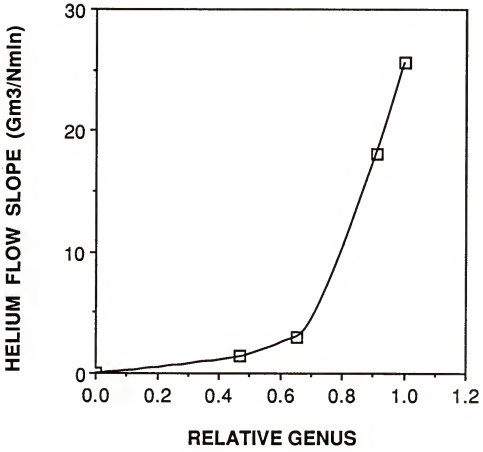

Figure 6.46 Variation of the helium flow slope as a function of relative genus (γ).

monoliths correlates better with the pore connectivity than with porosity.

6.5 Structological Analysis

Structures are usually complex and involve many different geometric aspects. Therefore, it should not be expected that simplistic approaches to the problem of correlating structures with physical properties are likely to yield meaningful relationships. The more complex a structure is the larger the number of structural parameters required to describe it. The introduction of topological parameters in describing gel-silica structures adds to the understanding of how a particular structure correlates to its physical properties. Table 6.1 summarizes the results obtained for the structure-properties relationships derived in this work. The use of topological parameters should be intended to complement information given by metric parameters and not to replace then.

Considering for instance the problem of impregnating the porous gel-silica with a certain type of molecules, many structural features have to be brought up. First, one has to consider whether the volume fraction of pores is compatible or not with the amount of impregnating material intended to be introduced in the matrix. If the porosity is adequate that is not a guarantee that the impregnation procedure is going to be successful. If the porosity is adequate but the pores are closed, there will be no impregnation. Therefore, the knowledge of the

Table 6.1 Coefficients of correlation (R^2) between physical properties and metric (V_v) and topological parameters (ß and γ). A (3) after the number means that R^2 was taken out of a third order polynomial. No number indicates a first order polynomial (straight line).

TEST	R^2 V_v	R^2 ß	R^2 γ
VHN	0.963	0.991 (3)	0.937 (3)
Flexural Strength	0.954	0.994	0.994
Flexural Modulus	0.809	0.907	0.907
Compression Strength (A1)	0.555	0.860	0.899
Compression Modulus (A1)	0.337	0.731	0.796
Compression Modulus (A2)	0.873	0.910	0.895
Tensile Strength (A1)	0.749	0.881	0.880
Tensile Strength (A2)	0.997 (3)	0.995 (3)	0.982 (3)
Tensile Modulus	0.910	0.967	0.967
Dimensional Change	0.695	0.863	0.957
Helium Flow	0.395	0.451	0.711

pore interconnectivity is a must for controlled impregnation and doping procedures. Besides the porosity and connectivity, the size of the pores also plays a decisive role during doping and impregnation. If the porosity and connectivity of the sample are adequate but the size of the pores are too small for the impregnating molecules to go through, again the impregnation will not occur. Therefore, a combination of structural parameters (metric and topological) are necessary to create a more complete picture of a given practical situation.

The VHN data obtained for silica gel monoliths correlate better with the volume fraction of pores than with the connectivity of pores. This result is possibly related to the fact that a hardness test measures directly the resistance of the material against the penetration of the diamond indenter. That means that the resistance to the penetration is directly proportional to the cross sectional area that is opposing the diamond indenter; i.e., the actual area fraction of material (Figure 6.47). Since the areal fraction is equal to the volume fraction, this parameter (V_V) is appropriate to describe the expected hardness of a material.

The data on strength and modulus of silica gel monoliths correlate better with the topological parameters (ß and γ) than with the volume fraction of pores. It is possible that these results come from a higher concentration of stresses in a pore with several branches than in a pore with one or no branch (Figure 6.48). It was shown that the mechanical properties variations with densification, can be divided into two distinct regions: the first one is at lower temperatures, when the strength of the silica gel monoliths increases relatively slowly with densification

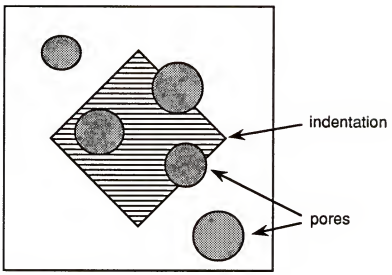

Figure 6.47 Schematic of the actual area in a specimen that resists the penetration of a hardness indenter.

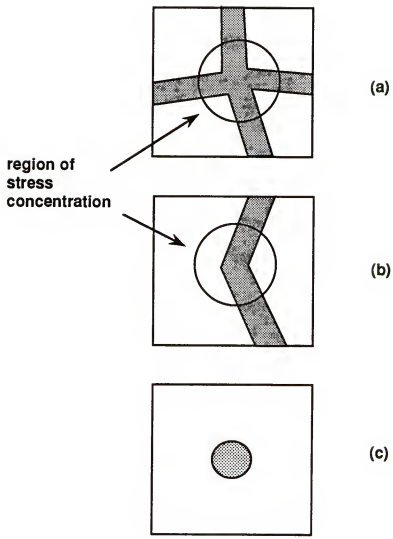

Figure 6.48 Schematic of the reduction in concentration of stresses when the pore connectivity decreases. (a) CN = 4; (b) CN = 2; (c) CN = 0.

temperature; the second region is at higher temperatures, when there is a more pronounced increase in strength as densification proceeds. In the first region the pores have many branches, which act as stress risers, decreasing the strength of the material. When the pores start closing in the second region (during the third stage of densification), the strength increases dramatically, because of the decrease in concentration of stress as the branches and nodes disappear.

As observed in this research, the dimensional change correlates better with the pore connectivity than with volume fraction of pores. It is possible that this effect be related with the reasoning that follows. When V_V of pores vary, but the solid matrix is continuous (Figure 6.49) it is expected that the dimensional change of the solid matrix will not be affected. By other hand, when the pore connectivity changes (Figure 6.50), even though the matrix is still connected in the three-dimensional space, the branched pores change the thermal behavior of the material. These changes could come from interferences in the heat flow through the sample caused by movement of vapor inside the connected pores, and from interference in the overall dimensional change caused by expansion (or contraction) of the connected pores.

The flow of gas through the silica gel monoliths correlates better with the pore connectivity than with V_V. This result is expected, since a gas can flow through a connected pore, and the flow stops when the pores are closed.

The introduction of topological characterization to the study of gel-silica monoliths opens up opportunities for better understanding of the

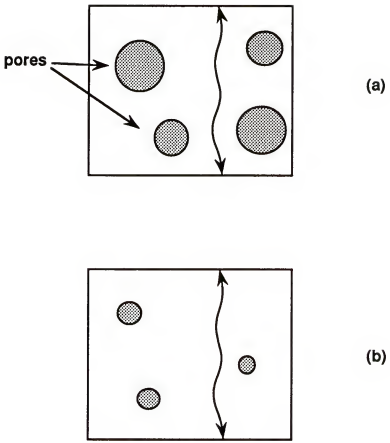

Figure 6.49 The schematic structure shown in (a) has a larger Vv of pores than the structure shown in (b), however both structures have a continuous matrix.

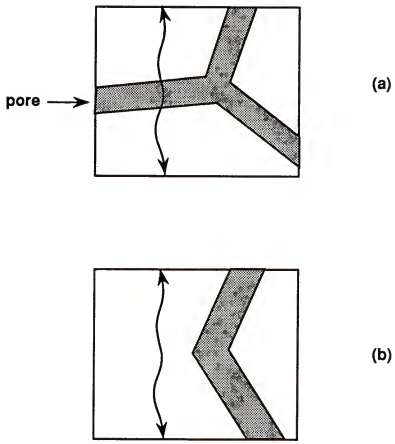

Figure 6.50 The schematic structure shown in (a) has a larger pore connectivity than the structure shown in (b).

problem of structure-properties correlations. A more comprehensive description of the structure is more likely to lead to more accurate relationships with physical properties. The ultimate goal of such a type of structural description is to make feasible the designing and obtaining of sets of desired properties in a material through controlled processing.

CHAPTER 7
CONCLUSIONS AND SUGGESTIONS FOR FUTURE WORK

The objectives of this research were to study the evolution of structural and physical properties during densification of silica gel monoliths and to provide new knowledge on the relationships between structure and properties. The main conclusions of this research can be summarized as follows:

1) Nitrogen gas adsorption experiments show that as the densification of silica gels proceeds, the volume fraction of pores (V_V) and the surface area of pores per unit volume (S_V) decrease towards zero porosity for the fully dense material. Meanwhile, the average size of pores remains approximately constant during densification of silica gel monoliths with pores of 12 Å initial average pore size. For silica gels of larger initial pore sizes, the average pore size slightly decreases during the beginning of densification.

2) As the densification proceeds, there is a significant variation in the structural density of the silica gels. The structural density initially increases from the dried samples and assumes maximum values in the temperature range of 800-1000 °C (1073-1273 K), depending on the average pore size of the gels. Increasing the densification temperature beyond that maximum the structural density falls off again.

3) The variation in structural metric parameters for silica gels shows that the structural evolution during densification can be roughly divided

into two major regions, which depend on the pore size of the silica gel. For silica gels of 12 Å average pore size the first region goes from 180 °C (453 K) (dried sample) until a temperature of about 800 °C (1073 K). In this region the structural transformations with densification temperature are less pronounced than for the second region, which goes from about 800 °C (1073 K) until the sample is fully dense (at about 1150 °C, 1423 K).

4) It is possible to use model geometric shapes together with experimentally obtained values of V_V and S_V to obtain topological information on a structure. Three types of models (spherical, tetrahedral and cylindrical) were used to describe the evolution of topological properties of silica gels during densification. As the densification proceeds, the number of nodes and branches associated with the gel structure decreases. The genus decreases during densification and goes to zero at a temperature which depends on the pore size. The region where the genus becomes zero characterizes the beginning of the third stage of densification. The pore closing associated with the third stage of densification is responsible for water trapping and foaming when water is not removed before the genus becomes zero.

5) In order to make it easier to compare the structural state and characterize the structural evolution during sintering two topological indices are used: (1) the relative genus γ and (2) the fraction of removed branches ß. The relative genus is used to identify the different stages of

densification. The topological index ß is associated to pore network transformations during the entire process.

6) In general the mechanical property variations during densification for silica gels samples show the presence of two distinct regions: at low temperatures the variations in the mechanical properties are less pronounced than in a second region corresponding to higher sintering temperatures.

7) Comparisons between the thermal properties behavior of silica gels are carried out by using the coefficient of dimensional change measured in a temperature range that lies at the same time above the temperature range in which the presence of physical water in the samples cause an expansion, and below the temperature in which the sample was previously heat treated.

8) Application of "structology," or the obtaining of relationships between structural properties and physical properties, reveal a general good agreement between the changes in physical properties and the topological transformations that occur in the silica gel samples. It is suggested that the first region of variation of physical properties is related with the region in which the pores are connected. The second region is associated with pore closure. For instance, as the connectivity decreases, the pore coordination number decreases and the stress concentration decreases, rising the strength of the material.

This research showed the importance of a complete understanding of the structure, involving both metric and topological properties, in order for the behavior of materials be understood. However, many additional

questions and problems are brought up by this work. Important questions and problems that deserve further study are the following:

1) The full densification of silica gel monoliths, although a feasible process (as shown in this research), still is a time-consuming and elaborate process. In order for sol-gel derived materials of optical quality become more attractive commercially, more research is necessary in order to improve and decrease the costs of processing. The initial structure of silica gels seems to have a profound effect on the behavior of the material during densification. Therefore, it would be useful a study on the effect of the transformations that occur during gelation and aging on the structural and physical evolution of silica gel monoliths during the densification process.

2) The type of atmosphere inside the furnace affects the densification of silica gel monoliths. It is of practical interest to explore the effects of various gases, including combinations of gases, on the densification of silica gel monoliths. The pressure inside the furnace and the partial pressure of the gases used are important variables that need to be better understood.

3) Silica gel monoliths with relatively large pore size structures (>50 Å of pore radius) have potential use in impregnation and doping applications. Therefore, a comprehensive study on structural and physical (mechanical and thermal) properties of these materials is necessary.

4) This research indicates the importance of topological properties in determining physical properties of silica gel monoliths. The

introduction of topological parameters in the description of the structure opens up opportunities for the control of impregnation, doping and diffusion applications. It is suggested that impregnation, doping and diffusion experiments be carried out in silica gel monoliths of known topological properties, in order to check for the applicability of the proposed topological models, and to derive working relationships between the structural properties and processing conditions.

5) Further studies are necessary to explain the physical mechanisms responsible for the structure-property relationships observed in this research. For example, a mechanical analysis to describe the stress concentration effects associated with pore connectivity is necessary, as well as to explain the correlation between the local levels of stress concentration and the strength of the material. The relative and quantitative importances of pore coordination and curvature of pores in the local level of stress have to be evaluated in order to clarify the mechanisms responsible for the mechanical strength of silica gel monoliths.

APPENDIX

For the four point bending the maximum deflection (Δ) at the center of the beam can be given by the tangential deviation (t) which is given by [533]

$$\Delta = t_{VU} = \int_{V}^{U} \frac{M}{E} \frac{x}{I} dx , \qquad (A.1)$$

where t_{VU} is the tangential deviation between two generic points V and U;

M is the bending moment;

x is the position;

E is the elastic modulus;

I is the moment of inertia.

Considering the rectangular beam shown in Figure A.1, the reactions R_1 and R_2 are equal, because of symmetric loading. Consequently both R_1 and R_2 are P/2, where P is the total testing load.

The variation of bending moment with position between points A and B (M_{AB}) is given by

$$M_{AB} = \frac{P}{2} x. \qquad (A.2)$$

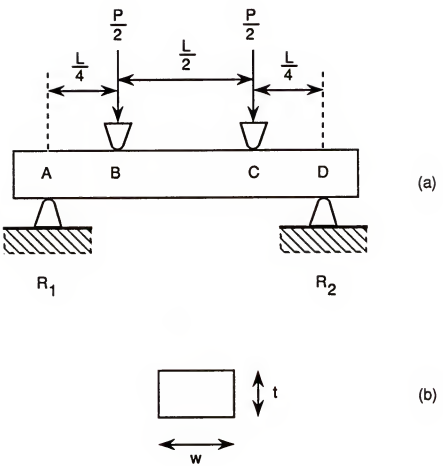

Figure A.1 (a) Schematic of a four point bending beam with the cross section shown in (b).

The variation of bending moment between points B and C (midspan of the bending beam) is given by

$$M_{BC} = \frac{P}{2}x - \frac{P}{2}\left(x - \frac{L}{4}\right), \tag{A.3}$$

where L is the length of span.

Introducing Eqs.(A.2) and (A.3) into Eq.(A.1) one obtains

$$\Delta = \int_{0}^{\frac{L}{4}} \left(\frac{P}{2}x\right)\frac{x}{E\,I}dx + \int_{\frac{L}{4}}^{\frac{L}{2}} \left(\frac{P}{2}x - \frac{P}{2}\left(x - \frac{L}{4}\right)\right)\frac{x}{E\,I}dx\,. \tag{A.4}$$

The solution of Eq.(A.4) is

$$\Delta = \frac{7\,P\,L^3}{384\,E\,I}. \tag{A.5}$$

The moment of inertia (I) of a rectangular beam is given by [534]

$$I = \frac{w\,t^3}{12}, \tag{A.6}$$

where w is the width of the beam;

t is the thickness of the beam.

Substituting Eq.(A.6) into Eq.(A.5) one obtains:

$$\Delta = \frac{7\ P\ L^3}{32\ E\ w\ t^3}. \tag{A.7}$$

The elastic modulus for four points flexural testing (E_b) is directly obtained from Eq.(A.7) as

$$E_b = \frac{7\ P\ L^3}{32\ \Delta\ w\ t^3}. \tag{A.8}$$

REFERENCES

[1] W. Vogel, *Chemistry of Glass* (Am. Ceramic Soc., Columbus, Ohio, 1985).

[2] R.H. Doremus, *Glass Science* (Wiley, New York, 1973).

[3] W.H. Zachariasen, *J. Amer. Chem. Soc.*, 54 (1932) 3841.

[4] B.E. Warren, *Phys. Rev.*, 45 (1934) 657.

[5] B.E. Warren, *J. Amer. Cer. Soc.*, 17 (1934) 249.

[6] W.H. Zachariasen, *J. Chem. Phys.*, 3 (1935) 162.

[7] B.E. Warren, *J. Appl. Phys.*, 8 (1937) 645.

[8] L.W. Tilton, *J. Res. NBS*, 59 (1957) 139.

[9] L.W. Tilton, *J. Res. NBS*, 60 (1958) 351.

[10] A.A. Lebedev, in: *The Structure of Glass*, Vol.2, transl. from Russian (Consultants Bureau, New York, 1960) p.3.

[11] R.J. Bell and P. Dean, *Nature*, 212 (1966) 1354.

[12] R.J. Bell and P. Dean, *Phys. Chem. Glass*, 9 (1968) 125.

[13] P. Dean, *J. Phys. Soc. Japan*, 68 (Suppl. 1969) 20.

[14] R.L. Mozzi and B.E. Warren, *J. Appl. Cryst.*, 2 (1969) 164.

[15] R.J. Bell, P. Dean, and D.C.H. Butler, *J. Phys.*, C3 (1970) 2111.

[16] R.J. Bell and P. Dean, *Phil. Mag.*, 25 (1972) 1381.

[17] R.J. Bell, N.F. Bird, and P. Dean, *J. Phys.*, C7 (1974) 2457.

[18] A.C. Wright and A.J. Leadbetter, *Phys. Chem. Glasses*, 17 (1976) 122.

[19] J.F. Shackelford, *J. Non. Cryst. Solids*, 49 (1982) 299.

[20] A.C. Wright, G. Etherington, J.A.E. Desa, R.N. Sinclair, G.A.N. Connell, and J.C. Mikkelsen Jr., *J. Non-Cryst. Solids*, 49 (1982) 63.

[21] P.A.V. Johnson, A.C. Wright, and R.N. Sinclair, *J. Non-Cryst. Solids*, 58 (1983) 109.

[22] R. Zallen, *J. Non-Cryst. Solids*, 75 (1985) 3.

[23] A.C. Wright, *J. Non-Cryst. Solids*, 75 (1985) 15.

[24] F.V. Tooley, *The Handbook of Glass Manufacture* (Books for Industry, New York, 1974).

[25] W.D. Kingery, H.K. Bowen, and D.R. Uhlmann, *Introduction to Ceramics*, 2nd ed. (Wiley, New York, 1976).

[26] C.L. Babcock, *Silicate Glass Technology Methods* (Wiley, New York, 1977).

[27] J. Hlavac, *The Technology of Glass and Ceramics* (Elsevier, Amsterdam, 1983).

[28] L.L. Hench and J.K. West, *Chem. Reviews*, in press.

[29] S.H. Wang, *Gel-Silica Optics*, Ph.D. Dissertation (University of Florida, Gainesville, 1988).

[30] L.L. Hench, S.H. Wang, and J.L. Nogues, *Multifunctional Materials, SPIE,* 878 (1988) 76.

[31] M. Grayson, Ed., *Encyclopedia of Glass, Ceramics, Clay and Cement* (Wiley, New York, 1985).

[32] R.K. Iler, *The Chemistry of Silica and Silicates* (Cornell University, Ithaca, 1955).

[33] R.K. Iler, *The Chemistry of Silica* (Wiley, New York, 1979).

[34] C. Okkerse, in: *Physical and Chemical Aspects of Adsorbents and Catalysts*, B.G. Linsen, Ed. (Academic Press, London, 1970) p.213.

[35] L.L. Hench, Ed., *Ultrastructure Processing of Advanced Structural and Electronic Materials* (Noyles, Park Ridge, New Jersey, 1984).

[36] L.L. Hench and D.R. Ulrich, Eds., *Ultrastructure Processing of Ceramics, Glasses and Composites* (Wiley, New York, 1984).

[37] L.L. Hench and D.R. Ulrich, Eds., *Science of Ceramic Chemical Processing* (Wiley, New York, 1986).

[38] D.R. Ulrich, *J. Non-Cryst. Solids*, 100 (1985) 174.

[39] H. Dislich, *J. Non-Cryst. Solids*, 73 (1985) 599.

[40] J.D. MacKenzie, *J. Non-Cryst. Solids*, 73 (1985) 631.

[41] G.W. Scherer, *J. Non-Cryst. Solids*, 73 (1985) 661.

[42] J. Wenzel, *J. Non-Cryst. Solids*, 73 (1985) 693.

[43] D.R. Uhlman, B.J.J. Zelinsky, and G.E. Wnek, in: *Better Ceramics Through Chemistry*, C.J. Brinker, D.E. Clark, and D.R. Ulrich, Eds. (Elsevier, New York, 1984) p.59.

[44] M. Ebelmen, *Ann. de Chimie et de Phys.*, 16 (1846) 129.

[45] M. Ebelmen, *Comptes Rend. de L'Acad. des Sciences*, 25 (1847) 854.

[46] T. Graham, *J. Chem. Soc.*, 17 (1864) 318.

[47] R.E. Liesegang, *Photo. Archiv.*, (1896) 221.

[48] W.Z. Ostwald, *Phys. Chem.*, 27 (1897) 365.

[49] L. Rayleigh, *Phil. Mag.*, 38 (1919) 738.

[50 D.J. Lloyd, in: *Colloid Chemistry*, J. Alexander, Ed. (Chemical Catalog Co., New York, 1926) p.767.

[51] H.N. Holmes, in: *Colloid Chemistry*, J. Alexander, Ed. (Chemical Catalog Co., New York, 1926) p.796.

[52] K.H. Stern, *Bibliography of Liesegang Rings*, Miscellaneous Publication No. 292 (National Bureau of Standards, Washington, 1967).

[53] H.K. Heinisch, *Crystal Growth in Gels* (Pennsylvania State University, State College, 1970).

[54] W. Geffcken and E. Berger, *Dtsch. Reichspatent 736411* (1939).

[55] D.M. Roy and R. Roy, *Am. Mineralogist*, 39 (1954) 957.

[56] R. Roy, *J. Am. Ceram. Soc.*, 39 (1956) 145.

[57] R. Roy, *J. Am. Ceram. Soc.*, 52 (1969) 344.

[58] G.J. McCarthy, R. Roy, and J.M. McKay, *J. Am. Ceram. Soc.*, 54 (1971) 637.

[59] W. Stober, A. Fink, and E. Bohn, *J. Colloid Interface Sci.*, 26 (1968) 62.

[60] C.G. Tan, B.D. Bowen, and N. Epstein, *J. Colloid Interface Sci.*, 118 (1987) 290.

[61] H. Dislich, P. Hinz and R. Kaufmann, *FRG Patent 19 41 191* (1969).

[62] L. Levene and I.M. Thomas, *DAS 20 09 653* (1969).

[63] K.S. Mazdiyasni, R.T. Dollof, and J.S. Smith II, *J. Am Ceram. Soc.*, 52 (1969) 513.

[64] K.S. Mazdiyansni, R.T. Dollof, and J.S. Smith II, *J. Am. Ceram. Soc.*, 53 (1970) 91.

[65] H. Dislich, *Angew. Chem. Int. Ed. Engl.*, 10 (1971) 363.

[66] J. Th.G. Overbeek, *Adv. Colloidal Interface Sci.*, 16 (1982) 17.

[67] J. Th. G. Overbeek, *Adv. Colloidal Interface Sci.*, 15 (1982) 251.

[68] T. Sugimoto, *Adv. Colloidal Interface Sci.*, 28 (1987) 65.

[69] E. Matijevic, M. Bundnick, and L. Meites, *J. Colloidal Interface Sci.*, 61 (1977) 302.

[70] E. Matijevic, in: *Ultrastructure Processing of Ceramics, Glasses and Composites*, L.L. Hench and D.R. Ulrich, Eds. (Wiley, New York, 1984) p.334.

[71] E. Matijevic, in: *Science of Ceramic Chemical Processing*, L.L. Hench and D.R. Ulrich, Eds. (Wiley, New York, 1986) p.463.

[72] E. Matijevic, in: *Ultrastructure Processing of Advanced Ceramics*, J.D. Mackenzie and D.R. Ulrich, Eds. (Wiley, New York, 1988) p.429.

[73] E.A. Barringer and H.K. Bowen, *J. Am. Ceram. Soc.*, 65 (1982) C199.

[74] B. Fegley Jr. and E.A. Barringer, in: *Better Ceramics Through Chemistry*, C.J. Brinker, D.E. Clark, and D.R. Ulrich, Eds. (Elsevier, New York, 1984) p.187.

[75] B. Fegley Jr., P. White, and H.K. Bowen, *J. Am. Ceram. Soc.*, 64 (1985) 1115.

[76] B. Fegley, E.A. Barringer, and H.K. Bowen, *J. Am. Ceram. Soc.*, 67 (1984) C113.

[77] A. Hardy, G. Gowda, T.J. McMahon, R.E. Riman, W.E. Rhine, and H.K. Bowen, in: *Ultrastructure Processing of Advanced Ceramics*, J.D. Mackenzie and D.R. Ulrich, Eds. (Wiley, New York, 1988) p.407.

[78] M.E.A. Hermans, *Sci. Ceram.*, 5 (1970) 523.

[79] K. Kamiya, S. Sakka, and Y. Tatemichi, *J. Mater. Sci.*, 15 (1980) 1765.

[80] K. Susa, *Electronics Lett.*, 18 (1982) 499.

[81] E.M. Rabinovich, D.W. Johnson, Jr., J.B. MacChesney, and E.M. Vogel, *J. Non-Cryst. Solids*, 47 (1982) 435.

[82] E.M. Rabinovich, D.W. Johnson, Jr., J.B. MacChesney, and E.M. Vogel, *J. Am. Ceram. Soc.*, 66 (1983) 683.

[83] D.W. Johnson, E.M. Rabinovich, J.B. MacChesney, and E.M. Vogel, *J. Am. Ceram. Soc.*, 66 (1983) 688.

[84] E.M. Rabinovich, J.B. MacChesney, D.W. Johnson Jr., J.R.Simpson, B.W. Meagher, F.V. Mimarcello, D.L. Wood, and E.A. Sigety, *J. Non-Cryst. Solids*, 63 (1984) 155.

[85] E.M. Rabinovich, J.B. MacChesney, and D.W. Johnson Jr., in: *Science of Ceramic Chemical Processing*, L.L. Hench and D.R. Ulrich, Eds. (Wiley, New York, 1986) p.208.

[86] C.Z.C. Porczynski, *Advanced Materials* (Chemical Publishing Co., New York, 1962).

[87] L.R. McCreight, H.W. Rauch Sr., and W.H. Sutton, *Ceramic Fibers and Fibrous Composite Materials* (Academic Press, New York, 1965).

[88] H.W. Rauch Sr., W.H. Sutton, and L.R. McCreight, *Ceramic Fibers and Fibrous Composite Materials* (Academic Press, New York, 1968).

[89] L.E. Seufert, *U.S. Patent No. 3,808,015* (April 30, 1974).

[90] K. Miyahara and N. Nakayama, *U.S. Patent No. 4,159,205* (1979).

[91] M. Leitheiser and H.G. Snowman, *U.S. Patent Appl. 145,383* (1980).

[92] H. Dislich and P. Hinz, *J. Non-Cryst. Solids*, 48 (1982) 11.

[93] Prospect *IROX® Solar-Reflective Glass. Function and Design in Modern Architecture. The Completely Color-Neutral Glass from Schott* (Schott Glaswerke, Mainz, FRG, 1969).

[94] H. Schroeder, *Opt. Acta*, 9 (1962) 249.

[95] J.D. Mackenzie, *J. Non-Cryst. Solids*, 41 (1982) 1.

[96] J.D. Mackenzie, in: *Ultrastructure Processing of Ceramics,Glasses and Composites*, L.L. Hench and D.R. Ulrich, Eds. (Wiley, New York, 1984) p.15.

[97] J. Wenzel, in: *Glass-Current Issues*, A.F. Wright and A.F. Dupuy, Eds. (Martinus Nijhojj, Dordrecht, Netherlands, 1985) p.224.

[98] B.E. Yoldas, *J. Non-Cryst. Solids*, 51 (1982) 105.

[99] B.E. Yoldas, *J. Non-Cryst. Solids*, 63 (1984) 145.

[100] L.L. Hench, M.J.R. Wilson, C. Balaban, and J.L. Nogues, in: *Proc. 4th International Conference on Ultrastructure Processing of Ceramics, Glasses and Composites*, Tucson, Arizona (February, 1989)

[101] L.L. Hench and S.H. Wang, *Phase Transitions J.*, in press.

[102] S.J. Teichener, *Adv. Colloid Interf. Sci.*, 5 (1976) 245.

[103] G. Carturan, *J. Non-Cryst. Solids*, 48 (1982) 219.

[104] G. Carturan , *J. Non-Cryst. Solids*, 63 (1984) 273.

[105] J.A. Carns, D.L. Segal, and J.L. Woodhead, *Proc. Materials Research Society Spring Meeting*, Albuquerque (February, 1984).

[106] R.V. Ramaswamy, T. Chia, R. Srivastava, A. Miliou, and J.K. West, *Multifunctional Materials, SPIE*, 878 (1988) 86.

[107] M. Rubin and C.M. Lampert, *Solar Energy Mater*, 7 (1983) 393.

[108] D.E. Clark and J.J. Lannutti, in: *Ultrastructure Processing of Ceramics, Glasses and Composites*, L.L. Hench and D.R. Ulrich, Eds. (Wiley, New York, 1984) p.126.

[109] J.J. Lannutti and D.E. Clark, in: *Better Ceramics Through Chemistry*, C. Brinker, D. Clark, and D. Ulrich, Eds. (Elsevier, New York, 1984) p.369.

[110] J.J. Lannutti and D.E. Clark, in: *Better Ceramics Through Chemistry*, C. Brinker, D. Clark, and D. Ulrich, Eds. (Elsevier, New York, 1984) p.375.

[111] J.J. Lannutti and D.E. Clark, in: *Proc. 8th Annual Meeting on Advanced Ceramics and Composites*, Cocoa Beach, Florida (January, 1984).

[112] D.E. Clark, in: *Science of Ceramic Chemical Processing*, L.L. Hench and D.R. Ulrich, Eds. (Wiley, New York, (1986) p.237.

[113] H. Dislich and E. Hussmann, *Thin Solid Films*, 77 (1981) 129.

[114] C.J. Brinker and M.S. Harrington, *Solar Energy Mater.*, 5 (1981) 159.

[115] N.J. Arfsten, *J. Non-Cryst. Solids*, 63 (1984) 243.

[116] B.E. Yoldas and D.E. Partlow, *Appl. Optics*, 23 (1984) 1418.

[117] J.P. Boilot, P. Colomban, and N. Blanchard, *Solid St. Ionics*, 9-10 (1983) 639.

[118] D.C. Tran and K.P. Koo, *Electron Lett.*, 17 (1981) 187.

[119] E. Leroy, C.R.-Brosse, and J.P. Torre, in: *Ultrastructure Processing of Ceramics, Glasses and Composites*, L.L. Hench and D.R. Ulrich, Eds. (Wiley, New York, 1984) p.219.

[120] B. I. Lee and L.L. Hench, in: *Science of Ceramic Chemical Processing*, L.L. Hench and D.R. Ulrich, Eds. (Wiley, New York, 1986) p.231.

[121] G. Orcel and L.L. Hench, in: *Science of Ceramic Chemical Processing*, L.L. Hench and D.R. Ulrich, Eds. (Wiley, New York, 1986) p.224.

[122] H. Dislich and P. Hinz, *J. Non-Cryst. Solids*, 48 (1982) 11.

[123] J. Schlichting and S. Neuman, *J. Non-Cryst. Solids*, 48 (1982) 185.

[124] S.P. Mukherjee, *Proc. Topical Meeting on Gradient Index Optical Imaging Systems*, Honolulu (May, 1980).

[125] D.C. Tran, *U.S. Patent No. 4 333 847.*

[126] C.J. Brinker, *J. Am. Ceram. Soc.*, 65 (1982) C4.

[127] D. Hoffman, R. Roy, and S. Komarneni, *Mater. Lett.*, 2 (1984) 245.

[128] T. Hayashi and H. Saito, *J. Mat. Sci.*, 15 (1980) 1971.

[129] H.G. Sowman and M.A. Leitheiser, *U.S. Patent No. 4,314,827* (1982).

[130] Oak Ridge Nat. Lab., development reported in: *Am. Ceram. Soc. Bull.*, 62 (1983) 1089.

[131] H. Dislich, in: *Treatise on Glass*, D.R. Uhlmann and N.J. Kreidl, Eds. (Academic Press, New York, 1984).

[132] N.J. Arfsten, R. Kaufmann, and H. Dislich, in: *Ultrastructure Processing of Ceramics, Glasses and Composites*, L.L. Hench and Ulrich, Eds. (Wiley, New York, 1984) p.189.

[133] G. Carturan, G. Facchin, G. Navazio, V. Gottardi, and G. Cocco, in: *Ultrastructure Processing of Ceramics, Glasses and Composites*, L.L. Hench and D.R. Ulrich, Eds. (Wiley, New York, 1984) p.197.

[134] B.D. Fabes, W.F. Doyle, L. Silverman, B.J. Zelinski, and D.R. Uhlmann, in: *Science of Ceramic Chemical Processing*, L.L. Hench and D.R. Ulrich, Eds. (Wiley, New York, 1986) p.217.

[135] B. Jirgensons and M.E. Straumanis, *Colloid Chemistry* (Macmillan, New York, 1962).

[136] J.S. Reed, *Introduction to the Principles of Ceramic Processing* (Wiley, New York, 1988).

[137] P.J. Flory, *Principles of Polymer Chemistry* (Cornell University Press, Ithaca, 1953).

[138] J. Fricke, Ed., *Aerogels*, Springer Proc. in Physics, Vol.6 (Springer-Verlag, Heidelberg, 1986).

[139] J. Fricke and R. Caps, in: *Ultrastructure Processing of Advanced Ceramics*, J.D. Mackenzie and D.R. Ulrich, Eds. (Wiley, New York, 1988) p.613.

[140] C.J. Brinker and G.W. Scherer, *Sol-Gel Science* (Academic Press, New York, 1989).

[141] J. Mahanty and B.W. Ninham, *Dispersion Forces* (Academic Press, New York, 1976).

[142] S. Voyutsky, *Colloid Chemistry* (Mir Publishers, Moscow, 1978).

[143] R.J. Hunter, *Zeta Potential in Colloid Science* (Academic Press, New York, 1981).

[144] J. Depasse and A. Watillon, *J. Colloid Interface Sci.*, 33 (1970) 431.

[145] G.C.J. Rouweler and J.Th.G. Overbeek, *Trans. Faraday Soc.*, 67 (1971) 2117.

[146] F. Dumont and A. Watillon, *Faraday Soc. Disc.*, 52 (1971) 375.

[147] D. Tabor and R.H.S. Winterton, *Nature*, 219 (1986) 1120.

[148] G.D. Parfitt, *Dispersion of Powders in Liquids* (Applied Science Publishers, London, 1981).

[149] J.D.F. Ramsay and B.O. Booth, *J. Chem. Soc. Faraday Trans. 1*, 79 (1983) 173.

[150] D.W. Schaefer and K.D. Keefer, *Phys. Rev. Lett .*, 53 (1984) 1383.

[151] K.D. Keefer, in: *Science of Ceramic Chemical Processing*, L.L. Hench and D.R. Ulrich, Eds. (Wiley, New York, 1986) p.131.

[152] A. Aelion, A. Loebel, and F. Eirich, *J. Am. Chem. Soc.*, 72 (1950) 5705.

[153] H. Schmidt and A. Kaiser, *Glastechn Ber.*, 54 (1981) 338.

[154] I. Artaki, S. Sinha, and J. Jones, *J. Mater. Sci. Lett.*, 2 (1984) 448.

[155] H. Schmidt, H. Scholze, and A. Kaiser, *J. Non-Cryst. Solids*, 63 (1984) 1.

[156] R.A. Assink and B.D. Kay, in: *Better Ceramics Through Chemistry*, C.J. Brinker, D.E.Clark, and D.R. Ulrich, Eds. (Elsevier, New York, 1984) p.301.

[157] I. Artaki, S. Sinha, A.D. Irwin, and J. Jones, *J. Non-Cryst. Solids,* 72 (1985) 391.

[158] H. Schmidt and H. Scholze, in: *Glass-Current Issues*, A.F. Wright and A.F. Dupuy, Eds. (Martinus Nijhojj, Dordrecht, Netherlands, 1985) p.253.

[159] I. Artaki, T. Zerda, and J. Jones, *J. Mater. Sci. Lett.*, 3 (1985) 493.

[160] L.L. Hench and G. Orcel, *J. Non-Cryst. Solids*, 82 (1986) 1.

[161] H. Schmidt, A. Kaiser, M. Rudolph, and A. Lentz, in: *Science of Ceramic Chemical Processing*, L.L. Hench and D.R. Ulrich, Eds. (Wiley, New York, 1986) p.87.

[162] I. Artaki, M. Bradley, T.W. Zerda, J. Jonas, G. Orcel, and L.L. Hench, in: *Science of Ceramic Chemical Processing*, L.L. Hench and U.R. Ulrich (Wiley, New York, 1986) p.73.

[163] D.R. Uhlmann, B.J. Zelinski, L. Silverman, S.B. Warner, B.D. Fabes, and W.F. Doyle in: *Science of Ceramic Chemical Processing,* L.L. Hench and D.R. Ulrich, Eds. (Wiley, New York, 1986) p.173.

[164] S. Sakka and Y. Kamiya, *J. Non-Cryst. Solids*, 42 (1950) 403.

[165] G. Orcel, *The Chemistry of Silica Sol-Gel*, Ph.D. Dissertation (University of Florida, Gainesville, 1987).

[166] G. Orcel, L.L. Hench, I. Artaki, J. Jones, and T.W. Zerda, *J. Non-Cryst. Solids*, 105 (1988) 223.

[167] G.G. Klemperer and S.D. Ramamurthi, in: *Better Ceramics Through Chemistry III*, C.J. Brinker, D.E. Clark, and D.R. Ulrich, Eds., Vol.121 (Materials Research Society, Pittsburgh, 1988) p.1.

[168] W.G. Klemperer, V.V. Mainz, S.D. Ramamurthi and F.S. Rosenberg, in: *Better Ceramics Through Chemistry III*, C.J. Brinker, D.E. Clark, and D.R. Ulrich, Eds., Vol.121 (Materials Research Society, Pittsburgh, 1988) p.15.

[169] B.E. Yoldas, *J. Non-Cryst. Solids*, 63 (1984) 145.

[170] M. Prassas and L.L. Hench, in: *Ultrastructure Processing of Ceramics, Glasses and Composites*, L.L. Hench and D.R. Ulrich, Eds. (Wiley, New York, 1984) p.100.

[171] B.D. Kay and R.A. Assink, in: *Better Ceramics Through Chemistry II*, C.J. Brinker, D.E. Clark, and D.R. Ulrich, Eds., Vol.73 (Materials Research Society, Pittsburgh, 1986) p.157.

[172] G. Orcel and L.L. Hench, *J. Non-Cryst. Solids*, 79 (1986) 177.

[173] L.L. Hench, G. Orcel, and J.L. Nogues, in: *Better Ceramics Through Chemistry II*, C.J. Brinker, D.E. Clark, and D.R. Ulrich, Eds., Vol.73 (Materials Research Society, Pittsburgh, 1986) p.35.

[174] R.K. Iler, in: *Soluble Silicates*, J.S. Falcone, Ed., American Chem. Society Symp. Series 194 (ACM, Washington, 1982).

[175] T.W. Zerda and G. Hoang, *J. Non-Cryst. Solids*, in press.

[176] M.J.S. Dewar and W. Theil, *J. Am. Chem. Soc.*, 99 (1977) 4899.

[177] M.L. McKee, W.N. Lipscomb, *J. Am. Chem. Soc.*, 103 (1981) 4673.

[178] M.J.S. Dewar and E. Healy, *Organometallics*, 1 (1982) 1705.

[179] M.S. Gordon, *J. Am. Chem. Soc.*, 104 (1982) 4352.

[180] T.A. Holme, M.S. Gordon, S. Yabushita, and M.W. Schmidt, *Organometallics*, 3 (1984) 583.

[181] M.J.S. Dewar, E.G. Zoebisch, E.F. Healy, and J.J.P. Stewardt, *J. Am. Chem. Soc.*, 107 (1985) 3902.

[182] L.P. Davis and L.W. Burggraf, in: *Science of Ceramic Chemical Processing*, L.L. Hench and D.R. Ulrich, Eds. (Wiley, New York, 1986) p.400.

[183] L.P. Davis, *Proc. Materials Research Society Symposium*, 73 (1986) 529.

[184] L.P. Davis, *Chemically Modified Surfaces*, Gordon and Breach Science, 1 (1986) 157.

[185] L.W. Burggraf and L.P. Davis, in: *Better Ceramics Through Chemistry II*, C.J. Brinker, D.E. Clark, and D.R. Ulrich, Eds., Vol.73 (Materials Research Society, Pittsburgh, 1986) p.529.

[186] L.W. Burggraf and L.P. Davis, *Chemically Modified Surfaces*, 1 (1986) 157.

[187] L.P. Davis and L.W. Burggraf, in: *Ultrastructure Processing of Advanced Ceramics*, J.D. Mackenzie and D.R. Ulrich, Eds. (Wiley, New York, 1988) p.367.

[188] R. Damrauer, L.W. Burggraf, L.P. Davis, and M.S. Gordon, *J. Am. Chem. Soc.*, 110 (1988) 6601.

[189] L.P. Davis, L.W. Burggraf, and M.S. Gordon, *J. Am. Chem. Soc.*, 110 (1988) 3056.

[190] C.B. Hurd, *Chem. Rev.*, 22 (1938) 403.

[191] M.F. Betchtold, W. Mahler, and R.A. Schunn, *J. Polym. Sci.*, 18 (1980) 2823.

[192] S. Sakka and K. Kamiya, *J. Non-Cryst. Solids*, 48 (1982) 31.

[193] S. Sakka, in: *Glass III*, Treatise of Materials Science and Technology, Vol.22, M. Tomozawa and R. Doremus, Eds. (Academic Press, New York, 1982) p.129.

[194] M.M. Akhtar, *Factors Controlling the Sol-Gel Conversion in TEOS*, Ph.D. Dissertation (Alfred University, Alfred, 1983).

[195] S. Sakka and K. Kamiya, in: *Emergent Methods for High Technology Ceramics*, Materials Science Research, Vol.17, R.F. Davis, H. Palmour III, and R.L. Porter, Eds. (Plenum, New York, 1984) p.83.

[196] S. Sakka, in: *Better Ceramics Through Chemistry*, C.J. Brinker, D.E. Clark, and D.R. Ulrich, Eds. (Elsevier, New York, 1984) p.91.

[197] M. Yamane, S. Inoue, and A. Yasumori, *J. Non-Cryst. Solids*, 63 (1984) 13.

[198] J.D. Mackenzie, in: *Science of Ceramic Chemical Processing*, L.L. Hench and D.R. Ulrich, Eds. (Wiley, New York, 1986) p.113.

[199] J.C. Debsikdar, *Adv. Ceram. Mater.*, 1 (1986) 93.

[200] M.D. Sacks and R.S. Sheu, in: *Science of Ceramic Chemical Processing*, L.L. Hench and D.R. Ulrich, Eds. (Wiley, New York, 1986) p.100.

[201] R.K. Iler, in: *Science of Ceramic Chemical Processing*, L.L. Hench and D.R. Ulrich, Eds. (Wiley, New York, 1986) p.3.

[202] M.W. Colby, A Osaka, and J.D. Mackenzie, *J. Non-Cryst. Solids*, 99 (1988) 129.

[203] S.A. Khan, E.M. Rabinovich, R.K. Prudhomme, M.J. Sammon, and N.J. Kopylor, in: *Better Ceramics Through Chemistry III*, C.J. Brinker, D.E. Clark, and D.R. Ulrich, Eds., Vol.121 (Materials Research Society, Pittsburgh, 1988) p.73.

[204] O. Kinouchi Filho and M. Aegerter, *J. Non-Cryst. Solids*, 105 (1988) 191.

[205] M.D. Sacks and R.S. Sheu, *J. Non-Cryst. Solids*, 92 (1987) 383.

[206] M. Nogami and Y. Moriya, *J. Non-Cryst. Solids*, 37 (1980) 191.

[207] C.J. Brinker, K.D. Keefer, D.W. Schaefer, and C.S. Ashley, *J. Non-Cryst. Solids*, 48 (1982) 47.

[208] J.C. Debskikdar, *Adv. Ceram. Mater.*, 1 (1986) 93.

[209] C.J. Brinker, K.D. Keefer, D.W. Schaefer, R.A. Assink, B.D. Kay, and C.S. Ashley, *J. Non-Cryst. Solids*, 63 (1982) 45.

[210] D.W. Schaefer, J.E. Martin, P.W. Wiltzius, and D.S. Cannell, in: *Kinetics of Aggregation and Gelation*, F. Family and D.P. Landau, Eds. (North Holland, Amsterdam, 1984) p.71.

[211] D.W. Schaefer and K.D. Keefer, in: *Better Ceramics Through Chemistry*, C.J. Brinker, D.E. Clark, and D.R. Ulrich, Eds., Materials Research Society, Vol.82 (North Holland, New York, 1985) p.1.

[212] D.W. Schaefer, in: *Proc. Materials Research Society Spring Meeting*, Palo Alto, California (April, 1986).

[213] K.D. Keefer, in: *Proc. Materials Research Society Spring Meeting*, Palo Alto, California (April, 1986).

[214] R. Zallen, *The Physics of Amorphous Solids* (Wiley, New York, 1983).

[215] P.J. Flory, *J. Am. Chem. Soc.*, 63 (1941) 3083.

[216] P.J. Flory, *J. Am. Chem. Soc.*, 63 (1941) 3091.

[217] P.J. Flory, *J. Am. Chem. Soc.*, 63 (1941) 3096.

[218] P.J. Flory, *J. Phys. Chem.*, 46 (1942) 132.

[219] W.H. Stockmayer, *J. Chem. Phys.*, 11 (1943) 45.

[220] P.J. Flory, *Faraday Discussions of the Chem. Soc.*, 57 (1974) 7.

[221] P.J. Flory, in: *Science of Ceramic Chemical Processing*, L.L. Hench and D.R. Ulrich, Eds. (Wiley, New York, 1986) p.415.

[222] D. Stauffer, A. Coniglio, and M. Adam, *Advances in Polymer Science*, 44 (1982) 103.

[223] J. Zarzycki, in: *Science of Ceramic Chemical Processing*, L.L. Hench and D.R. Ulrich, Eds. (Wiley, New York, 1986) p.21.

[224] B. Mandelbrot, *The Fractal Geometry of Nature* (Freeman, New York, 1977).

[225] B. Mandelbrot, *Fractals: Form, Chance, and Dimension* (Freeman, San Francisco, 1977).

[226] T.A. Witten and L.M. Sander, *Phys. Rev. Lett.*, 47 (1981) 1400.

[227] T.A. Witten and L.M. Sander, *Phys. Rev. B.*, 27 (1983) 5686.

[228] T.A. Witten and M.E. Cates, *Science*, 232 (1986) 1607.

[229] D. Avnir, D. Farin, and P. Pfeifter, *Nature*, 308 (1984) 261.

[230] H.D. Bale and P.W. Schmidt, *Phys. Rev. Lett.*, 53 (1984) 596.

[231] A. Craievich, M. Aegerter, D.I. Santos, T. Woignier, and J. Zarzycki, *J. Non-Cryst. Solids*, 86 (1986) 394.

[232] T.W. Zerda, I. Artaki, and J.J. Jonas, *J. Non-Cryst. Solids*, 81 (1986) 365.

[233] L.W. Ketls, N.J. Effinger, and S.M. Melpolder, *J. Non-Cryst. Solids*, 83 (1986) 353.

[234] D.M. Smith, C.L. Glaves, P.J. Davis, and C.J. Brinker, in: *Better Ceramics Through Chemistry III*, C.J. Brinker, D.E. Clark, and D.R. Ulrich, Eds., Vol.121 (Materials Research Society, Pittsburgh, 1988) p.657.

[235] G. Orcel, L.L. Hench, I. Artaki, J. Jonas, and T.W. Zerda, *J. Non-Cryst. Solids*, 105 (1988) 223.

[236] B.E. Yoldas, *J. Mat. Sci.*, 21 (1986) 1087.

[237] G.W. Scherer, in: *Better Ceramics Through Chemistry III*, C.J. Brinker, D.E. Clark, and D.R. Ulrich, Eds., Vol.121 (Materials Research Society, Pittsburgh, 1988) p.179.

[238] S.P. Prakash and N.R. Dhar, *J. Ind. Chem. Soc.*, 7 (1930) 417.

[239] A.C. Pierre and D.R. Uhlmann, in: *Better Ceramics Through Chemistry III*, C.J. Brinker, D.E. Clark, and D.R. Ulrich, Eds., Vol.121 (Materials Research Society, Pittsburgh, 1988) p.207.

[240] Y.P. Kimentova, L.F. Kiricheko, and Z.Z. Vysotakii, *Ubr. Khim. Zh.*, 26 (1970) 49.

[241] Z.Z. Voysotskii and D.N. Strazhesko, in: *Adsorption and Adsorbents*, D.N. Strazhesko, Ed., Vol.1 (Wiley, New York, 1973) p.55.

[242] Z.Z. Voysotskii, V.I. Galinskaya, V.I. Kolychev, V.V. Strelko, and D.N. Strazhesko, in: *Adsorption and Adsorbents*, D.N. Strazhesko, Ed., Vol.1 (Wiley, New York, 1973) p.72.

[243] R.Yu. Sheinfain and I.E. Neimark, in: *Adsorption and Adsorbents*, D.N. Strazhesko, Ed., Vol.1 (Wiley, New York, 1973) p.87.

[244] E.G. Acker, *J. Colloid Interface Sci.*, 32 (1970) 41.

[245] W.M. Jones and D.B. Fischbach, *J. Non-Cryst. Solids*, 101 (1988) 123.

[246] C.J. Brinker and G.W. Scherer, J. Non-Cryst. Solids, 70 (1985) 301.

[247] Dauger, F. Chaput, J.C. Pouxuiel, and J.F. Boilot, *J. de Physique*, 18 (1985) 79.

[248] A.C. Pierre and D.R. Uhlmann, in: *Ultrastructure Processing of Advanced Ceramics*, J.D. Mackenzie and D.R. Ulrich, Eds. (Wiley, New York, 1988) p.865.

[249] T.K. Sherwood, *Ind. Eng. Chem.*, 21 (1929) 12.

[250] T.K. Sherwood, *Ind. Eng. Chem.*, 24 (1929) 976.

[251] T.K. Sherwood, *Ind. Eng. Chem.*, 22 (1930) 132.

[252] F. Moore, *Trans. Brit. Ceram. Soc.*, 60 (1961) 517.

[253] R.B. Keey, *Drying, Principles and Practice* (Pergamon, New York, 1972).

[254] S. Whitaker, *Adv. Heat Transfer*, 13 (1977) 119.

[255] A.R. Cooper, in: *Ceramics Processing Before Firing*, G.Y. Onoda Jr. and L.L. Hench, Eds. (Wiley, New York, 1978) p.261.

[256] A.S. Mujumdar, Ed., *Advances in Drying*, Vol.1 (Hemisphere, New York, 1980).

[257] A.S. Mujumdar, Ed., *Advances in Drying*, Vol.2 (Hemisphere, New York, 1983).

[258] R.W. Ford, *Ceramics Drying* (Pergamon, New York, 1986).

[259] G.W. Scherer, *J. Non-Cryst. Solids*, 87 (1986) 199.

[260] G.W. Scherer, *J. Non-Cryst. Solids*, 89 (1987) 217.

[261] G.W. Scherer, *J. Non-Cryst. Solids*, 91 (1987) 83.

[262] G.W. Scherer, *J. Non-Cryst. Solids*, 91 (1987) 101.

[263] G.W. Scherer, *J. Non-Cryst. Solids*, 92 (1987) 122.

[264] G.W. Scherer, *J. Non-Cryst. Solids*, 100 (1988) 77.

[265] G.W. Scherer, in: *Ultrastructure Processing of Advanced Ceramics*, J.D. Mackenzie and D.R. Ulrich, Eds. (Wiley, New York, 1988) p.295.

[266] G.W. Scherer, in: *Proc. 4th International Conference on Ultrastructure Processing of Ceramics, Glasses and Composites*, Tucson, Arizona (February, 1989).

[267] T. Kawaguchi, J. Jura, N. Taneda, H. Hishikura, and Y. Kokubu, *J. Non-Cryst. Solids*, 82 (1986) 50.

[268] R.K. Dwivedi, *J. Mater. Sci. Lett.*, 5 (1986) 373.

[269] M. Fortes and M.R. Okos, in: *Advances in Drying*, A.S. Mujumdar, Ed., Vol.1 (Hemisphere, New York, 1980) p.119.

[270] S. Bruin and K.Ch.A.M. Luyben, in: *Advances in Drying*, A.S. Mujumdar, Ed., Vol.1 (Hemisphere, New York, 1980) p.155.

[271] J. van Brakel, in: *Advances in Drying*, A.S. Mujumdar, Ed., Vol.1 (Hemisphere, New York, 1980) p.217.

[272] H.H. Macey, *Trans. Brit. Ceram. Soc.*, 41 (1942) 73.

[273] M. Suzuki and S. Maeda, *J. Chem. Eng. Japan*, 1 (1968) 26.

[274] M.J.R. Wilson, *Drying Kinetics of Pure Silica Xerogels*, M.S. thesis (University of Florida, Gainesville, 1989).

[275] M.J.R. Wilson and L.L. Hench, in: *Proc. 4th International Conference on Ultrastructure Processing of Ceramics, Glasses and Composites*, Tucson, Arizona (February, 1989).

[276] M.J.R. Wilson and L.L. Hench, *J. Non-Crystal. Solids*, in press.

[277] S. Wallace and L.L. Hench, in: *Better Ceramics Through Chemistry III*, C.J. Brinker, D.E. Clark, and D.R. Ulrich, Eds., Vol.121 (Materials Research Society, Pittsburgh, 1988) p.355.

[278] S. Wallace and L.L. Hench, in: *Ultrastructure Processing of Advanced Ceramics*, J.D. Mackenzie and D.R. Ulrich, Eds. (Wiley, New York, 1988) p.873.

[279] S. Wallace and L.L. Hench, in: *Proc. 4th. International Conference on Ultrastructure Processing of Ceramics, Glasses and Composites*, Tucson, Arizona (February, 1989).

[280] S. Wallace, *Structure of Silica Gel Monoliths and Water*, Ph.D. Dissertation (University of Florida, Gainesville, 1989).

[281] S. Whitaker, in: *Advances in Drying*, A.S. Mujumdar, Ed., Vol.1 (Hemisphere, New York, 1980) p.23.

[282] T.M. Shaw, in: *Better Ceramics Through Chemistry II*, C.J. Brinker, D.E. Clark and D.R. Ulrich, Eds., Vol.73 (Materials Research Society, Pittsburgh, 1986) p.215.

[283] T.M. Shaw, *Phys. Rev. Lett.*, 59 (1987) 1671.

[284] F.N. Rhines, *Plansee Proceedings,* 3rd seminar, Reutte, Tyrol (1958) 38.

[285] F.N. Rhines, *Trans. AIME*, 166 (1946) 474.

[286] D.L. Johnson, in: *Processing of Crystalline Ceramics*, H. Palmour III, Ed. (Plenum, New York, 1978) p.137.

[287] H.E. Exner and G. Petzow, *Mat. Res.*, 13 (1980) 107.

[288] W.L. Vasconcelos, R.T. DeHoff, and L.L. Hench, in: *Proc. 4th International Conference on Ultrastructure Processing of Ceramics, Glasses and Composites*, Tucson, Arizona (February, 1989).

[289] G. Tamman, *Z. Anorg. Allg. Chem.*, 157 (1926) 321.

[290] J.A. Hedvall and E. Helin, *Jernkont. Ann.*, 82 (1927) 265.

[291] M. Ju. Balshin, *Vestn. Metalloprom.*, 16 (1939) 87.

[292] G.F. Huttig, *Kolloid Zeitschr.*, 97 (1941) 137.

[293] G.F. Huttig, *Kolloid Zeitschr.*, 97 (1941) 227.

[294] G.F. Huttig, *Kolloid Zeitschr.*, 97 (1941) 281.

[295] G.F. Huttig, *Kolloid Zeitschr.*, 98 (1942) 6.

[296] G.F. Huttig, *Kolloid Zeitschr.*, 98 (1942) 263.

[297] G.F. Huttig, *Metallwirtschaft*, 23 (1944) 367.

[298] G.F. Huttig, *Arch. Matallkunde*, 2 (1948) 93.

[299] J. Frenkel, *J. Phys. USSR*, 9 (1945) 385.

[300] B.Ja. Pines, *Zhur. Tekh. Fiz.*, 16 (1946) 737.

[301] J.K. Mackenzie and R. Shuttleworth, *Proc. Phys. Soc.*, 62 (1949) 833.

[302] G.C. Kuczynski, *J. Appl. Phys.*, 20 (1949) 1160.

[303] G.C. Kuczynski, *Met. Trans. AIME*, 185 (1949) 169.

[304] G.C. Kuczynski, *J. Appl. Phys.*, 21 (1950) 623.

[305] R.T. DeHoff, in: *Quantitative Microscopy*, R.T. DeHoff and F.N. Rhines, Eds. (McGraw-Hill, New York, 1968) p.291.

[306] R.K. Stringer, C.E. Warble, and L.S. Williams, in: *Kinetics of Reactions in Ionic Systems*, T.J. Gray and V.D. Frochette, Eds. (Plenum, New York, 1969) p.53.

[307] L.J. Buteau, *Applications of Topology to Sintering*, Ph.D. Dissertation (University of Florida, Gainesville, 1962).

[308] J.H. Steele, *A Topological Approach to Studying Microstructures*, Ph.D. Dissertation (University of Florida, Gainesville, 1967).

[309] E.H. Aigeltinger, *Experimental Determination of the Topological Properties of Sintered Structures*, Ph.D. Dissertation (University of Florida, Gainesville, 1969).

[310] P. Pinheiro S.N., *Cold Strength of Synthetic Ferric Oxide-Slag Briquettes in Relation to their Microstructural Evolution During Sintering*, Ph.D. Dissertation (University of Florida, Gainesville, 1973).

[311] F.R.N. Nabarro, in: *The Strength of Solids*, Report of Bristol Conference (Physical Society, London, 1948) p.75.

[312] H. Frohlich and R. Sack, *Proc. Roy. Soc. A.*, 185 (1946) 415.

[313] M.D. Sacks and T.Y. Tseng, *J. Am. Ceram. Soc.*, 67 (1984) 532.

[314] G.W. Scherer, *J. Am. Ceram. Soc.*, 60 (1977) 236.

[315] G.W. Scherer, *J. Am. Ceram. Soc.*, 60 (1977) 239.

[316] G.W. Scherer, *J. Am. Ceram. Soc.*, 60 (1977) 243.

[317] J. Brinker and G. Scherer, in: *Ultrastructure Processing of Ceramics, Glasses, and Composites*, L.L. Hench and D.R. Ulrich, Eds. (Wiley, New York, 1984) p.43.

[318] G.W. Scherer, *J. Am. Ceram. Soc.*, 67 (1984) 709.

[319] L.R. Snyder and J.W. Ward, *J. Phys. Chem.*, 70 (1966) 3941.

[320] M.L. Hair and W. Hertle, *J. Phys. Chem.*, 72 (1968) 2372.

[321] A.V. Kiselev and V.L. Lygin, *Infrared Spectra of Surface Compounds* (Wiley, New York, 1975).

[322] K. Susa, I. Matsuyama, S. Satoh, and T. Suganuma, *J. Non-Cryst. Solids*, 79 (1986) 165.

[323] H.A. Benesi and A.C. Jones, *J. Phys. Chem.*, 63 (1957) 179.

[324] A.V. Kiselev, in: *Structure and Properties of Porous Materials*, Vol.10, Colston Papers (Butterworth, London, 1958) p.195.

[325] R.S. McDonald, *J. Phys. Chem.*, 62 (1958) 1168.

[326] G.J. Young, *J. Colloid Sci.*, 13 (1958) 67.

[327] J.A. Hockey and B.A. Pethica, *Trans. of Faraday Soc.*, 57 (1961) 2247.

[328] M.L. Hair, *Infrared Spectroscopy in Surface Chemistry* (Dekker, New York, 1967).

[329] M. Yamane, S. Aso, and T. Sakano, *J. Mat. Sci.*, 14 (1979) 607.

[330] I. Matsuyama, K. Susa, S. Satoh, and T. Suganuma, *J. Am. Ceram. Bull.*, 63 (1984) 1408.

[331] L.C. Klein, T.A. Gallo, and G.J. Garvey, *J. Non-Cryst. Solids*, 63 (1984) 23.

[332] D.M. Krol and J.G. van Lierop, *J. Non-Cryst. Solids*, 63 (1984) 131.

[333] L.C. Klein and G.J. Garvey, in: *Ultrastructure Processing of Ceramics, Glasses, and Composites*, L.L. Hench and D.R. Ulrich, Eds. (Wiley, New York, 1984) p.88.

[334] T. Kawaguchi, H. Hishikura, J. Iura, and Y. Kokubu, *J. Non-Cryst. Solids*, 63 (1984) 61.

[335] T.A. Gallo and L.C. Klein, *J. Non-Cryst. Solids*, 82 (1986) 198.

[336] T. Mizuno, Ph.D. Dissertation (Université des Sciences et Techniques du Languedoc, Montpellier, France, 1985).

[337] T. Mizuno, J. Phalippou, and J. Zarzycki, *J. Glass Tech.*, 26 (1985) 39.

[338] J.F. Quinson, J. Dumas, and J. Serughetti, in: *Proc. 3rd Int. Conference on Non-Crystalline Solids*, C. Janot and A.F. Wright, Eds. (Physique, Paris, 1985).

[339] T.A. Gallo, C.J. Brinker, L.C. Klein, and G.W. Scherer, in: *Better Ceramics Through Chemistry*, C.J. Brinker, D.E. Clark, and D.R. Ulrich, Eds. (Elsevier, New York, 1984) p.85.

[340] A. Duran, C. Serna, V. Fornes, and J.M.F. Navarro, *J. Non-Cryst. Solids*, 82 (1986) 69.

[341] C.J. Brinker, E.P. Roth, D.R. Tallant, and G.W. Scherer, in: *Science of Ceramic Chemical Processing*, L.L. Hench and D.R. Ulrich, Eds. (Wiley, New York, 1986) p.37.

[342] C.J. Brinker, G.W. Scherer, and E.P. Roth, *J. Non-Cryst. Solids*, 72 (1985) 345.

[343] S. Lowell and J.E. Schields, *Powder Surface Area and Porosity*, 2nd ed. (Champion and Hall, London, 1984).

[344] F. London, *Z. Phys.*, 63 (1930) 245.

[345] S. Brunauer, L.S. Demig, W.S. Deming, and E. Teller, *J. Amer. Chem. Soc.*, 62 (1940) 1723.

[346] I. Langmuir, *J. Amer. Chem. Soc.*, 40 (1918) 1368.

[347] S. Brunauer, P.H. Emmett, and E. Teller, *J. Amer. Chem. Soc.*, 60 (1938) 309.

[348] J.H. de Boer, in: *The Structure and Properties of Porous Materials*, D.H. Everett and F.S. Stone, Eds. (Butterworths, London, 1958) p.68.

[349] V.W. McBain, *J. Amer. Chem. Soc.*, 57 (1935) 699.

[350] J.C.P. Broekhoff and B.G. Linsen, in: *Physical and Chemical Aspects of Adsorbents and Catalysts*, B.G. Linsen, Ed. (Academic Press, London, 1970) p.1.

[351] W.B. Spencer Jr., *Determination of the Porous Properties of Some Silica Gels*, M.S. thesis (University of Pittsburgh, Pittsburgh, Pennsylvania, 1950).

[352] B.F. Roberts, *Proc. 145th National Meeting of the Amer. Chem. Soc.*, New York (September, 1963).

[353] S. Brunauer, R. Sh. Mikhail, and E.E. Bodor, *J. Colloid and Interface Sci.*, 24 (1967) 451.

[354] R. Sh. Mikhail, S. Brunauer, and E.E. Bodor, *J. Colloid and Interface Sci.*, 26 (1968) 54.

[355] W. Cao, R. Gerhardt, and J.B. Watchman Jr., *J. Am. Ceram. Soc.*, 71 (1988) 1108.

[356] S.P. Mukherjee, J.F. Cordaro, and J.C. Debsikdar, *Adv. Ceram. Mater.*, 3 (1988) 463.

[357] R.T. DeHoff, in: *Encyclopedia of Materials Science and Engineering*, M.B. Bever, Ed. (Pergamon, Oxford, 1986) p.4633.

[358] D.J. Struik, *Lectures on Classical Differential Geometry* (Addison-Wesley, Cambridge, 1950).

[359] J.W. Cahn, *Trans. AIME*, 239 (1967) 611.

[360] R.T. DeHoff, *Trans. AIME*, 239 (1967) 617.

[361] J.E. Hilliard, in: *Quantitative Microscopy*, R.T. DeHoff and F.N. Rhines, Eds. (McGraw-Hill, New York, 1968) p.45.

[362] E.E. Underwood, in: *Quantitative Microscopy*, R.T. DeHoff and F.N. Rhines, Eds. (McGraw-Hill, New York, 1968) p.77.

[363] F.N. Rhines, R.T. DeHoff, and J. Kronsbein, *A Topological Study of the Sintering Process*, Final Report for the U.S. Atomic Energy Commission (University of Florida, Gainesville, 1969).

[364] E.E. Underwood, *Quantitative Stereology* (Addison-Wesley, Reading, Massachusetts, 1970).

[365] F.N. Rhines, *Microstructology* (Riederer-Verlag, Stuttgart, 1986).

[366] R.T. DeHoff, *Metall. Trans. A.*, 10 (1979) 1948.

[367] W.L. Vasconcelos, P. Pinheiro, and C.A. Bottrel-C., *Metalurgia-ABM*, 38 (1982) 289.

[368] P. Pinheiro and W.L. Vasconcelos, *Proc. 3rd Conference on Physical Metallurgy and Heat Treatment-ABM*, São Paulo, Brasil (1982) p.25.

[369] P. Pinheiro and W.L. Vasconcelos, *Metalurgia-ABM*, 39 (1983) 527.

[370] W.L. Vasconcelos, P. Pinheiro, and C.A. Bottrel-C., *Proc. 38th Annual Congress of the ABM*, Vol.4, São Paulo, Brasil (1983) p.369.

[371] J. Stillwell, *Classical Topology and Combinatorial Group Theory* (Springer-Verlag, New York, 1980).

[372] B.E. Sims, *Fundamentals of Topology* (Macmillan, New York, 1976).

[373] W.J. Thron., *Topological Structures* (Holt, Rinehart and Winston, New York, 1966).

[374] L. Euler, *Novi Comment. Acad. Sci. Petrop.*, 4 (1752) 109.

[375] J.B. Listing, *Gottinger Studien* (1847) 811.

[376] G. Cantor, *Math. Ann.*, 21 (1883) 545.

[377] B. Reimann, *Gesammette Mathematische Werke*, 2nd ed., Leipzig (1982).

[378] H. Poincaré, *J. Ecole Polytechnique*, 1 (1895) 1.

[379] F. Riesz, *Math. Naturwiss. Ber. Ungarn*, 24 (1906) 309.

[380] M. Fréchet, *Rend. Palermo*, 22 (1906) 1.

[381] E.H. Moore, *Proc. Natl. Acad. Sci. U.S.*, 1 (1915) 628.

[382] S. Eilenberg and N. Steenrod, *Foundations of Algebraic Topology* (Princeton University Press, 1952).

[383] E.M. Patterson, *Topology*, 2nd ed. (Addison-Wesley, Reading, Massachusetts, 1961).

[384] P.S. Aleksandrov, *Combinatorial Topology*, Vol.3 (Graylock Press, Albany, 1960).

[385] J.G. Hocking and G.S. Young, *Topology* (Addison-Wesley, Reading, Massachusetts, 1961).

[386] P. Alexandroff, *Elementary Concepts of Topology* (Dover, New York, 1961).

[387] J. Vick, *Homology Theory* (Academic Press, New York, 1973).

[388] J.L. Kelley, *General Topology* (Springer-Verlag, New York, 1975).

[389] W.S. Massey, *Algebraic Topology: An Introduction* (Springer-Verlag, New York, 1977).

[390] J.R. Weeks, *The Shape of Space* (Marcel Dekker, New York, 1985).

[391] P.J. Giblin, *Graphs, Surfaces and Homology* (Chapman and Hall, London, 1977).

[392] M. Henle, *A Combinatorial Introduction to Topology* (W.H. Freeman, San Francisco, 1979).

[393] R.T. DeHoff, E.H. Aigeltinger, and K.R. Craig, *J. Microsc.*, 95 (1972) 69.

[394] J.W. Cahn and R.L. Fullman, *Trans. Metall. Soc. AIME*, 206 (1956) 610.

[395] R.T. DeHoff, *Trans. Metall. Soc. AIME*, 224 (1962) 474.

[396] R.T. DeHoff, *Trans. Metall. Soc. AIME*, 230 (1964) 764.

[397] R.T. DeHoff, *Trans. Metall. Soc. AIME*, 233 (1965) 25.

[398] F.N. Rhines and R.T. DeHoff, in: *Sintering and Homogeneous Catalysis*, G.C. Kuczynszi, A.E. Miller, and G.A. Sargent, Eds. (Plenum, New York, 1984) p.49.

[399] G.E. Dieter, *Mechanical Metallurgy*, 3rd ed. (McGraw-Hill, New York, 1986).

[400] J.J. Gilman, in: *The Physics and Chemistry of Ceramics*, C. Klingsberg, Ed. (Gordon and Breach, New York, 1963) p.240

[401] S.M. Wiederhorn, in: *Mechanical and Thermal Properties of Ceramics*, J.B. Watchman Jr., Ed., Special Publications 303 (National Bureau of Standards, Washington, 1969) p.217.

[402] W.B. Hillig, *J. Appl. Phys.*, 32 (1961) 74.

[403] B.A. Proctor, J. Whitney, and J.W. Johnston, *Proc. Roy. Soc.*, 297A (1967) 534.

[404] A.A. Griffith, *Philos. Trans. R. Soc. London*, 221A (1920) 163.

[405] A.A. Griffith, *Trans. Am. Soc. Met.*, 61 (1968) 871.

[406] C.E. Inglis, *Trans. Inst. Nav. Archit.*, 55 (1913) 219.

[407] J. Cornelissen and A.L. Zijlstra, in: *Symposium Sur la Resistance Mecanique du Verre et les Moyens de L'améliorer* (Union Scientifique Continentale du Verre, Florence, 1961) p.337.

[408] B.R. Lawn, *Fract. Mech. Ceram.*, 5 (1983) 1.

[409] R.E. Reed-Hill, *Princípios de Metalurgia Física*, 2nd ed. (Guanabara Dois, Rio de Janeiro, 1982).

[410] J.G. Williams, *Fracture Mechanics of Polymers* (Horwood, Chichester, 1984).

[411] P.J. Blau and B.R. Lawn, *Microindentation Techniques in Materials Science and Engineering*, Publication 889 (ASTM, Philadelphia, 1985).

[412] D.R. Clarke and K.J. Faber, *J. Phys. Chem. Solids*, 48 (1987) 1115.

[413] H. Rawson, *Glastech. Ber.*, 61 (1988) 231.

[414] S. Ho and M. Tomozawa, *J. Am. Ceram. Soc.*, 65 (1982) 368.

[415] Y. Bando, S. Ho, and M. Tomozawa, *J. Am. Ceram. Soc.*, 67 (1984) C36.

[416] B.R. Lawn, K. Jakus, and A.C. Gonzalez, *J. Am. Ceram. Soc.*, 68 (1985) 25.

[417] M. Tomozawa, K. Hirao, and P.E. Bean, *J. Am. Ceram. Soc.*, 69 (1986) C186.

[418] K. Hirao and M. Tomozawa, *J. Am. Ceram. Soc.*, 70 (1987) 43.

[419] K. Hirao and M. Tomozawa, *J. Am. Ceram. Soc.*, 70 (1987) 377.

[420] P.K. Gupta and N.J. Jubb, *J. Am. Ceram. Soc.*, 64 (1981) 112.

[421] Y. Kimura, T. Yagasaki, and T. Kunio, J. *Soc. Mater. Sci. Japan*, 32 (1983) 315.

[422] R.F. Cook, B.R. Lawn, and C.J. Fairbanks, *J. Am. Ceram. Soc.*, 68 (1985) 616.

[423] D.H. Roach and A.R. Cooper, *J. Am. Ceram. Soc.*, 68 (1985) 632.

[424] M. Yoda, *Proc. Conf. Japan Soc. Design and Drafting* (1986).

[425] M. Yoda, *Engineering Fracture Mechanics*, 28 (1987) 77.

[426] M.G. Mendiratta and J.J. Petrovic, *J. Mater. Sci.* 11 (1976) 973.

[427] E.G. Evans and E.A. Charles, *J. Am. Ceram. Soc.*, 59 (1976) 371.

[428] J.J. Petrovic and M.G. Mendiratta, in: *Fracture Mechanics Applied to Brittle Materials*, S.W. Freiman, Ed. (ASTM, Philadelphia, 1979) p.83.

[429] P. Chantikul, G.R. Anstis, B.R. Lawn, and D.B. Marshall, *J. Am. Ceram. Soc.*, 64 (1981) 533.

[430] G.R. Anstis, P. Chantikul, B.R. Lawn, and D.B. Marshall, *J. Am. Ceram. Soc.*, 64 (1981) 539.

[431] R.F. Cook and B.R. Lawn, *J. Am. Ceram. Soc.*, 66 (1983) C200.

[432] W.C. LaCourse, *Glass Industry* (June, 1987) 14.

[433] R. Bourne, N.D. Cowan, and S.M. Budd, *Glass Technology*, 25 (1984) 145.

[434] A. Rudnick, *The evaluation and Interpretation of Mechanical Properties of Brittle Materials*, DCIC Report 68-3 (Battelle Memorial Institute, Columbus, Ohio, 1968).

[435] W.F. Brace, in: *The Effects of Voids on Material Deformation*, S.C. Cowin and M.M. Carroll, Eds. (ASME, New York, 1976) p.1.

[436] W. Weibull, *Ing. Ventenskaps Akad. Handl*, No.151, Stockholm (1939).

[437] W. Weibull, *Ing. Vertenskaps Akad. Handl.*, No.153, Stockholm (1939).

[438] W. Weibull, *J. Appl. Mech.*, 18 (1951) 293.

[439] W. Weibull, *Mater. Res. Stds.* (May, 1962) 405.

[440] A.M. Freudenthal, in: *Fracture. An Advanced Treatise*, Vol.2, H. Liebowitz, Ed. (Academic Press, New York, 1968) p.591.

[441] V.V. Bolotin, *Statistical Methods in Structural Mechanics* (Holden-Day, San Francisco, 1969).

[442] D.G. Holloway, *The Physical Properties of Glass* (Wykeham Publications, London, 1973).

[443] Testing Method for Flexural Strength (Modulus of Rupture of High Performance Ceramics, *Japanese Industrial Standard*, JIS R 1601-1981 (Japanese Standards Association, 1981).

[444] M.F. Ashby and D.R.H. Jones, *Engineering Materials 2* (Pergamon, Oxford, 1986).

[445] M.F. Ashby and S.D. Hallam, *Acta. Metall.*, 34 (1986) 497.

[446] C.G. Sammis and M.F. Ashby, *Acta. Metall.*, 34 (1986) 511.

[447] A.R. Jumikis, *Rock Mechanics*, 2nd ed. (Gulf Publishing, Houston, 1983).

[448] F.L.L.B. Carneiro and A. Barcellos, *Union of Testing and Research Laboratories for Materials and Structures*, No.13. (March, 1953).

[449] P.J.F. Wright, *Magazine of Concrete Research*, 7 (1955) 87.

[450] R. Berenbaum and I. Brodie, *British J. Appl. Phys.* 10 (1959) 281.

[451] L. Leerivain and B. Lamberg, *L' Ind. Ceramique*, No.534 (1961) 367.

[452] A. Rudnick, A.R. Hunter, and F.C. Holden, *Mater. Res. Stand.*, 3 (1963) 283.

[453] R.M. Spriggs, L.A. Brissette, and T Vasilos, *Mater. Res. Stand.*, 4 (1964) 218.

[454] L. Mordfin and M.J. Kerper, in: *Mechanical and Thermal Properties of Ceramics*, J.B. Watchman Jr., Ed., Special Publications 303 (National Bureau of Standards, Washington, 1969) p.243.

[455] S.W. Freiman and L.L. Hench, *J. Am. Ceram. Soc.*, 55 (1972) 86.

[456] J.A. Hudson, *A Critical Examination of Indirect Tensile Strength Tests for Brittle Rocks*, Ph.D. Dissertation (University of Minnesota, 1970).

[457] D.G. Holloway, *Glass Technol.*, 27 (1986) 120.

[458] M.G. Lofthouse and P. Burroughs, *J. Thermal Analysis*, 13 (1978) 439.

[459] S. Timoshenko, *Vibration Problems in Engineering*, 3rd ed. (Wiley, New York, 1954).

[460] D.R. Bland, *The Theory of Linear Viscoelasticity* (Pergamon, Oxford, 1960).

[461] D.J. Massa, *J. Appl. Phys.*, 44 (1973) 2595.

[462] T. Kaneko, *J. Phys. D. Appl. Phys.*, 8 (1975) 1927.

[463] B.E. Read and G.E. Dean, *The Determination of Dynamic Properties of Polymer and Composites* (Wiley, New York, 1978).

[464] F.A. Hummel, *J. Am. Ceram. Soc.*, 35 (1952) 64.

[465] K.M. Merz, W.R. Brown, and H.P. Kirchner, *J. Am. Ceram. Soc.*, 45 (1962) 531.

[466] O.M. Stansfield, *J. Am. Ceram. Soc.*, 48 (1965) 436.

[467] V.J. Tennery, *J. Am. Ceram. Soc.*, 49 (1966) 483.

[468] W.D. Kingery, *J. Am. Ceram. Soc.*, 37 (1954) 602.

[469] J.H. Lauchner, R.L. Cook, and A.I. Andrews, *J. Am. Ceram. Soc.*, 40 (1957) 410.

[470] P.K. Foster and I.R. Hughes, *J. Am. Ceram. Soc.*, 49 (1966) 515.

[471] B.R. Karstetter and R.O. Voss, *J. Am. Ceram. Soc.*, 50 (1967) 133.

[472] H.P. Kirchner, R.M. Gruver, and R.E. Walker, *J. Am. Ceram. Soc.*, 50 (1967) 169.

[473] G.H. Beall, B.R. Karstetter, and H.L. Rittler, *J. Am. Ceram. Soc.*, 50 (1967) 181.

[474] A.Q. Tool, *J. Am. Ceram. Soc.*, 31 (1948) 177.

[475] H.N. Ritland, *J. Am. Ceram. Soc.*, 39 (1956) 403.

[476] H.E. Hagy and H.N. Ritland, *J. Am. Ceram. Soc.*, 40 (1957) 436.

[477] T. Takamori, *J. Am. Ceram. Soc.*, 46 (1963) 366.

[478] E.A. Bush and F.A. Hummel, *J. Am. Ceram. Soc.*, 42 (1959) 388.

[479] R. Brueckner, *Glastech. Ber.*, 37 (1964) 459.

[480] R.L. Coble and W.D. Kingery, *J. Am. Ceram. Soc.*, 38 (1955) 33.

[481] R.L. Coble and W.D. Kingery, *J. Am. Ceram. Soc.*, 39 (1956) 377.

[482] R.E. Fryxell and B.H. Chandler, *J. Am. Ceram. Soc.*, 47 (1964) 283.

[483] D.R. Gaskell, *Introduction to Metallurgical Thermodynamics*, 2nd ed. (McGraw-Hill, New York, 1981).

[484] R.E. Hummel, *Electronic Properties of Materials* (Springer-Verlag, New York, 1985).

[485] G.R. Clusener, in: *ALP. Conf. Proc. No.3-Thermal Expansion (American Institute of Physics*, New York, 1972) p.51.

[486] W.A. Plummer, in: *ALP Conf. Proc. No.17-Thermal Expansion* (American Institute of Physics, New York, 1974) p.147.

[487] Y.S. Touloukian, R.K. Kirby, R.E. Taylor, and T.Y.R. Lee, Eds., *Thermophysical Properties of Matter*, Vol.13 (Plenum, New York, 1978).

[488] O.J. Wittemore Jr. and N.N. Ault, *J. Am. Ceram. Soc.*, 39 (1956) 274.

[489] R.O. Simmons and R.W. Balluffii, *Phys. Rev.*, 117 (1960) 52.

[490] J. Otto and W. Thomas, *Z. Physik*, 175 (1963) 337.

[491] T.H. Nielsen and M.H. Leipold, *J. Am. Ceram. Soc.*, 46 (1963) 381.

[492] B.R. Miccoli and P.J.B. Shaffer, *J. Am. Ceram. Soc.*, 47 (1964) 351 and 536 (correction).

[493] B. Ohnysky and F.K. Rose, *J. Am. Ceram. Soc.*, 47 (1964) 398.

[494] J.B. Conway and A.C. Losekamp, *Trans. Met. Soc. AIME*, 236 (1966) 702.

[495] B.D. Rothrock and R.K. Kirby, *J. Res. NBS*, 71C (1967) 85.

[496] P.S. Gaal, *High Temp. High Press.*, 4 (1972) 49.

[497] J.B. Saunders, *J. Res. NBS*, 23 (1939) 179.

[498] F.C. Nix and D. MacNair, *Rev. Sci. Instr.*, 12 (1941) 66.

[499] L.A. Willey and W.L. Fink, *Am. Inst. Mining Met. Engrs., Technical Publication No.1859* (AIME, 1944).

[500] J.B. Saunders, *J. Res. NBS*, 35 (1945) 157.

[501] R.L. Ersner, *Rev. Sci. Instr.*, 29 (1958) 521.

[502] D.B. Fraser, *Can. J. Phys.*, 43 (1965) 193.

[503] J. Dyson, *Interferometry as a Measuring Tool* (Hunt Barnard, Asbury, New Jersey, 1970).

[504] F.A. Mauer and L.H. Bolz, in: *Advances in X-Ray Analysis*, W.M. Mueller, Ed., Vol.5 (Plenum, New York, 1961) p.546.

[505] W. Ostertag and G.R. Fischer, *Rev. Sci. Instr.*, 39 (1968) 888.

[506] F.A. Mauer and T.A. Hahn, in: *AIP Conf. Proc. No.3-Thermal Expansion* (American Institute of Physics, New York, 1972) p.139.

[507] G.K. White, *Cryogenics*, 1 (1961) 151.

[508] J.F. Kos and J.L.G. Lamarche, *Can. J. Phys.*, 47 (1969) 2509.

[509] J.S. Browder and S.S. Ballard, *Appl. Opt.*, 8 (1969) 793.

[510] W.F. Schlosser, G.M. Grahan, and P.P.M. Meincke, *J. Phys. Chem. Solids*, 32 (1971) 927.

[511] G.K. White and J.G. Collins, *J. Low Temp. Phys.*, 7 (1972) 43.

[512] F.A. Hummel, *J. Am. Ceram. Soc.*, 33 (1950) 102.

[513] C. Zwikker, *Physical Properties of Solid Materials* (Pergamon, London, 1954).

[514] P. Chappuis, *Verh. Naturf. Ges. Basel*, 16 (1903) 173.

[515] H. Donaldson, *Proc. Phys. Soc. London*, 24 (1912) 186.

[516] H.L. Callendar, *Nature,* 92 (1913) 467.

[517] N.E. Wheeler, *Trans. Roy. Soc.* Can., 8 (1914) 139.

[518] K. Scheel and W. Heuse, *Verh. Dtsch. Physc. Ges.*, 16 (1914) 1.

[519] J.A. Beattle, B.E. Blaisdell, J. Kaye, H.T. Gerry, and C.A. Johnson, *Amer. Acad. Arts Sci.*, 74 (1941) 371.

[520] J. Biscoe, C.S. Robinson Jr., and B.E. Warren, *J. Am. Ceram. Soc.*, 22 (1939) 180.

[521] L.F. Oldfield, *Glass Techn.*, 5 (1964) 41.

[522] D.H. Wienberg, J.R. Gott III, and A.L. Melott, *The Astrophysical J.*, 321 (1987) 2.

[523] F.N. Rhines, C.R. Craig, and R.T. DeHoff, *Met. Trans.*, 5 (1974) 413.

[524] F.N. Rhines and J.B. Hernu, *Scripta Met.*, 11 (1977) 155.

[525] R.A. Gregg and F.N. Rhines, *Met. Trans.*, 4 (1973) 1365.

[526] E.H. Aigeltinger and R.T. DeHoff, *Met. Trans. A*, 6 (1975) 1853.

[527] F.N. Rhines and J.S. Wolf, *Trans. AIME*, 1 (1970) 1701.

[528] F.N. Rhines and R.G. Connell, *J. Electr. Soc.*, 124 (1977) 1122.

[529] W.J. Babyak and F.N. Rhines, *Trans. AIME*, 218 (1960) 21.

[530] F.N. Rhines, *Met. Trans.*, 1 (1970) 1105.

[531] F.N. Rhines, W.E. Bond, and M.A. Kissel, *Trans. ASM*, 48 (1956) 919.

[532] P. Pinheiro and F.N. Rhines, *Proc. 35th Annual Congress of the ABM*, Vol.1, São Paulo, Brasil (1980).

[533] F.B. Seely and J.O. Smith, *Resistance of Materials*, 4th ed. (Wiley, New York, 1962).

[534] A.P. Boresi and O.M. Sidebottom, *Advanced Mechanics of Materials*, 4th ed. (Wiley, New York, 1985).

BIOGRAPHICAL SKETCH

Wander Luiz Vasconcelos was born October 13, 1958, in Varginha, State of Minas Gerais, Brazil. He attended local schools and graduated from high school in 1975. In 1981 Mr. Vasconcelos graduated with honors from *Universidade Federal de Minas Gerais* (Federal University of Minas Gerais), Belo Horizonte, Brazil, with a degree of Metallurgical Engineer. From 1982 to 1984 he enrolled in the Graduate School of the *Universidade Federal de Minas Gerais*, from which he received a title of Specialist in Physical Metallurgy in 1984, and the degree of Master of Science in metallurgical engineering, also in 1984. From 1982 to 1985 Mr. Vasconcelos worked as consulter of the *Companhia Vale do Rio Doce*, Belo Horizonte, Brazil, in the areas of microstructural identification and characterization of iron ores. In 1982 he joined the faculty of the *Universidade Federal de Minas Gerais* as Assistant Professor.

In the Fall of 1985 he entered the Graduate School of the University of Florida, from which he received a degree of Master of Science in materials science and engineering in 1988. Since then he has pursued work toward the degree of Doctor of Philosophy in materials science and engineering.

The author is married to the former Josiane Lagares Côrtes Costa from Governador Valadares, Brazil, and is the father of one son. He is

a member of the Brazilian Society for Metals, American Ceramic Society, The ASM International, The Minerals, Metals and Materials Society, Sigma Xi, Keramos, and Alpha Sigma Mu.

I certify that I have read this study and that in my opinion it conforms to acceptable standards of scholarly presentation and is fully adequate, in scope and quality, as a dissertation for the degree of Doctor of Philosophy.

Larry L. Hench, Chair
Graduate Research Professor of
Materials Science and Engineering

I certify that I have read this study and that in my opinion it conforms to acceptable standards of scholarly presentation and is fully adequate, in scope and quality, as a dissertation for the degree of Doctor of Philosophy.

Robert T. DeHoff, Cochair
Professor of Materials Science
and Engineering

I certify that I have read this study and that in my opinion it conforms to acceptable standards of scholarly presentation and is fully adequate, in scope and quality, as a dissertation for the degree of Doctor of Philosophy.

Robert E. Reed-Hill
Professor Emeritus of Materials
Science and Engineering

I certify that I have read this study and that in my opinion it conforms to acceptable standards of scholarly presentation and is fully adequate, in scope and quality, as a dissertation for the degree of Doctor of Philosophy.

E. Dow Whitney
Professor of Materials Science
and Engineering

I certify that I have read this study and that in my opinion it conforms to acceptable standards of scholarly presentation and is fully adequate, in scope and quality, as a dissertation for the degree of Doctor of Philosophy.

Richard L. Scheaffer
Professor of Statistics

This dissertation was submitted to the Graduate Faculty of the College of Engineering and to the Graduate School and was accepted as partial fulfillment of the requirements for the degree of Doctor of Philosophy.

August 1989

Dean, College of Engineering

Dean, Graduate School